

Marcus Vinicius Duarte Ferreira

**ESTUDO TERMO-ESTRUTURAL DE POÇOS EQUIPADOS
COM TUBOS ISOLADOS A VÁCUO**

Tese submetida ao Programa de Pós-Graduação em Engenharia Mecânica da Universidade Federal de Santa Catarina para a obtenção do Grau de Doutor em Engenharia Mecânica.

Orientador: Prof. Jader Riso Barbosa Jr., PhD

Co-orientador: Prof. Alexandre Kupka da Silva, PhD

Florianópolis
2017

Marcus Vinicius Duarte Ferreira

**THERMAL-STRUCTURAL STUDY OF WELLBORES WITH
VACUUM INSULATED TUBINGS**

Thesis submitted to the Program of
Post-Graduation in Mechanical
Engineering of Federal University of
Santa Catarina to apply for Doctorate
Degree in Mechanical Engineering.

Advisor: Prof. Jader Riso Barbosa Jr.,
PhD

Co-advisor: Prof. Alexandre Kupka da
Silva, PhD

Florianópolis
2017

Ficha de identificação da obra elaborada pelo autor, através do Programa de Geração Automática da Biblioteca Universitária da UFSC.

Ferreira, Marcus Vinicius Duarte
Estudo termo-estrutural de poços equipados com
tubos isolados a vácuo / Marcus Vinicius Duarte
Ferreira ; orientador, Jader Riso Barbosa Jr,
coorientador, Alexandre Kupka da Silva, 2017.
255 p.

Tese (doutorado) - Universidade Federal de Santa
Catarina, Centro Tecnológico, Programa de Pós
Graduação em Engenharia Mecânica, Florianópolis, 2017.

Inclui referências.


1. Engenharia Mecânica. 2. Aumento de pressão no
anular (APB). 3. Tubos isolados a vácuo (VIT). 4.
Escoamento multifásico. 5. Transferência de calor.
I. Barbosa Jr, Jader Riso. II. Silva, Alexandre
Kupka da. III. Universidade Federal de Santa
Catarina. Programa de Pós-Graduação em Engenharia
Mecânica. IV. Título.

Marcus Vinicius Duarte Ferreira

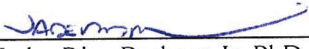
ESTUDO TERMO-ESTRUTURAL DE POÇOS EQUIPADOS COM TUBOS ISOLADOS A VÁCUO

Esta Tese foi julgada adequada para obtenção do Título de “Doutor em Engenharia Mecânica”, e aprovada em sua forma final pelo Programa de Pós-Graduação em Engenharia Mecânica.


Florianópolis, 24 de Novembro de 2017.



Prof. Jonny Carlos da Silva, PhD
Coordenador do Curso

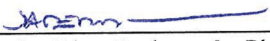


Prof. Jader Riso Barbosa Jr, PhD – Orientador
Universidade Federal de Santa Catarina




Prof. Alexandre Kupka da Silva, PhD – Co-orientador
Universidade Federal de Santa Catarina

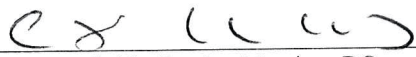
Banca Examinadora:



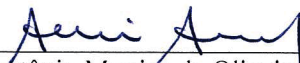
Prof. Jader Riso Barbosa Jr, PhD – Orientador
Universidade Federal de Santa Catarina



Angela Ourivio Nieckele, PhD
Pontifícia Universidade Católica do Rio de Janeiro



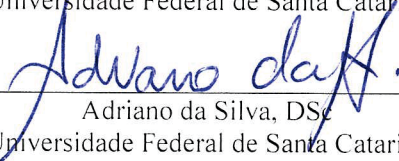
André Leibsohn Martins, DSc
PETROBRAS/CENPES



Amir Antônio Martins de Oliveira Junior, PhD
Universidade Federal de Santa Catarina



Marcia Barbosa Henriques Mantelli, PhD
Universidade Federal de Santa Catarina



Adriano da Silva, DSc
Universidade Federal de Santa Catarina

I would like to dedicate this thesis to my grandmother Rosa who passed away while I was away from her, on the 2nd of November of 2014, and to my loving family who has been my support team throughout this investigation.

ACKNOWLEDGMENTS

Throughout the last four years of systematically developing my thesis, I have continuously expanded my knowledge by deeply exploring the subject. I have always received so much support and encouragement from numerous people along the way.

I would like to express my appreciation and gratitude to my academic advisor, Prof. PhD Jader Barbosa. His rigorous attitude towards science and diligent style of work have deeply affected my thesis and me personally. The completion of this thesis has been strongly influenced by his vast research expertise.

I would like to express my appreciation and gratitude to my co-advisor Prof. PhD Alex Kupka. His profound expertise, friendly disposition and great sense of humor have also positively affected many sections of my thesis.

I wish to express my gratitude to MSc Thomas Hafemann and MSc Johann Barcelos for providing me with kind suggestions and references for my thesis.

I am thankful to Prof. PhD Rashid Hasan for hosting me at Texas A&M University, for his continued interest in the research issues and for his support during my stay in College Station.

I acknowledge the friends I made at Texas A&M University, my officemates and the whole staff from the Department of Petroleum Engineering.

I wish to thank the Brazilian team in College Station, all the friends I made in the city, especially DSc. Cesar Kiono, who helped me in developing code.

I wish to thank the entire POLO staff and all the students who always offered their support and even those who just brightened up a hard day by telling a joke.

I thank my colleagues from CENPES, Andre, Alex, Hugo, Kadu, Isabel, Izabelle, Mauro, Camila, everyone. I also wish to thank my current manager, André Concatto and my ex-managers Antônio Lage and Augusto Borella for fully supporting me.

I wish to thank all my friends and relatives from the WhatsApp groups called “Rural” and “Os Granado ou Ferreira” for supporting me throughout this journey.

I wish to thank the Federal University of Santa Catarina for accepting me as a doctoral student and for giving me the opportunity to participate in classes given by an international level team of professors.

I wish to thank the Petrobras S.A. for supporting my study both in Florianopolis and in College Station/USA, despite the company's financial hardship during my studies.

I acknowledge the Texas A&M University for accepting me as a visiting researcher and for giving me all support to conduct my thesis.

Finally, I would like to express my gratitude towards my family. Thank you to my grandparents Braz and Rosa (in memoriam) and to my parents Carlos and Mary for trusting me, supporting me and for all the infinite love shown. A special thanks to my wife, Gleice Ferreira, for helping me and sticking by my side on even the toughest days, for supporting the kids and me and for following me wherever I go; I love you. Last, but not least, I wish to thank my sons, Vinicius and Marx Ferreira, for bringing me so much joy and happiness when returning home and for accompanying me on this journey. Sorry for those hard days and I cannot thank you enough. I have fallen in love with you.

*Knowledge is the key to unlocking your
potential.
(Unknown Author)*

RESUMO

A exploração e produção de reservatórios de elevada pressão e temperatura e com grande potencial de produção de hidrocarbonetos, em cenários de águas profundas, impõe diversos desafios no que tange a integridade estrutural de poços de petróleo. Um problema recorrente é causado pelo fenômeno conhecido como APB (*Annular Pressure Buildup*), consequência do processo de aquecimento do poço durante a produção de hidrocarbonetos oriundos do reservatório. Este aquecimento afeta o espaço anular do poço, que se encontra completamente selado e preenchido com fluido de perfuração, que sofre expansão térmica. A expansão do fluido aumenta a pressão anular para níveis que podem ultrapassar a resistência mecânica dos elementos tubulares que compõem o poço, levando à perda de sua integridade. A fim de evitar o colapso do tubo, várias estratégias são utilizadas para mitigar o APB, tal como o *Vacuum Insulated Tubing* (VIT). A técnica consiste na utilização de dois tubos de produção concêntricos que são soldados nas suas extremidades, formando um espaço anular, que então é evacuado, reduzindo a transferência de calor radial. No entanto, uma vez que a conexão entre cada dois tubos não é termicamente isolada, a transferência de calor pode ser significativa nesta região. O presente trabalho propõe um estudo teórico da transferência de calor no sistema VIT. Primeiramente, o problema térmico foi modelado e simulado com o auxílio de um software comercial utilizando o método dos volumes finitos (MVF). Foi proposto um modelo em regime permanente baseado em circuito térmico equivalente bidimensional (modelo nodal). Um refino do modelo nodal foi efetuado para que apresentasse resultados similares aos encontrados utilizando o MVF, sendo uma alternativa fácil para incorporação em um simulador multifísico de produção de petróleo em poços. Desta forma, o modelo térmico nodal do VIT foi acoplado a um simulador de produção de poços (hidrodinâmico-térmico-estrutural) gerando resultados mais realistas do que os atualmente empregados na indústria de petróleo. Estes resultados foram validados com dados de campo para dois poços de petróleo e contra resultados oriundos de um software comercial extensivamente utilizado por engenheiros de petróleo em projeto de poços.

Palavras-chave: VIT, APB, Poço, Petróleo, Análise nodal, Simulação numérica.

ABSTRACT

Annular Pressure Buildup (APB) is a recurring problem that affects high pressure and high temperature wells during oil exploration and production in deepwater scenarios. Wellbore heating is caused by the upward flow of heated hydrocarbons towards the wellhead. The temperature rise affects the annular space of the borehole, which is often sealed and completely filled with drilling fluid, causing its expansion. The expansion of the fluid increases the annulus pressure to levels that can surpass the structural limits of the materials, posing a risk to the wellbore integrity. In order to avoid the collapse of the tube, several strategies are commonly used to mitigate APB, such as the use of Vacuum Insulated Tubing (VIT). This technique consists of using two concentric metallic tubes that are welded at their extremities, forming an annular space that is subsequently evacuated to minimize radial heat transfer. However, since the connection between each pair of tubes is not insulated, heat transfer can be significant in VIT junction region. This work proposes a theoretical analysis of the heat transfer in wells assisted by VIT systems. Firstly, the thermal problem was modeled and simulated using the finite volume method (FVM) with a commercial software package. A steady-state equivalent thermal network (ETN) model was developed and its mesh refinement was adjusted such that it provides results similar to those obtained with the FVM, but with a much lower computational cost. The VIT ETN model was then coupled to a multiphysics wellbore simulator (hydrodynamic-thermal-structural), producing potentially more realistic results for the oil industry. Such results have been compared and validated with field data from two actual petroleum wells and against data from a commercial software package extensively used by the major oil companies in wellbore design.

Keywords: APB, VIT, Wellbore, Petroleum, Nodal analysis, Numerical simulation.

LIST OF FIGURES

FIGURE 1.1 – SUBSEA VERTICAL WELL PRODUCTION SCHEME.	34
FIGURE 1.2 – 0.4064 M (16 IN) OUTER DIAMETER CASING COLLAPSED DURING HOT FLUID CIRCULATION DUE TO APB (PATTILLO <i>ET AL.</i> , 2006).....	35
FIGURE 1.3 – TYPICAL CASING DESIGN OF A SUBSEA WELL (YIN <i>ET AL.</i> , 2014).	36
FIGURE 2.1 – COMPARISON OF MEASURED AND PREDICTED BOTTOMHOLE PRESSURE (BELLARBY, 2009 ADAPTED FROM PUCKNELL <i>ET AL.</i> , 1993).	42
FIGURE 2.2 – DIFFERENT FLOW REGIMES IN VERTICAL PIPE (COLLIER AND THOME, 1994).....	44
FIGURE 2.3 – WELLBORE ARCHITECTURE AS A THERMAL RESISTANCE NETWORK (SHOUSHTARI <i>ET AL.</i> , 2012 AFTER INCROPERA <i>ET AL.</i> , 2007).	47
FIGURE 2.4 – COMPARISON BETWEEN ANNULUS GAP APPROACHES FOR PREDICTING CONVECTION HEAT TRANSFER (XIONG <i>ET AL.</i> , 2015).	53
FIGURE 2.5 – WELLBORE ARRANGEMENTS: (A) CEMENTED INTERVAL, (B) CEMENT/FORMATION INTERFACE (MODIFIED FROM HALAL AND MITCHELL, 1994).	55
FIGURE 2.6 – DETERMINING FACTORS OF THE APB (BELLARBY, 2009).	58
FIGURE 2.7 – SCHEMATIC FIGURES OF A SUBSEA (A) AND A SURFACE (B) WELLHEAD SYSTEM (SULTAN <i>ET AL.</i> , 2008).	64
FIGURE 2.8 – VIT CONNECTION DETAILS.....	64
FIGURE 2.9 – VIT CONFIGURATIONS (BELLARBY, 2009).	66
FIGURE 2.10 – HEAT FLUXES (ARROWS) IN THE VIT BODY AND CONNECTION SECTIONS (MODIFIED FROM AZZOLA <i>ET AL.</i> , 2004).	68
FIGURE 2.11 – RADIAL HEAT FLUX AND VIT OUTER SURFACE TEMPERATURE UNDER FORCED CONVECTION (PATTILLO <i>ET AL.</i> , 2003).	69
FIGURE 2.12 – FINITE DIFFERENCE CODE DISCRETIZATION SCHEME (AZZOLA <i>ET AL.</i> , 2004).....	71
FIGURE 2.13 – A BASIC VIT CONFIGURATION WITH THE THREAD ON THE OUTER TUBE (NOWINKA <i>ET AL.</i> , 2005).	73
FIGURE 2.14 – EFFECT OF THE VIT ON THE PRODUCTION THERMAL PROFILE OF AN ARCTIC DEVIATED WELL (SINGH <i>ET AL.</i> , 2005).	75
FIGURE 2.15 – WELLBORE SCHEMATIC ASSUMING 1,100 M OF VIT JUST BELOW THE WELLHEAD (FERREIRA <i>ET AL.</i> , 2012).	76
FIGURE 2.16 – APB AS A FUNCTION OF PRODUCTION TIME (FERREIRA <i>ET AL.</i> , 2012).	76
FIGURE 2.17 – EFFECT OF THE ANNULUS CONVECTION APPROACH ON THE PRODUCTION ANNULUS TEMPERATURE PROFILE IN A WELLBORE WITH VIT (KANG <i>ET AL.</i> , 2015).	78
FIGURE 3.1 – VIT GEOMETRY (API CONNECTION THREAD). SCHEMATIC REPRESENTATION OF THE FIVE SECTIONS OF THE VIT.	82
FIGURE 3.2 – GENERIC NODE THERMAL NETWORK SCHEMATICS.	84

FIGURE 3.3 – DIRICHLET BOUNDARY CONDITIONS APPLIED AT THE VIT INTERNAL SURFACE AND IN THE AIR SURROUNDING THE VIT.	86
FIGURE 3.4 – COMPUTATIONAL GRID FOR THE VIT SYSTEM.	87
FIGURE 3.5 – 3 ½" × 2 3/8" VIT THERMAL MAP FOR AN INTERNAL PRESCRIBED TEMPERATURE OF 398 K AND EMISSIVITY OF 0.7.	88
FIGURE 3.6 – EXTERNAL SURFACE TEMPERATURE PROFILE FOR A 3 ½" × 2 3/8" VIT (3-D FVM CALCULATIONS).	89
FIGURE 3.7 – EFFECT OF ETN GRID REFINEMENT ON THE 3 ½" × 2 3/8" VIT EXTERNAL SURFACE TEMPERATURE. COMPARISON WITH THE 3-D FVM RESULTS.	90
FIGURE 3.8 – FLOWCHART SOLUTION OF THE WM MODEL.	96
FIGURE 3.9 – CAUCHY BOUNDARY CONDITION FOR THE HEAT TRANSFER FROM/TO A VIT JOINT.	97
FIGURE 3.10 – VIT EXTREMITIES BOUNDARY CONDITIONS.	99
FIGURE 3.11 – MODELING OF HEAT EXCHANGE IN A WELLBORE WITH VIT (HEAT FLUX – BLUE ARROWS).	100
FIGURE 3.12 – VIT EQUIVALENT THERMAL RESISTANCE (FOR THE WELLBORE MESH) CALCULATION DETAILS.	102
FIGURE 3.13 – FLOWCHART SOLUTION OF THE COUPLED MODEL (WM AND VIT ETN MODELS).	104
FIGURE 3.14 – WORKFLOW TO DEVELOP THE INTEGRATED MODEL AND THE MAIN OUTPUTS GENERATED FROM EACH INDIVIDUAL MODEL.	105
FIGURE 4.1 – WELL A SCHEMATIC.	108
FIGURE 4.2 – WELL B GEOMETRIC DETAILS.	110
FIGURE 4.3 – WELL B TRAJECTORY.	111
FIGURE 4.4 – FIELD DATA AND SIMULATION RESULTS FOR WELL A FOR A PRODUCTION TIME OF 1 DAY.	114
FIGURE 4.5 – FIELD DATA AND SIMULATION RESULTS FOR WELL A.	115
FIGURE 4.6 – WELLBORE FLUID TEMPERATURES OBTAINED FROM THE THERMAL AND MULTIPHASE FLOW MODEL AND WellCAT FOR WELL A FOR A PRODUCTION TIME OF 1 DAY.	116
FIGURE 4.7 – WELLBORE FLUID TEMPERATURES OBTAINED FROM THE THERMAL AND MULTIPHASE FLOW MODEL AND WellCAT FOR WELL A FOR A PRODUCTION TIME OF 5 DAYS.	117
FIGURE 4.8 – WELLBORE FLUID TEMPERATURES OBTAINED FROM THE THERMAL AND MULTIPHASE FLOW MODEL AND WellCAT FOR WELL A FOR A PRODUCTION TIME OF 10 DAYS.	117
FIGURE 4.9 – WELLBORE TEMPERATURE BEHAVIOR CLOSE TO THE WELLHEAD DEPTH.	118
FIGURE 4.10 – FT AND TD RELATIONSHIP FOR DIFFERENT FORMATION LAYERS.	119
FIGURE 4.11 – FLOWING FLUID TEMPERATURE PROFILE FOR SEVERAL PRODUCTION TIME STEPS.	120

FIGURE 4.12 – ANNULUS A TEMPERATURE PROFILE FOR SEVERAL PRODUCTION TIME STEPS.	120
FIGURE 4.13 – EFFECT OF THE FLUID TYPE ON THE FLOWING FLUID TEMPERATURE PROFILE.	121
FIGURE 4.14 – EFFECT OF THE FLUID TYPE ON THE ANNULUS A TEMPERATURE PROFILE.	122
FIGURE 4.15 – EFFECT OF THE FLUID TYPE ON THE FLOWING FLUID AND ANNULUS A WELLHEAD TEMPERATURE.	123
FIGURE 4.16 – EFFECT OF THE ANNULUS CONVECTION APPROACH ON THE WELLBORE FLUIDS TEMPERATURE PROFILES FOR VERY SHORT TRANSIENT ($T = 0^+$ H).....	124
FIGURE 4.17 – EFFECT OF THE ANNULUS CONVECTION APPROACH ON THE WELLBORE FLUIDS TEMPERATURE PROFILES FOR SHORT TRANSIENT (1-DAY PRODUCTION). ...	125
FIGURE 4.18 – EFFECT OF THE ANNULUS CONVECTION APPROACH ON THE WELLBORE FLUIDS TEMPERATURE PROFILES FOR STEADY-STATE (10-DAY PRODUCTION).	126
FIGURE 4.19 – EFFECT OF THE FORMATION MODEL ON THE ANNULUS A TEMPERATURE PROFILE FOR TWO DIFFERENT PRODUCTION TIMES.	127
FIGURE 4.20 – EFFECT OF THE FORMATION MODEL ON THE WELLBORE FLUIDS TEMPERATURE PROFILES FOR A 2-DAY PRODUCTION TIME.	128
FIGURE 4.21 – WELLBORE PRESSURE PROFILES FOR THE 0^+ -DAY PRODUCTION TIME....	129
FIGURE 4.22 – WELLBORE PRESSURE PROFILES FOR THE 1-DAY PRODUCTION TIME.	130
FIGURE 4.23 – WELLBORE PRESSURE PROFILES FOR THE 2-DAY PRODUCTION TIME.	130
FIGURE 4.24 – WELLBORE PRESSURE PROFILES FOR THE 10-DAY PRODUCTION TIME. ...	131
FIGURE 4.25 – TUBE DEFORMATIONS FOR 0^+ -DAY PRODUCTION TIME SIMULATION. ...	133
FIGURE 4.26 – TUBE DEFORMATIONS FOR 1-DAY PRODUCTION TIME SIMULATION.....	133
FIGURE 4.27 – TUBE DEFORMATION FOR 10-DAY PRODUCTION TIME SIMULATION.	134
FIGURE 4.28 – PRESSURE DATA SET FOR WELL A ALONG THE PRODUCTION TIME. BHP – BOTTOMHOLE PRESSURE (REGISTERED AT THE PDG), WHP – WELLHEAD PRESSURE (OF THE FLOWING FLUID), AP – ANNULUS PRESSURE.	136
FIGURE 4.29 – WELLBORE FLUID PRESSURES OBTAINED FROM THE PRESENT MODEL AND COMMERCIAL SOFTWARE FOR THE WELL A FOR 1-DAY PRODUCTION TIME USING N_2 FILLED ANNULUS A.	137
FIGURE 4.30 – WELLBORE FLUID PRESSURES OBTAINED FROM THE PRESENT MODEL AND COMMERCIAL SOFTWARE FOR WELL A FOR 10-DAY PRODUCTION TIME USING N_2 FILLED ANNULUS A.	138
FIGURE 4.31 – WELLBORE FLUID PRESSURES OBTAINED FROM THE PRESENT MODEL AND COMMERCIAL SOFTWARE FOR WELL A FOR 1-DAY PRODUCTION TIME USING BRINE FILLED ANNULUS A.	139
FIGURE 4.32 – WELLBORE FLUID PRESSURES OBTAINED FROM THE PRESENT MODEL AND COMMERCIAL SOFTWARE FOR WELL A FOR 10-DAY PRODUCTION TIME USING BRINE FILLED ANNULUS A.	139

FIGURE 4.33 – WELLBORE PRESSURES WHILE USING N2 OR BRINE FILLED ANNULUS FOR THE 1-DAY PRODUCTION TIME.	140
FIGURE 4.34 – WELL A TEMPERATURE PROFILES WHILE USING 10 VIT JOINTS.	141
FIGURE 4.35 – WELL A PRESSURE AND HEAT TRANSFER PROFILES WHILE USING 10 VIT JOINTS.	142
FIGURE 4.36 – HEAT TRANSFER BEHAVIOR ON THE VIT JOINTS.....	143
FIGURE 4.37 – CONVECTION HEAT TRANSFER COEFFICIENTS BEHAVIOR ALONG THE WELL A.	144
FIGURE 4.38 – VIT TEMPERATURE PROFILES AT THE INTERNAL AND EXTERNAL SURFACES.	145
FIGURE 4.39 – ANNULUS A TEMPERATURE CALCULATED ASSUMING THREE DIFFERENT VALUES OF VIT CAVITY SURFACE EMISSIVITY FOR A 0 ⁺ -DAY PRODUCTION TIME. ...	146
FIGURE 4.40 – ANNULUS A TEMPERATURE CALCULATED ASSUMING THREE DIFFERENT VALUES OF VIT CAVITY SURFACE EMISSIVITY FOR A 1-DAY PRODUCTION TIME.....	146
FIGURE 4.41 – ANNULUS A TEMPERATURE CALCULATED ASSUMING THREE DIFFERENT VALUES OF VIT CAVITY SURFACE EMISSIVITY FOR A 10-DAY PRODUCTION TIME....	147
FIGURE 4.42 – WELLBORE FLUID TEMPERATURE PROFILES FOR A SIMULATION AT 1-DAY PRODUCTION TIME USING THE PRESENT MODEL.....	148
FIGURE 4.43 – WELLBORE FLUID TEMPERATURE PROFILES FOR A SIMULATION AT 10-DAY PRODUCTION TIME USING THE PRESENT MODEL.....	149
FIGURE 4.44 – WELLBORE FLUID TEMPERATURE PROFILES FOR A SIMULATION AT 1-DAY PRODUCTION TIME WITH THE COMMERCIAL SOFTWARE USING A SINGLE K-VALUE FOR THE VIT JOINTS.	150
FIGURE 4.45 – WELLBORE FLUID TEMPERATURE PROFILES FOR A SIMULATION AT 10-DAY PRODUCTION TIME WITH THE COMMERCIAL SOFTWARE USING A SINGLE K-VALUE FOR THE VIT JOINTS.	150
FIGURE 4.46 – WELLBORE FLUID TEMPERATURE PROFILES FOR A SIMULATION AT 1-DAY PRODUCTION TIME WITH THE COMMERCIAL SOFTWARE USING TWO K-VALUES (ONE FOR THE CONNECTION AND ANOTHER FOR THE VIT BODY) FOR THE VIT JOINTS. ...	151
FIGURE 4.47 – WELLBORE FLUID TEMPERATURE PROFILES FOR A SIMULATION AT 10-DAY PRODUCTION TIME WITH THE COMMERCIAL SOFTWARE USING TWO K-VALUES (ONE FOR THE CONNECTION AND ANOTHER FOR THE VIT BODY) FOR THE VIT JOINTS. ...	151
FIGURE 4.48 – PRESSURE PROFILES IN EACH ANNULI FOR A 1-DAY PRODUCTION TIME USING THE THREE APPROACHES.....	153
FIGURE 4.49 – PRESSURE PROFILES IN EACH ANNULI FOR A 10-DAY PRODUCTION TIME USING THE THREE APPROACHES.....	154
FIGURE 4.50 – ANNULI PRESSURE PROFILES AS A FUNCTION OF THE PRODUCTION TIME FOR SIMULATIONS PERFORMED USING THE PRESENT MODEL.	155
FIGURE 4.51 – DEFORMATION OF THE TUBES FOR 0 ⁺ -DAY PRODUCTION TIME. SIMULATION USING VIT JOINTS.	157

FIGURE 4.52 – DEFORMATION OF THE TUBES FOR A 1-DAY PRODUCTION TIME. SIMULATION USING VIT JOINTS.	157
FIGURE 4.53 – DEFORMATION OF THE TUBES FOR A 10-DAY PRODUCTION TIME. SIMULATION USING VIT JOINTS.	158
FIGURE 4.54 – INFLUENCE OF VIT JOINTS ON THE PRESSURE PROFILES OF EACH ANNULUS FOR A 0 ⁺ -DAY PRODUCTION TIME.....	160
FIGURE 4.55 – INFLUENCE OF VIT JOINTS ON THE PRESSURE PROFILES OF EACH ANNULUS FOR A 1-DAY PRODUCTION TIME.	160
FIGURE 4.56 – INFLUENCE OF VIT JOINTS ON THE PRESSURE PROFILES OF EACH ANNULUS FOR A 10-DAY PRODUCTION TIME.	161
FIGURE 4.57 – FIELD DATA AND SIMULATION RESULTS FOR THE WELL B.....	163
FIGURE 4.58 – PRESSURE DATA SET FOR WELL B ALONG THE PRODUCTION TIME.	164
FIGURE 4.59 – TEMPERATURE AND PRESSURE PROFILES FOR THE HYDROCARBON STREAM FOR SIMULATIONS PERFORMED WITH THE PRESENT MODEL AND USING THE COMMERCIAL SOFTWARE FOR WELL B.	165
FIGURE 4.60 – PRESSURE PROFILES IN THE THREE ANNULI OF WELL B FOR SIMULATIONS FOR 10-DAY PRODUCTION TIME.....	167
FIGURE 4.61 – HEAT EXCHANGE AND HYDROCARBON LIQUID AND GAS SUPERFICIAL VELOCITIES FOR A SIMULATION AT 0 ⁺ -DAY PRODUCTION.	168
FIGURE 4.62 – THERMAL RESISTIVITY PROFILES OF THE WELLBORE COMPONENTS FOR A SIMULATION AT 0 ⁺ -PRODUCTION TIME.	169
FIGURE 4.63 – WELLBORE FLUID TEMPERATURE PROFILES FOR A 0 ⁺ -DAY PRODUCTION TIME.	170
FIGURE 4.64 – WELLBORE FLUID TEMPERATURE PROFILES FOR A 10-DAY PRODUCTION TIME.	171
FIGURE 4.65 – TUBE DEFORMATIONS FOR A 0 ⁺ -DAY PRODUCTION TIME FOR WELL B...	172
FIGURE 4.66 – TUBE DEFORMATIONS FOR A 10-DAY PRODUCTION TIME FOR WELL B. .	173

LIST OF TABLES

TABLE 2.1 – TYPICAL DIMENSIONS OF COMMERCIAL VIT SYSTEMS.....	65
TABLE 3.1 – SUMMARY OF THE DIMENSIONS FEATURED FOR BOTH VIT MODELS.....	82
TABLE 3.2 – 2-D SIMULATION INPUT DATA	85
TABLE 3.3 – COMPARISON OF HEAT TRANSFER RATE (IN W/M) IN EACH VIT SECTION FOR THE TWO DEVELOPED APPROACHES.	90
TABLE 3.4 – VIT THERMAL PARAMETERS QUANTIFICATION FOR 4 DIFFERENT TEMPERATURES AND THREE DIFFERENT EMISSIVITY VALUES.....	91
TABLE 4.1 – WELL A SIMULATION / OPERATIONAL PARAMETERS	108
TABLE 4.2 – WELL A DESIGN DETAILS	109
TABLE 4.3 – THERMOPHYSICAL AND MECHANICAL PROPERTIES OF THE FORMATION LAYERS FOR THE WELL A (EPELBAUM <i>ET AL.</i> , 2014)	109
TABLE 4.4 – WELL B SIMULATION / OPERATIONAL PARAMETERS	111
TABLE 4.5 – WELL B ANNULI DESIGN DETAILS.....	112
TABLE 4.6 – THERMOPHYSICAL AND MECHANICAL PROPERTIES OF THE FORMATION LAYERS FOR THE WELL B (EPELBAUM <i>ET AL.</i> , 2014)	112
TABLE 4.7 – APB SUMMARY FOR DIFFERENT PRODUCTION TIME STEPS.....	131
TABLE 4.8 – ANNULI VOLUME RESULTS AT VARIOUS PRODUCTION TIME STEPS.....	135
TABLE 4.9 – SUMMARY OF PRESSURE DATA AS A FUNCTION OF THE PRODUCTION TIME.	136
TABLE 4.10 – AVERAGE SIMULATED ANNULUS A TEMPERATURE AT THE CENTER POSITION OF THE VIT JOINT FOR DIFFERENT PRODUCTION TIME STEPS.	147
TABLE 4.11 – SUMMARY OF ANNULI AVERAGE TEMPERATURES FOR SIMULATIONS USING THE PRESENT MODEL AND THE COMMERCIAL SOFTWARE (WELLCAT) FOR ANNULI A, B AND C.	152
TABLE 4.12 – SUMMARY OF THE APB VARIATION AS A FUNCTION OF THE PRODUCTION TIME FOR ALL ANNULI	155
TABLE 4.13 – SUMMARY OF THE ANNULUS VOLUME VARIATION AS A FUNCTION OF THE PRODUCTION TIME.....	158
TABLE 4.14 – SUMMARY OF THE APB IN ALL ANNULI FOR SIMULATIONS PERFORMED FOR 0^+ , 1 AND 10-DAY PRODUCTION TIMES.....	161
TABLE 4.15 – SUMMARY OF THE AVERAGE TEMPERATURES IN THE ANNULI FOR SIMULATIONS AT 10-DAY PRODUCTION TIME USING THE PRESENT MODEL AND THE COMMERCIAL SOFTWARE (WELLCAT)	165
TABLE 4.16 – SUMMARY OF THE APB FOR SIMULATIONS FOR 0^+ AND 10-DAY PRODUCTION TIMES ACCORDING TO THE PRESENT MODEL	171
TABLE 4.17 – SUMMARY OF THE ANNULUS VOLUME VARIATION AS A FUNCTION OF THE PRODUCTION TIME FOR WELL B	173

ABBREVIATION AND ACRONYMS

AFE	Annulus Fluid Expansion
APB	Annulus Pressure Buildup
API	American Petroleum Institute
BHP	Bottomhole Pressure
BOP	Blowout Preventer
CFD	Computational Fluid Dynamics
ETN	Equivalent Thermal Network
FVM	Finite Volume Method
GRAMP	General Runge-Kutta Annular Modeling Program
HPHT	High Pressure High Temperature
IADC	International Association of Drilling Contractors
KOP	Kick of Point
MAASP	Maximum Allowable Annulus Surface Pressure
MD	Measure Depth
MPD	Managed Pressure Drilling
PDG	Permanent Downhole Gauge
PETROBRAS	Petróleo Brasileiro S.A.
PVT	Pressure-Volume-Temperature
ROV	Robot Operated Vehicle
SAGD	Steam-Assisted Gravity Drainage
SPU	Stationary Production Unit
TOC	Top of Cement
UFSC	Universidade Federal de Santa Catarina
TVD	True Vertical Depth
VIC	Vacuum Insulated Casing
VIT	Vacuum Insulated Tubing
WHP	Wellhead Pressure

NOMENCLATURE

Symbols:

A	$[m^2]$	Cross sectional area
C_f	$[Pa^{-1}]$	Fluid compressibility
c_p	$[J/kg.K]$	Specific heat capacity
d	$[m]$	Tubing internal diameter
D_{coupl}	$[m]$	Coupling external diameter
D_i	$[m]$	Internal Diameter
D_{ii}	$[m]$	Internal diameter of the inner tube
D_o	$[m]$	External diameter
D_{io}	$[m]$	External diameter of the inner tube
D_{oi}	$[m]$	Internal diameter of the outer tube
D_{oo}	$[m]$	External diameter of the outer tube
d_h	$[m]$	Hydraulic diameter
E	$[Pa]$	Young's modulus
E_{ft}	$[Pa]$	Formation Young's modulus
f	$[-]$	Friction factor
$f(t)$	$[-]$	Dimensionless transient temperature function
g	$[m/s^2]$	Acceleration of gravity
G	$[kg/m^2.s]$	Mass flux
Gr	$[-]$	Grashof number
h	$[W/m^2.K]$	Convective heat transfer coefficient
H	$[J/kg]$	Specific enthalpy (fluid)
\bar{h}	$[W/m^2.K]$	Average convective heat transfer coefficient
h_a	$[W/m^2.K]$	Annulus gap natural convection heat transfer coefficient
h_c	$[W/m^2.K]$	Natural convection heat transfer coefficient
h_r	$[W/m^2.K]$	Radiative heat transfer coefficient
h_{ti}	$[W/m^2.K]$	Forced convection heat transfer coefficient
h_{∞}	$[W/m^2.K]$	Natural convection heat transfer coefficient of the surrounding fluid
k	$[W/m.K]$	Thermal conductivity
k_a	$[W/m.K]$	Thermal conductivity of the annulus fluid
k_{air}	$[W/m.K]$	Thermal conductivity of the surrounding air
k_c	$[W/m.K]$	Casing thermal conductivity

k_{cem}	[W/m.K]	Thermal conductivity of the cement
k_d	[W/m.K]	Air diffusion thermal conductivity
k_{ef}	[W/m.K]	Effective thermal conductivity of the VIT
k_{fin}	[W/m.K]	Thermal conductivity of the fin
k_{ft}	[W/m.K]	Formation thermal conductivity
k_r	[W/m.K]	Radiative equivalent thermal conductivity
k_t	[W/m.K]	Tubing thermal conductivity
k_v	[W/m.K]	Equivalent thermal conductivity of the vacuum
L	[m]	Length
L_R	[m ⁻¹]	Length relaxation parameter
m	[kg]	Fluid mass
n	[-]	Number of reflective wraps
Nu	[-]	Nusselt number
P	[Pa]	Pressure
Pr	[-]	Prandtl number
q	[W]	Heat transfer rate
q_{cond}	[W]	Conduction heat transfer rate
$q_{freeconv}$	[W]	Free convection heat transfer rate
q_{rad}	[W]	Radiation heat transfer rate
q'	[W/m]	Heat transfer rate per unit length
q''	[W/m ²]	Heat flux
r	[m]	Radius
r_c	[m]	Casing radius
r_{ci}	[m]	Casing internal radius
r_{co}	[m]	Casing external radius
r_{coup}	[m]	Coupling radius
r_{int}	[m]	Internal radius
r_{out}	[m]	External radius
r_{ti}	[m]	Tubing internal radius
r_{to}	[m]	Tubing external radius
r_{wb}	[m]	Wellbore radius
R	[K.m ² /W]	Thermal resistance
R_{eq}	[K.m ² /W]	VIT equivalent thermal resistance
R_{ext}	[K.m ² /W]	Surrounding fluid thermal resistance
R_{fin}	[K.m ² /W]	Thermal resistance of the fin
R_{VIT}	[K.m ² /W]	VIT thermal resistance
Ra	[-]	Rayleigh number
t	[s]	time

t_D	[-]	Dimensionless diffusion time function
T	[K]	Temperature
\bar{T}	[K]	Average temperature
T_{cas}	[K]	Casing inner surface temperature
T_e	[K]	External surface temperature
T_{ee}	[K]	Temperature at the external surface of the VIT
T_f	[K]	Flowing fluid temperature
T_{ft}	[K]	Formation temperature
T_i	[K]	Internal surface temperature
T_{io}	[K]	Temperature at the external surface of the inner tube
T_{oi}	[K]	Temperature at the internal surface of the outer tube
T_{wb}	[K]	Wellbore/formation interface temperature
T_∞	[K]	Temperature of the surrounding fluid
U	[W/m ² .K]	Overall heat transfer coefficient
U_{ef}	[W/m ² .K]	Effective overall heat transfer coefficient of the VIT
U_{to}	[W/m ² .K]	Wellbore overall heat transfer coefficient
v_m	[m/s]	Fluid mixture velocity
v_{sg}	[m/s]	Superficial gas velocity
v_{sl}	[m/s]	Superficial liquid velocity
V	[m ³]	Volume
V_a	[m ³]	Annulus volume
V_o	[m ³]	Initial volume
w	[kg/s]	Mass flow rate
z	[m]	Axial position

Greeks:

α	[m ² /s]	Thermal diffusivity
α_{ft}	[m ² /s]	Formation thermal diffusivity
β	[K ⁻¹]	Coefficient of thermal expansion
β_f	[K ⁻¹]	Coefficient of thermal expansion of the fluid
γ	[°]	Inclination angle
ΔP_i	[Pa]	Cylinder internal pressure variation

ΔP_o	[Pa]	Cylinder external pressure variation
Δr_i	[m]	Annulus internal radius variation
Δr_o	[m]	Annulus external radius variation
ΔT	[K]	Temperature variation
ΔV_a	[m ³]	Annular space volume variation
ΔV_z	[m ³]	Volume variation due to change in annulus axial dimensions
Δz	[m]	Axial position difference
$\Delta \epsilon_r$	[-]	Change in radial strain
$\Delta \epsilon_z$	[-]	Change in axial strain
$\Delta \epsilon_\theta$	[-]	Change in hoop strain
$\Delta \rho_i$	[kg/m ³]	Internal change in fluid density
$\Delta \rho_o$	[kg/m ³]	External change in fluid density
$\Delta \sigma_r$	[N/m ²]	Radial stress variation
$\Delta \sigma_z$	[N/m ²]	Axial stress variation
$\Delta \sigma_\theta$	[N/m ²]	Hoop stress variation
ϵ	[-]	Emissivity
ϵ	[-]	Strain
ϵ_r	[-]	Radial strain
ϵ_z	[-]	Axial strain
ϵ_θ	[-]	Hoop strain
ρ	[kg/m ³]	Fluid density
ρ_{ft}	[kg/m ³]	Formation density
ρ_g	[kg/m ³]	Gas density
ρ_l	[kg/m ³]	Liquid density
μ_g	[Pa.s]	Gas viscosity
μ_l	[Pa.s]	Liquid viscosity
σ_r	[Pa]	Radial stress
σ_z	[Pa]	Axial stress
σ_θ	[Pa]	Hoop stress
σ_{SB}	[-]	Stefan-Boltzmann constant
ν	[-]	Poisson's ratio
ν_{ft}	[-]	Formation Poisson's ratio
ω	[-]	Ratio between formation and wellbore heat capacities

SUMMARY

1	INTRODUCTION	33
1.1	Problem statement	33
1.2	Motivation	37
1.3	Objectives	39
1.4	Document outline	40
2	Literature review	41
2.1	Wellbore multiphysics phenomena	41
2.1.1	Multiphase flow models in wellbores	41
2.1.2	Heat transfer models in wellbores	46
2.1.3	Tubular and Formation Mechanical Models	53
2.2	APB Behavior Prediction and Field History	57
2.3	APB Mitigation	61
2.4	VIT Basics	63
2.4.1	The k-value (U-value) concept	66
2.4.2	VIT thermal models	67
2.4.3	VIT thermal and mechanical evaluations	72
2.5	VIT Assisted Wellbore Applied to APB Mitigation	74
2.6	Summary	78
3	MODELING	81
3.1	VIT Geometry	81
3.2	2-D ETN Model	83
3.2.1	Hypotheses and governing equations	83
3.2.2	Model Implementation	84
3.2.3	Validation using a 3-D FVM model	85
3.3	Wellbore Multiphysics Model	93
3.4	Coupling the ETN Model with the WM Model	96
3.4.1	Adaptation of the ETN Model and Boundary Conditions	97

3.4.2	Computational Implementation of the Integration Between the Models	100
4	RESULTS	107
4.1	Description of the Cases Studied	107
4.1.1	Description of the Case 1 – Well A	107
4.1.2	Description of the Case 2 – Well B	109
4.2	Thermal-Hydraulic Evaluation	113
4.2.1	Hydraulic model	113
4.2.2	Thermal model	115
4.2.3	Effect of the production time on the wellbore thermal- hydraulic behavior	119
4.2.4	Effect of the annulus fluid type	121
4.2.5	Effect of the annulus convection heat transfer correlation	124
4.2.6	Effect of the formation thermal model	126
4.2.7	APB prediction	128
4.2.8	Mechanical model validation	135
4.3	Analysis of Heat Transfer in a VIT Assisted Wellbore	140
4.3.1	Wellbore with 10 VIT Joints	141
4.3.2	Comparison of the integrated model with the commercial software	147
4.4	Evaluation of the Integrated Model using a Real VIT Assisted Well	162
4.4.1	Validation of the Integrated Model	162
4.4.2	Thermal-structural study of well B	167
5	CONCLUSIONS AND FUTURE RESEARCH NEEDS	175
5.1	Conclusions	175
5.2	Future Research Needs	180
	REFERENCES	181
	appendix A	199
	Appendix b	202
	B.1 conduction	202
	B.2 convection	203

B.3 radiation	205
B.4 energy balance - system of equations	205
B.4.1 Lower extremity of the VIT joint	206
B.4.2 Interface between sections 2 and 3	210
B.4.3 Interface between sections 1 and 2	218
Appendix C	225
C.1 The separated flow model	225
C.2 The bubble flow regime	225
C.3 The bubble to slug regime transition	226
C.4 THE SLUG FLOW regime	226
C.5 The slug to churn regime transition	231
C.6 The churn flow regime	233
C.7 The churn to annular regime transition	235
C.8 The annular flow regime	235
Appendix d	244
appendix e	245
appendix f	246
appendix g	249
G.1 Evaluation of the annulus natural convection model	249
G.1.1 Hasan and Kabir (1991)	249
G.1.2 Hasan and Kabir (2002)	250
G.1.3 Zhou (2013)	250
G.1.4 Xiong <i>et al.</i> (2015)	250
G.2 Evaluation of the formation model	251

1 INTRODUCTION

1.1 Problem statement

The increasing demand for hydrocarbon resources has compelled oil companies to focus on deep and ultra-deep water environments, as well as to explore unconventional reservoirs. As a result, well integrity has become one of the most critical aspects during well construction and operation.

Some of the offshore oil reserves recently discovered in Brazil lie in reservoirs located at long depths, far away from the coast. For example, the pre-salt area in the Santos basin is characterized by water columns up to 2,300 m deep and target depths greater than 5,000 m, with salt layers reaching thicknesses of 2,500 m. The large light-oil reservoirs (28 to 32 degrees API) in the pre-salt region have typical pressures of 60 MPa and temperatures up to 390 K.

Along with the growth of petroleum exploration and production in harsh environmental conditions, numerous technical challenges have emerged, such as well construction in harsh conditions (ultra-deep water, thick salt layers, high hardness reservoir rocks, high pressure wells), complex flow assurance strategies (hydrate and wax formation inhibition, scale mitigation) and the choice of suitable enhanced oil recovery methods.

Given the large costs involved in deep water operations, the produced hydrocarbons are expected to be transported from the well to the often remote processing facilities with the least amount of energy (flow and thermal) losses. From the reservoir rock to the surface facilities, three different stages of hydrocarbon flow can be identified (considering a subsea vertical well):

- Radial liquid or gas-liquid flow through the permeable reservoir rock to the wellbore;
- Vertical gas-liquid flow through a circular pipe from the bottom hole to the wellhead;
- Horizontal flow followed an inclined pipe flow through the flowline from the wellhead to the SPU (Stationary Production Unit).

In each of those stages, the flow behaves differently and the corresponding pressure loss and temperature distributions are governed by different sets of variables. In this work, only the wellbore flow stage

will be considered, since it is responsible for the major portion of the pressure loss. Figure 1.1 illustrates the production scheme of a subsea vertical well and the path followed by the produced fluid from the reservoir to the production facilities (yellow arrows).

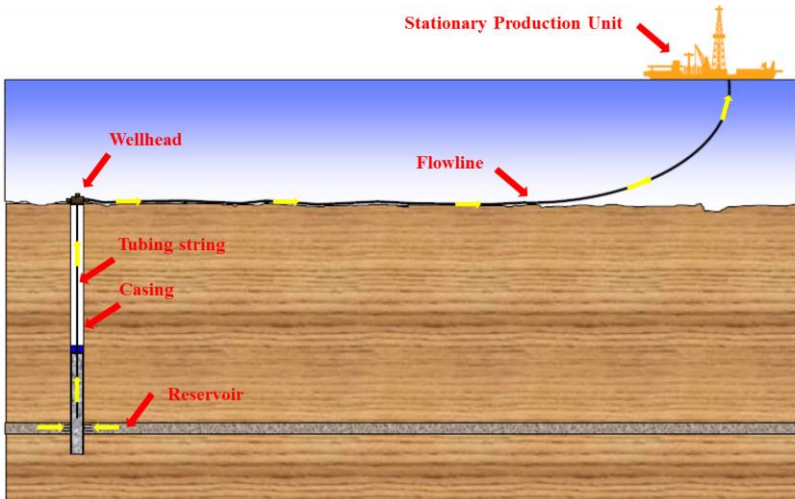


Figure 1.1 – Subsea vertical well production scheme.

Similar to the fluid flow, a heat transfer analysis and its impact on the wellbore structure is of major importance in well design. Thermal phenomena play an important role in several aspects of deep water oil production, such as tubing and casing stress analysis, material selection (metals and elastomers) and tubing well performance and sizing (BELLARBY, 2009).

Furthermore, knowledge of the wellhead temperature during well production is an important issue, since directly affects the flow line sizing and primary oil processing operations on the SPU. Knowing the temperature gradient along the well depth is essential in well design and construction, since the fluids and equipment used in drilling and completion are selected based on the local pressure and temperature conditions. Therefore, controlling thermal events and their consequences has been a concern for oil companies since the early days of deep water production in the 1960s (EZELL *et al.*, 2010).

Other reasons for controlling the temperature of a wellbore during oil and gas production can be outlined as follows:

- Prevention or reduction of wax deposition in the tubing;

- Tubing scale mitigation;
- Prevention of hydrate blockage;
- Reducing thermal loads on the surrounding casing;
- Maintaining low-viscosity fluid flow;
- Reduction in annular pressure buildup.

Generally speaking, all of the above issues require reducing the outward heat transfer from the well. In particular, reducing wellbore heating during hydrocarbon production is crucial to the safety of the production process. For instance, two main problems can be highlighted regarding the well integrity: (i) the casing collapse and (ii) the casing connection compression failure. The first is caused by the APB (Annulus Pressure Buildup), which occurs when the hydrocarbon flow heats up the entire region close to the production string, forcing the expansion of the surrounding fluids and, consequently, the pressurization of the well annuli. The increase in pressure may exceed the mechanical strength of the casings, causing them to collapse, as shown in Figure 1.2. The second problem arises due to casing dilation. Casing strings are set at the wellhead on the high-pressure housing through the casing hanger, and fixed to the rock formation by the cement. Thermally induced dilation causes the casing string to be compressed to a point at which the casing connection resistance is surpassed.



Figure 1.2 – 0.4064 m (16 in) outer diameter casing collapsed during hot fluid circulation due to APB (PATTILLO *et al.*, 2006).

The thermal/mechanical response of the well to the upward flow of hydrocarbons is related to its inner structure as well as to the surrounding formation. For instance, cementing operations are mandatory in all drilling activities as they assure the hydraulic insulation between permeable layers of the formation besides keeping the casing

fixed to the borehole walls. The well cementing process is made gradually following the drilling of each phase, which is defined by a length that depends on the rock formation pressures. As the wellbore is drilled, its diameter decreases and a new casing needs to be set and cemented. In the first couple of phases, the entire annular space between the borehole walls and the casing is completely filled by cement up to the wellhead. In the following phases, the cement slurry usually does not fill the well up to the wellhead. In turn, the region above the top of cement (TOC) is completed with the drilling fluid used to drill that phase of the well. Figure 1.3 illustrates a typical casing design of a subsea well with three annuli (A, B and C) filled by different fluids. In this text, the symbol A always denotes the innermost annulus, followed by the symbols B, C and so on, as the radial distance increases.

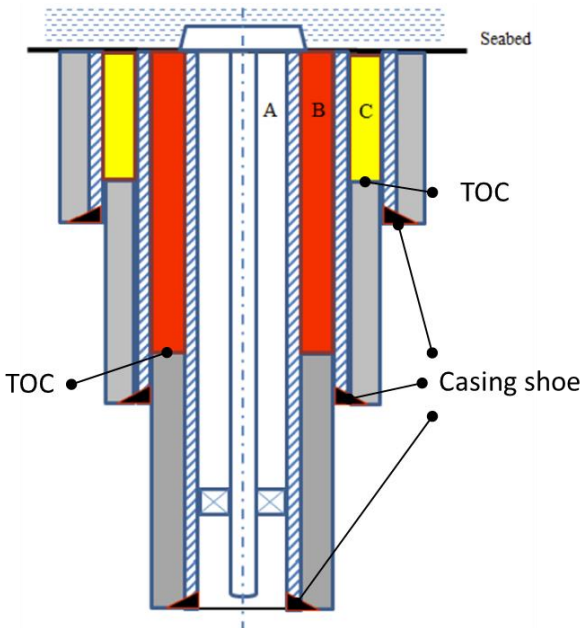


Figure 1.3 – Typical casing design of a subsea well (YIN *et al.*, 2014).

Therefore, depending on the location of the TOC in the annular space (i.e., above or below the casing shoe), the drilling fluid can be confined or not. Generally, the pressure increase is limited by the formation fracture resistance (FERREIRA *et al.*, 2012). At this condition, when the annulus pressure reaches the so-called formation

leak-off pressure, an amount of fluid proportional to the volume increase due to the annulus expansion flows into the formation until the annulus and the formation pressures become equal. However, if the TOC is placed above the casing shoe, the annulus is not in contact with the “safety valve” provided by nature (MOE and ERPELDING, 2000). As a result, the annular pressure cannot be relieved, which increases the stress in the tubulars, leading eventually to a well failure (HASAN *et al.*, 2009).

Despite the efforts made in the last two decades, the discovery of new production scenarios and the development of new technologies created a need for identifying and predicting the key variables that control the annular pressure buildup (APB). Consequently, this work intends to model, predict and propose strategies to mitigate this phenomenon in deep water wells. To this end, a fully-coupled multiphysics model has been proposed to account for all main hydrodynamic, thermal and mechanical aspects encountered in real wells. Furthermore, in order to reduce the heat transfer to the formation, the use of VIT (Vacuum Insulated Tubing) joints is considered in detail. Hence, the major contribution of this thesis is the development of a VIT thermal model that, when incorporated into a wellbore simulator, can provide an accurate evaluation of its APB mitigation potential. In the following section, the motivation and the goals of the thesis are presented.

1.2 Motivation

APB has been a concern in the petroleum industry since the 1990s due to a failure in a Marlin field well in the Gulf of Mexico (AZZOLA *et al.*, 2004, GOSCH *et al.*, 2004, ELLIS *et al.*, 2004). Since then, an increasingly important issue in deep water exploitation has been the evaluation of appraisal wells as possible production wellbores. The reason is that it is difficult to justify economically the abandonment of a wellbore that has cost tens of millions of dollars to drill, a typical figure for the Santos Basin Pre-Salt Cluster. On the other hand, the potential consequences of a well failure during its production cannot be neglected. Central to this evaluation is the consideration of well integrity issues associated with APB.

Therefore, the use of insulated tubes to thermally assist critical wells is a more attractive alternative than the undesirable restriction of the production stream, which directly limits profit. In fact, the frequent

need for thermal insulation systems in oil wells in the appraisal and development phases of the Santos Basin Pre-Salt Cluster alone serves as motivation for the present study.

While there are few relevant publications concerning insulation materials applied to wellbores, most of them are related to testing and application of thermal insulation materials in flowlines, manifolds, Christmas trees and risers. The main concerns are associated to the cooling effect due to the cold seawater (HUDSON *et al.*, 2000; RUSCHAU *et al.*, 2010; GREALISH and RODDY, 2002) and, in many cases, there are no restriction on insulation thickness to reach a suitable performance (WATKINS, 2000; MELVE, 2001; MCKECHNIE, 2002; GOU *et al.*, 2004).

However, during well construction and production operations, several heat exchange phenomena occur between the rock formation, the wellbore fluids (produced fluid, drilling fluid and completion fluid), the drilling and tubing string components, the casings and the cement. Temperature and pressure prediction in each section has an important role in the planning of critical operations. The rate of heat transfer from the wellbore is affected by many parameters, such as the formation type and fluid properties, well geometry, operation time, flow rates and water depth.

Numerical simulation allows an accurate prediction of these phenomena, enabling a safer and more efficient planning of some well operations. Most simulators are based on the finite difference and finite volume methods to solve the governing equations for the thermal-hydraulic behavior of the multiphase system. However, there are specific points to be improved in the available well numerical simulators, such as the coupling with the reservoir and the insertion of multiple thermal insulation sections in the production string, which directly affects the radial heat transfer from the wellbore and the APB.

Therefore, the development of detailed multiphysics models capable of accurately predicting the hydrodynamic, thermal and mechanical behavior of oil wells, as well as their behavior while assisted by thermal insulation systems (e.g., VIT) will certainly contribute to more efficient wellbore design strategies in the Pre-salt Cluster.

Important to realize that uncertainties about formation properties and even related to wellbore sensors data employed as input parameters may lead to incorrect predictions obtained from wellbore simulators. Also, it is worth mentioning the importance to comprehensively handle all the multiphysics aspects taking place in the wellbore for all time scales experienced by the well during production.

1.3 Objectives

The overall objective of the thesis is to carry out a comprehensive analysis of the multiphase flow and heat transfer in wellbores along with its mechanical behavior, including a detailed evaluation of thermally insulated tubing sections in the production string. The appropriate prediction of the temperature field in the wellbore deserves somewhat attention, since the mechanical responses and, consequently, the APB quantification are directly affected by the local heat transfer calculation. Thus, the specific goals of the present work are:

- To develop a heat transfer model based on the analogy between thermal and electrical circuits, aiming to quantify the thermal design parameters of the VIT unit (overall heat transfer coefficient and effective thermal conductivity). Because of its two-dimensional form, this approach is able to capture important aspects of the heat transfer in the junction region at a reduced computational cost and can, therefore, be easily integrated in wellbore heat transfer simulators. A validation of the equivalent thermal network (ETN) model is carried out using a commercial software package to solve the combined heat transfer (conduction-radiation) equations in differential form via the Finite Volume Method;
- To incorporate the two-dimensional VIT thermal model in an in-house multiphysics (hydrodynamic, thermal, structural) wellbore (MW) model (Hafemann, 2015) and evaluate multiple scenarios involving different operating conditions and parameters of the VIT. The results of this analysis are expected to provide insight into VIT applications to mitigate APB and its effects on the wellbore mechanical integrity.
- To validate the full model (ETN + MW models) using field data and commercial software results. For the latter, the commercial package Wellcat™, offered by Halliburton/Landmark and extensively employed by petroleum engineers during well design phase to predict the wellbore thermal-hydraulic and mechanical behaviors, has been used.

1.4 Document outline

This document is composed of five chapters. Chapter 2 consists of a literature review, in which numerical models of multiphase flow and heat transfer in wellbores are presented highlighting the quantification of the APB. Moreover, experimental works and heat transfer models relating to the VIT performance and field application are also described. In the end of this section the main insights about the literature review is briefly described and the contributions of this thesis to cover the gaps found in the literature are highlighted. Chapter 3 describes a theoretically based methodology developed to assess the thermal performance of VIT systems through a parametric evaluation of their thermal properties and geometrical parameters. Two independent formulations were tested, namely a 3-D numerical differential model (3-D FVM) and a 2-D nodal approach (2-D equivalent thermal network – ETN model). The similarities and differences of each model are explored through a fundamental analysis of the VIT performance. Then, the methodology to incorporate the 2-D ETN model into a wellbore simulator is described. Chapter 4 refers to the results reached in this thesis emphasizing the importance of incorporation the VIT thermal approach into the wellbore simulator. In addition, two case studies using actual wells are suggested to predict the thermal-structural behavior of wellbores as well as to validate the coupled model. Chapter 5 presents the conclusions and recommendations for future works.

2 LITERATURE REVIEW

In this chapter, a review of the existing numerical and analytical multiphase flow and heat transfer models applied to wellbores are presented, while highlighting their assumptions and limitations, and their use on the quantification of APB. The review is extended by presenting experimentally based studies related to the VIT's performance and field application.

2.1 Wellbore multiphysics phenomena

The calculation of production parameters influenced by fluid flow and heat transfer in wellbores is unquestionably challenging. For instance, rigorous prediction of a multiphase multicomponent flow system in wellbores is complex phenomenon, since it is related to the phase change of mixtures pressure, temperature and liquid holdup. Despite the technical difficulties, modeling of multiphase flow and heat transfer during oil and gas production to predict the pressure and temperature profiles in the tubing string and in well annuli is a core skill for any oil company. It is fundamental to predict flow rates, select the correct size of tubulars and equipment, and consider the occurrence of corrosion and erosion rates and many other tasks. Therefore, the complex nature of these multiphysics phenomena have boosted a series of studies, which will be reviewed in the following sections.

2.1.1 Multiphase flow models in wellbores

Multiphase flow in wellbores takes place in several activities during well construction and production/injection phases. Even though several works deal with thermal fluid flow in wellbores, there are some challenges involved in the modeling of multiphase flows to simulate petroleum production in different types of wells (tubing diameter, well trajectory), operational conditions (pressure, temperature), and hydrocarbon composition. However, given the wide range of different flowing systems and regimes, a multitude of multiphase flow models, most of which numerically-based, were developed by the literature aiming to precisely mimic the complex phenomenological nature existing in wellbores worldwide. Due to the complex nature of the

petroleum production process and the high number of variables involved in estimating pressure and temperature profiles, many approaches have been used to solve the fluid flow in oil wells. Earlier approaches were based on empirical or semi empirical methods and were not able to capture the entire physics of the multiphase flow. Additionally, these methods may not be suitable for predicting pressure and liquid holdup transients. More recently, however, there has been a shift towards a more fundamental modeling of flow in wells, using the so-called mechanistic approach (CANDIA and CRUZ, 2004). This approach is based on the solution of local averaged conservation equations for the variables of interest (pressure, temperature, velocity, and liquid holdup) (CANDIA and CRUZ, 2004), and can be extended to more general problems, such as three-dimensional and transient flows.

Pucknell *et al.* (1993) published a survey focusing on models used to predict the wellhead pressure in 212 oil wells. Figure 2.1 shows the error associated with some multiphase flow models, which are widely accepted in the oil industry, in relation to field data. According to Figure 2.1, the average error was relatively low, between 7.6 and 14%, and all models reported show consistency.

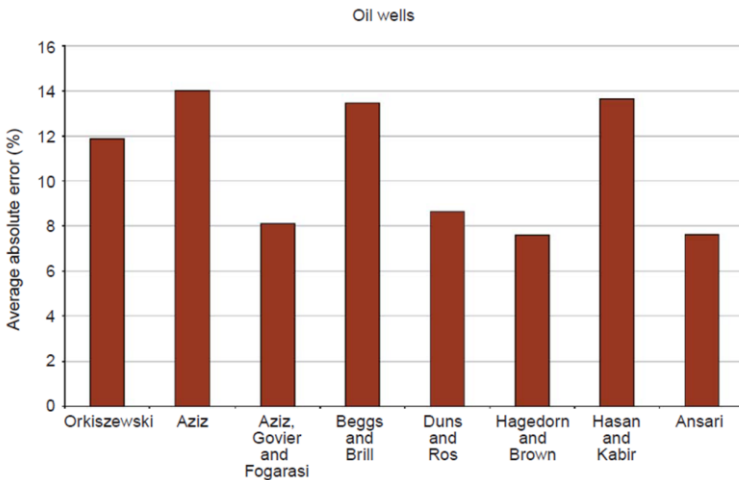


Figure 2.1 – Comparison of measured and predicted bottomhole pressure (BELLARBY, 2009 adapted from PUCKNELL *et al.*, 1993).

One of the major difficulties in dealing with multiphase flows is that mass, momentum, and energy transfer rates and processes can be sensitive to the geometric distribution of the components within the flow

(BRENNEN, 2005) and, therefore, require a fully coupled solution. The interface between phases can take on a variety of configurations, known as flow patterns (CHENG *et al.*, 1998). There are three basic approaches to estimate the pressure drop and void fraction in a production stream using one-dimensional models: the homogeneous model, the separated flow model and the mechanistic model based on flow patterns. It should be mentioned that the choice of approach to be adopted depends on the well data available, such as trajectory, produced fluid type (vapor-liquid equilibrium study - PVT analysis), tubing diameter, and operational data from drill stem test, among others.

The simplest approach to model multiphase flows is the homogeneous flow model, which considers the fluids intimately mixed, so they can be treated as a single-phase fluid with average properties. Flow patterns are, therefore, ignored in the homogeneous model. The intrinsic assumptions of the homogeneous model are as follows (CORRADINI, 1997):

- The slip (relative) velocity between the phases is zero;
- The two fluids are uniformly mixed and move as a pseudo fluid at the mixture velocity;
- There is thermodynamic equilibrium between the phases.

The flow patterns *likely* to take place in a vertical well producing a gas-liquid mixture are shown in Figure 2.2 (COLLIER and THOME, 1994).

The flow regimes shown in Figure 2.2 have been described based on laboratory observations through transparent pipes. In order of increasing gas content, the flow configurations in a vertical pipe are explained as follows:

- Bubbly flow: The liquid is the continuous phase. The low-velocity gas or vapor phase is dispersed as uniformly distributed bubbles within the liquid. The two-phase static head is the main component of the pressure gradient in a vertical conduit, as the friction part is expected to be smaller due to the relatively low mixture velocity.
- Slug flow: The liquid is still the continuous phase, even though the gas velocity is higher. The dispersed bubbles coalesce and form large bullet shaped bubbles (Taylor bubbles). A falling liquid film surrounds the Taylor bubbles. The so-called slug flow unit cell consists of two parts: the Taylor bubble region and the liquid slug region. The latter often contains small dispersed bubbles.

- Churn flow: Both phases are continuous due to the breakdown of the liquid slugs as the gas velocity is increased. Liquid flow reversals (oscillatory motion) are the main features of this flow regime as the gas lacks enough momentum to move the liquid upwards. Interfacial friction plays an important role in determining the pressure drop in this flow regime.
- Annular flow: As the gas velocity increases, the flow becomes unidirectional (upward) and high interfacial shear gives rise to droplet entrainment in the vapor core. A thin liquid film covers the pipe wall, with liquid droplets being continuously entrained from and deposited back on the film. Due to the low liquid content associated with this flow regime, frictional effects are the main component of the pressure gradient.

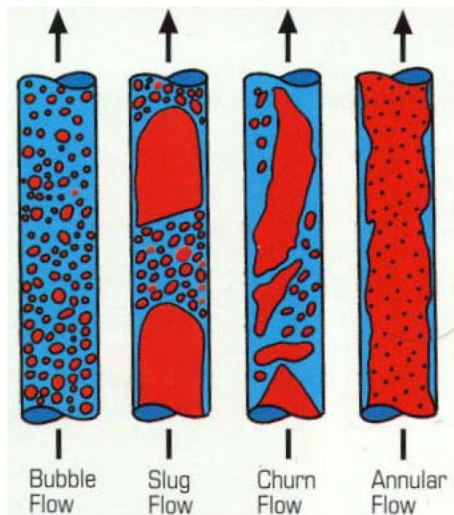


Figure 2.2 – Different flow regimes in vertical pipe (COLLIER and THOME, 1994).

The drift-flux model (ZUBER and FINDLAY, 1965) is a mixture model with a constitutive relationship for the relative motion between the phases, which itself depends on the flow regime (COLLIER and THOME, 1994). The drift-flux model can be extended to incorporate energy transport effects (ISHII and HIBIKI, 2006).

The separated flow model considers each phase individually, for which individual mass, momentum and energy balance equations are

formulated. The balance equations contain interaction terms to incorporate the interfacial transfer of mass, momentum and energy between the phases. Without these terms in the balance equations, the two phases are essentially independent and can be analyzed by single-phase flow equations (CORRADINI, 1997).

The separated flow approach can be developed in two ways: from experimentally based correlations or mechanistic modeling (POURAFSHARY, 2007). The experimentally based approach relies heavily on empirical correlations for the closure relationships needed in the models. The other approach is based on mechanistic models to describe the distribution of the phases in the channel. This method consists in recognizing the hydrodynamic conditions that lead to several flow patterns and proposes individual models for each flow regime to predict pressure losses and liquid hold up.

As for the mechanistic models, Taitel and Dukler (1976) presented the first formulation for the transition between the five basic flow patterns in horizontal flow: stratified smooth, stratified wavy, intermittent, annular dispersed and dispersed bubble. Following that, there have been several efforts to determine the dependence of the flow pattern on component volume fluxes, volume fraction and the fluid properties such as density, viscosity, and surface tension, for both vertical and horizontal tubes (ANSARI, 1994; GOMEZ, 1999; HASAN and KABIR, 1999; ZHANG *et al*, 2006). The results are often displayed in the form of a flow regime map, which identifies the flow patterns occurring in various parts of a parameter space defined, for instance, by the superficial phase velocities or momentum fluxes.

Briefly explaining, in order of increasing complexity, the homogeneous model assumes no slippage between the phases and makes no distinction between flow patterns. The separated flow model considers different phase velocities (slip) and requires an additional equation for the void fraction. However, it does not consider explicitly different flow patterns. Mechanistic models incorporate mathematical relationships for the transition between flow patterns in addition to governing equations for each specific flow pattern.

The first wellbore multiphase flow model developments date back to 1930s. Early investigators developed very limited methods of multiphase flow through vertical pipes as to their range of applications (VERSLUYS, 1930; MOORE and WILDE, 1931; MOORE and SCHILTHUIS, 1933; GOSLINE, 1936; MAY, 1935). Only in the 1950s, the first empirical or semi-empirical models widely applicable in the oil industry were proposed. Poettmann & Carpenter (1952)

developed the first general method for predicting the pressure profile in oil and gas wells and in gas lift vertical wells under steady state conditions, considering the flowing fluid as a single homogeneous phase. This semi-empirical model was based in field data of 49 wells operating over a wide range of conditions. Later, Baxendell & Thomas (1961) proposed a new method to estimate the pressure profile in oil wells for high flow rate scenarios based on the methodology provided by Poettmann and Carpenter (1952).

Fancher and Brown (1963) developed a separated flow friction-correlation based model. Duns and Ross (1963) also provided a separated flow model. This model, which was based on experimental work, showed good agreement for all range of tested conditions. Hagedorn and Brown (1965) developed a separated flow friction/holdup-correlation model based on experimental work. The model was validated with several field data showing a very good agreement for the whole range of conditions.

Brill *et al.* (1966) provided a model combining the use of vertical and horizontal correlations for determining the maximum flow rate possible from both flowing and gas lift wells. Mukherjee and Brill (1983) developed experimental correlations for multiphase flow in vertical and inclined pipes.

In the last ten years, several coupled thermal multiphase flow models in wellbores were developed (AMARA *et al.*, 2006; IZGEC *et al.*, 2007; POURAFSHARY *et al.*, 2007; HU *et al.*, 2007; LIVESCU *et al.*, 2008; LIVESCU *et al.*, 2009; SHIRDEL and SEPEHRNOORI, 2009; PAN and OLDENBURG, 2014; FOROUZANFAR *et al.*, 2015), with the ultimate goal providing a coupled wellbore/reservoir solution. Some of these studies focused on the determination of the pressure and temperature profile of the production stream, emphasizing the local heat and pressure loss in the interface wellbore-formation in a vertical, deviated and/or horizontal well.

2.1.2 Heat transfer models in wellbores

The wellbore is essentially a multi-layer cylindrical system with a multi-mode radial heat transfer between the wellbore fluid and the surrounding formation (HASAN and KABIR, 2002), as depicted in Figure 2.3 for production through a single string (SHOUSHTARI *et al.*, 2012 after INCROPERA *et al.*, 2007).

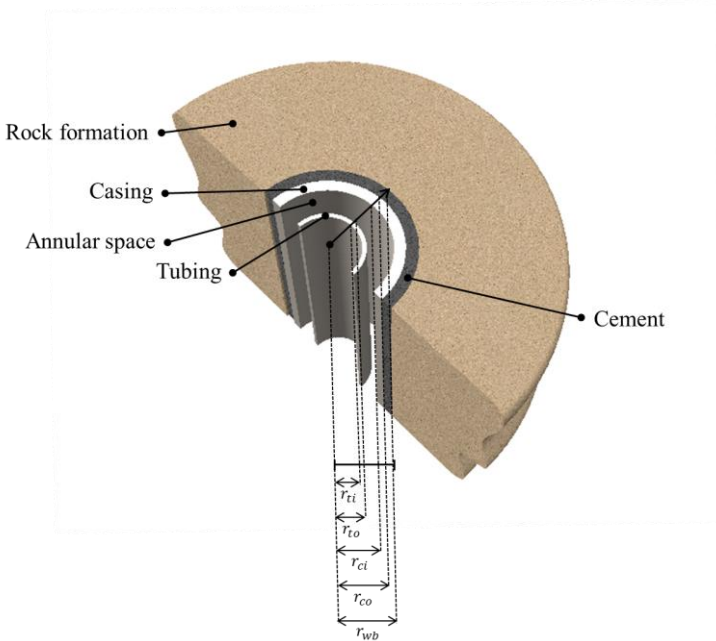


Figure 2.3 – Wellbore architecture as a thermal resistance network.

For such configuration, the overall heat transfer coefficient (based on the tubing external surface heat exchange area) can be defined by the following expression (HASAN and KABIR, 2012):

$$\frac{1}{U_{to}} = \frac{r_{to}}{r_{ti} \cdot h_{ti}} + \frac{r_{to} \cdot \ln(r_{to}/r_{ti})}{k_t} + \frac{r_{to}}{r_{to} \cdot (h_c + h_r)} + \frac{r_{to} \cdot \ln(r_{co}/r_{ci})}{k_c} + \frac{r_{to} \cdot \ln(r_{wb}/r_{co})}{k_{cem}}, \quad (2.1)$$

which can be modified by adding or removing thermal resistances to adapt the thermal circuit to a particular situation. It should be noted that in Eq. 2.1 the interfacial contact resistances were neglected. In addition to the conduction from the inner radius, r_{ti} , to the wellbore radius (outer radius), r_{wb} , the composite system approach takes into account the internal and external convective heat transfer represented by the first and the third terms on the right-hand side of Eq. 2.1, where r_{to} is the outer radius of the tubing, r_{ci} is the inner radius of the casing and r_{co} is the outer radius of the casing.

The first heat transfer studies that attempted to estimate the wellbore fluid temperatures were proposed by Lesem *et al.* (1957) and Moss and White (1959) for long-time water injection operations, and with the ultimate target of improving oil recovery. The classical work of Ramey (1962) can be considered a landmark in the field, being used as the reference for major works until today. In his study, Ramey (1962) proposed a transient 1-D approximate solution to predict the temperature of fluids, tubing and casings as a function of depth and production/injection time. The single string wellbore is considered as a vertical cylindrical heat source that loses heat to the surrounding formation, which, in turn, is treated as a homogeneous semi-infinite solid. Boundary conditions include a known flow rate and a surface or a bottomhole temperature, besides considering a vanishingly small well radius and a prescribed temperature at the formation. The so-called formation temperature is the geothermal (undisturbed) temperature, i.e., a function of depth. Ramey modeled the rock formation using the one-dimensional heat diffusion equation:

$$\frac{\partial^2 T_{ft}}{\partial r^2} + \frac{1}{r} \frac{\partial T_{ft}}{\partial r} = \frac{\rho_{ft} c_{p,ft}}{k_{ft}} \frac{\partial T_{ft}}{\partial t}, \quad (2.2)$$

where T_{ft} is the formation temperature, ρ_{ft} , is the formation density, $c_{p,ft}$, is the formation specific heat and k_{ft} , is the thermal conductivity of the formation. Thus, the formation thermal diffusivity is defined as

$$\alpha_{ft} = \frac{\rho_{ft} \cdot c_{p,ft}}{k_{ft}}. \quad (2.3)$$

The boundary conditions applied to Eq. 2.2 considering a radial symmetry are given by

$$\begin{cases} T_{ft} |_{r \rightarrow \infty, t} = T_{ft,i} \\ \left. \frac{\partial T_{ft}}{\partial r} \right|_{r \rightarrow \infty} = 0 \end{cases} \quad (2.4)$$

Ramey (1962) applied the solution of transient heat diffusion available in Carslaw and Jaeger (1959) for a constant heat flux cylindrical heat source, for which the interface temperature between wellbore and formation shows a log-linear behavior for long production

times (high Fourier number). The solution is based on a transient diffusion temperature function, $f(t)$, which can be related to the heat transfer rate from the flowing fluid to the formation using the following equation as

$$dq = \frac{2\pi k_{ft}(T_{wb} - T_{ft,i})dz}{f(t)}, \quad (2.5)$$

where T_{wb} represents the wellbore/formation interface temperature and is defined as

$$T_{wb} = \frac{(k_{ft} \cdot T_{ft,i}) + (r_{to} \cdot U_{to} \cdot f(t) \cdot T_f)}{k_{ft} + (r_{to} \cdot U_{to} \cdot f(t))}, \quad (2.6)$$

$T_{ft,i}$ represents the initial formation temperature (defined by the formation geothermal gradient) and the transient temperature function is rewritten as

$$f(t) = \ln \frac{\sqrt{\alpha_{ft} t}}{r_{wb}} - 0.2886, \quad (2.7)$$

where α_{ft} is the formation thermal diffusivity, r_{wb} is the wellbore radius and the dimensionless time function, t_D , which represents the transient diffusion time, t , as follows

$$t_D = \frac{\alpha_{ft} \cdot t}{r_{wb}^2}. \quad (2.8)$$

It is important to restate that Eq. 2.7 is valid only for production times longer than 7 days according to Ramey (1962). Although useful for estimating wellbore temperatures during injection of hot fluid, the calculation method is based on many assumptions. For instance, it does not take into account phase change during the fluid flow, which has been corrected by Satter (1967), who included steam condensation during the calculations.

Willhite (1967) proposed a procedure to quantify the overall heat transfer coefficient based on the radial thermal resistances of each different layer in the wellbore, which was assumed known until then. To estimate the annuli natural convection coefficients, Willhite suggested

using results from the study of Dropkin & Sommerscales (1965) about natural convection heat transfer between enclosed vertical plates, assuming that the annuli curvatures were negligible. The radiative heat transfer coefficient was determined from Stefan-Boltzmann's Law, considering an infinite concentric annulus.

Ramey (1962) and Willhite (1967) pointed out that heat transmission from wellbores to the formation never actually reaches steady state, since a quasi-steady state is attained in which the rate of heat transfer per unit length monotonically decreases as a function of time. The dimensionless time function, t_D , proposed by Ramey, is a measure of how fast the rock formation conducts heat away from the wellbore. The overall heat transfer coefficient is time dependent, reflecting the variable effective thermal resistance of the rock formation. Raymond (1969) developed one of the first fully-transient models for wellbore heat transfer. This method was later improved with an advanced algorithm for the solution of the discretized equations (MARSHALL and BENTSEN, 1982).

Eickmeier *et al.* (1970) proposed a finite difference model to investigate transient wellbore temperatures during early times of injection or production (low Fourier numbers). The model considers many assumptions, such as constant heat transfer coefficient and thermal properties. Squier *et al.* (1970) provided an exact solution for early time injection of hot fluid into the reservoir. Again, strong assumptions were applied in the model that such as neglecting any thermal resistance in the wellbore.

After Kirkpatrick (1959), Shiu and Beggs (1980) proposed an empirical method for predicting temperature profiles in two-phase flowing wells based on field data from 270 wells. Xiao (1987) developed a simple equation for estimating the temperature profile of a flowing fluid in the wellbore considering many severe assumptions, such as constant fluid and solid properties. Yet, the results showed good agreement with field data from 14 onshore wells.

Wu and Pruess (1990) presented an analytical approach to solve the wellbore heat transfer in a layered formation with different thermal properties without introducing the simplifications of Ramey (1962), namely, neglecting the transient term in the heat balance in the tubing and ignoring temperature history effects on the heat losses. For this reason, Ramey's method is suitable for simulating the heat transfer only for long periods (high Fourier numbers).

Sagar *et al.* (1991) developed a method based on Coulter and Bardon's (1970) model that incorporated Ramey's and Willhite's heat

transfer mechanisms for wellbore with multiphase flow, while taking into account the kinetic energy and the Joule-Thompson expansion. The model, developed with temperature field data from 392 wells, assumes steady state heat transfer in the wellbore. Later, Alves *et al.* (1992), based on the same studies, i.e. Coulter and Bardon (1970) and Ramey (1962), developed a unified equation for predicting flowing temperature profiles in wellbores for the entire range of inclinations. In this work, they applied more rigorously assumptions regarding the thermodynamic behavior of the flowing fluid – for instance, the Joule-Thompson effect was properly accounted for.

Again, turning attention to the heat loss to the rock formation, Chiu & Thakur (1991) developed a semi-analytical model, which can determine the heat losses from deviated wells. The model provided a new transient diffusion dimensionless time function

$$f(t) = 0.982 \ln(1 + 1.81t_D), \quad (2.9)$$

and assumed steady state heat transfer in the wellbore.

Hasan & Kabir (1991) used a rigorous model based on the solution of the partial differential equation resulting from an energy balance on the formation. The solution was carried out using the Laplace Transform for a constant heat flow from the wellbore to the formation. A variation on the heat flow along the production time can be added to the model applying the principle of superposition. Furthermore, the authors proposed a new transient diffusion temperature function and compared the two solutions with those from Ramey's model. The approximate solution presented good agreement with the rigorous one for very low and high Fourier numbers. For the case that the dimensionless time meets values between 0.01 and 5, the dimensionless temperature deviates by 6%.

Hasan and Kabir (1994) proposed a new procedure to estimate the overall heat transfer coefficient adapting Willhite's work, by developing a novel correlation for the natural convection heat transfer coefficient and neglecting the thermal resistance due to the flowing fluid. The correlation was proposed based on an adaptation of the Dropkin and Somerscales (1965) relationship for natural convection between parallel plates ($5 \times 10^4 < Ra < 7.17 \times 10^8$)

$$h_c = \frac{0.049 \cdot (Gr \cdot Pr)^{1/3} \cdot Pr^{0.074} \cdot k_a}{r_{out} \cdot \ln(r_{out}/r_{int})}. \quad (2.10)$$

Hasan *et al.* (1996) and Kabir *et al.* (1996) developed a generalized analytical model capable of predicting the circulating fluid temperature during drilling, workover and well control operations. Hasan *et al.* (1997) proposed a non-isothermal wellbore model coupled to an analytical reservoir approach.

An extension of the Ramey's wellbore heat transfer method, also applicable to the early stages of formation heating process (small Fourier numbers), was proposed by Hagoort (2004). Cheng *et al.* (2011) developed a new formation heat transfer model taking into account the wellbore heat capacity and, so a new analytical transient heat conduction temperature function was proposed.

$$f(t) = \ln(2\sqrt{t_D}) - 0.2886 + \frac{1}{4t_D} \left[1 + \left(1 - \frac{1}{\omega} \right) \cdot \ln(4t_D) + 0.5772 \right], \quad (2.11)$$

where ω is the ratio of the formation heat capacity and the wellbore heat capacity as follows:

$$\omega = \frac{(\rho c_p)_{ft}}{(\rho c_p)_{wb}} \quad (2.12)$$

They observed that the wellbore heat capacity has a considerable influence on the transient diffusion time function, mainly for short time steam injection. Moreover, they found that the new analytical time function depends on the dimensionless time and the ratio between the formation heat capacity and the wellbore heat capacity. Later, Nian *et al.* (2014) compared the most traditional $f(t)$ functions with the one proposed by Cheng (2011). The results were validated with field data showing the importance of the wellbore heat capacity on the accuracy of the heat loss to the formation.

Bahonar *et al.* (2009) proposed a 2-D heat diffusion numerical model to deal with the formation transient heat transfer, aiming to estimate oil recovery with steam injection. One year later, Bahonar *et al.* (2010) compared several formation temperature treatment approaches (two numerical and three analytical approaches) and showed that the 2-D numerical model can better predict casing and interface temperatures especially at the top and bottom well boundaries.

Recently, Xiong *et al.* (2015) proposed a new correlation to account for the natural convection in the annulus, based on a FLUENT CFD study, expressed as

$$h_c = \frac{0.9512 \cdot \left(\frac{r_{int}}{r_{out}}\right)^{1.0987} \cdot k_a \cdot Ra^{0.2469}}{d_h} \quad (2.13)$$

Simulations were performed in steady-state using typical approaches used to deal with natural convection between two long cylinders, as shown in Figure 2.4. The maximum mismatch error between the correlation proposed and the CFD results was 6.7%. However, for the other approaches performed this error was larger than 100% in some cases.

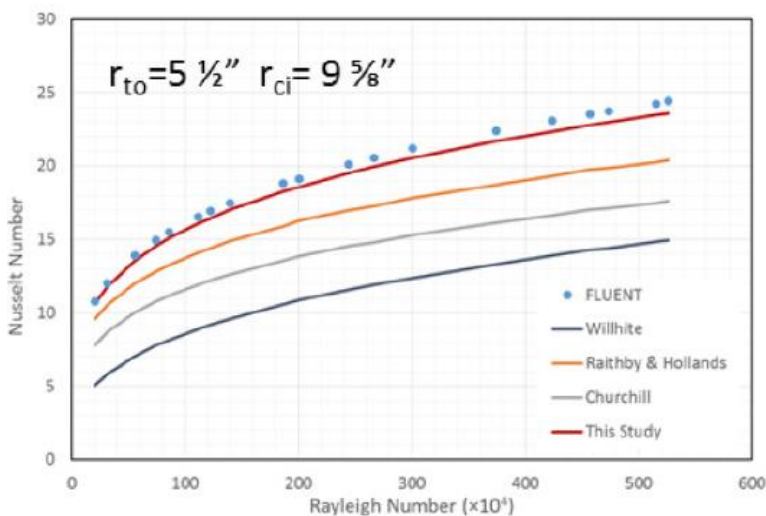


Figure 2.4 – Comparison between annulus gap approaches for predicting convection heat transfer (Xiong *et al.*, 2015).

2.1.3 Tubular and Formation Mechanical Models

Concerning the mechanical approaches used to assess the wellbore integrity, Klementich and Jellison (1986) were one of the first authors to develop a more robust stress analysis of the wellbore. Based on the widely accepted criterion for yielding of ductile, homogeneous

and isotropic materials, the Henky-von Mises theory, the mathematical statement of this theory considers that the expressions for the hoop and radial stresses are derived from Lamé's equations for stresses in a thick-walled cylinder. Hence, the change in hoop strain, $\Delta\epsilon_\theta$, is calculated using Hooke's law as follows:

$$\Delta\epsilon_\theta = \frac{[\Delta\sigma_\theta - \nu \cdot (\Delta\sigma_r - \Delta\sigma_z)]}{E} + \beta \cdot \Delta T \quad (2.14)$$

where E is the Young's modulus¹, ν is the Poisson's ratio², β is coefficient of linear thermal expansion, $\Delta\sigma_r$ and $\Delta\sigma_\theta$ are the radial and hoop stresses and $\Delta\sigma_z$ is the axial stress, calculated according to the local geometric configuration of the wellbore.

From there, the American Petroleum Institute (API) provided a set of formulas and calculations for wellbore tubulars aiming to standardize the stress-loading analysis (API Bulletin 5C3, 1989). Adams and MacEachran (1991) extended the work of Klementich and Jellison (1986) for a multilayer casing wellbore scenario, namely the multistring model. Using a multistring approach means that the annuli are interrelated, so the deformation of an annulus will affect the other ones.

Thus, the annular volume variation due to the fluid expansion and tubular deformation assuming radial symmetry and homogeneous isotropic properties of each annulus present in the wellbore can be calculated as follows:

$$\Delta V_a = \pi \int [(\Delta r_o^2 + 2r_o\Delta r_o) - (\Delta r_i^2 + 2r_i\Delta r_i)] dz + \Delta V_z \quad (2.15)$$

where r_o and r_i are the outer and inner radii of the annulus, respectively; while Δr denotes the variation of the radius of each tubular wall. ΔV_z is the volume change due to annulus axial dimensions variation resulting from expansion or contraction of annulus walls.

Halal and Mitchell (1994) proposed a model for multilayer string that accounted for the interaction between axial stresses and heat up

¹ Young's Modulus – also known as the elastic modulus, is a measure of elasticity, equal to the ratio of the stress acting on a material to the strain produced.

² Poisson's ratio – is the signed ratio of transverse strain to axial strain. In other words, is the amount of transversal expansion divided by the amount of axial compression, for small values of these changes.

pressures, and that included the effects of nonlinear fluid behavior as a function of temperature, pressure, and composition. The authors considered two different scenarios to compute $\Delta\sigma_z$, cemented and uncemented intervals, as depicted in Figure 2.5. Also, a cement/formation interface section is also illustrated.

For uncemented intervals that are fixed at both ends (i.e. casing hanger and TOC), $\Delta\sigma_z$ is a function of the pressure variation and the fluid densities, besides the mechanical properties and geometric characteristics as follows:

$$\Delta\sigma_z = \frac{2\nu[r_i^2(\Delta P_i - g \cdot \Delta z \Delta \rho_i) - r_o^2(\Delta P_o - g \cdot \Delta z \Delta \rho_o)]}{(r_o^2 - r_i^2) - E\beta\Delta T} \quad (2.16)$$

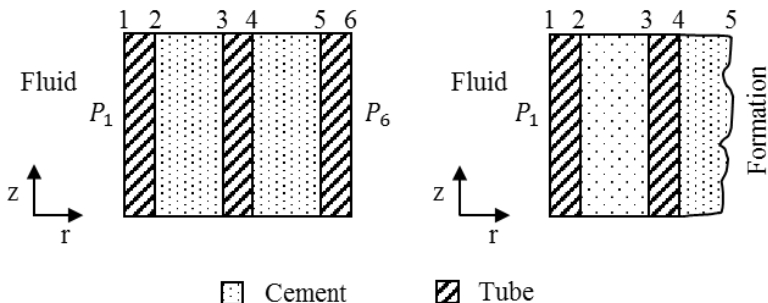


Figure 2.5 – Wellbore arrangements: (a) cemented interval, (b) cement/formation interface (modified from Halal and Mitchell, 1994).

When an annulus is formed between cemented tube walls (cemented interval), then $\Delta\sigma_z$ is obtained from the condition that each point is axially fixed, in other words, $\Delta\epsilon_z = 0$, which yields:

$$\Delta\sigma_z = \frac{2\nu(r_i^2\Delta P_i - r_o^2\Delta P_o)}{(r_o^2 - r_i^2)} - E\beta\Delta T \quad (2.17)$$

Finally, to close the equation system, the variation in hoop strain at the cement/formation interface evaluated for the formation assumes the form:

$$\Delta\epsilon_\theta = \frac{(1 - \nu_{ft}) \cdot \Delta P_o}{E_{ft}} \quad (2.18)$$

where ΔP_o denotes the pressure variation at the cement/formation interface and ν_{ft} and E_{ft} are the formation mechanical properties.

Halal and Mitchell (1994) suggested a matrix formulation to deal with the continuity of the stress distribution between the solids in order to estimate the volumetric annulus variation. The pressure distribution at each interface between the different wellbore elements was performed adopting a tridiagonal matrix algorithm. The integrated model predictions were compared with results from single-string analyses demonstrating the strong interaction between casing strings.

Oudeman and Bacarreza (1995) evaluated the effect of the formation response on the wellbore in the particular case where the inner casing was not cemented into the shoe of the outer casing. In this scenario, the fluid leak off to the formation drives the pressure build up behavior. Later, Oudeman and Kerem (2006) developed an experimental method to predict the pressure increase behavior in confined annuli under transient conditions. The method was able to provide some insights about the annulus build up pressure over time.

Sathuvalli *et al.* (2005) advanced a more rigorous model including the role of formation elasticity on the APB, considering the rock formation as an elastic foundation. In this case, the cement sheath outside the casing was treated as part of the formation due to the fact that the elastic constants were on same order of magnitude. Hence, this approach avoids an additional unknown quantity, i.e. the pressure changes in the formation near the wellbore, which arose from the Halal and Mitchell (1994) approach.

Recently, Hafemann *et al.* (2015) adopted the same multistring approach to predict the interface pressures using the GMRES (generalized Minimal Residual) method to solve the resulting system of linear equations. Barcelos *et al.* (2017) improved Hafemann's model assuming that each annulus behaves as a pressure vessel. As the mass in each annulus does not change, considering that annuli are fully closed, after running the thermal model, the resulting annulus average temperature is used to compute the pressure variation due to the fluid expansion.

2.2 APB Behavior Prediction and Field History

As previously discussed, annular pressure buildup (APB) can be understood as the increase in pressure due to thermal expansion of fluids confined in one or more annuli within a wellbore. However, a more general definition of APB is provided by the Global Standards from the International Association of Drilling Contractors (IADC) in 2010 (API STD 65 – Part 2):

“Pressure generated within a sealed annulus by thermal expansion of trapped wellbore fluids typically during production. May also occur during drilling operations when trapped annular fluids at cool shallow depths are exposed to high temperatures from fluids circulating in deep, hot hole sections. This thermally induced pressure is defined and listed in API RP 90 as thermal casing pressure. APB is also referred to as annular fluid expansion (AFE)”.

Due to the increase in the APB scenarios in the last years with the development of extreme water depths and hole depth in many modern offshore wells, IADC proposed a new definition of APB (API RP 96):

“Pressure generated within an annulus by thermal expansion of wellbore fluids, typically during production”.

However, two notes followed the definition: the first one is that the APB can also occur during drilling operations when trapped annular fluids at cool shallow depths are exposed to high temperatures induced by fluids circulating from deep, hot hole sections. This thermally induced pressure is defined and listed in API RP 90 as thermal casing pressure. The second one stated that the APB can also occur from migration of formation fluids, as defined in API RP 90.

Although there is a vast literature on the physics of APB (ADAMS and MACEACHRAN, 1991; BELLARBY, 2009, HAFEMANN 2015), and most theoretical aspects has been explored (HALAL and MITCHELL, 1994; SATHUVALLI *et al.*, 2005; OUDEMAN and KEREM, 2006; HASAN and KABIR 2012; YIN and GAO, 2014, HAFEMANN, 2015) there is still lack of a comprehensive approach that accurately predicts the multilayer APB magnitude.

According to Sathuvalli *et al.* (2016), the boundary conditions and the fluid thermo behavior determine the type and the stiffness³ of the wellbore annuli. The pressure increase is essentially the outcome of how each wellbore annulus behaves as heat is transferred from the flowing fluid to the formation, and how each annulus mechanically reacts when subjected to this thermal effect.

Changes in the containment volume alleviate the annular pressure due to ballooning or reverse ballooning, and thermal dilation/contraction of the casing strings. The pressure in the annulus may also be reduced by bleeding the inner fluid from the annulus at the wellhead or leaking through the formation below an open casing shoe, as seen in Figure 2.6 (BELLARBY, 2009).

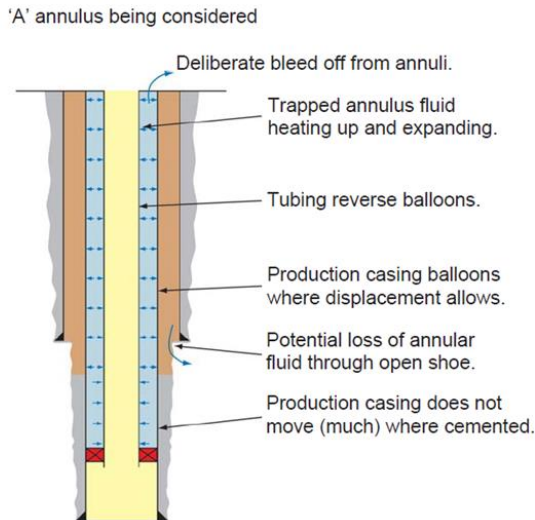


Figure 2.6 – Determining factors of the APB (BELLARBY, 2009).

Despite beliefs that open shoes can ensure annular fluid bleed off (PELIANO *et al.*, 2014), some authors claim that the sedimentation of solids in the drilling fluids creates a non-permeable layer above on top of cement that prevents fluid flow to the formation (ZAMORA and BELL, 2004; OMLAND, 2009).

³ Stiffness – The annulus stiffness is a measure of the expected pressure increase in the annulus fluid per unit increase of temperature (Sathuvalli *et al.* (2016).

APB can be quantified by the following equation (Eq. 2.19), which relates the change in pressure to changes in the mass of the confined fluid, volume and temperature of the annulus (OUDEMAN and BACAREZZA, 1995):

$$\Delta P = \left(\frac{\partial P}{\partial m} \right)_{V,T} \cdot \Delta m + \left(\frac{\partial P}{\partial V} \right)_{m,T} \cdot \Delta V + \left(\frac{\partial P}{\partial T} \right)_{m,V} \cdot \Delta T, \quad (2.19)$$

where the first term represents a change in pressure due to fluid leakage to the formation, the second term represents the change in pressure caused by changes in annulus containment that is induced by thermal or hydraulic loads on the tubing/casing and the third one represents the increase in pressure as the temperature increases assuming a constant volume. After manipulation, Eq. 2.19 can be rewritten in the following form (OUDEMAN and KEREM, 2006):

$$\Delta P = \frac{\Delta V_f}{C_f \cdot V_f} + \frac{\Delta V}{C_f \cdot V} + \frac{\beta_f \cdot \Delta T}{C_f}, \quad (2.20)$$

where C_f is the fluid compressibility coefficient, V_f is the fluid volume in the annular space, V is the annulus volume, and β_f is the thermal expansion coefficient of the annulus fluid.

According to Oudeman and Kerem (2006), in a sealed annular, the third term is usually dominant and the second term is on the order of 10 to 20% of the third term. Hasan and Kabir (2009) stated that the third term or pressure increase caused by liquid expansion accounts for well over 80% of the total APB in most cases. Halal & Mitchell (1994) claim that neglecting the second term most likely will lead in a non-reliable calculation.

In a fully trapped annular, the first term in Eqs. 2.19 and 2.20 can be neglected since the amount of annular liquid fluid does not change. Thus, the APB depends basically on the two last terms of Equation 2.20. By knowing the magnitude of the fluid volume change and the mechanical response of the annular to pressure and temperature changes, the magnitude of APB in one or more annuli can be calculated. Bellarby (2009) named the limit load in the annulus as MAASP – Maximum Allowable Annular Surface Pressure, which can be related to the tubular collapse or burst resistance.

Even though the root cause of the problem arises from a thermal process, the outcome is strictly structural, hence, the importance of

developing a comprehensive multiphysics model to deal with it. While conceptually simple, there are huge challenges concerning the APB quantification. In fact, the level of accuracy of an APB model depends strongly on each of its constituting models, the assumptions regarding fluid and formation properties and the numerical mesh size. Sathuvalli *et al.* (2005) stated that most industry standard wellbore thermal simulators included an uncertainty of at least ± 3 K and another source of uncertainty came from the fluid thermal physical properties calculation.

Recent works attempted to estimate APB both analytically and numerically. Many assumptions have been stated making the solution method less accurate, such as: use of single-phase flow model, steady state condition, use of constant thermophysical properties, neglecting the deformation of tubes, disregard the wellbore thermal capacity to quantify the $f(t)$ function, among others.

Hasan *et al.* (2010) presented two approaches to estimate the APB assuming a transient and a quasi-steady formulation to model the heat transfer in the wellbore. However, both models disregarded the structural changes in the wellbore due to the deformation of the tubes. Alcofra (2014) developed a wellbore thermal model that considered a multistring approach to deal with annuli volume and pressure changes due to heat transmission from a single-phase oil flow under steady state condition.

Hafemann (2015) developed a numerical approach that overcame several limitations encountered in previous models, including:

- a steady-state flow pattern-based multiphase flow model;
- a compositional model to calculate the changes in hydrocarbon properties;
- a transient heat transfer model that used a $f(t)$ function based on the heat capacity of the wellbore;
- a multistring approach to deal with annuli volume and pressure change;
- variable thermodynamic properties of the annular fluids;
- different types of rock formations.

Even though the work of Hafemann *et al.* (2015) has shown meaningful advances with respect to the thermo-hydraulic coupling and the structural modeling of the wellbore, it was only in the subsequent work of Barcelos *et al.* (2017) that a practical way of calculating APB was successfully implemented. In the latter study, a new approach was proposed based on the formulation of Oudeman and Kerem (2004) that

considered each annulus is treated as an integral volume (pressure vessel approach), so that the pressure change in the annulus caused by local volume variation is assumed to be transmitted throughout each annulus instantly. In other words, despite computing local volume deformations, the increase in pressure was calculated for entire annulus and updated every time step.

2.3 APB Mitigation

APB issues are dealt with carefully, depending on the scenario. Managing procedures and/or mitigation techniques are often required as reported by Nelson (2002). Accidents arising from pressure increase in annulus are essentially a consequence of an unsuitable well design caused by a thermal behavior that was not anticipated and/or an undersized equipment application. The consequences can be catastrophic, ranging from well losses and severe environmental damage to the loss of human lives.

In onshore wells and offshore platforms, the “Christmas tree” is able to alleviate the annulus pressure by bleeding off through the surface accessible wellhead equipment. However, in subsea offshore wells, the primary annulus formed by the tubing and production casing is the only one accessible. All other annuli are sealed and do not allow bleeding (VARGO *et al.*, 2003; WILLIAMSON *et al.*, 2003).

Based on the above, two conditions are required for the APB phenomenon to take place: an increase in temperature due to hydrocarbon production and the presence of sealed annulus filled by packer/drilling fluid. While pressure buildup in the annular is a common occurrence, regardless whether the annulus is sealed or not, casing failure will only occur if the annulus is confined and the pressure increase exceeds the casing mechanical resistance. This condition is commonly present in all subsea producing wells, but it is most evident in deepwater environments. Deepwater wells are more vulnerable to APB because of the cold seafloor temperatures (below 280 K), which contrast with the high subsea wellhead temperatures that commonly range from 340 to 400 K during hydrocarbon production.

In order to avoid the tube collapse, several strategies are commonly used to mitigate APB as reviewed in (PATTILLO, 2011; MOE and ERPELDING, 2000; WILLIAMSON *et al.*, 2003). For instance, the following equation presented by Ellis *et al.* (2004)

describes the important parameters that can be varied in the design of a well to reduce APB, considering the annular space as a rigid container:

$$\Delta P = \left(\frac{\beta_f \cdot \Delta T \cdot V_o - \Delta V}{V_o} \right) \cdot \frac{1}{C_f}, \quad (2.21)$$

where ΔP is the annulus pressure variation, β_f is the fluid thermal expansion coefficient, ΔT is the temperature variation, V_o is the initial volume of the fluid, ΔV is the volume change and C_f is the fluid compressibility coefficient. Equation 2.21 shows that fluid properties and change in volume and temperature are important parameters to control the APB. In fact, the change in volume depends on the fluid properties, which in turn also affects the heat transfer process and the temperature difference.

The many alternatives to avoid well failure due to APB were classified below according to their working principle:

- Enhanced tubular design: this strategy focuses on the increase in casing capability to accommodate a higher pressure level buildup without a negative effect on the wellbore. Several studies provide advances in probabilistic performance properties of tubulars and so, upgrade the tubing and casing to withstand the loads (ROSLAND *et al.*, 2013; SHAHREYARAND and FINLEY, 2014).
- Annulus flexibility: the objective here is to create a preferred leak path or bleed port. Casing rupture-disk technology allows a casing design to fail in a predictable condition. The disk is set in the casing and the wellbore is designed to vent outward rather than collapse inward. Extensive testing and design optimization of rupture disks have been performed associated with this application (VARGO *et al.*, 2003; SANTOS *et al.* 2015). A rougher, but efficient strategy one may treat the casing perforating a hole to relieve the pressure to a non-permeable zone or even drill a hole at the wellhead with a world class ROV⁴ and special tools, allowing the expanded fluid escape to the sea (DOS SANTOS *et al.* 2012).

⁴ ROV – Remotely operated underwater vehicle is a submersible vehicle remotely operated by a person onboard in a drilling rig. It is used to conduct and supervise operations in deep water environments.

- Controlling gained volume: the purpose of this alternative is to control the expanded volume by the trapped fluid as heating occurs. There are three ways to do this: the first one is the use of compressible fluids with a relatively small amount of nitrogen to absorb enough liquid volume expansion to prevent casing failure. Another option is using a spacer fluid that shrinks with increasing temperature (BLOYS *et al.*, 2007). The third one deals with attaching crushable foam wrap to the outer casing wall (SATHUVALLI *et al.*, 2005). The syntactic foam consists of hollow thin-walled glass microspheres composed of sodium borosilicate glass and filled with air at atmospheric pressure. When the annular pressure reaches a certain value, the hollow spheres collapse generating an extra volume in the annular space and preventing further pressure increase from expansion.
- Application of insulation materials: this strategy aims to reduce the radial heat transfer from the production string to the annuli. The insulation can be the annular fluid such as the drilling and/or packer fluid or insulated tubes, for instance, the vacuum insulated tubing (VIT). VIT systems are better used in scenarios that require high insulation capacity. However, many drawbacks and uncertainties follow the VIT application. Low thermal conductivity aqueous-based packer fluids have been used in less severe APB scenarios in deepwater environments (JAVORA *et al.*, 2002; ERIKSEN *et al.*, 2014). Osgouei *et al.* (2014) proposed a set of guidelines to improve the insulation performance of annular fluids (drilling fluids) based on its rheological behavior.

Sathuvalli *et al.* (2005) developed a screening procedure and a computational tool to allow an examination of operational scenarios and identification of the key parameters that control the APB phenomenon. Santos *et al.* (2015) offered a good explanation about the several APB mitigation techniques, outlining design procedures and illustrating guidelines for application scenarios.

2.4 VIT Basics

The VIT technique consists of an inner production tubing welded to an outer tube at both ends, forming an annular cavity that is evacuated

(see Figure 2.7), with the aim of minimizing the radial heat transfer (AZZOLA *et al.*, 2007).

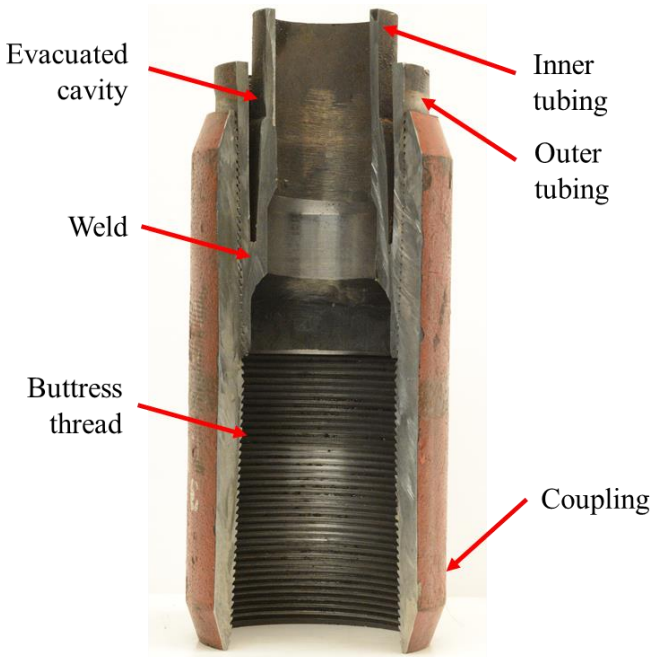


Figure 2.7 – VIT connection details.

The manufacturing process of vacuum insulated tubes was described by Bellarby (2009) as follows: before the tubings are welded, a port is drilled in the outer tubing and an absorbent is added to the space. Once welded, the space between the tubes is evacuated, heated to activate the absorbent, filled with argon and then evacuated again. Finally, a vacuum plug is installed. However, there is a short section, typically between 0.15 and 0.25 m at each coupling, which does not have a cavity to be evacuated. Since the junction between every two tubes is not insulated, heat transfer can be significant at this location. This section has a more serious impact on the overall heat loss than its relative length as reported by Pattillo *et al.* (2004). Convection cells build up above each connection, transporting heat away from the connection.

VIT systems can be manufactured according to different material and dimensional specifications. Typical ranges of overall tubing length,

coupling length, tubing diameters and tubing material of commercial VIT systems are shown in Table 2.1.

Table 2.1 – Typical dimensions of commercial VIT systems

Overall length	6.096 to 12.192 m
Coupling length	0.2540 to 0.1461 m
Outer tubing external diameter	0.178 to 0.089 m (7 to 3 ½ in)
Inner tubing internal diameter	0.140 to 0.060 m (5 ½ to 2 3/8 in)

If the connections are effectively insulated, the equivalent thermal conductivity of VIT can be excellent, reducing by more than 60% the heat loss rate through the connection. This benefit can be reached using a PTFE (Polytetrafluoroethylene) or thin film (a modified liquid epoxy coating) multilayer insulation (HORN and LIVELY, 2001), inside and/or outside the tubings, depending on the welding configuration. Overall conductivities will depend on the connection insulation, annular fluids and soil properties (AZZOLA *et al.*, 2004). There are advantages and disadvantages of each VIT configuration, as shown in Figure 2.8, relating mainly to cost, strength and quality control (BELLARBY, 2009). Thus, it should be noted that the VIT joints are stacked (connected) one above the other until reaching the depth that it is desired to reduce the radial heat transfer.

Despite the many years of experience on well insulation technologies applied to oil and gas production, the technical literature on VIT systems is still somewhat limited, with many unanswered questions concerning its thermal performance, applicability and most relevant physical mechanisms. For instance, aspects related to the effective thermal conductivity, heat loss through the connection and main body, and the impact of the vacuum level on thermal performance, need to be properly quantified before VIT systems become consolidated in Brazilian offshore wells.

Furthermore, VIT systems are expensive, heavy, take up a significant portion of the annular space and require high-strength tubulars due to high stresses on the tubular bodies and welds (BELLARBY, 2009; JAVORA *et al.*, 2002; EZELL *et al.*, 2010). Due to operational, engineering and cost constraints, the VIT joints are often combined with bare tubings. Typically, VIT joints are installed from the

mudline to a chosen depth, which depends on the wellbore architecture and thermal and mechanical requirements (SATHUVALLI *et al.*, 2016).

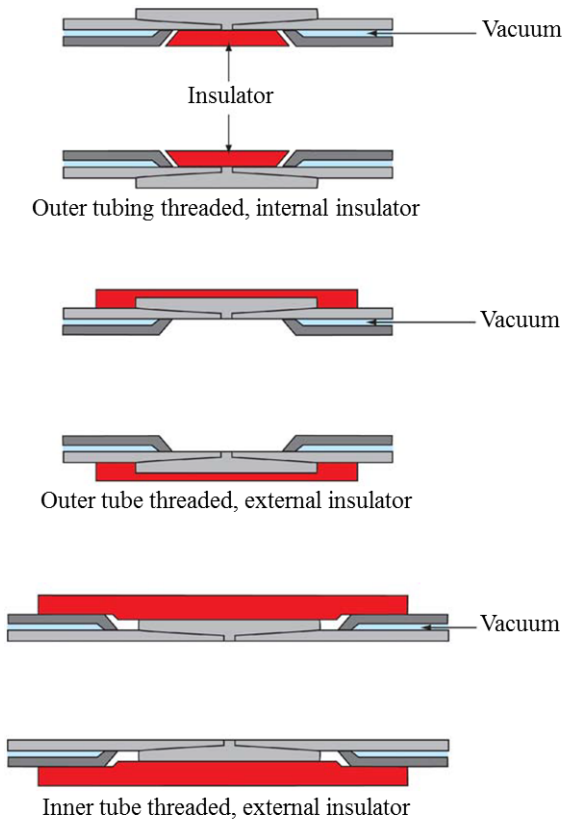


Figure 2.8 – VIT configurations (BELLARBY, 2009).

2.4.1 The k-value (U-value) concept

For simplicity, the petroleum industry has successfully adopted a single value to characterize the VIT insulation performance, which has been called k-value, an equivalent thermal conductivity of the VIT system (FEENEY, 1997; AZZOLA *et al.*, 2004; AZZOLA *et al.*, 2007; SINGH *et al.*, 2005; FERREIRA *et al.*, 2012; YUE *et al.*, 2013; KARRA *et al.*, 2014; AL SHAIBI, 2015), despite understanding that the actual k-value may vary along the length of the VIT. In fact, the VIT's

k-value and/or U-value (equivalent overall heat transfer coefficient of the VIT) depends on the boundary conditions and may vary with annular fluid types and soil properties (AZZOLA *et al.*, 2004).

It will be shown later in this section that the k-value has a somewhat broader meaning than the thermal conductivity. While the latter is a physical property of a given material, the k-value concept is used in the oil industry to quantify an equivalent thermal conductance (per unit length) of interconnected heat transfer processes between a given temperature difference. Although its definition is very similar to that of the overall heat transfer coefficient, U, the k-value is the quantity used as a thermal performance indicator in wellbore thermal flow simulators (Wellcat™, OLGA®).

The main issue regarding the application of a single value of equivalent thermal conductivity to represent the thermal behavior of a VIT joint is that it frequently misrepresents the multidimensional nature of the temperature and heat transfer behavior in the connection section. Since the temperature distribution in the solid regions of the VIT in the vicinity of the connection section are affected by the local thermal conductances in the surrounding domains (e.g., natural convection and the radiation in the annuli, forced convection in the production tubing), the k-value becomes very much dependent on the well operating conditions. As a result, wellbore completion designers often consider high k-values in their completion projects to meet conservative pressure increase estimates in their APB calculations.

2.4.2 VIT thermal models

For a better description of the heat transfer in VIT systems, their geometry is usually divided into two parts: the VIT body and the connection. The VIT body consists basically of the two concentric tubes and the vacuum space, forming a thermally insulated region, through which the heat transfer rate per unit length is designed to be minimal. The second part is the connection between the two VIT bodies. In this section, there is no vacuum and, therefore, the heat loss to the surrounding environment is expected to be much higher. Azzola *et al.* (2004) presented the heat paths through the VIT, as illustrated in Figure 2.9.

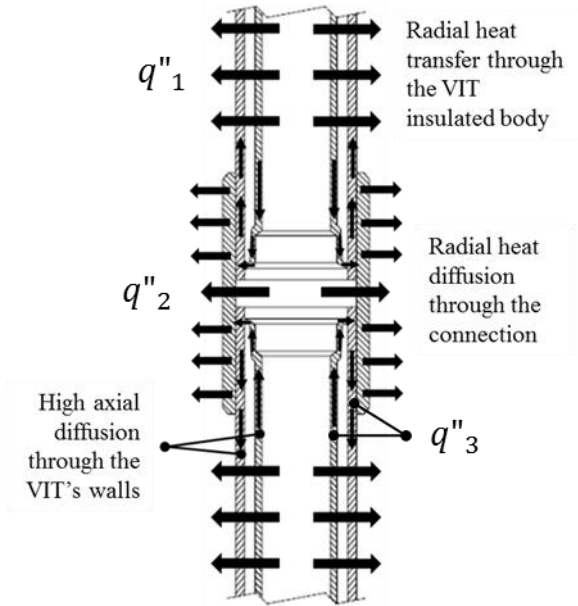


Figure 2.9 – Heat fluxes (arrows) in the VIT body and connection sections (modified from Azzola *et al.*, 2004).

Three different heat fluxes can be associated with the VIT system, as shown in Figure 2.9. q''_1 is the radial heat flux through the vacuum space, q''_2 is the radial heat flux through the connection and q''_3 is the axial heat flux through the tube walls. Given the high thermal resistance offered by the vacuum and the high thermal conductivity of the steel tubes, the axial conduction heat flux q''_3 is created, allowing heat to travel from the inner tube wall towards the weld, then through the weld and back towards the VIT's outer tube. The preferred path followed by the heat flux leads to a high heat loss through the connection by convection to the external environment. Figure 2.10 highlights such phenomenon and shows the behavior of the radial heat flux and the external temperature of the VIT surface as a function of the distance from the center of the connection (PATTILLO *et al.*, 2003).

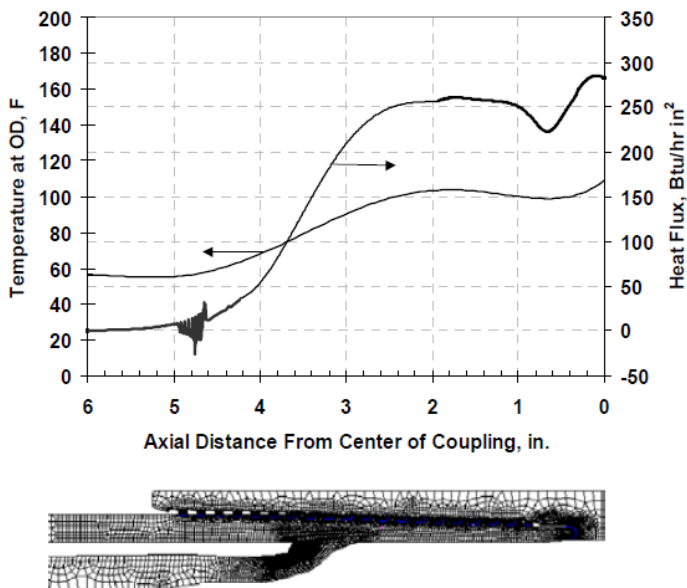


Figure 2.10 – Radial heat flux and VIT outer surface temperature under forced convection (Pattillo *et al.*, 2003).

Azzola *et al.* (2004) developed an analytical model to assess the VIT thermal performance. They assumed that q''_1 was governed by the radiation thermal resistance in the vacuum space. Additionally, since the conduction thermal resistance in the tube wall is much lower than the outside VIT connection thermal resistance, q''_2 is assumed to depend only on the outside VIT connection thermal resistance (convection). On the other hand, it is not straightforward to determine q''_3 , since the heat flux is directly affected by the size of the hot zone around the weld, which, in turn, is directly dependent on the magnitude of the convective heat loss through this region. Azzola *et al.* (2004) computed this heat flux through an analogy with an extended surface formulation considering an adiabatic-tip fin, which is a function of h_c (convection heat transfer coefficient of the fluid surrounding the fin), k_{fin} (thermal conductivity of the fin) and the fin geometry. Hence, the fin thermal resistance itself is:

$$R_{fin} \equiv R_{fin}(R_{ext}, k_{fin}). \quad (2.22)$$

Although the heat transfer in the VIT shares some similarities with an extended surface, the VIT performance is also a function of the vacuum equivalent thermal conductivity. Thus:

$$R_{VIT} \equiv R_{VIT}(R_{ext}, k_t, k_v), \quad (2.23)$$

The equivalent thermal conductivity of the vacuum space was calculated assuming a parallel arrangement between the thermal resistances associated with the residual air diffusion (pressure lower than 13 Pa) driven by k_d , the thermal conductivity of the air and the radiation contribution,

$$k_v = k_d + k_r, \quad (2.24)$$

where the radiative equivalent thermal conductivity, k_r , is nonlinear with respect to absolute temperature and can be estimated by (AZZOLA *et al.*, 2004):

$$k_r \cong \frac{\varepsilon \cdot \sigma \cdot (D_{oi} - D_{io}) \cdot (T_{io}^2 + T_{oi}^2) \cdot (T_{io} + T_{oi})}{4n}. \quad (2.25)$$

Since the vacuum space in VIT systems frequently contains aluminum foil wraps separated by glass fiber foils, k_r is a function of the tubes surface emissivity, ε , the absolute temperatures of the outer surface of the inner tube and the inner surface of the outer tube and n , which is the number of reflective wraps.

Azzola *et al.* (2004) also described the development of a two-dimensional axisymmetric finite-difference code to model the VIT thermal performance. The VIT geometry was divided into three regions, where the external convection heat transfer coefficient was assumed to be uniform - at the coupling, weld region (0.0508 m in extent beyond weld), and VIT body. The scheme of the finite difference code exhibited by Azzola *et al.* (2004) is depicted in Figure 2.11. From the element discretization, the energy balance in the inner tube and in the outer tube was performed. The heat balances took into account the transient heat transfer, the axial heat diffusion through the tubing walls, the radial radiative heat transfer through the vacuum space and the internal or external convective heat transfer depending on where the energy balance is applied, if in the inner tube or the outer tube.

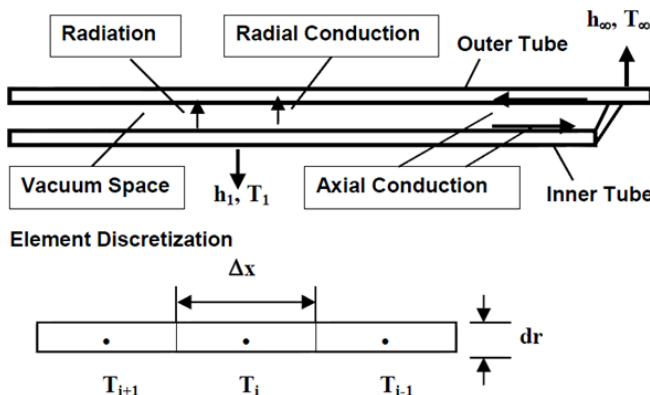


Figure 2.11 – Finite difference code discretization scheme (AZZOLA *et al.*, 2004).

Azzola *et al.* (2004) proposed two definitions of the effective thermal conductivity of the VIT as follows:

$$k_{ef,1} = \frac{q' \cdot \ln(D_{oo}/D_{ii})}{2\pi \cdot (T_i - T_\infty)} \quad (2.26)$$

$$k_{ef,2} = \frac{q' \cdot \ln(D_{oi}/D_{io})}{2\pi \cdot (T_i - T_\infty)} \quad (2.27)$$

In Equation 2.26, the effective thermal conductivity was defined relative to the outer diameter of the outer tube and the inner diameter of the inner tube, while in Equation 2.27 it was defined relative to the inner diameter of the outer tube and the outer diameter of the inner tube. It was concluded that the $k_{ef,2}$ thermal property is a better parameter to characterize the VIT's effective thermal conductivity because, as the external thermal resistance increases, the insulation system performance expressed by $k_{ef,2}$ converges to the vacuum value. Thus, by choosing $k_{ef,2}$ as a definition, it is easy to recognize how well the insulation system performs relative to an ideal performance level. The following equation was proposed by Azzola *et al.* (2004) to assess $k_{ef,2}$ meaning with respect to a dimensionless external thermal resistance:

$$\frac{R_{ext}}{R_{int}} = \frac{2 \cdot k_v}{h_{\infty} \cdot D_{oo} \ln(D_{oi}/D_{io})} \quad (2.28)$$

Also, an expression to estimate the overall heat transfer coefficient was also proposed by Azzola *et al.* (2004) based on the $k_{ef,2}$ value

$$U_{ef} = \frac{2k_{ef,2}}{D_i \ln\left(\frac{D_o}{D_i}\right)} \quad (2.29)$$

2.4.3 VIT thermal and mechanical evaluations

Despite the numerous successful cases, one should recognize the many challenges faced by oil companies to develop deepwater environment oilfields using VIT technologies. For instance, deepwater scenarios pose significant drawbacks for selecting suitable VIT tubulars to ensure long-term reliability under combined mechanical and thermal loads.

Ellis *et al.* (2002) performed an extensive study of the VIT thermal behavior in a full-scale experimental test facility - a VIT system consisting of a 0.1397-m (5 ½-in) OD, 0.1143-m (4 ½-in) ID tubing was used. The experiments were able to determine average and local values of the overall heat transfer coefficients of the VIT system. Several configurations of the VIT were tested varying the coupling insulation and annuli fluid type. Results showed that the heat loss at the coupling drives the thermal performance of a VIT joint. Additionally, the authors concluded that, for this case, the VIT without coupling insulators could not be employed in the remaining wells of the Marlin field in the Gulf of Mexico.

Gosch *et al.* (2004) used the test results obtained by Ellis *et al.* (2002) to design a suitable VIT system and described the methodology to install VITs and monitor the pressure and temperature behavior using fiber optic gauges in the remaining Marlin field wells in the Gulf of Mexico.

Mechanical loads over the VIT were studied before by Pattillo *et al.* (2003) and Nowinka *et al.* (2005). The interrelation of the inner and outer tube, constrained at the weld, induces internal loads in the VIT joint that are foreign to conventional tubing design. Figure 2.12 presents

a basic VIT configuration with the thread on the outer tube (NOWINKA *et al.*, 2005).

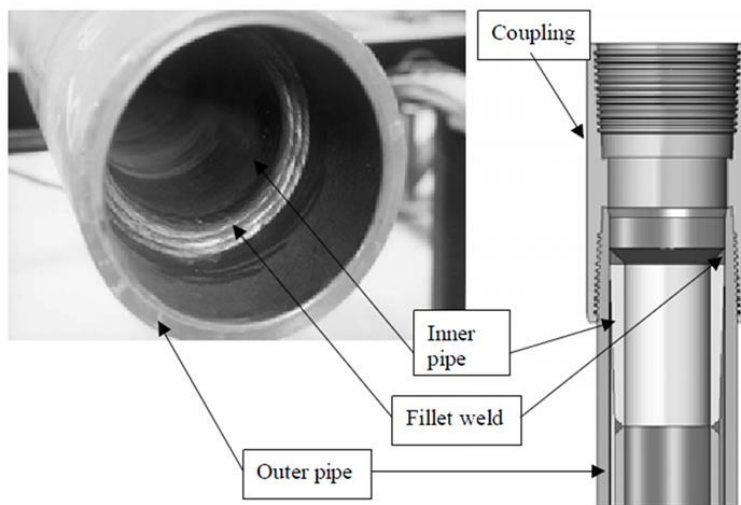


Figure 2.12 – A basic VIT configuration with the thread on the outer tube (NOWINKA *et al.*, 2005).

Another challenge faced by VIT system designers is the increase in axial load due to the large weight of these systems. Additionally, the interaction of the two tubes constituting the vacuum space introduces new considerations regarding burst and collapse resistances. Among them, one can cite (PATTILLO *et al.*, 2003):

- The lack of back up pressure on both inner and outer tubings;
- The unique axial load in the separate tubes due to their displacement constraint at the weld;
- The possibility of vacuum failure due to weld damage by corrosion or fatigue.

Mechanical design of VIT systems deals with their structural integrity and sealing capability. Nowinka *et al.* (2005) described an extensive experimental setup to assess the mechanical behavior of full-scale VIT systems. As expected, the structural integrity of the weld is critical for the VIT's performance. According to Nowinka *et al.* (2005), if the weld fails, the VIT will lose its thermal insulation properties and pressure integrity. In addition to the physical evaluation, a finite element analysis was conducted to quantify the deformations and stresses that

are present in a typical VIT section. A total of seven load cases were numerically considered and twenty-two load cases were carried out in the experiential test. The tests showed that the VIT exhibited good structural integrity and sealability in the combined load test. There was no indication of weld failure throughout the test. The finite element analysis results indicated that the load case involving simultaneous application of maximum internal and external pressure proved to be the most severe combination of loads.

Thus, Kim *et al.* (2005) and Kim and Cernocky (2005) evaluated the welding performance and stated a set of guidelines to ensure structural integrity, acceptable corrosion resistance properties and sealing.

Azzola *et al.* (2007) described a thermal experimental analysis using two connected VIT joints. Two configurations were tested: with and without an external polyurethane coupling insulator. Tests results showed that the VIT overall heat loss is 61% lower when the coupling insulator is employed.

2.5 VIT Assisted Wellbore Applied to APB Mitigation

Feeney (1997) described several applications of VIT systems in subsea completions to prevent hydrate formation and wax deposition. U-values in the magnitude of $0.095 \text{ W/m}^2\cdot\text{K}$ are used in the completion designs by Shell in the Gulf of Mexico. VIT systems integrated with polyurethane coupling insulation have been used to control paraffin deposition in the Norman wells field (PURDY and CHAYNE, 1991). Singh *et al.* (2005) used a value of $0.023 \text{ W/m}\cdot\text{K}$ as an equivalent thermal conductivity of the VIT to simulate the effect of insulation in the wax deposition in a deviated production well using the OLGAs software, a commercial transient multiphase flow and thermal software, as illustrated in Figure 2.13. The computational results showed a significant increase in the wellhead circulating temperature while using VIT joints. Even though the wellhead circulating temperature was not higher than the wax appearance temperature of the crude oil, the increase in temperature with the increase in VIT length caused a significant reduction in heat transfer and wax deposition rates.

Ferreira *et al.* (2012) presented two cases where VITs were considered in the wellbore design phase as a means to prevent APB in deepwater scenarios. In one of them, the VIT technique met the design requirements and could be used as a wellbore insulator. In contrast, in

the other case, due to noncompliance with the assumptions set in the design phase regarding the production string integrity, the VIT could not be used to solve the APB problem between the 0.508-m (20-in) surface and 0.340-m (13 3/8-in) intermediate casings. Figure 2.14 shows the wellbore schematic diagram for the first case, with the possible APB problem occurring between the 0.508-m (20-in) casing and the 0.340-m (13 3/8-in) casing due to an estimated production of 0.035 m³/s (19,000 BPD). A production through the tubing string was simulated with and without a 1,000 m VIT section comprising a 0.1683-m (6 5/8-in) OD 0.1397-m (5 1/2-in) ID tubing.

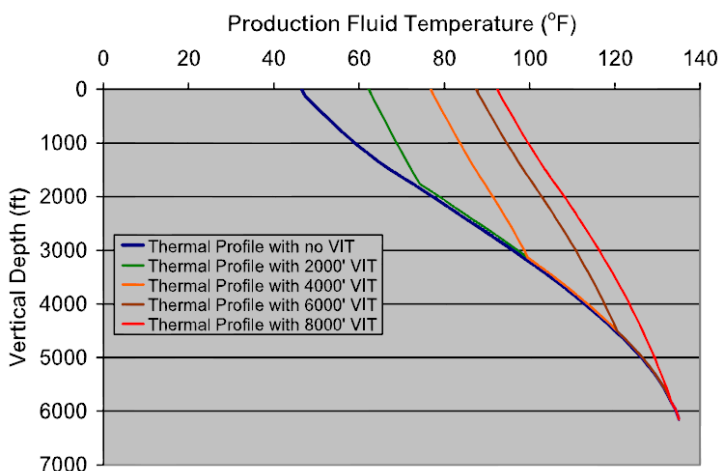


Figure 2.13 – Effect of the VIT on the production thermal profile of an arctic deviated well (SINGH et al., 2005).

The buildup pressure in the “C” (i.e., the outermost) annulus, formed by the 20-in and the 13 3/8-in OD casings, was simulated using a commercial software, Wellcat™, assuming an equivalent thermal conductivity of the VIT equal to 0.074 W/m.K. The predicted APB in the production annular as a function of the production time is illustrated in Figure 2.15. An APB difference of approximately 13.8 MPa (2,000 psi) after 1 day of production was found when nearly 1,100 m of bare pipe was substituted by the same length of VIT. After 1 year of production, i.e., steady-state, the buildup pressure difference increased to nearly 17.9 MPa (2,600 psi).

In the second case, VITs could not be used and important issues were raised regarding the mechanical integrity performance. According

to Ferreira *et al.* (2012), some operational limitations were met during the load cases computational simulation. For instance, when the tubing evacuation load criterion was applied, the tubing string collapse safety factor was exceeded even though the APB problem between the intermediate and surface casings was solved. This case is a good example that the use of VIT joints need to be study for each operational condition.

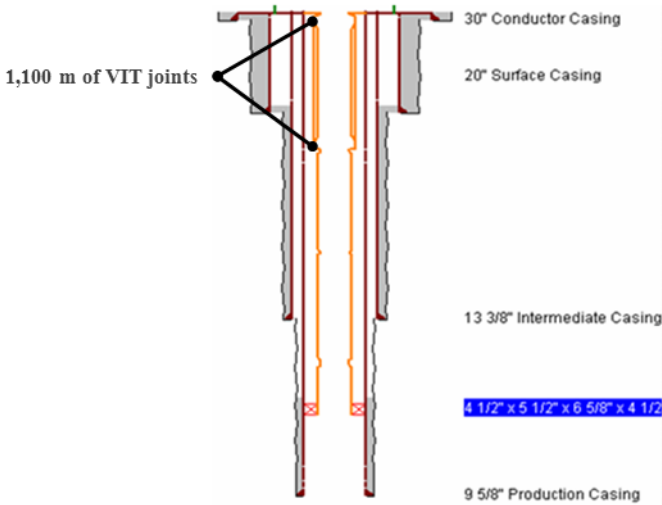


Figure 2.14 – Wellbore schematic assuming 1,100 m of VIT just below the wellhead (FERREIRA *et al.*, 2012).

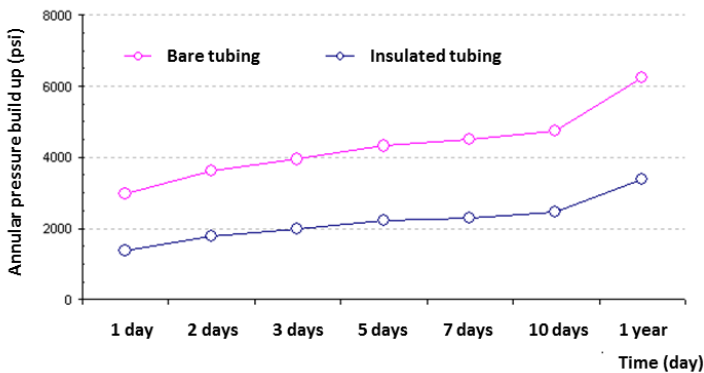


Figure 2.15 – APB as a function of production time (FERREIRA *et al.*, 2012).

Recently, to demonstrate the benefits of VIT compared to bare tubing injector string, Karra *et al.* (2014) carried out a CFD study aiming to provide a comparison of heat loss in both VIT and bare tubing concentric and eccentric configurations during SAGD operations. It was assumed a k-value of 0.006 W/m.K as the VIT equivalent thermal conductivity. The computed results successfully demonstrate the benefits of VIT over bare tubing in maintaining steam quality in the vertical section of the wellbore. Additionally, as expected, the study shows reduction in steam quality for eccentric position of the bare tubing compared to concentric position, since in the eccentric arrangement the tubing can be in contact with casing. Thus, conduction also takes place in addition to the natural convection and radiation heat transfer in the annulus gap.

Kang *et al.* (2015) proposed a thermal approach to deal with VIT joints in wellbores by using an enhanced free convection Nusselt number based on a combination of a horizontal and a vertical Nusselt numbers. The authors claimed that, since the thermal resistance change significantly along the VIT length, there is an expressive thermal gradient along the VIT system. Thus, the axial temperature gradient cannot be neglected since it drives the convection heat transfer in the VIT annulus. Figure 2.16 shows the temperature profiles in the production annulus for the two studied cases: using the enhanced free convection Nusselt number (blue line) and using a single Nusselt number (red line).

The results revealed that when the proposed enhanced Nusselt number is employed, the average temperature in annulus “A” (i.e., the innermost) increases in the range of 22 to 33 K on average. Although interesting, the proposed approach does not solve the heat exchange through the VIT. It is just another approach to dealing with convection into the annulus gap.

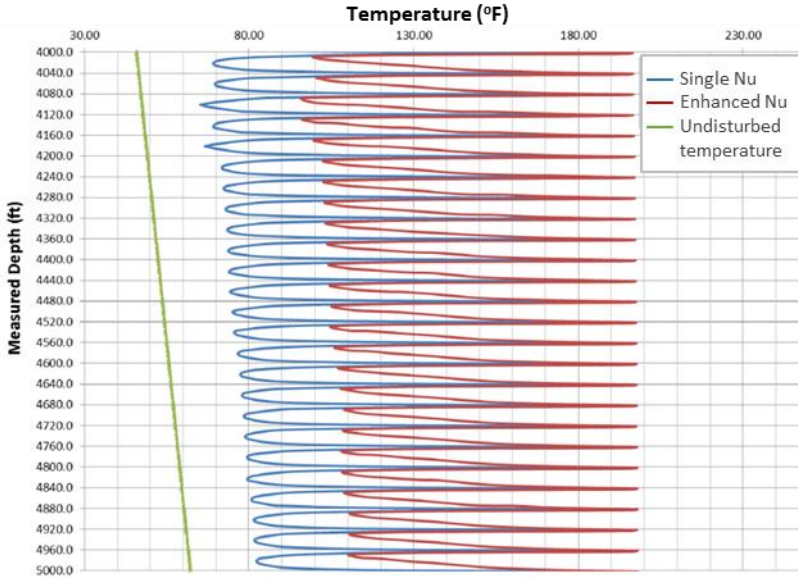


Figure 2.16 – Effect of the annulus convection approach on the production annulus temperature profile in a wellbore with VIT (Kang *et al.*, 2015).

2.6 Summary

This chapter reviewed the main advances in wellbore fluid flow and heat transfer modeling, focusing on APB calculation methods, along with the most important studies on VIT applied to petroleum wells.

According to the literature review, it was identified four types of approaches to handle the heat transfer and multiphase flow in wellbores and, in some cases, their relationship with the APB quantification:

- the works that focus on the fluid stream, generally account for a rigorous method to estimate the fluid transport properties and the fluid flow behavior, with the main objective of predicting pressure and temperature distribution along the tubing string.
- the works that deal with the thermal behavior in the wellbore taking into account the time dependent formation thermal resistance. Here, the objective is to estimate the temperature profile in the wellbore (tubing and annuli), in a steam injector and in oil production well.

- some simulators coupled wellbore and reservoir models using black oil or compositional model with the goal of predicting the behavior of production parameters, such as flow rate, pressure, temperature, gas oil ratio, liquid holdup both in vertical and deviated wells.
- the approaches that focus on the APB calculation. These models include an estimation of volume and temperature change in the wellbore components due to the heat transfer from the wellbore to the formation. Thus, the resulting loads are computed to obtain the deformation of the tubes from the coupling between the pressure predictions and the structural model of tubulars. So, the increase in pressure is reached due to the two contributions, the fluid expansion and the annular space deformation.

In terms of VIT modeling, it has been observed that more work is needed to overcome the main uncertainties associated with the thermal performance of the VIT, such as the determination of its effective thermal conductivity and the calculation of the heat lost through the connection in comparison with the VIT's body. This can be considered the bottom line for achieving the proposed goals of this work.

So far, all the efforts to model a VIT assisted wellbore focused on improving predictive approaches to heat transfer at the annulus and the use of unique equivalent thermal conductivity for VIT, namely k -value, and in some cases two conductivities, one representing the tube body and one for the connection region. One might conclude that there is no dedicated work to model the heat transfer through the VIT in an integrated process to the wellbore, and to investigate its effect on the wellbore thermal behavior.

Thus, the major contribution of this thesis is to develop an integrated model in which the VIT system is thermally modeled and coupled to a wellbore simulator. Then, the effect of the VIT on the wellbore thermal-structural behavior can be comprehensively studied.

3 MODELING

In this chapter, the theoretical approach proposed in this thesis to model the heat transfer through VIT joints will be presented, together with the procedure developed to incorporate it into a wellbore simulator.

As mentioned in the Introduction, the main advantage of the two-dimensional equivalent thermal network (ETN) model is its low computational cost. A full three-dimensional model based on the FVM was also implemented to better understand the heat transport through the VIT and validate the ETN model developed.

3.1 VIT Geometry

In order to model the heat transfer through a VIT joint, its geometry is divided into 5 or 4 axial sections, depending on the type of connection thread used, API⁵ or Premium⁶. Figure 3.1 illustrates the VIT geometry for an API connection thread, where the five different sections are described as follows:

- Section 1 – *VIT body*. This is the longest region in a VIT joint. There is vacuum insulation in the annular gap between the tubes. This region is not in contact with the coupling;
- Section 2 – *VIT body and coupling interface*;
- Section 3 – *Weld region*. This is the region where the inner and outer tubing are welded together;
- Section 4 – *Outer tubing and coupling interface*;
- Section 5 – *Coupling section*.

The two VIT models implemented in this study are referred to according to the sizes (in inches) of the outer diameters of the outer and inner tubing. Thus, the $3\frac{1}{2} \times 2\frac{3}{8}$ model has an API connection thread, and the $6\frac{5}{8} \times 5\frac{1}{2}$ model has a Premium connection. In addition to the dimension differences between the two models, other features that must be pointed out, namely (i) the different heat transfer surface area and

⁵ API connection – Thread usually employed in onshore, low pressure oil wells. The thread shows an internal diameter discontinuity.

⁶ Premium connection – Thread usually employed in tubings and casings for offshore environments. The thread does not have an internal diameter discontinuity.

size of the annulus gap, (ii) the absence of Section 5 (coupling section) in the larger VIT system and (iii) the uniform internal radius relative to the inner tubing in the larger VIT system. Table 3.1 illustrates the dimensions of the two models.

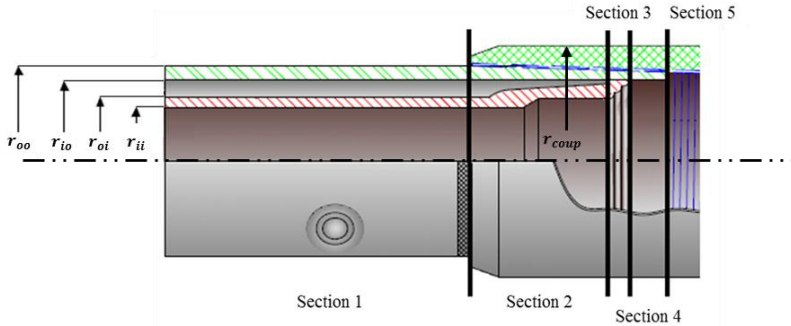


Figure 3.1 – VIT geometry (API connection thread). Schematic representation of the five sections of the VIT.

Table 3.1 – Summary of the dimensions featured for both VIT models

Dimension	3 ½ × 2 ¾	6 ⅝ × 5 ½
Inner diameter of the internal tubing	0.051 m (1.995 in)	0.124 m (4.892 in)
Outer diameter of the internal tubing	0.060 m (2.375 in)	0.140 m (5.5 in)
Inner diameter of the internal tubing after the folding region	0.060 m (2.375 in)	-
Outer diameter of the internal tubing after the folding region	0.068 m (2.692 in)	-
Inner diameter of the external tubing	0.076 m (2.992 in)	0.150 m (5.921 in)
Outer diameter of the external tubing	0.089 m (3.5 in)	0.168 m (6.625 in)
Outer diameter of the connection	0.108 m (4.25 in)	0.183 m (7.191 in)
Maximum thickness of the evacuated layer	0.008 m (0.3085 in)	0.005 m (0.2105 in)

3.2 2-D ETN Model

3.2.1 Hypotheses and governing equations

The two-dimensional equivalent thermal network (ETN model) consists in solving an energy balance in each node of a grid generated for a specified VIT geometry. Due to space restrictions, the ETN model grid for a specific VIT joint is shown in Figures A.2 and A.3, in Appendix A. The individual nodes are connected by thermal resistances, and the solution to the system of equations (one for each node) gives the temperature distribution in the VIT. The energy balances for the VIT consider axisymmetric steady-state conduction-radiation in a concentric cylinder system, without heat generation. Also, the following assumptions were adopted in the present validation of the VIT ETN model:

- Constant thermophysical properties in each VIT region (all metallic parts, including the weld, have the same physical properties);
- Negligible thermal contact resistances;
- All surfaces in the annular enclosure are gray and diffuse;
- Perfect vacuum (i.e., absence of convective heat transfer in the gap);
- The radiation heat exchange between the VIT external surface and the external environment is neglected;
- The ends of each tubing are considered adiabatic due to the symmetry plane;

At steady state, the energy balance equation for a generic node in the 2-D grid is given by:

$$\sum q_{i,j} = 0, \quad (3.1)$$

or, in terms of the thermal resistances surrounding the node:

$$\frac{T_{i,j-1} - T_{i,j}}{R_{i,j-1}} + \frac{T_{i,j+1} - T_{i,j}}{R_{i,j+1}} + \frac{T_{i-1,j} - T_{i,j}}{R_{i-1,j}} + \frac{T_{i+1,j} - T_{i,j}}{R_{i+1,j}} = 0 \quad (3.2)$$

where $T_{i,j}$ is the temperature at the central node of the grid and $T_{i,j+1}$, $T_{i+1,j}$, $T_{i,j-1}$ and $T_{i-1,j}$ are the temperatures at the adjacent nodes.

$R_{i-1,j}$, $R_{i+1,j}$, $R_{i,j-1}$ and $R_{i,j+1}$ represent the thermal resistances to the south, north, west and east of the central node. A schematic representation of the thermal resistance network surrounding a generic central node is shown in Figure 3.2.

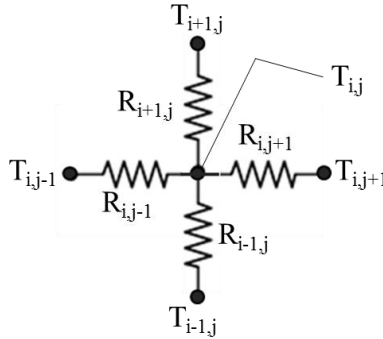


Figure 3.2 – Generic node thermal network schematics.

Thus, each thermal resistance is quantified according to the heat transfer mode present in a specific region of the VIT (i.e., conduction, convection and radiation). The energy balance equations of the ETN model can be found in detail in Appendix B.

3.2.2 Model Implementation

In order to generate results to be validated against the 3-D FVM simulation, the ETN model was implemented on the EES (Engineering Equation Solver) platform, which uses the Newton-Raphson method to simultaneously solve the set of algebraic equations.

The main properties and parameters computed in the EES platform for each section are:

- the heat transfer rate;
- the VIT effective overall heat transfer coefficient and equivalent thermal conductivity;
- the outer surface temperature of the VIT.

The following inputs are needed:

- the outer tube and inner tube radius;
- the length of each VIT section;

- the prescribed temperature in the bulk fluid surrounding the VIT;
- the prescribed internal temperature;
- the environment pressure;
- the fluid properties outside the VIT, such as the thermal expansion coefficient, thermal conductivity, viscosity and density;
- the tubes surface emissivity;
- the tubes thermal conductivity.

Table 3.2 shows the input data used in the 2-D simulations.

Table 3.2 – 2-D simulation input data

Surrounding fluid	air	-
Surrounding fluid temperature	293	K
Internal temperature of the VIT	323 - 398	K
Tube surface emissivity	0.60 – 0.85	dimensionless
Thermal conductivity of the steel tube	60	W/m.K
Environment pressure	101.325	kPa
Length of Section 1	0.2962 – 5.8962	m
Length of Section 2	0.0663	m
Length of Section 3	0.0039	m
Length of Section 4	0.0085	m
Length of Section 5	0.0100	m

3.2.3 Validation using a 3-D FVM model

A three-dimensional thermal model of the VIT joint was implemented using the ANSYS 14.5.7 Workbench platform. The model assumed that heat transfer occurred in a VIT displayed horizontally, as modeled in the 2-D ETN model. Although the aim of this exercise is to validate the stand alone VIT thermal model (ETN model), the 3-D FVM model allows understanding the heat transport throughout the VIT joint and the identification of the key points influencing the heat exchange.

In the present analysis, idealized boundary conditions were taken into account in order to validate the ETN model against the 3-D-FVM results considering a stand-alone VIT joint displayed horizontally and surrounding by stagnant air. Hence, prescribed temperatures of the internal wall of the VIT, T_{ii} , and bulk fluid surrounding the VIT, T_{∞} , were chosen. Figure 3.3 summarizes the boundary conditions employed in the present approach.

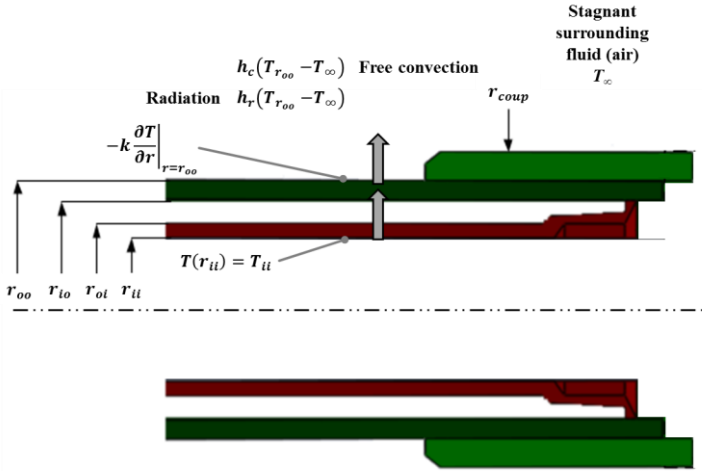


Figure 3.3 – Dirichlet boundary conditions applied at the VIT internal surface and in the air surrounding the VIT.

Furthermore, adiabatic surface planes were assumed at both ends of the VIT due to the symmetry plane.

The heat transfer problem is solved through the solution of the energy conservation equation in each finite volume. Thus, in order to better represent the VIT system, all sections (see Fig. 3.1) must be modeled, including the vacuum space. The constant-property, transient 3-D heat diffusion equation in cylindrical coordinates for the solid parts is given by:

$$\alpha_t \left[\frac{1}{r} \frac{\partial}{\partial r} \left(r \frac{\partial T}{\partial r} \right) + \frac{1}{r^2} \frac{\partial}{\partial \theta} \left(\frac{\partial T}{\partial \theta} \right) + \frac{\partial}{\partial z} \left(r \frac{\partial T}{\partial z} \right) \right] = \frac{\partial T}{\partial t}, \quad (3.3)$$

where α_t is the thermal diffusivity of carbon steel.

The VIT geometry was drawn in the SolidWorks 2013 software and exported to the ANSYS platform. The mesh generation was implemented using ANSYS ICEM CFD, as shown in Figure 3.4. More attention was given to the coupling region, where the geometry is more complex, thus requiring a finer grid. A grid with approximately 700,000 finite volumes was generated for a nearly 6-m long VIT. Hexahedral block structured grids facilitate a parametric assessment of the VIT length. The mesh was more refined close to the edges of the domain, with a linear expansion rate of 1.2.

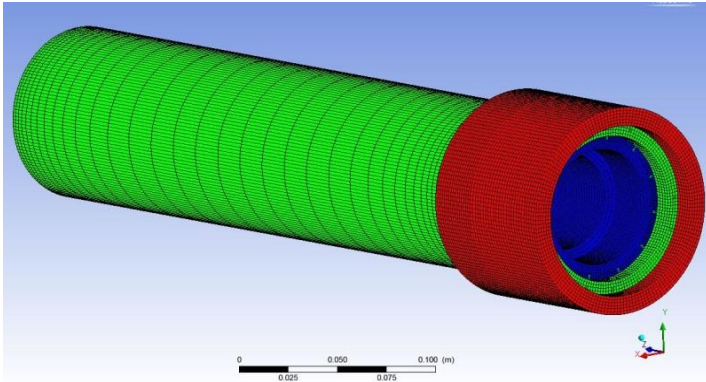


Figure 3.4 – Computational grid for the VIT system.

Natural convection was assumed on the outer surface of the VIT. The convection coefficient, h_{∞} , was estimated via the Churchill & Chu (1975) Nusselt number correlation for a long horizontal isothermal cylinder given by:

$$\overline{Nu}_D = \left\{ 0.6 + \frac{0.387 \cdot Ra_D^{1/6}}{\left[1 + \left(0.559/Pr \right)^{9/16} \right]^{8/27}} \right\}^2, \quad (3.4)$$

which is valid for $Ra_D \leq 10^{12}$. The physical properties of the surrounding fluid were assumed identical to those of atmospheric air, and based on the film temperature between the outer surface and the bulk air.

The radiation heat transfer in the annular gap was solved using the Monte Carlo method, a numerical technique used to determine the view factor based on the statistical characteristics of physical processes (MIRHOSSEINI and SABOONCHI, 2011). Thus, the net radiation exchange between the inner tube and the outer tube can be calculated assuming a diffuse, gray surface behavior of the enclosure (annular space formed by the two long concentric cylinders). A nonparticipating medium is assumed within the enclosure.

Initially, the heat transport through the VIT system is illustrated using the temperature field obtained from a FVM simulation. Figure 3.5 shows the thermal map in a $3 \frac{1}{2}'' \times 2 \frac{3}{8}''$ VIT system submitted to an internal prescribed temperature of 398.2 K and a tube surface emissivity of 0.7.

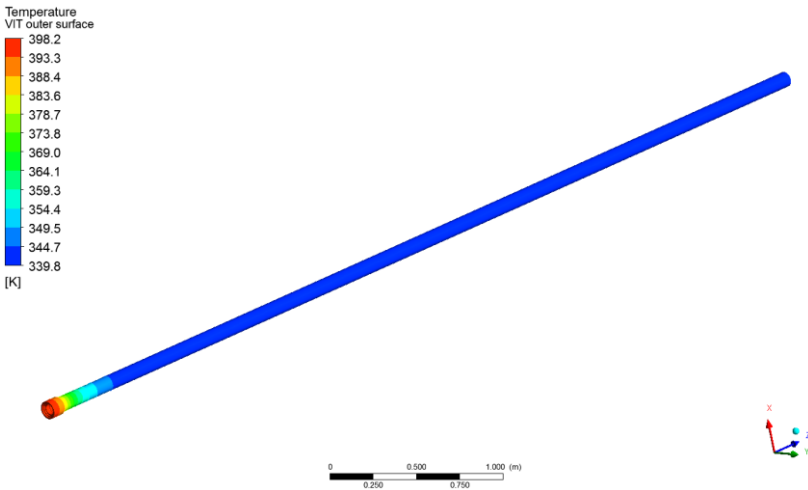


Figure 3.5 – $3 \frac{1}{2}'' \times 2 \frac{3}{8}''$ VIT thermal map for an internal prescribed temperature of 398 K and emissivity of 0.7.

The VIT thermal map points to a significant influence of the 2-D heat diffusion through the VIT walls up to 1 m from the connection. From there, a constant temperature is observed at the external surface of the VIT, suggesting that the axial conduction heat effect has vanished. Therefore, the heat transport is driven by the radiative axial heat exchange through the evacuated annulus. Figure 3.6 shows the temperature field at the VIT external surface computed via the 3-D FVM approach, confirming that the temperature plateaus roughly 1 m away from the connection.

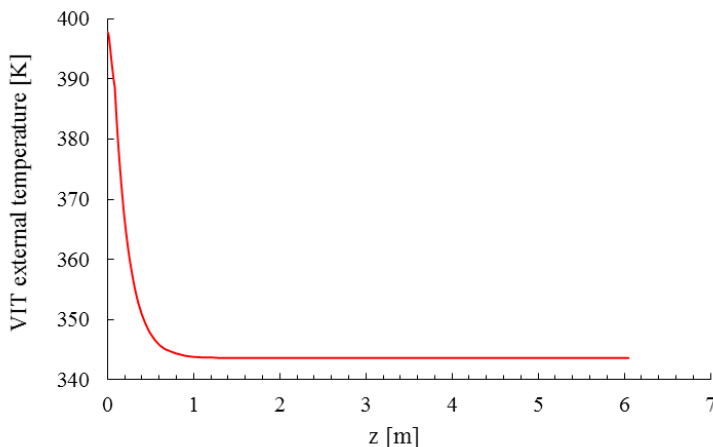


Figure 3.6 – External surface temperature profile for a 3 ½” × 2 ⅜” VIT (3-D FVM calculations).

Next, a comparison between the ETN model and the FVM is performed to validate the standalone nodal thermal model. Firstly, the trade-off between different meshes is assessed in order to establish an optimum refinement at the expense of a longer computational time. Therefore, Figure 3.7 shows the effect of the mesh on the VIT’s external surface temperature. Note that a log scale is used in the abscissas to facilitate the comparison between the curves.

As expected, a finer mesh provides a better accuracy, but also results in a higher computational cost. However, the coarse mesh is not capable of capturing the high thermal gradients that occur at the interface between the connection and the VIT body. Also, the intermediate mesh does not accurately reproduce the thermal profile in this region. Hence, the refined grid with 53 nodes fitted the FVM thermal profile without posing a large computation time penalty. A maximum discrepancy of 1 K was observed and, therefore, this mesh was used as a baseline for further studies.

Having determined the best grid refinement for the ETN simulations, the heat transfer rate per unit length was determined for each VIT section using the two approaches (ETN and FVM). Table 3.3 – Comparison of heat transfer rate (in W/m) in each VIT section for the two developed approaches. shows the results in each VIT section considering a variable VIT body length for the 3 ½ × 2 ⅜ VIT system. A

prescribed internal wall temperature of 373.15 K and an emissivity of 0.8 were assigned to the inner and outer tubing surfaces. All simulations were performed assuming a prescribed temperature of the surrounding fluid of 293.15 K.

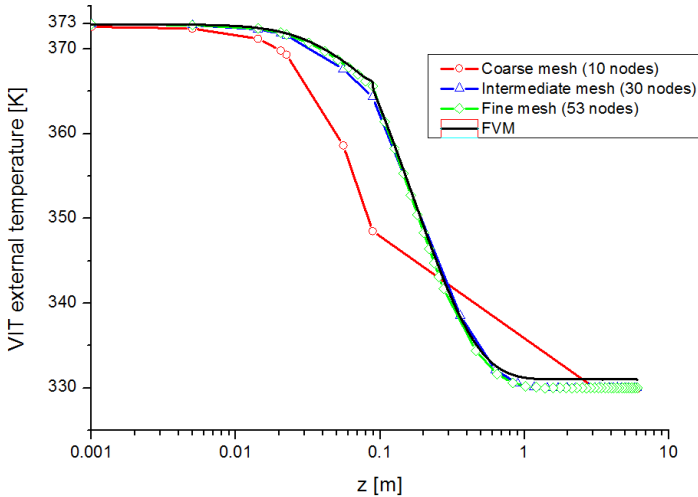


Figure 3.7 – Effect of ETN grid refinement on the 3 1/2” x 2 3/8” VIT external surface temperature. Comparison with the 3-D FVM results.

Table 3.3 – Comparison of heat transfer rate (in W/m) in each VIT section for the two developed approaches.

VIT body length (m)	Thermal model	q'1	q'2	q'3	q'4	q'5
		(W/m)				
0.4	ETN	89.8	182.6	170.5	172.0	173.1
	FVM	92.1	182.3	170.9	172.2	173.2
1.6	ETN	64.0	182.3	170.5	171.9	173.1
	FVM	66.7	182.2	170.9	172.2	173.2
6.0	ETN	58.0	182.3	170.5	171.9	173.1
	FVM	60.4	182.1	170.9	172.2	173.2

Regardless of the VIT body length, the heat lost to the external environment in Sections 3 to 5 (i.e., without vacuum) is nearly the same.

This is because the heat transport is controlled mainly by conduction and convection resistances, which are the same for the two approaches. Regarding the heat transfer rate per unit length, the ETN model and the FVM showed very similar results, with differences between 0.1 and 6% for all simulated cases.

A summary of the VIT thermal property calculations using the ETN approach is presented in Table 3.4 – for the case of 6 ⅜ x 5 ½ VIT system designed with premium thread.

Table 3.4 – VIT thermal parameters quantification for 4 different temperatures and three different emissivity values.

T_{ii} [K]	ε [-]	U_1 [$\frac{W}{m^2 \cdot K}$]	U_2 [$\frac{W}{m^2 \cdot K}$]	U_3 [$\frac{W}{m^2 \cdot K}$]	U_4 [$\frac{W}{m^2 \cdot K}$]	U_{ef} [$\frac{W}{m^2 \cdot K}$]	k_{ef} [$\frac{W}{m \cdot K}$]
323	0.65	1.750	5.011	4.605	4.910	1.823	0.046
	0.75	1.971	5.016	4.608	4.910	2.039	0.052
	0.85	2.190	5.021	4.611	4.911	2.252	0.057
348	0.65	2.059	5.861	5.391	5.757	2.144	0.055
	0.75	2.326	5.867	5.395	5.758	2.405	0.061
	0.85	2.592	5.874	5.399	5.758	2.665	0.068
373	0.65	2.350	6.415	5.902	6.307	2.441	0.062
	0.75	2.657	6.422	5.907	6.308	2.741	0.070
	0.85	2.960	6.429	5.912	6.309	3.037	0.078
398	0.65	2.643	6.818	6.274	6.706	2.736	0.070
	0.75	2.985	6.827	6.280	6.707	3.070	0.078
	0.85	3.317	6.835	6.286	6.708	3.395	0.087

In Table 3.4 – , both the VIT internal temperature and tube surface emissivity were varied given their considerable influence on the VIT's thermal performance. The simulations were performed for a nearly 6-m long VIT. The calculation of U_{ef} was based on the weighted average of U_j given by:

$$U_{ef} = \frac{\sum_{j=1}^5 (U_j \cdot L_j)}{\sum_{j=1}^5 L_j} \quad (3.5)$$

where the outer surface area of the external tube (diameter D_{oo}) was chosen as the reference area for all overall heat transfer coefficients. The effective thermal conductivity of the VIT, k_{ef} , was quantified based on U_{ef} as follows:

$$k_{ef} = \frac{U_{ef} \cdot D_{oo} \ln\left(\frac{D_{oo}}{D_{ii}}\right)}{2}. \quad (3.6)$$

Although, U_{ef} and k_{ef} have different meanings — the former is a performance parameter that involves an overall temperature difference and the latter is a material specific physical property — in this case, the effective thermal conductivity is also being defined so as to quantify the combined thermal resistance, including the one due to external convection. This approach was adopted to be consistent with wellbore thermal flow simulators, which use k_{ef} as a thermal performance parameter. Furthermore, it also serves as a quantity that can be directly compared to those of other insulating materials.

As can be seen from Table 3.4 – , the larger the emissivity and the temperature difference, the higher the values of the thermal parameter. In terms of the VIT annular gap surface emissivity, reducing the thermal radiation resistance (by increasing the emissivity from 0.65 to 0.85) represents a loss of insulation performance of about 20%. Since the problem was formulated considering prescribed temperatures, increasing the VIT internal surface temperature while keeping a fixed surrounding fluid temperature results in a higher temperature difference and, therefore, in a larger VIT effective overall heat transfer coefficient.

For simulations with the same prescribed temperatures, the U_j values are almost constant in Sections 2, 3 and 4, while for Section 1 it increases with the emissivity. This can be explained by the fact that Sections 3 and 4 are not influenced by radiative heat transfer. Also, Section 2 is basically insensitive to changes in the tubes' emissivity. Additionally, even though the U values are higher in Sections 2, 3 and 4, U_{ef} is nearly unaffected by them, since those three regions comprise a small share of the VIT joint. This shows the great influence of Section 1 on U_{ef} .

This section presented an equivalent thermal network (ETN) model for solving the two-dimensional heat transfer in a VIT joint. The mesh refinement was calibrated against results from the commercial software ANSYS FLUENT. In order to evaluate the performance of VIT

joints at conditions typical of a real well, where they are incorporated into the tubing strings to mitigate APB, the ETN model has to be integrated with a well simulator. The wellbore model used in this project will be presented in the next section.

3.3 Wellbore Multiphysics Model

This section describes the Wellbore Multiphysics (WM) model, which contains methods for calculating physical properties, multiphase flow, thermal and mechanical parameters of the well. The model was initially developed by Hafemann *et al.* (2015) and was later improved by Barcelos *et al.* (2017). The VIT ETN model proposed in the previous section was incorporated into the WM model framework to generate the main results presented in this thesis.

The WM model considers the thermal-hydraulic effects in the production tubing and the thermal properties of the annulus, cement, casing and adjacent rock formation. The fundamental hypothesis of the WM model is that, because of the difference in characteristic thermal time scales between the well and the formation, the former can be modeled assuming quasi steady state.

Due to the large aspect ratio of the well (length/diameter), a one-dimensional formulation is adopted for the fluid flow in the wellbore. The linear momentum balance is written in terms of the total pressure gradient components (frictional, gravitational and accelerational) in differential form (Brill and Mukherjee, 1999):

$$-\frac{dP}{dz} = -\left(\frac{dP}{dz}\right)_f - \left(\frac{dP}{dz}\right)_g - \left(\frac{dP}{dz}\right)_{ac}. \quad (3.7)$$

Although single-phase flow may exist in the reservoir and at the bottom of the well, vapor flashing may occur as the pressure decreases towards the wellhead and becomes lower than the saturation pressure at the local temperature and composition. Thermodynamic equilibrium was assumed in the calculation of the vapor content in the two-phase flow.

While several approaches are available to describe the friction and phase fraction behavior in multiphase flow, Hafemann *et al.* (2015) relied on a flow pattern based approach by Barbosa and Hewitt (2006) to provide more accurate predictions of pressure drop, liquid holdup and

flow regime transitions. A detailed description of the multiphase flow model is provided in Appendix C.

The energy balance for the flowing fluid is given by:

$$-\frac{dH}{dz} = \frac{q'}{G \cdot A} + g \cdot \sin \gamma + v_m \cdot \frac{dv_m}{dz}, \quad (3.8)$$

where H is the fluid enthalpy, v_m is the fluid mixture velocity, G is the mixture mass velocity and q' is the heat transfer rate per unit length, which is computed assuming a one-dimensional heat transfer in the radial direction via a thermal network model. Also, γ is the inclination angle relative to the vertical axis.

In this model, each horizontal layer of the multistring well geometry is modeled as an individual resistance as illustrated in Figure 2.3. The heat transfer rate per unit length is defined based on the total conductance and the overall temperature difference between the hydrocarbon internal flow and the geothermal temperature profile as follows:

$$q' = 2\pi r_{to} U_{to} (T_f - T_{rf}) \quad (3.9)$$

where the overall heat transfer coefficient, U_{to} , is obtained from a global resistance model considering each well layer, as shown in Eq. 2.1. The two-phase internal forced convection heat transfer coefficient, h_{ti} , was calculated using the two-phase forced convection part of the Chen (1966) convective boiling correlation, that is, without the nucleate boiling contribution, but considering the two-phase flow enhancement factor.

In order to estimate the wellbore/formation interface temperature, T_{rf} , a hybrid approach based on the dimensionless time, t_D , has been proposed to compute $f(t)$ considering the models of Ramey (1962), Hasan and Kabir (1991) and Cheng *et al.* (2011):

$$f(t) = \begin{cases} 1.1281\sqrt{t_D} \cdot (1 - 0.3\sqrt{t_D}), & \text{if } t_D \leq 0.5 \\ \ln(2\sqrt{t_D}) - 0.2886 \\ + \frac{1}{4t_D} \left[1 + \left(1 - \frac{1}{\omega}\right) \cdot \ln(4t_D) + 0.5772 \right], & \\ \ln(2\sqrt{t_D}) - 0.2886, & \text{if } t_D > 20 \end{cases} \quad (3.10)$$

The reason for adopting this approach meets the observations made by Cheng *et al.* (2011) and Hasan and Kabir (1991). The former pointed out that, for very short transient ($t_D < 0.5$), the correlation based on the ratio between the formation and wellbore heat capacities should not be employed since there is no significant contribution of the formation to the wellbore thermal behavior. The latter stated that, for very short and for long transients, their approach presented an excellent agreement with the exact solution for the transient diffusion in the formation.

Given the geothermal profile and the reservoir pressure and temperature at the PDG as boundary conditions, the pressure and temperature of the flowing fluid are calculated assuming a known flow rate. The momentum and energy equations are integrated from the bottom hole to the wellhead. The equations were implemented on Matlab[®] and solved numerically using the Dormand-Prince method (an adaptive technique based on the Runge-Kutta method). Phase equilibrium and physical properties of the hydrocarbon mixture and the annuli fluids are calculated via the commercial software Multiflash[™]. At each time step, the pressure and the enthalpy, together with the overall composition of the mixture, are used to compute the local equilibrium (bubble-point) temperature and the vapor quality.

In order to calculate the APB, the mechanical model takes into account the three contributions described in Eq. 2.20. The model considers the multistring approach implemented in the work of Barcelos *et al.* (2017). Thus, each annular is treated as an integral volume (the “pressure vessel approach”), so that the annular pressure change caused by every local volume variation is transmitted through all annuli instantly. This way, even though local volume deformations are computed, the calculated APB value is an overall parameter for each annular, updated at every time step.

As can be seen in the flowchart shown in Figure 3.8, the solution procedure of the WM model sequentially solves the hydraulic and thermal equations, followed by the mechanical model.

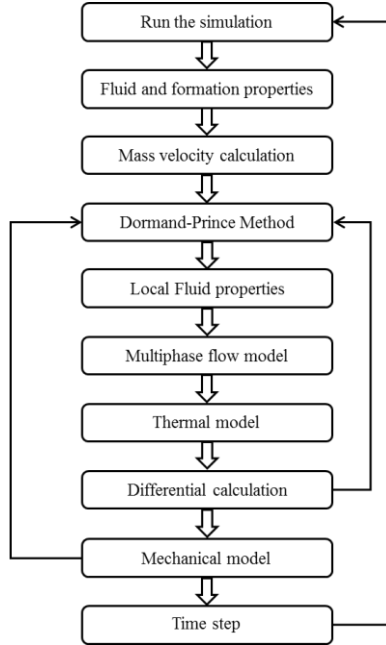


Figure 3.8 – Flowchart solution of the WM model.

3.4 Coupling the ETN Model with the WM Model

After showing that the ETN model can produce results that are consistent with a full FVM simulation of the multi-dimensional heat conduction in a VIT, the 2-D model will be incorporated into the WM model to predict the influence of VIT joints on the overall thermal behavior of the well.

The original versions of the WM model (Hafemann *et al.*, 2015; Barcelos *et al.*, 2017) treated the heat transfer as one-dimensional in the radial direction and modeled the VIT joints using a single k-value (AZZOLA *et al.*, 2004; AZZOLA *et al.*, 2007), which is a simplistic representation of the heat transfer problem in the VIT. Therefore, in order to take into account the 2-D features of the ETN model and evaluate the overall impact of an axially dependent thermal conductance of the VIT joints, the original wellbore simulator had to be adapted.

The following sub-sections describe the mathematical procedure needed to couple the ETN model to the 1-D WM calculation framework adopted in the simulator.

3.4.1 Adaptation of the ETN Model and Boundary Conditions

When the ETN model is coupled to the well simulator, different boundary conditions are needed to accurately represent a real production well scenario. Therefore, the constant temperature boundary condition at the inner surface of the VIT (used to validate the model against the FVM simulation) was replaced by a Cauchy (convection) boundary condition (hydrocarbon flow at a temperature T_f in the production tubing). At the outer surface, appropriate natural convection and radiation heat transfer relationships are needed, as illustrated in Figure 3.9 – .

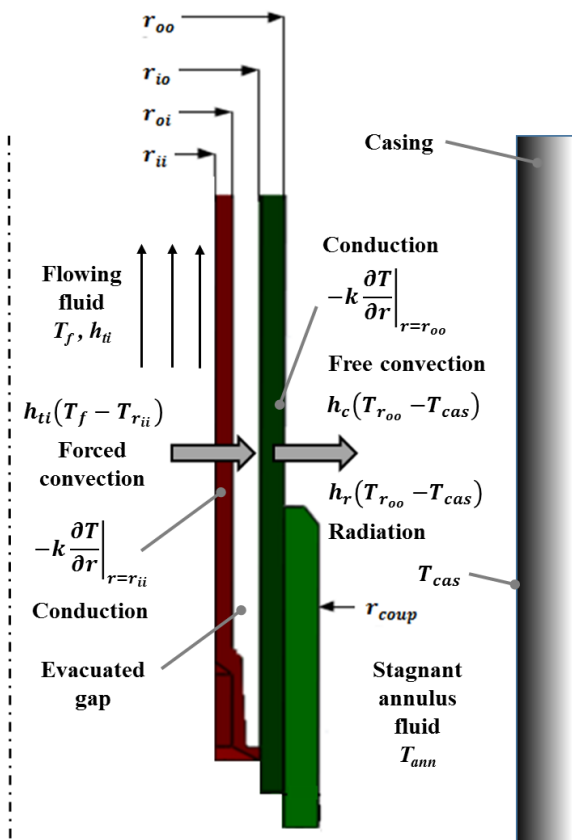


Figure 3.9 – Cauchy boundary condition for the heat transfer from/to a VIT joint.

The boundary conditions described above are applied to *each axial node* of the VIT inner and outer walls. At the inner surface, the convection boundary condition is given by

$$h_{ti}(T_f - T_{r_{ii}}) = -k \left. \frac{\partial T}{\partial r} \right|_{r=r_{ii}} \quad (3.11)$$

where T_f is the local temperature of the flowing hydrocarbons, calculated at each axial step as a function of the local pressure and enthalpy. At the outer surface, the following boundary condition is applied, considering natural convection and radiation in the cavity formed by the external surface of the VIT joint and the internal surface of the production casing:

$$-k \left. \frac{\partial T}{\partial r} \right|_{r=r_{oo}} = (h_c + h_r) \cdot (T_{r_{oo}} - T_{cas}), \quad (3.12)$$

where h_c is a convection heat transfer coefficient and h_r is an equivalent radiation heat transfer coefficient for the annulus space defined by:

$$h_r = \frac{\sigma \cdot (T_{r_{oo}} + T_{cas}) \cdot (T_{r_{oo}}^2 + T_{cas}^2)}{\frac{1}{\varepsilon} + \frac{(1-\varepsilon)}{\varepsilon} \left(\frac{r_{oo}}{r_{cas}} \right)}. \quad (3.13)$$

In the ETN model, additional boundary conditions are needed to describe the axial heat transfer at the ends of the VIT joints located at the top and bottom of the tubing string. It is worth to remember that the VIT joints are stacked (connected) one above the other until reaching the depth that it is desired to reduce the radial heat transfer, commonly from the wellhead to the bottom of the confined annulus. For simplicity, a thermal insulation boundary condition was applied to each node at those surfaces. Thus,

$$-k \left. \frac{\partial T}{\partial z} \right|_{z=VIT_Bottom} = 0 \quad (3.14)$$

$$-k \left. \frac{\partial T}{\partial z} \right|_{z=wellhead} = 0 \quad (3.15)$$

Figure 3.10 shows the two boundary conditions assumed in the model.

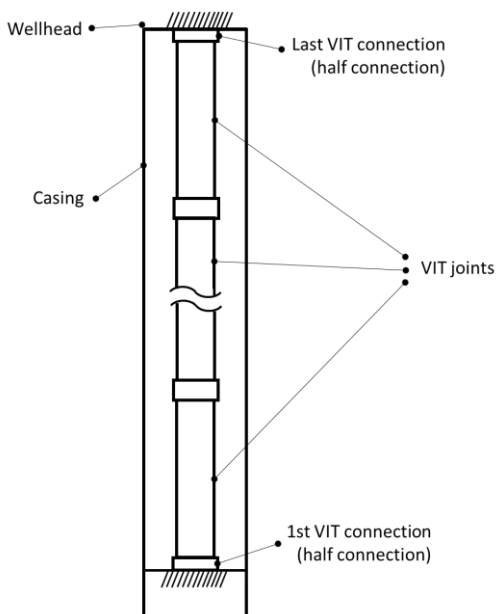


Figure 3.10 – Boundary conditions at the ends of the connected VIT joints.

The steady-state heat conduction equation that describes the heat transfer in the VIT joints is elliptic in the r and z directions. On the other hand, the momentum and energy equations that give the hydrocarbon pressure and enthalpy along the wellbore are parabolic in z . As will be seen in the next sub-section, an iterative calculation procedure has been developed to solve the 2-D ETN model within the 1-D wellbore modeling framework in order to extract, at each axial control volume of the wellbore grid, a heat transfer rate per unit length, q' , which takes into account the 2-D nature of heat flow in the VIT. In this way, two different numerical meshes can be used, namely a finer 2-D VIT grid (whose size was determined based on the comparison with the FVM simulations) and a coarser 1-D wellbore grid. This approach considerably reduces the computational cost involved in predicting the behavior of the system variables (pressures, temperatures and heat flow rates) as a function of space and time. Figure 3.11 illustrates schematically the directions of the heat transfer rates, according to the proposed model, for an oil well with a VIT joint (near the mud line).

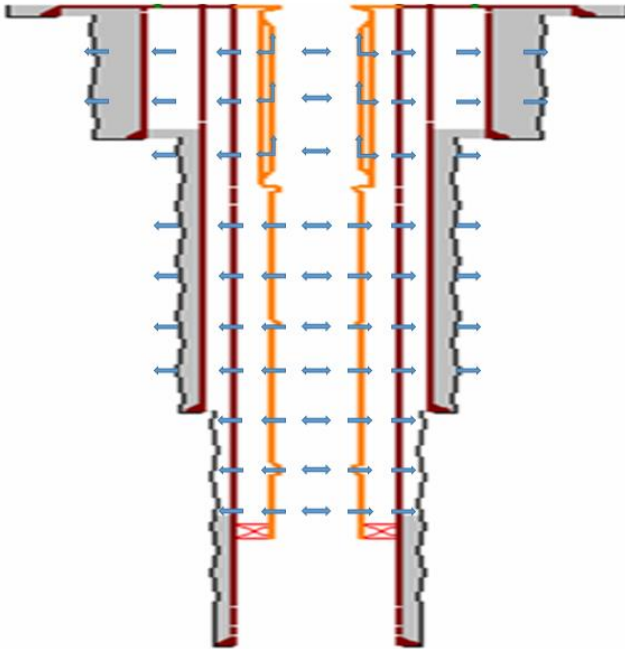


Figure 3.11 – Modeling of heat exchange in a wellbore with VIT (heat flux – blue arrows).

3.4.2 Computational Implementation of the Integration Between the Models

An approximate method was adopted to determine the temperatures and the heat flow at the nodes of the VIT numerical grid. As previously presented, the physical system is represented by a nodal network (see Appendix A, Figure A.2 and Figure A.3). Thus, the energy balances were applied to obtain a system of equations for the temperatures at each node. In the coupling of the 2-D ETN model with the wellbore simulator, the set of the algebraic equations is solved with the “*fsolve*” function in MATLAB[®] for each node of the numerical domain using the Levenberg-Marquardt algorithm (least squares) to deal with the non-linearities associated with the fourth-power radiation law. A procedure for solving the VIT field temperature is detailed as follows:

1. Set the VIT (finer, 2-D) mesh;

2. Interpolate the input variables $(T_f, T_{cas}, h_{ti}, h_c, h_r)$, from the wellbore (coarser, 1-D) grid;
3. Compute the VIT internal thermal resistances;
4. Set the algebraic equation system as a function of the unknown temperatures at each VIT node;
5. Establish the VIT boundary conditions;
6. Make initial guesses for all unknown temperatures;
7. Solve simultaneously the algebraic equations system using a Matlab[®] solver (*fsolve*, Levenberg-Marquardt algorithm);
8. Determine the temperature field for a specific convergence criterion.

Given the temperature field in the VIT, it is possible to determine the equivalent thermal resistance of the VIT in terms of the mesh employed in the wellbore, calculated as follows:

$$R_{eq,w} = \frac{\bar{T}_{i,w} - \bar{T}_{e,w}}{\sum L_j q'_j}, \quad (3.16)$$

where the subscript w represents the wellbore axial grid (WM model), the subscript j represents the VIT axial grid (ETN model) and \bar{T}_i and \bar{T}_e were determined based on the weighted mean

$$\bar{T}_{n,w} = \frac{\sum_j \bar{T}_{n,j} \cdot L_j}{\sum_j L_j}, \quad (3.17)$$

where n can be the internal or the external VIT surface temperature. Figure 3.12 presents the relation between the two grids applied in the VIT heat transfer problem to compute the equivalent thermal resistance.

Thus, the wellbore simulator uses the updated equivalent thermal resistances of the wellbore grid to calculate the heat transfer rate per unit length and obtain the new pressure and temperature fields along the wellbore. It is important to mention that, in the first iteration, the overall heat transfer coefficient, U_{to} , at each length step is computed taking into account the temperature difference between the flowing fluid and the wellbore/formation interface. Consequently, U_{to} includes all wellbore thermal resistances as shown in Eq. 2.1 and the heat transfer rate per unit length assumes the form of Eq. 3.9. In this case, Hasan and Kabir (1991) rewrote this equation so as to incorporate the transient approach

by adding the relaxation parameter, L_R , which depends on the transient function defined in Eq. 2.6 as follows:

$$q' = -wc_p L_R (T_f - T_{ft}), \quad (3.18)$$

where L_R is given by:

$$L_R = \frac{2\pi}{wc_p} \cdot \left[\frac{r_{to} \cdot U_{to} \cdot k_{ft}}{k_{ft} + (r_{to} \cdot U_{to} \cdot T_D)} \right]. \quad (3.19)$$

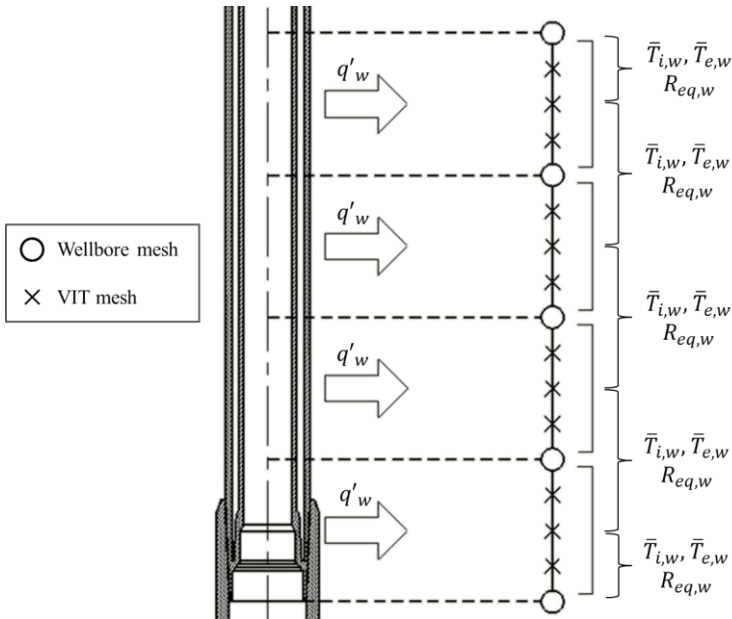


Figure 3.12 – VIT equivalent thermal resistance (for the wellbore mesh) calculation details.

When the VIT thermal model is incorporated into the wellbore simulator, U_{to} must be computed differently since, for a given length step of the wellbore grid, the heat transfer rate leaving the hydrocarbon stream is different from the one reaching the first annulus space (outer surface of the VIT). This is a consequence of the two-dimensional heat transfer taking place at the VIT joints. Thus, in other words, in order to satisfy the energy conservation, U_{to} for this new approach considers the

temperature difference between the VIT external surface and the wellbore/formation interface. So, for a wellbore with only one annulus, Eq. 2.1 is rewritten as:

$$\frac{1}{U_{to}} = \frac{r_{to}}{r_o(h_c + h_r)} + \frac{r_{to} \cdot \ln(r_{co}/r_{ci})}{k_c} + \frac{r_{to} \cdot \ln(r_{wb}/r_{co})}{k_{cem}}, \quad (3.20)$$

where the first term represents the annulus thermal resistance, the second term represents the casing resistance and the last one represents the cement thermal resistance. In addition, Eq. 3.18 is rewritten as follows

$$q' = -wc_p L_R (T_{r_{oo}} - T_{ft}), \quad (3.21)$$

where $T_{r_{oo}}$ is the VIT external surface temperature. Figure 3.13 presents a flowchart of the numerical solution of the WM-ETN coupled model. Initially, the fluid flow and heat transfer in the wellbore is computed from the well bottom to the wellhead. An arbitrary value for the VIT thermal conductivity is employed to determine the temperature field, which is used as an initial guess in the second step. To this end, a new grid, a finer one, is designed in order to capture the two-dimensional heat transfer through the VIT system. Thus, thermal resistances are calculated for the finer grid and a new temperature field is computed. Finally, equivalent thermal resistances are determined for the wellbore grid using Eq. 3.16.

The convergence criterion used in the iterative solution process is such that the heat transfer rate into a VIT joint (through its inner wall) must be equal to the heat transfer rate through its outer wall in order to satisfy the conservation of energy. Thus:

$$\frac{\int_{VIT\ bottom}^{wellhead} \frac{q'_{out}}{L_{VIT}} dz - \int_{VIT\ bottom}^{wellhead} \frac{q'_{in}}{L_{VIT}} dz}{\int_{VIT\ bottom}^{wellhead} \frac{q'_{in}}{L_{VIT}} dz} < 10^{-2}. \quad (3.22)$$

where L_{VIT} is the total length of the VIT joint and q'_{in} and q'_{out} are, respectively, the heat transfer rate per unit length on the inner and outer walls of the VIT (ETN model grid).

Figure 3.14 illustrates the flow of information between the parts of the integrated model (WM + 2-D ETN). In addition to validations

with field data, the integrated model will also be compared with WellCat™, a commercial software extensively used in the oil industry.

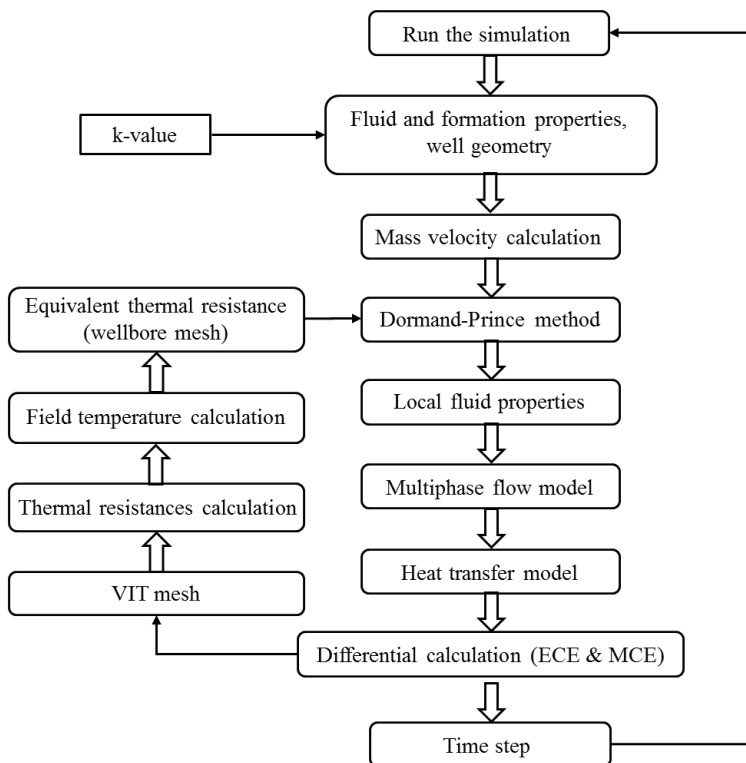


Figure 3.13 – Flowchart solution of the coupled model (WM and VIT ETN models).

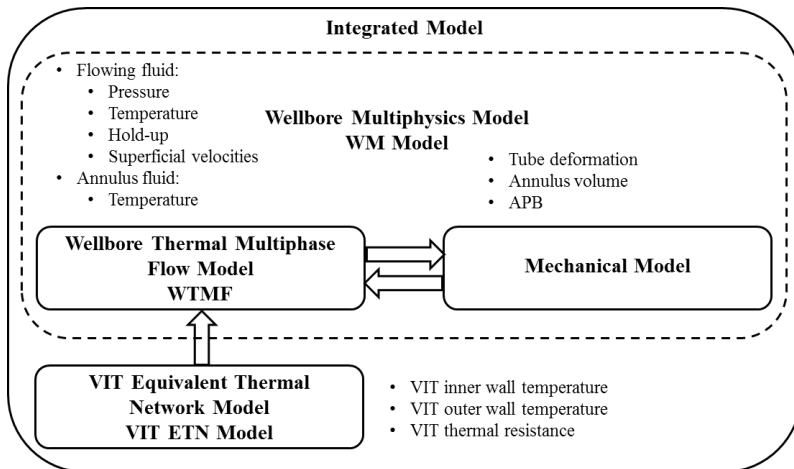


Figure 3.14 – Workflow to develop the integrated model and the main outputs generated from each individual model.

4 RESULTS

Two real deepwater wells located at the Brazilian coast were used to validate the existing models and to evaluate the current models developed in this thesis. This chapter presents the results of this thesis, namely a detailed thermal-hydraulic-mechanical assessment of both wells. The results were compared and validated against field data and numerical results generated by a commercial software package (WellCat™).

4.1 Description of the Cases Studied

4.1.1 Description of the Case 1 – Well A

The WM model initially developed by Hafemann *et al.* (2015) and Barcelos *et al.* (2017) was further verified in the present thesis against a more extensive dataset containing other field operating conditions. In this case, a deepwater vertical 4,700-m well (well A) drilled at an offshore location on the Brazilian coast is presented in Figure 4.1. Note that, although the present well A schematics contains a VIT column, the first simulations performed did not take them into account. The lithological column is also shown. The present simulations started with a pressure boundary condition at the pressure downhole gauge (PDG) located at the depth of 3,890 m. The simulation results are compared with the WellCat commercial software and field data. The basic properties of the reservoir fluid are summarized in Appendix D.

Case 1 considers the basic parameters presented in Table 4.1 and Table 4.2. Table 4.1 summarizes the operational data obtained from the field and some simulation inputs. Table 4.2 shows details of the well A design. As shown in Figure 4.1, seven types of rocks were drilled through, however, only four are found above the PDG, which is the wellbore region simulated in the present study.

The thermal behavior of the wellbore is highly affected by the adjacent formation, so it is fundamental to properly define key thermophysical properties of the formation layers impacting the wellbore. Also, the wellbore structural behavior depends on the mechanical properties of the formation layers. Both are summarized in Table 4.3.

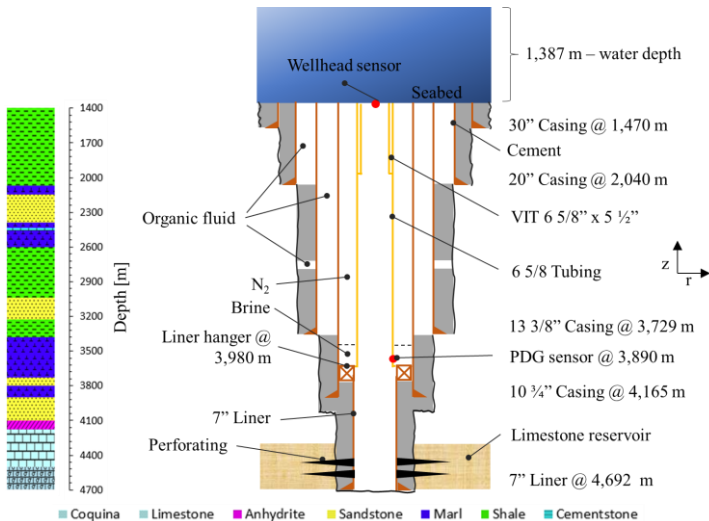


Figure 4.1 – Well A schematic.

Table 4.1 – Well A simulation / operational parameters

Parameter	Value / Unit / Comment
Flow rate	1,711 m ³ /d
Gas-oil ratio	211 std m ³ /std m ³
Basic Sediments and Water (BSW)	0.21%
Oil density	29.7 °API
Friction factor	1x10 ⁻⁵
Tubing surface emissivity	0.75
Casing surface emissivity	0.75
Bottomhole pressure @ 3,890 m	31 MPa
Bottomhole temperature @ 3,890 m	396.8 K
Seabed temperature @ 1387 m	277.1 K
Water depth	1,387 m
Perforating interval	4,390 - 4,564 m
Simulating length	2,503 m
Length step	10 m
Multiphase flow model	Barbosa and Hewitt (2006)

Annulus convection model	Zhou (2013)
Formation thermal model	Hybrid

Table 4.2 – Well A design details

Annulus	Casing seat [m]	Fluid type	Top of cement [m]
10 3/4" x 6 5/8" (Annular # A)	4166	N ₂ (up to 3806 m) and brine from 3806 to 4032 m	4032
13 3/8" x 10 3/4" (Annular # B)	3729	Water + glycerin	3759
20" (Annular # C)	2040	Water + glycerin	First isolation (2050-2955) m Second isolation (3050-3729) m

Table 4.3 – Thermophysical and mechanical properties of the formation layers for the well A (Eppelbaum *et al.*, 2014)

Rock type	c _p [J/kg.K]	k [W/m.K]	ρ [kg/m ³]	E [GPa]	ν [-]
shale	2,151	1.60	2,057	17.5	0.10
Marl	1,734	1.38	1,970	37.5	0.15
Sandstone	737	2.50	2,198	32.5	0.14
Limestone	887	2.19	2,540	45.0	0.3
Anhydrite	819	4.10	2,980	75.0	0.31
Cementstone	844	1.96	2,644	1.5	0.35

4.1.2 Description of the Case 2 – Well B

In order to fully validate the integrated model, the results are compared with field data from a deviated slender deepwater well located in the Campos Basin, here called well B.

The wellbore schematics shows a long, confined annulus (formed by the 13 3/8" and 20" casings) as depicted in Figure 4.2. Due to the risk of collapsing the intermediate casing and/or bursting the surface casing, nearly one hundred 6 5/8" x 5 1/2" VIT joints have been positioned from the wellhead (1,091 m) to a depth of 2,171 m deep to ensure the well integrity. It is important to emphasize that this is the only offshore well

in Brazil with VIT joints used to reduce APB. Basic properties of the reservoir fluid for this well are presented in Appendix E.

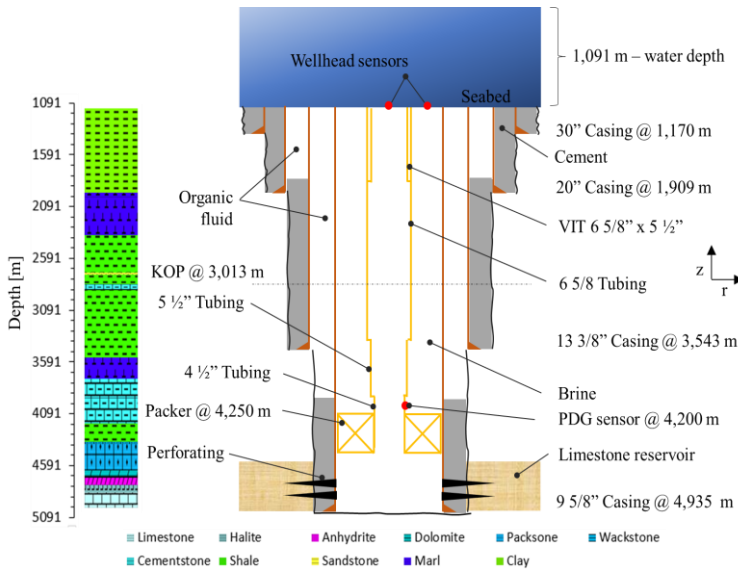


Figure 4.2 – Well B geometric details.

The multiphase flow was solved using the Beggs and Brill (1973) pressure loss correlation – for more details see Appendix F. This approach is one of the few correlations capable of handling all flow directions including, deviated wells operating with two-phase fluid. The method uses the general mechanical energy balance and the average in-situ density to calculate the pressure gradient. Accordingly, the slope term is now embedded into the momentum equation as follows

$$-\frac{dP}{dz} = \frac{f_{tp} \cdot \rho_n \cdot v_m^2}{2d} + \rho_s \cdot g \cdot \sin \gamma + \rho_s \cdot v_m \cdot \frac{dv_m}{dz}, \quad (4.1)$$

where g is the acceleration of gravity, q' is the heat transfer rate per unit length and v_m is the mixture average velocity. ρ_n is the no-slip mixture density, while ρ_s represents the slip mixture density. f_{tp} is the estimated friction factor based on the no-slip Fanning friction factor, f , considering the mixture as a one-phase flow. Also, γ is the inclination angle relative to the vertical axis, as shown in Figure 4.3.

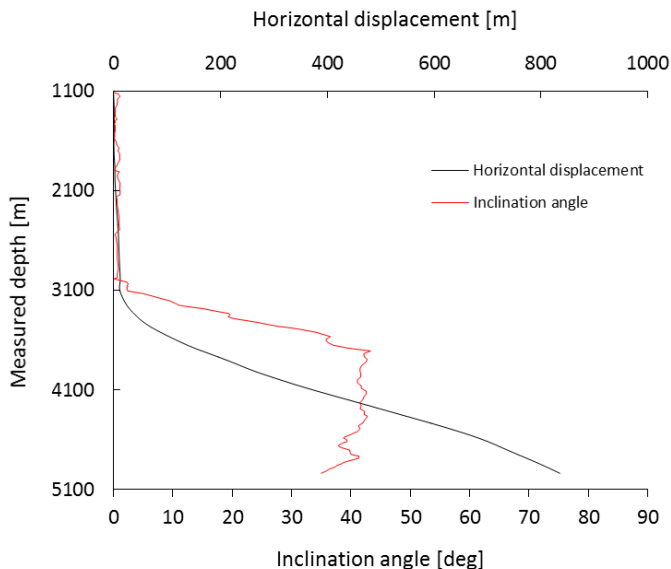


Figure 4.3 – Well B trajectory.

The wellbore inclination angle relative to the vertical direction is depicted in Figure 4.3. Table 4.4 summarizes the main simulation and operational parameters used in the numerical model.

Table 4.4 – Well B simulation / operational parameters

Parameter	Value / Unit / Comment
Flow rate	1,393 m ³ /d
Gas-oil ratio	121 std m ³ /std m ³
Basic Sediments and Water (BSW)	0.3%
Oil density	26.9 °API
Friction factor	1x10 ⁻⁵
Tubing surface emissivity	0.75
Casing surface emissivity	0.75
Bottomhole pressure @ 4,200 m	22.06 MPa
Bottomhole temperature @ 4,200 m	383.3 K
Seabed temperature @ 1,091 m	277.2 K
Water depth	1,091 m

KOP	3,013 m
Perforating interval	4,342 - 4,495 m
Simulating length (from PDG to Wellhead)	3,109 m
Length step	10 m
Multiphase flow model	Beggs and Brill (1973)
Annulus convection model	Zhou (2013)
Formation thermal model	Hybrid

Additionally, Table 4.5 shows some design details of the annuli configuration and Table 4.6 shows the key thermal and mechanical properties of the formation surrounding the well B.

Table 4.5 – Well B annuli design details

Annulus	Casing seat [m]	Fluid type	Top of cement / packer [m]
9 $\frac{5}{8}$ " x 6 $\frac{5}{8}$ " (Annular # A)	4,935	Brine	4,050
13 $\frac{3}{8}$ " x 9 $\frac{5}{8}$ " (Annular # B)	3,543	Brine + glycerin	1,802
20" x 13 $\frac{3}{8}$ " (Annular # C)	1,909	Brine + glycerin	1,091

As in the simulations of well A, the annulus convection approach proposed by Zhou (2013) and the formation thermal model proposed in this thesis, called here the hybrid approach, were also employed for well B. All the models and correlations implemented in the present model and employed to assess the effect of the different existing approaches on the wellbore thermal behavior are found in Appendix G and the results are described in the next sections.

Table 4.6 – Thermophysical and mechanical properties of the formation layers for the well B (Eppelbaum *et al.*, 2014)

Rock type	c_p [J/kg.K]	K [W/m.K]	ρ [kg/m ³]	E [GPa]	ν [-]
-----------	-------------------	--------------	--------------------------------	------------	----------------

Clay	2,127	1,42	2,080	0.4	0.45
Shale	2,151	1.60	2,057	17.5	0.10
Marl	1,734	1.38	1,970	37.5	0.15
Sandstone	737	2.50	2,198	32.5	0.14
Wackstone	390	3.16	2,590	69.0	0.19
Packstone	1,000	3.23	2,620	85.0	0.15
Limestone	887	2.19	2,540	45.0	0.3
Dolomite	933	3.56	2,840	116.0	0.29
Anhydrite	819	4.10	2,980	75.0	0.31
Halite	875	3.97	2,160	37.2	0.25
Cementstone	844	1.96	2,644	1.5	0.35

4.2 Thermal-Hydraulic Evaluation

In this section, the thermal and multiphase flow model was compared and validated against field data and the commercial software WellCat™. Later, a sensitivity analysis was performed to quantify the importance of each wellbore layer thermal resistance on the wellbore thermal behavior.

4.2.1 Hydraulic model

Figure 4.4 illustrates the simulated thermal and pressure profile along the wellbore and the field data for the two end points of the tubing string (*i.e.* at wellhead and PDG depths) after 1 day of production. The agreement is reasonable given the uncertainties involved, and the performance of the model is compatible with that obtained from Wellcat™. For a production time of 1 day, the hydrocarbon pressure and temperature at the wellhead were 16.61 MPa and 375 K, respectively. The present model showed deviations of 0.42 MPa (2.5 %) and less than 3.3 K at the wellhead depth. The deviations associated with the commercial software were about 0.56 MPa (3.4 %) and 3.7 K. As the production time increased, the deviations of both simulators decreased.

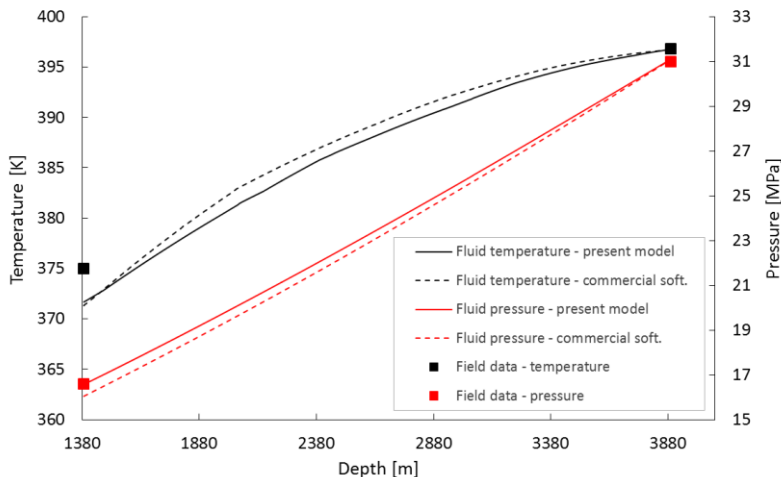


Figure 4.4 – Field data and simulation results for well A for a production time of 1 day.

Figure 4.5 shows a complete set of flowing fluid pressure and temperature data for well A, with the hydrocarbon production kick off at the zeroth hour on February 22nd, 2015. The sampling frequency of the PDG and wellhead pressure and temperature data was approximately 1 reading per hour. As can be seen in Figure 4.5, using the PDG pressure and temperature as an input, the calculated wellhead pressure and temperature at different production times (6 hours, 1, 2, 5 and 10 days) result in a very good agreement between the model and the field data.

At this point, it is important to define a reference time standard for the results presented along the text. Hence, the reference state corresponds to a condition of zero hydrocarbon flow and thermal equilibrium between the well and the formation. At this condition, referred to as $t = 0^-$ h, the temperatures of the wellbore and of the formation are represented by the geothermal gradient. Also, once the well kicks off, the hydrodynamic steady state is immediately achieved since the present transient formulation only applies to the formation thermal model. Note that this is a common approximation in the literature (RAMEY, 1962; CHIU and THAKUR, 1991; HASAN and KABIR, 1994), since the time required for the hydrodynamic model to reach steady state is several orders of magnitude smaller than the characteristic time scale of the heat transfer in the formation. For instance, Hasan and Kabir (1991) showed the difference in time scale

(about 10^{-5}) using a simple example of heat and pressure transmission in a porous medium.

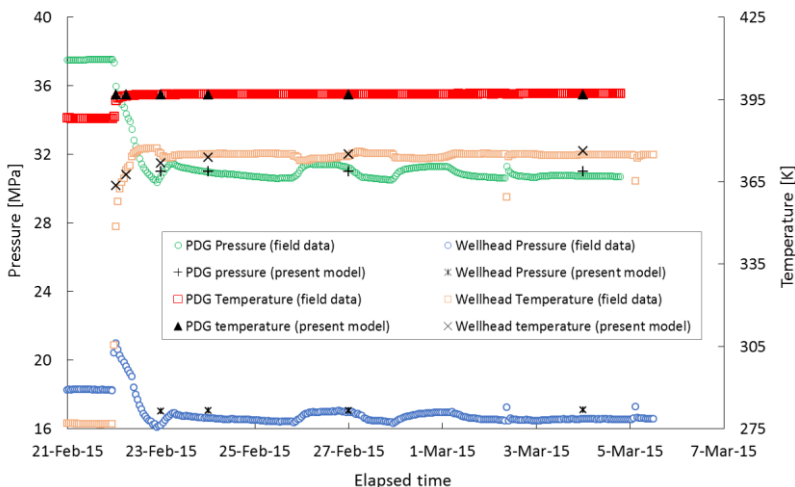


Figure 4.5 – Field data and simulation results for well A.

As shown in Figure 4.5, once the well is operational, the initial flow caused an increase in the mudline temperature, which approached a quasi-steady state temperature value of 375 K. Also noticeable is that the model agreed well with the field data regardless the time scale considered.

4.2.2 Thermal model

Figure 4.6, Figure 4.7 and Figure 4.88 compare the flowing hydrocarbon and annulus temperature profiles of the model and commercial software for production time steps of 1, 5 and 10 days. Even though the thermal behavior of all fluids (i.e. flowing fluid and annuli fluids) in both models are quite similar for higher production times (i.e. 5-day production or more), some points stand out: firstly, the largest temperature difference between the two models (2.4 K) was observed for the hydrocarbon stream at the wellhead; secondly, the model was significantly affected by the formation thermophysical properties presenting several discontinuities in the annuli thermal profiles. With respect to the short transient simulation (i.e. 1-day production), the simulated temperature profile of flowing fluid agrees well with that from

Wellcat. However, the temperature difference between the two sets of data increases as the well depth decrease, most likely due to the uncertainty of how the commercial code handles gas filled annular spaces – note that N_2 is present in annulus A.

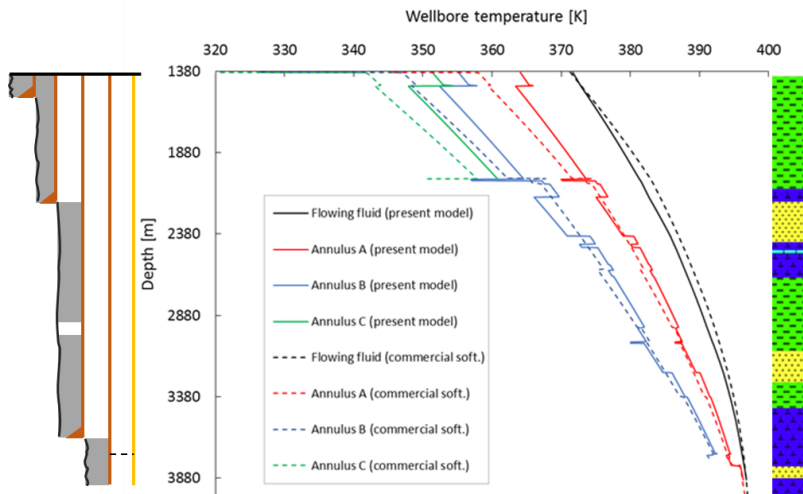


Figure 4.6 – Wellbore fluid temperatures obtained from the thermal and multiphase flow model and Wellcat for well A for a production time of 1 day.

It can be seen in Figure 4.6, Figure 4.7 and Figure 4.8 that near the wellhead, the annuli temperatures predicted by Wellcat decreased sharply. Figure 4.9 shows in greater detail the effect of the quick decrease in temperature experienced by the annuli fluid, for 1 day of production. The reasons for this temperature drop are unknown, but may result from a two-dimensional heat transfer model embedded into Wellcat™ to compute the axial heat loss from the wellbore to the sea. However, the phenomenon might not be evaluated properly. Even though there are no data of annulus temperature available to strengthen the hypothesis, a drop of about 40 K in less than 2 m distance is somewhat questionable.

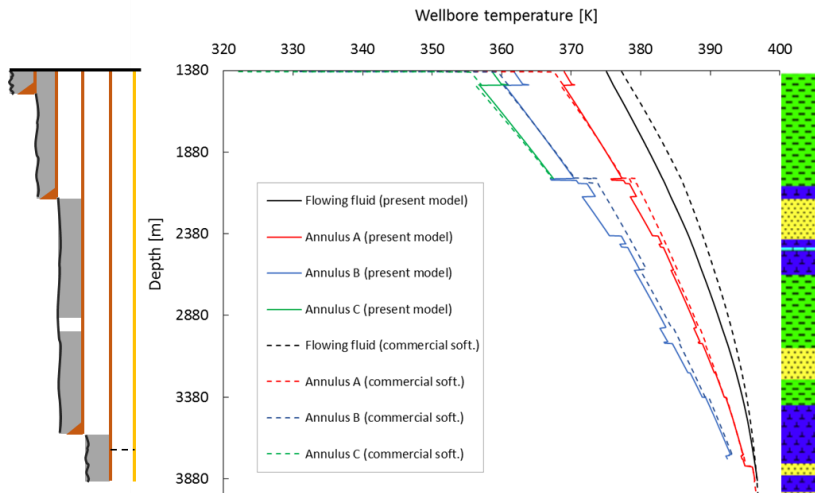


Figure 4.7 – Wellbore fluid temperatures obtained from the thermal and multiphase flow model and Wellcat for well A for a production time of 5 days.

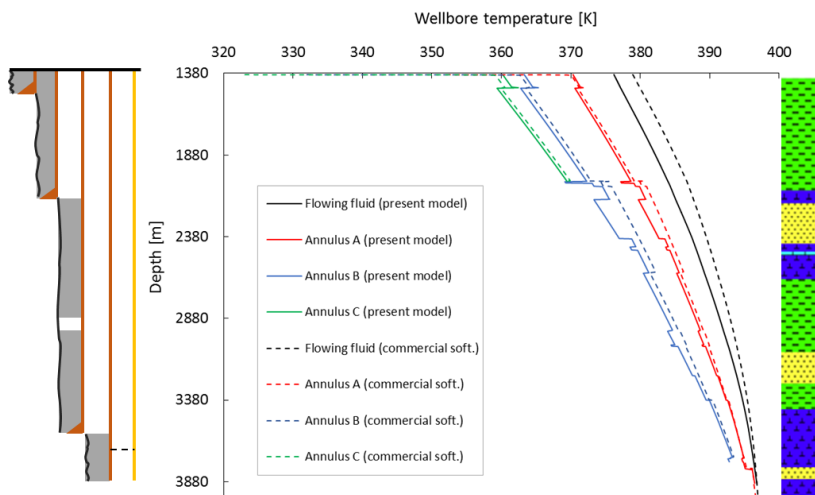


Figure 4.8 – Wellbore fluid temperatures obtained from the thermal and multiphase flow model and Wellcat for well A for a production time of 10 days.

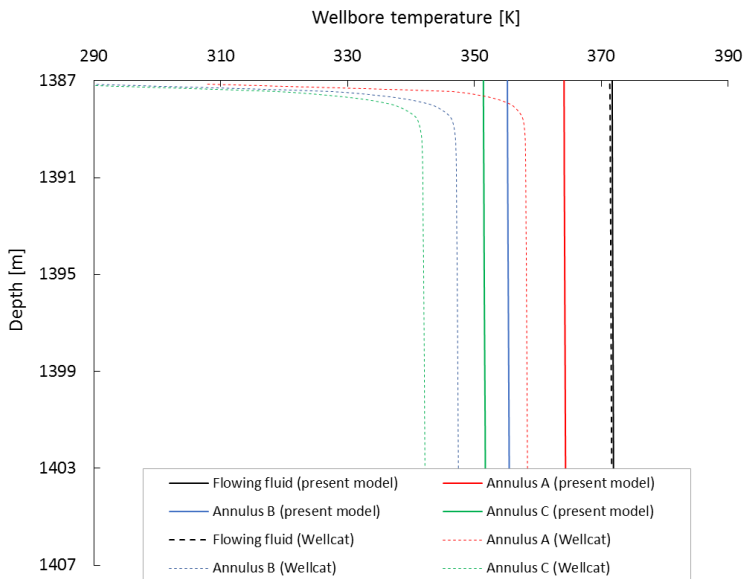


Figure 4.9 – Wellbore temperature behavior close to the wellhead depth for a simulation of 1 day of production.

Figure 4.10 illustrates the variation of $f(t)$ as a function of t_d (note that as the production time increases t_d increases as well) for different wellbore depths, that is, for different formation layers. It is important to emphasize that an accurate prediction of $f(t)$ is fundamental to the model's convergence, since it is used to calculate the interface temperature, which is an important parameter used in the code iteration.

Figure 4.10 shows that as t_d increases, the differences between the curves obtained for the several formations are reduced. For values of t_d larger than 20, the curves collapse into a single profile that is close to Ramey's (1962) long time asymptotic solution (RAMEY, 1962; WILLHITE, 1967; HASAN and KABIR, 1991, CHENG et al., 2011). Moreover, it shows that sandstone and cementstone are much faster in conducting heat away from the wellbore due to the higher thermal diffusivity of these two formation types in relation to the others.

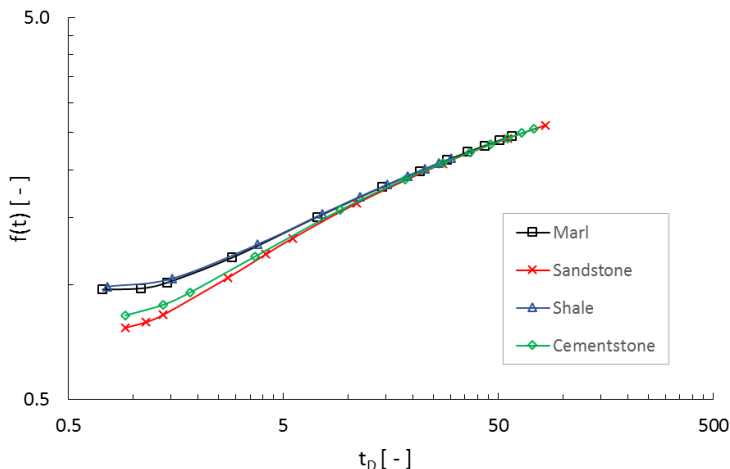


Figure 4.10 – $f(t)$ and t_d relationship for different formation layers.

4.2.3 Effect of the production time on the wellbore thermal-hydraulic behavior

Figure 4.11 and Figure 4.12 show, respectively, the temperature variation of the flowing fluid and annulus A through the well A for several different production times, according to the present mathematical model. For the initial flowing time, $t = 0^+$ h, the temperature profile is not influenced by the formation thermal resistance yet. At this time, the thermal behavior is only affected by the wellbore thermal resistances, especially by the cement sheaths, as observed at 1,470 and 2,040 m and by the annulus B fluid present between the two cement isolation sections (from 2,955 to 3,050 m).

For a longer time scale (i.e., 10 days), the heat transport is almost at steady state. The further the radial heat flow travels into the rock formation, the larger the influence of the formation thermophysical properties on the wellbore thermal profile and, therefore, the smaller the influence of the wellbore thermal resistances. In other words, as the Fourier number increases, the importance of the wellbore heat capacity on the wellbore thermal behavior becomes less relevant.

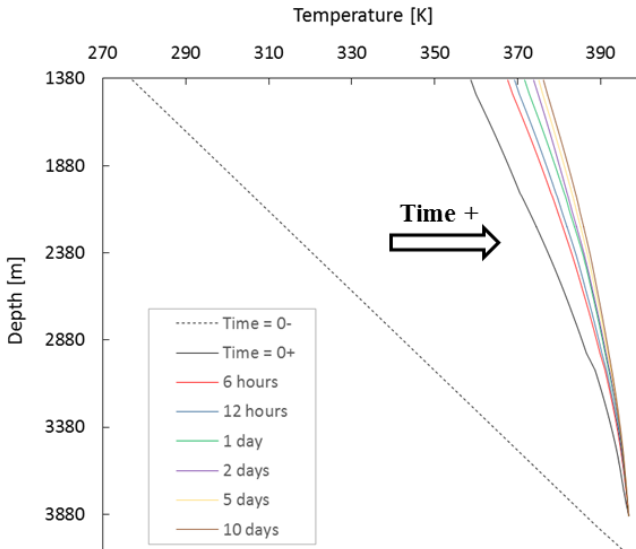


Figure 4.11 – Flowing fluid temperature profile for several production time steps.

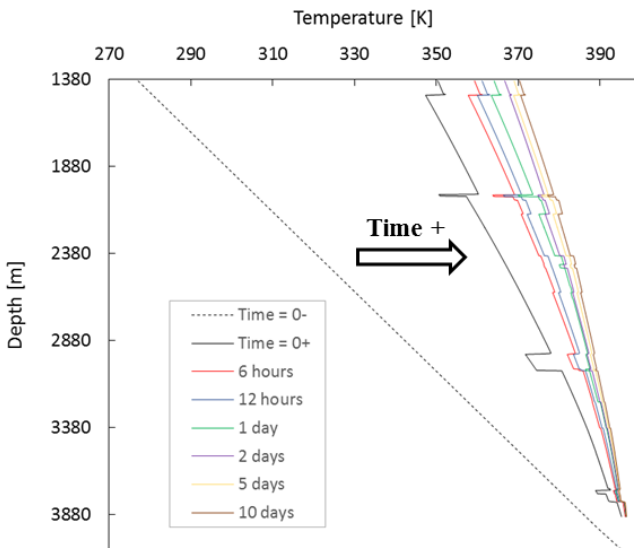


Figure 4.12 – Annulus A temperature profile for several production time steps.

4.2.4 Effect of the annulus fluid type

As mentioned above, well A was completed with the production annular (Annulus A) filled with nitrogen down to a depth of 3,806 m, where a gas lift valve was installed (see Figure 4.1). Below this depth, the remaining annulus space is filled with brine (water/sodium chloride, 73/27 % wt). The effect of the type of fluid on the wellbore thermal behavior, according to the present model, can be observed in Figure 4.13 and Figure 4.14. Figure 4.13 shows the temperature profile for the hydrocarbon stream for two different scenarios: production annulus filled only with brine or with N₂/brine, to reproduce the actual completion of well A.

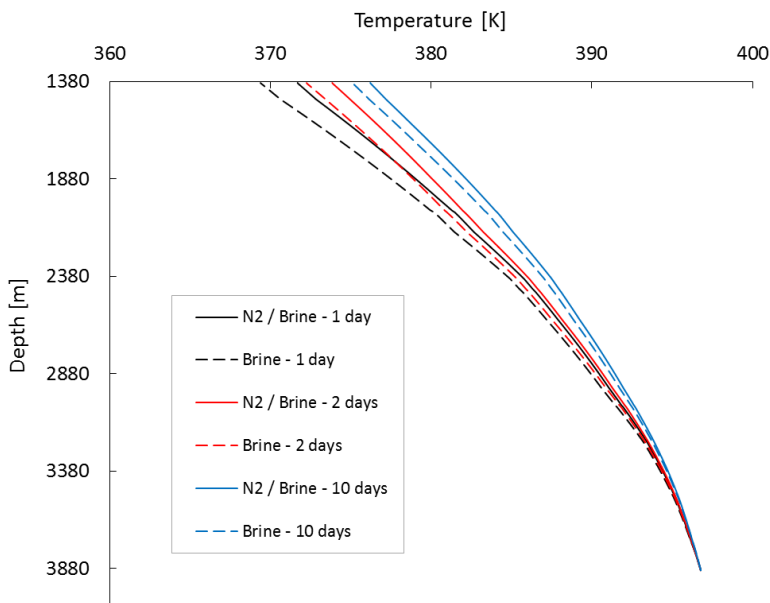


Figure 4.13 – Effect of the fluid type on the flowing fluid temperature profile.

Figure 4.14 shows the temperature profile for the production annulus considering it is entirely filled with brine and N₂/brine for three different production periods. The insulation provided by the N₂ contributed to the reduction of the production annulus wellhead temperature, which is explained by the lower thermal conductivity of the gas. Even though the use of N₂ as a packer fluid is not common in the

oil industry, it is justified since this well expected a gas-lift operation at later stages. The thermal characteristics of the materials involved in this configuration resulted in significant reductions of the heat transport to the outward annuli and of the wellhead temperature. While the tubing fluid temperature increases when N_2 is employed (see Figure 4.13), the reverse behavior is observed in the production annulus, as can be seen in Figure 4.14.

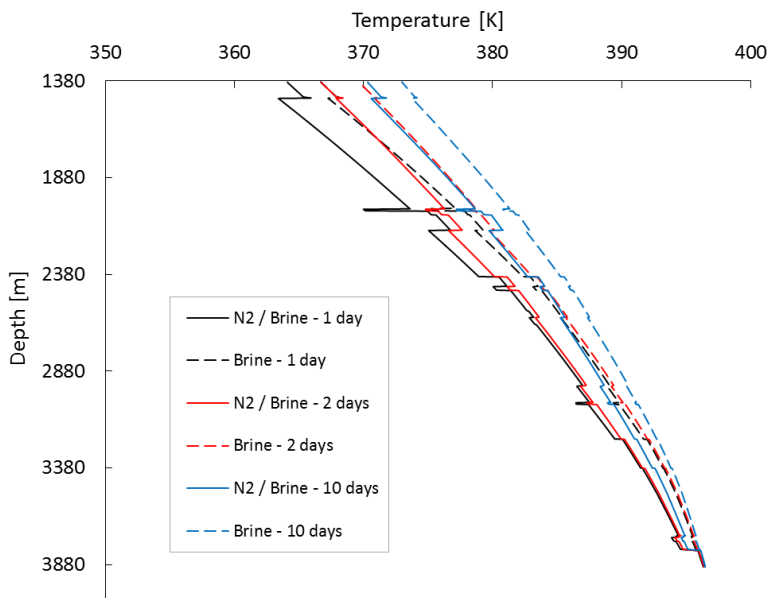


Figure 4.14 – Effect of the fluid type on the annulus A temperature profile.

For all production times, except for very short transient (i.e. $t=0^+$ day), the much higher thermal resistance associated with the N_2 -filled annulus results in a higher temperature of the tubing fluid at the wellhead and a lower temperature of the production annulus in comparison with the case where brine is used as a packer fluid (Figure 4.15). This behavior is due to the reduction in the radial heat loss. The temperature difference in the production annulus reached nearly 3 K for a 5-day production time frame. For very short transients, as presented in Figure 4.15, the temperature difference between the flowing fluid and the annular fluids is very large and the heat exchange into the wellbore is characterized by an intense heat transfer rate from the tubing fluid

towards the formation. In this case, the flowing fluid temperature difference at the wellhead is about 10 K higher for N_2 compared to brine. So, although N_2 is a better thermal insulator than brine, at the beginning of production, the wellhead temperature for the flowing fluid and annulus A fluids are higher in the case of N_2 -filled annulus due to the higher thermal diffusivity of the gas (2 or 3 order of magnitude higher).

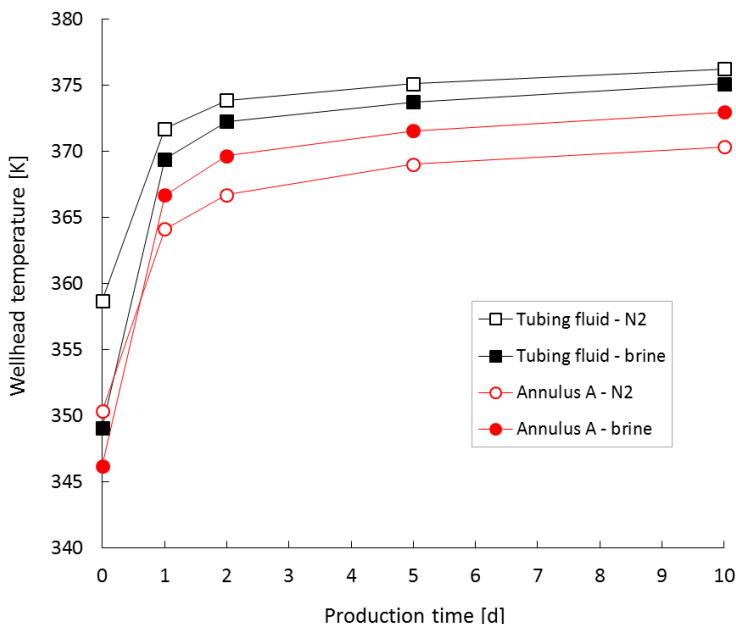


Figure 4.15 – Effect of the fluid type on the flowing fluid and annulus A wellhead temperature.

The nitrogen in annulus A also contributed to the reduction of the unwanted increase of the annular pressure when compared to brines due to the much larger compressibility coefficient. As mentioned above, although appropriate in a particular scenario involving gas-lift production during later stages, the use of N_2 in the production annulus to reduce the heat transport to the outward annuli is not common and should be carefully considered. This is because the gas may contain traces of hydrogen sulfide or even carbon dioxide, which cause corrosion of the production casing when in contact with water, and/or

leakage through the casing threads if an inappropriate connection is employed.

4.2.5 Effect of the annulus convection heat transfer correlation

Although there are many natural convection models available in the literature, no correlation has been derived specifically for large aspect ratio annuli, such as those found in petroleum wells. In order to explore the contribution of the annulus convection to the wellbore thermal behavior, Figure 4.16, Figure 4.17 and Figure 4.18 were plotted considering three different instants, namely 0^+ , 1-day and 10-day production (steady-state). The results revealed that for a very short production time (see Figure 4.16), when the annulus thermal resistance has a stronger effect on the wellbore thermal behavior, larger deviations between the annulus convection correlations are observed. The largest deviations between any two correlations in terms of the wellhead temperature were 2.4 K, 1.7 K and 0.7 K for the flowing fluid, annulus A and annulus B, respectively.

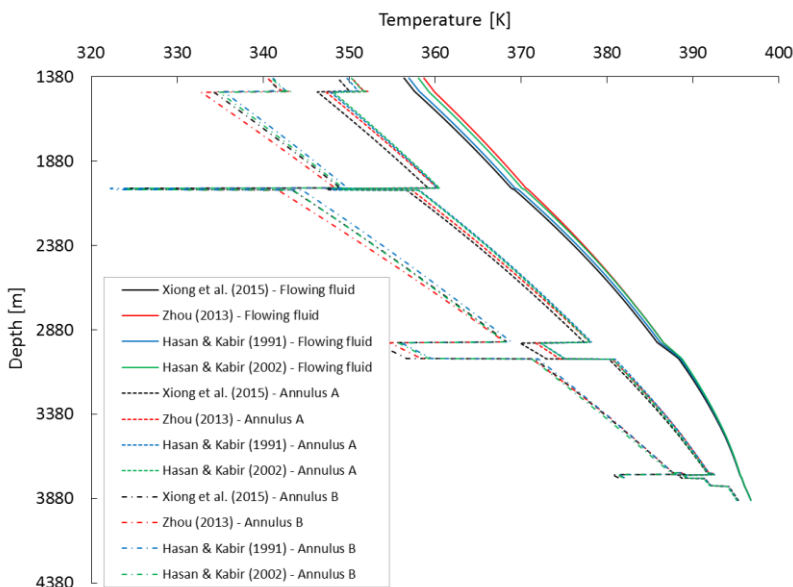


Figure 4.16 – Effect of the annulus convection approach on the wellbore fluids temperature profiles for very short transient ($t = 0^+$ h).

For 1-day production (see Figure 4.17) the discontinuities in the annular fluid temperature profiles due to the presence of the cement sheaths are still observed, but to a lesser extent when compared to the transitions between different formation layers.

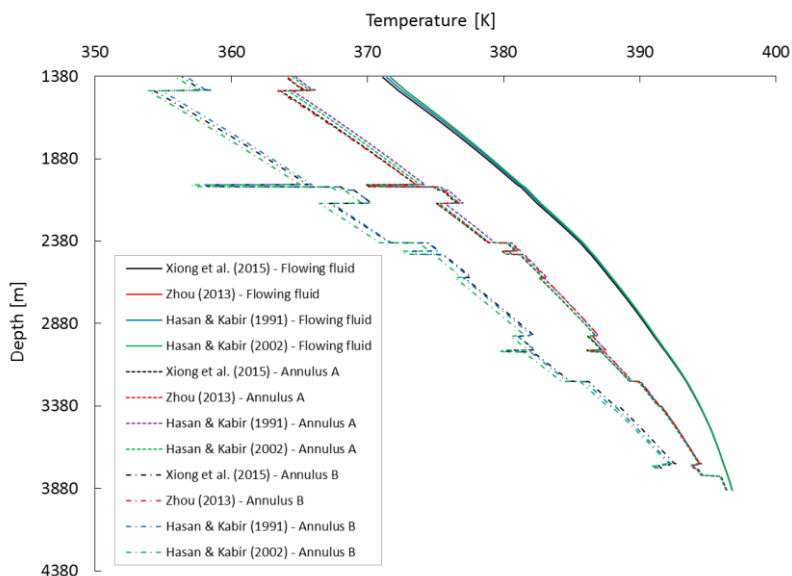


Figure 4.17 – Effect of the annulus convection approach on the wellbore fluids temperature profiles for short transient (1-day production).

As the production time increases, the contribution of the formation thermal resistance also increases and the convection correlation choice is no longer important, as shown in Figure 4.18.

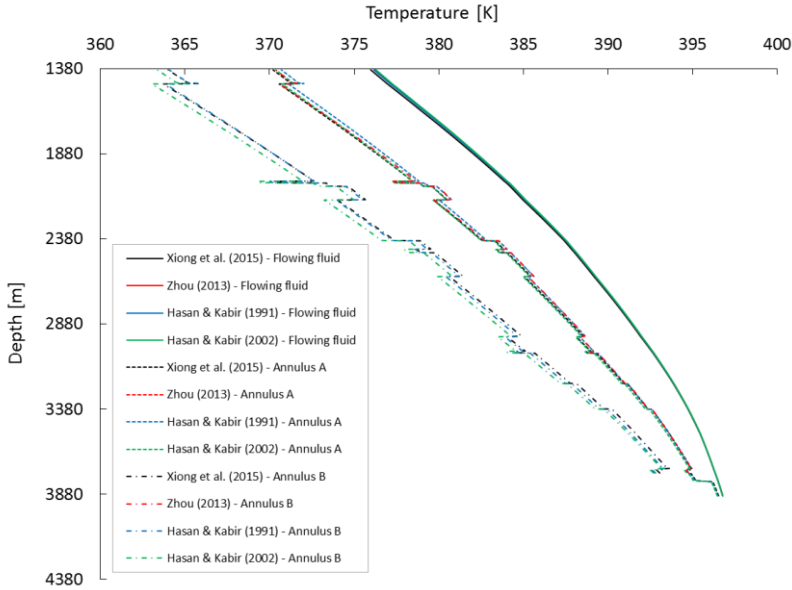


Figure 4.18 – Effect of the annulus convection approach on the wellbore fluids temperature profiles for steady-state (10-day production).

4.2.6 Effect of the formation thermal model

The influence of the production time was quantified for each formation model implemented in the simulator. Figure 4.19 shows the temperature profile for Annulus A for two different production times. For short periods, the model developed by Cheng *et al.* (2011) showed the largest deviation with respect to the other models. This was somewhat expected, since for low t_D values the formation heat capacity embedded in the transient temperature function, $f(t)$, has little influence on the wellbore heat transfer process. For large production times, the differences between the models decreases significantly, as previously reported (Nian *et al.*, 2014).

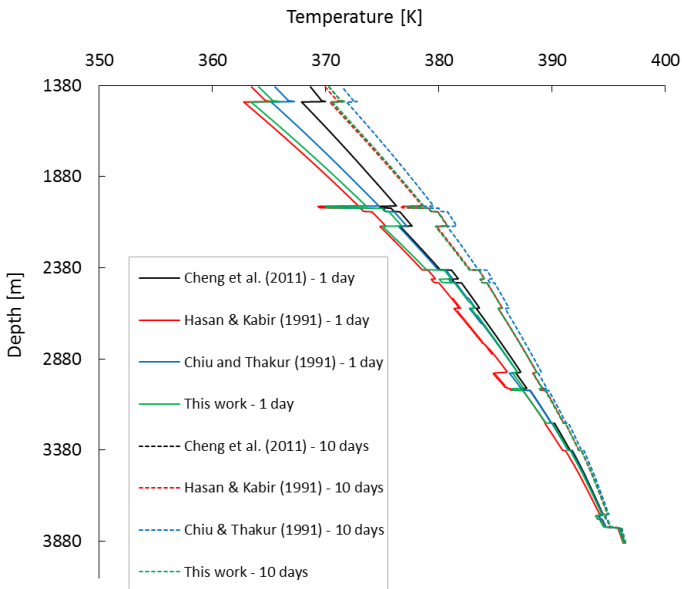


Figure 4.19 – Effect of the formation model on the annulus A temperature profile for two different production times.

Although the model of Hasan and Kabir (1991) predicts the lowest wellbore temperatures among all models, as shown in Figure 4.19 and Figure 4.20, the deviations between the models are relatively low – nearly 3 K for annulus B wellhead temperature. Additionally, the hybrid model implemented in this thesis eliminated the over estimation associated with very short periods found in the Cheng *et al.* (2011) model. As mentioned in Section 3.3, the hybrid model combines the best features of each model, namely the very short transient response of Hasan and Kabir (1991), the better agreement for short periods of Cheng *et al.* (2011) and the consistent behavior of the Ramey (1962) model for the late production stages.

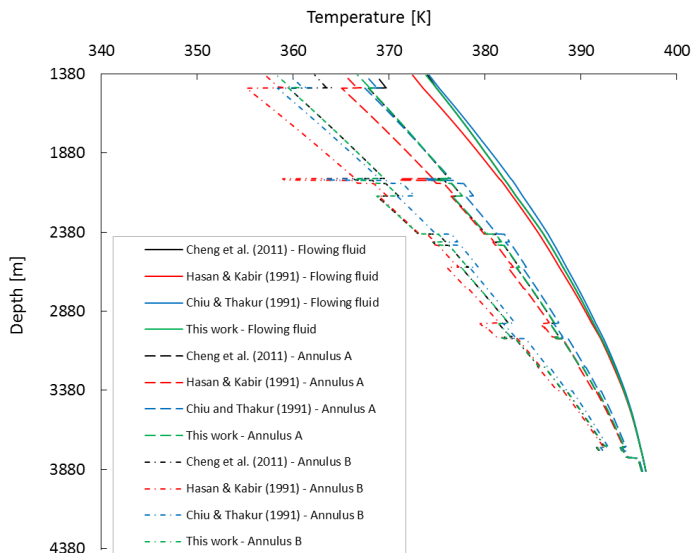


Figure 4.20 – Effect of the formation model on the wellbore fluids temperature profiles for a 2-day production time.

4.2.7 APB prediction

For the purpose of calculating the wellbore annuli increase in pressure, the multistring approach proposed in the recent study of Barcelos *et al.* (2017) was considered. In this case, all APB calculations (e.g., pressure variation, annular deformation) are determined with respect to $t = 0^-$ day. Figure 4.21 shows the wellbore pressure profiles for the 0^+ -day production time. In addition to the magnitude of the pressure being a concern to the wellbore integrity, the pressure difference between the inward and the outward tube is perhaps the most worrisome issue related to APB, since the loads originated from this difference might lead to the wellbore failure (i.e. casing and/or tubing bursting or collapsing). Hence, despite the fact that the magnitude of pressure in annulus C is the largest, the pressure difference between annulus A and B immediately above the TOC of annulus B is the highest for this production time step (e.g. 23 MPa) and, consequently, the most critical.

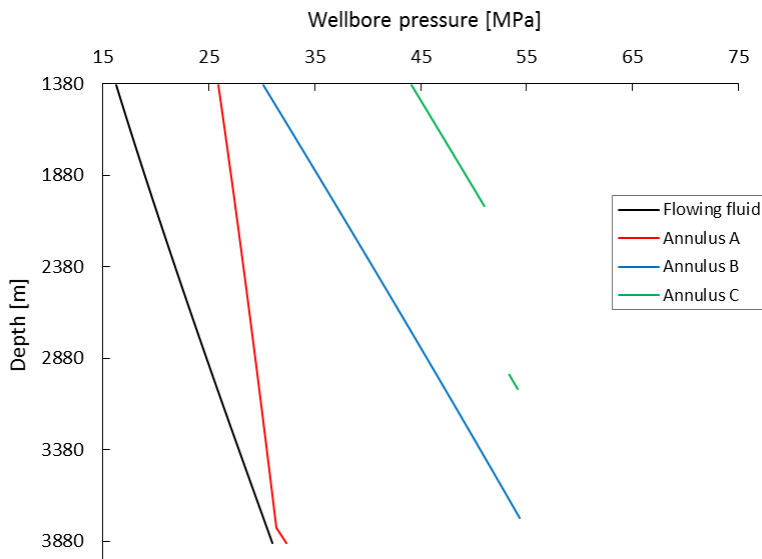


Figure 4.21 – Wellbore pressure profiles for the 0⁺-day production time.

The wellbore pressure profiles for the 1, 2 and 10-day production times are depicted in Figure 4.22, Figure 4.23 and Figure 4.24, respectively. The same behavior described above can be seen for longer production times. Hence, assuming that the collapse resistance for the 10 ³/₄" casing (the most critical casing) is 51.78 MPa (i.e. according to API 5CT/ISO 11960), the pressure differences calculated for 1, 2 and 10-day production times were 30.5, 31.6 and 34.3 MPa, respectively, which are lower than the MAASP – Maximum Allowable Annular Surface Pressure. Nevertheless, it is also important to evaluate the stresses on the other wellbore components, namely the 6 ⁵/₈" tubing and the 13 ³/₈" casing. With respect to the tubing, the largest pressure difference took place at the wellhead. Considering the worst case, i.e. the 10-day production time, the largest pressure difference was 10.89 MPa, while the 6 ⁵/₈" tubing collapse resistance is 43.51 MPa. Finally, regarding the 13 ³/₈" casing, the large pressure difference was 21.9 MPa, while the collapse resistance of such casing is 24.54 MPa.

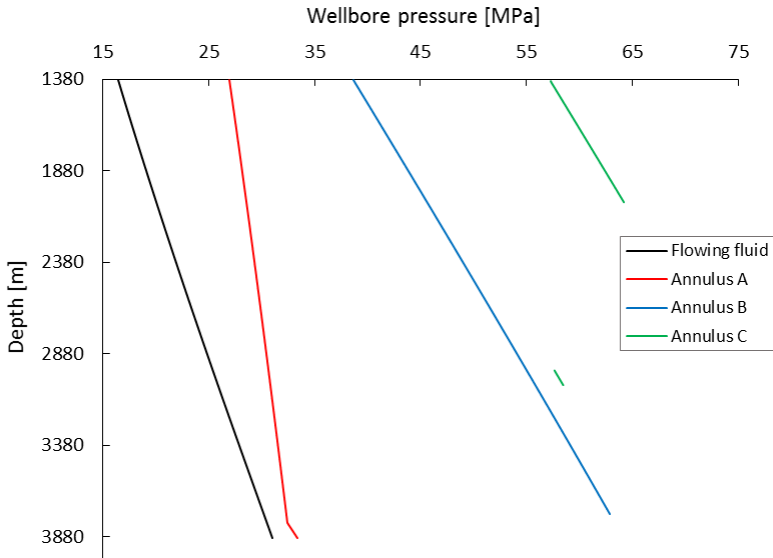


Figure 4.22 – Wellbore pressure profiles for the 1-day production time.

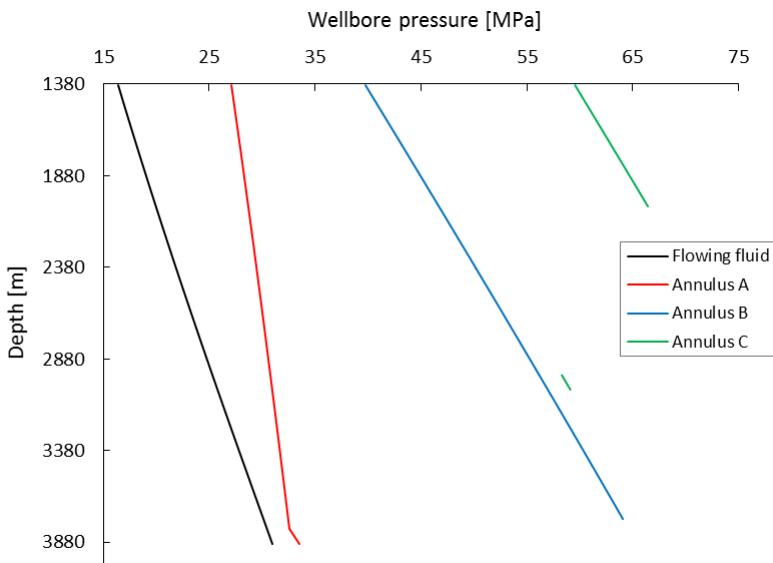


Figure 4.23 – Wellbore pressure profiles for the 2-day production time.

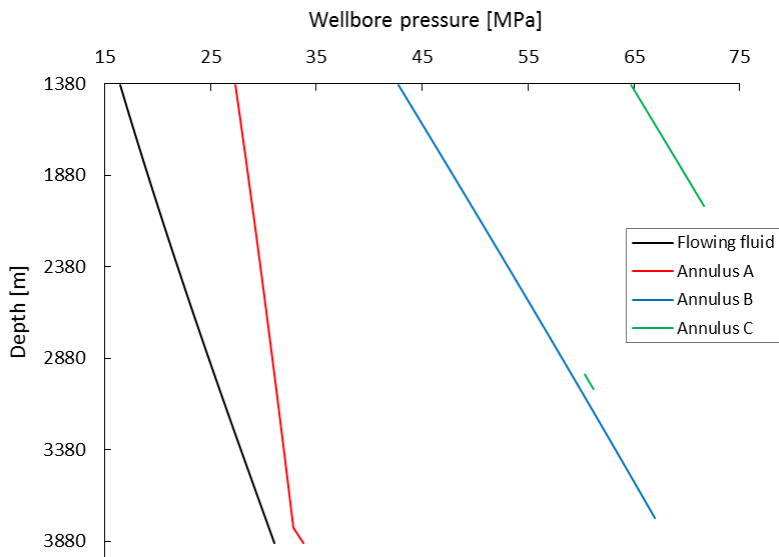


Figure 4.24 – Wellbore pressure profiles for the 10-day production time.

Table 4.7 shows the APB prediction for the three annuli for 5 production times. The APB contribution due the temperature variation only (fluid thermal expansion) is shown in Table 4.7 between brackets.

Table 4.7 – APB summary for different production time steps.

Annulus	APB [MPa] and (APB _T) [MPa] at various production times				
	0 ⁺ d	1 d	2 d	5 d	10 d
A	3.86	4.86	4.98	5.17	5.30
	(3.72)	(4.63)	(4.73)	(4.90)	(5.01)
B	16.18	24.70	25.85	27.56	28.85
	(28.74)	(42.11)	(43.86)	(46.25)	(48.02)
C	30.17	43.40	45.61	48.30	50.76
	(44.67)	(61.44)	(64.45)	(67.63)	(70.98)

It can be seen from Table 4.7 that for annuli B and C the APB caused by fluid expansion, namely APB_T, is higher than the combined

APB due to fluid expansion and tubular radial strains. This happens since the multistring approach allows the pressure inside an annulus to influence the pressure in other annuli. For instance, for annulus A, the average strain experienced by the 6 5/8" produced an extra volume that was larger than the volume reduction due to the 10 3/4" casing deformation. Thus, the APB_T contributed positively to the global APB. Conversely, for annulus B, the outward 13 3/8" casing, experienced lesser strain than the inward casing, yielding a negative contribution to the overall APB. In fact, the tube strain at a given production time is defined as

$$\Delta\epsilon_r^t = \frac{\Delta r_{ext}^t}{r_{ext}^t} \quad (4.2)$$

where r_{ext}^t is the external radius of the tube at a given production time, and Δr_{ext}^t is the difference between $r_{ext}^{0^-}$ and r_{ext}^t , with $r_{ext}^{0^-}$ being the external radius of the tube at instant 0⁻ days (initial time).

Figure 4.26, Figure 4.27 and Figure 4.27 show the tubular local deformations along the wellbore for 0⁺, 1 and 10-day production times. It should be noted that the internal and the external diameters of a given tube always experience the same elongation/shrinkage. Thus, only the external diameter of the tubes forming each annulus was plotted. For annulus C, the strain relative to the inner diameter of the casing was also plotted. Furthermore, the API states that the limit tube strain for steel-composed materials is 0.5% to ensure that the tube structural behavior is within the elastic limit.

As the tubes deformation is calculated locally, it is quite easy to observe the effect of the wellbore components and changes of formation layers on the tubing/casing diameter, as observed previously in the temperature profiles. For very short transients (i.e. 0⁺-day production time), the discontinuities observed in the strain curves are caused by the wellbore components as a consequence of changes in magnitude of the heat transfer rate. The most significant discontinuity is due to a short fluid layer ("fluid ring") between two cement sections in annulus C. Other discontinuities are due to the casing shoes.

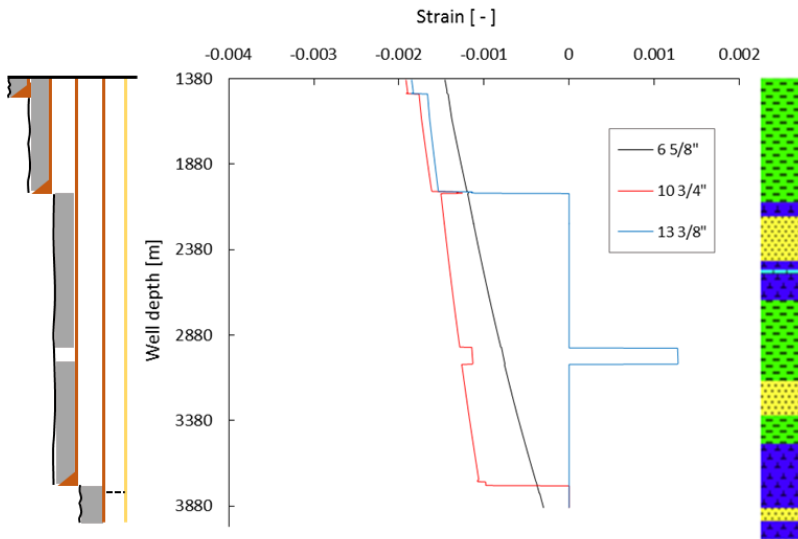


Figure 4.25 – Tube deformations for 0⁺-day production time simulation.

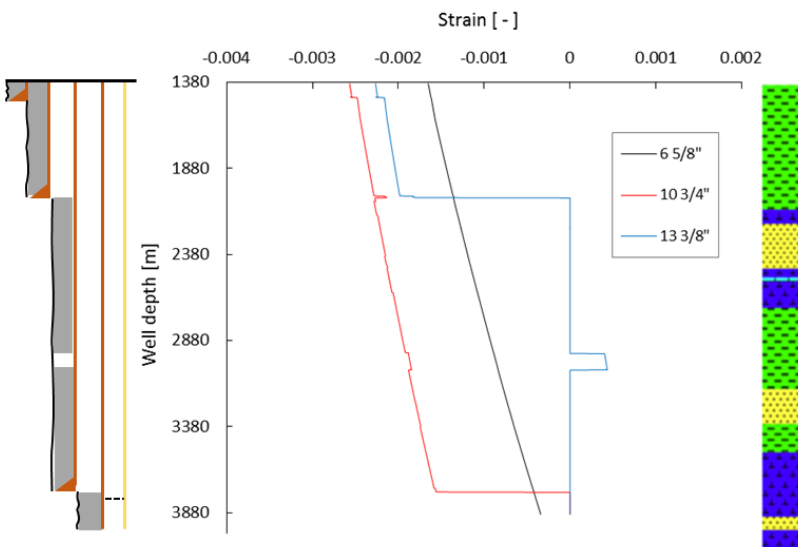


Figure 4.26 – Tube deformations for 1-day production time simulation.

Also, qualitatively the same behavior is observed for short transients (i.e. 1-day) and steady-state (i.e. 10-day) production times.

The discontinuity observed in the 13 3/8" casing strain curve is caused by the fluid ring, while the discontinuities seen in the 10 3/4" strain curve are due to the formation layer transitions. Similar to the thermal responses, at short production times, larger values of tube deformation are observed at the points of structural transition in the well, such as the depths of 1,470 m and 2040 m, where the casing seats are located. As the production time increases, the impact of the wellbore components on the deformation of the tubes decreases.

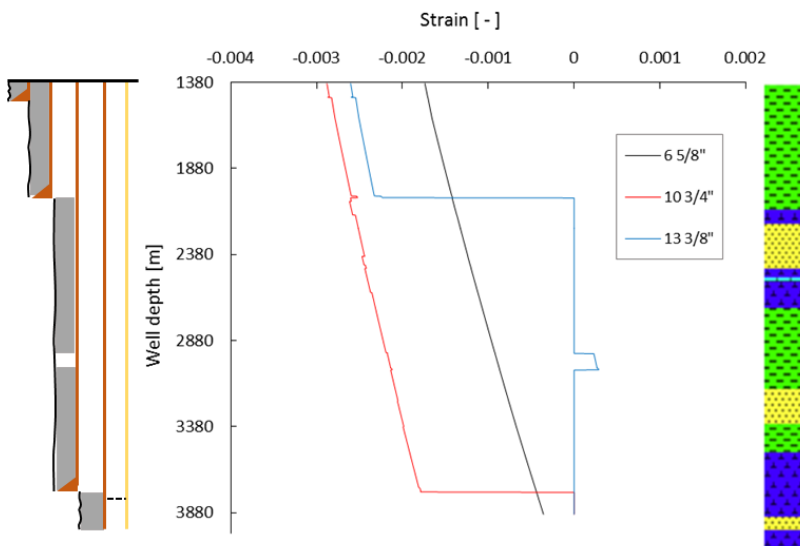


Figure 4.27 – Tube deformation for 10-day production time simulation.

It should be noted that the APB is undeniably accompanied by a variation of the annulus volume, as previously explained. This volume variation may be positive or negative depending whether the diameter of the tubes forming that annulus has decreased or increased. The variation in the annulus volume was calculated as follows:

$$\Delta V_a^t = \left(\frac{V_a^t - V_a^{0^-}}{V_a^{0^-}} \right) \cdot 100 \quad (4.3)$$

where V_a^t is the annulus volume at a given production time in days and $V_a^{0^-}$ is the initial annulus volume, that is, the annulus volume at instant 0⁻ days.

The annuli volume variations for the 5 simulated production times are presented in Table 4.8. Note that the initial volume of annulus A, B and C were 63.62, 44.24 and 52.80 m³, respectively.

Table 4.8 – Annuli volume results at various production time steps.

Annulus	Annulus volume [m ³] and volume variation [%] at various production times				
	0 ⁺ d	1 d	2 d	5 d	10 d
A	63.39	63.23	63.21	63.19	63.17
	-0.38	-0.61	-0.64	-0.69	-0.72
B	44.66	44.85	44.87	44.91	44.93
	0.93	1.38	1.42	1.50	1.54
C	53.25	53.39	53.42	53.45	53.48
	0.84	1.11	1.17	1.22	1.28

Results from Table 4.8 reiterates the fact that the largest pressure difference observed in annulus B produced the highest annulus volume variation, i.e., an increase of 1.54 % in the volume of annulus B due to the reduction in the 10 ¾” and 13 ⅜” casing diameters, which contributed to alleviating the pressure increase. In other words, the results from Table 4.7 and Table 4.8 show the importance of both fluid expansion and tube deformation contributions on the APB prediction.

4.2.8 Mechanical model validation

In order to validate the APB results, the values calculated by the mechanical model were compared with field data. Figure 4.28 shows a complete set of flowing fluid and production annulus pressure data available for well A with the hydrocarbon production kick off at the zeroth hour on February 22nd. As observed in Figure 4.28, using the pressure data as an input, the calculated annulus wellhead pressure at different production times (0⁺, 1, 2, 5 and 10 days) agreed well with the field data.

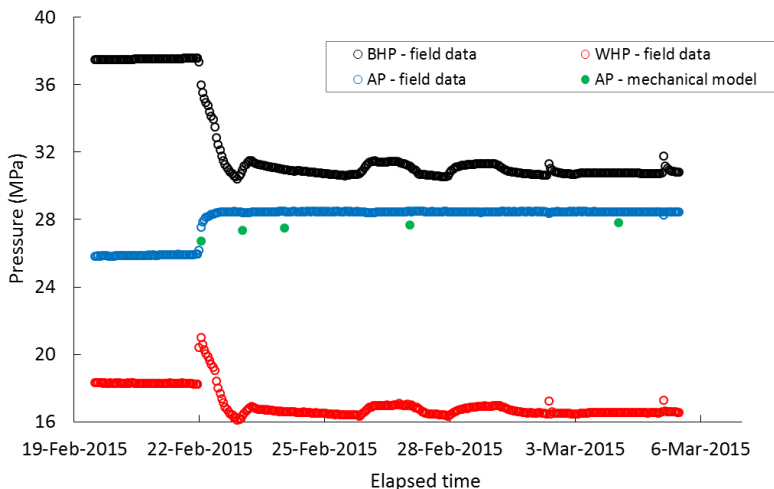


Figure 4.28 – Pressure data set for well A along the production time. BHP – Bottomhole pressure (registered at the PDG), WHP – Wellhead pressure (of the flowing fluid), AP – Annulus pressure.

Table 4.9 shows the absolute pressure values and the deviations relative to field data for several production times.

Table 4.9 – Summary of pressure data as a function of the production time.

Data	Wellhead annulus pressure [MPa] at various production time				
	0 ⁺	1 d	2 d	5 d	10 d
Field data	27.50	28.40	28.45	28.46	28.42
Present work	26.70	27.35	27.47	27.65	27.77
Deviation [%]	2.93	3.71	3.45	2.84	2.29
Wellcat	55.62	78.79	81.42	83.94	87.33
Deviation [%]	102.2	177.4	186.2	194.9	207.3

Deviations as low as 3.71 % were observed for the entire data set. At earlier production times, larger deviations of the calculated annulus pressure relative to field data due to the APB are observed. As the production time increases, the deviation decreases, reaching a value around 2% at steady state.

As a means to further validate the proposed calculation method, the APB predictions were compared against the commercial software WellCat™. Figure 4.29 and Figure 4.30 show the wellbore pressure profiles for simulations at the following production times: 1 and 10 days.

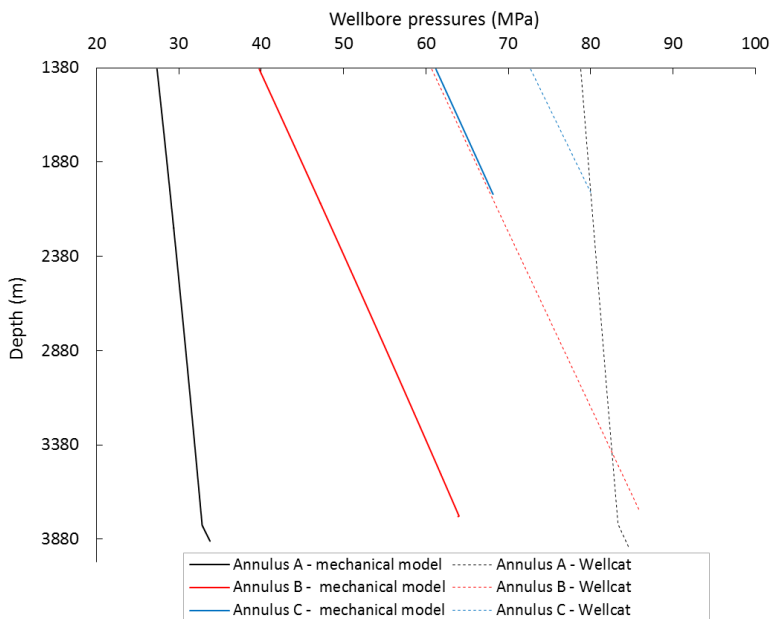


Figure 4.29 – Wellbore fluid pressures obtained from the present model and commercial software for the well A for 1-day production time using N₂ filled annulus A.

The comparison revealed that the commercial software overestimated the pressures in the annuli, especially in annulus A. One should notice that while the reasoning for the high-pressure difference is somewhat unclear, such difference could be associated to how the commercial software models gas filled annulus – note that the difference in pressure for annulus A between the simulations was over 50 MPa. In this case, if well A had been subjected to this pressure magnitude, the 6 5/8” tubing would have collapsed.

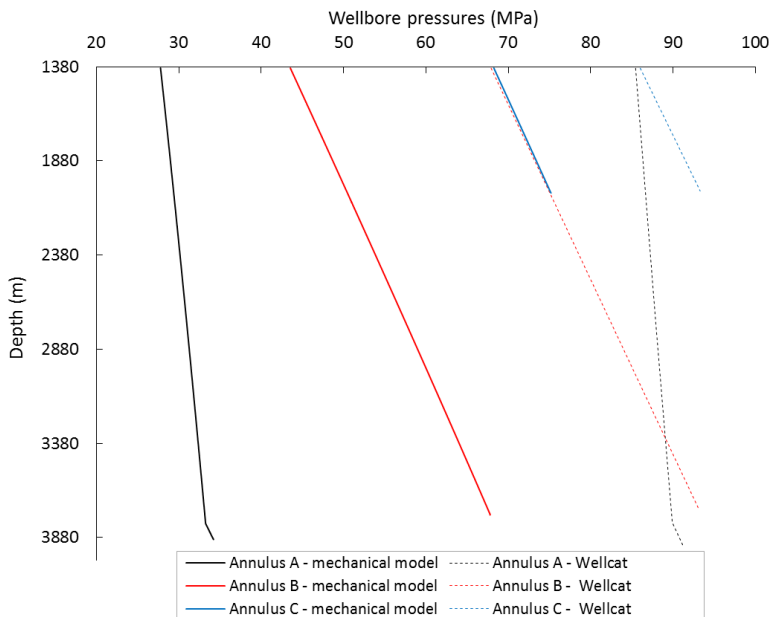


Figure 4.30 – Wellbore fluid pressures obtained from the present model and commercial software for well A for 10-day production time using N_2 filled annulus A.

More compelling evidences that the commercial software cannot handle compressible fluids properly were provided from simulations performed using only brine as a packer fluid (i.e., N_2 is replaced with brine). Figure 4.31 and Figure 4.32 show the pressure profiles obtained from both simulators for production times of 1 and 10 days. When brine entirely fills annulus A, the deviation between the models is significantly reduced. Also, the results showed that when a compressible fluid such as N_2 is used in the production annulus, besides providing thermal insulation as observed in Section 4.2.4, it has a major effect on the wellbore mechanical behavior. For instance, for a 1-day production time, the wellhead pressure in annulus A changed from 27.35 MPa to 71.74 MPa by replacing N_2 with brine. This behavior is somewhat expected since an almost incompressible fluid, such as brine, has a high impact on the deformation of tubes.

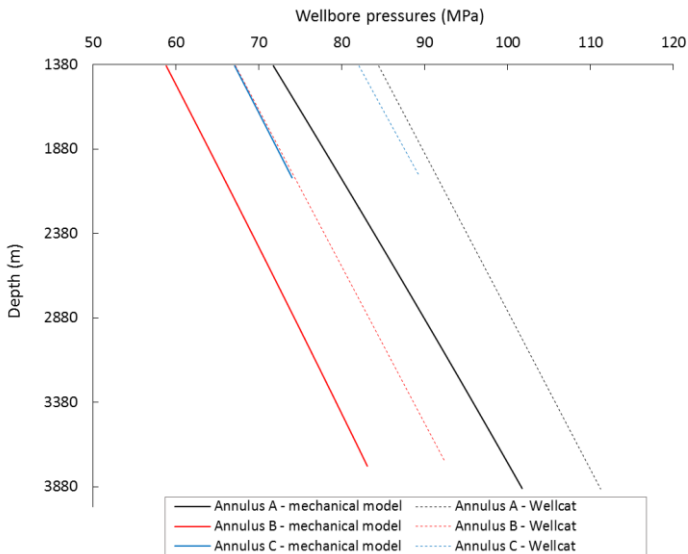


Figure 4.31 – Wellbore fluid pressures from the present model and commercial software for well A for 1-day production time using brine filled annulus A.

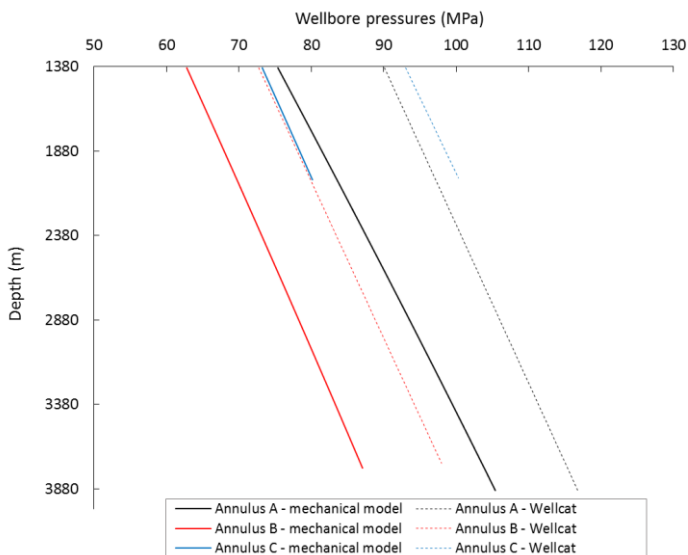


Figure 4.32 – Wellbore fluid pressures from the present model and commercial software for well A for 10-day production time using brine filled annulus A.

From the results presented in this section, one concludes that the magnitude of the pressures in the wellbore increases dramatically when brine was employed as a packer fluid. To better quantify these differences, Figure 4.33 shows the wellbore pressures for both cases (N_2 and brine filled annulus) considering a production time of 1 day. Even though the N_2 present in annulus A is capable of reducing the pressure throughout the well, this reduction is much greater in the Annulus A itself, about 44.4 MPa, while in annuli B and C, this value was 19.1 and 5.9 MPa, respectively.

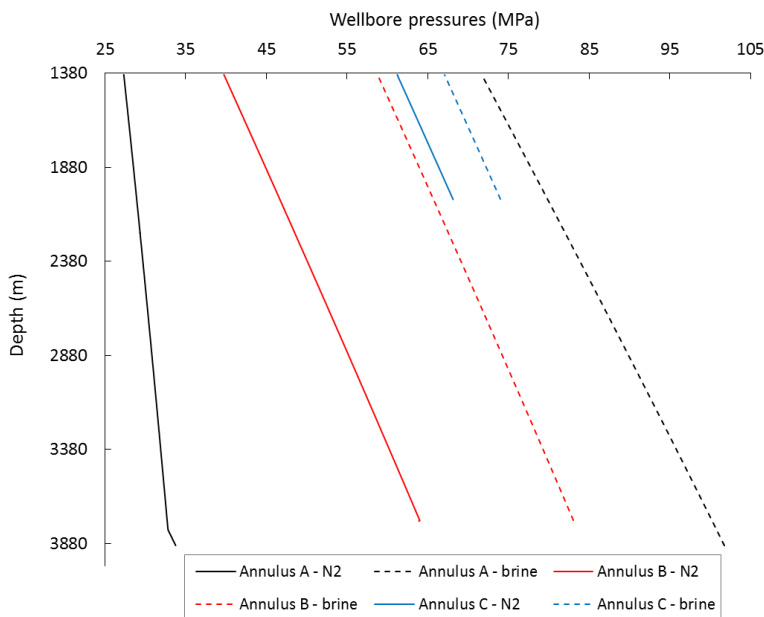


Figure 4.33 – Wellbore pressures while using N_2 or brine filled annulus for the 1-day production time.

4.3 Analysis of Heat Transfer in a VIT Assisted Wellbore

Heat transfer in wellbores with VIT joints is singular since the thermal resistances of the insulated tubes may be larger than those of associated with the formation. As a result, the wellbore thermal resistance plays an important role for both short transient and longer production times.

Initial simulations were performed considering a string with only 10 VIT joints, which represents the first 100 m from the wellhead. In this preliminary assessment, the inner and outer VIT surface temperature profiles were analyzed, as well as the VIT equivalent thermal resistance and the radiative heat transfer coefficient in the VIT evacuated enclosure.

In a second step, well A is modeled with 60 VIT joints aiming to eliminate the risk on the wellbore integrity due to APB. Results obtained from the Wellcat™ software were used to reinforce the validity of the present numerical approach.

4.3.1 Wellbore with 10 VIT Joints

The results from the simulations performed for well A with 10 VIT joints are depicted in Figure 4.34 and Figure 4.35 in terms of the wellbore fluid temperatures (Figure 4.34), the flowing fluid pressure and heat transfer rate per unit length (Figure 4.35), respectively, for a 10-day production (almost steady-state). In these simulations, the emissivity of the evacuated surfaces was set as 0.75.

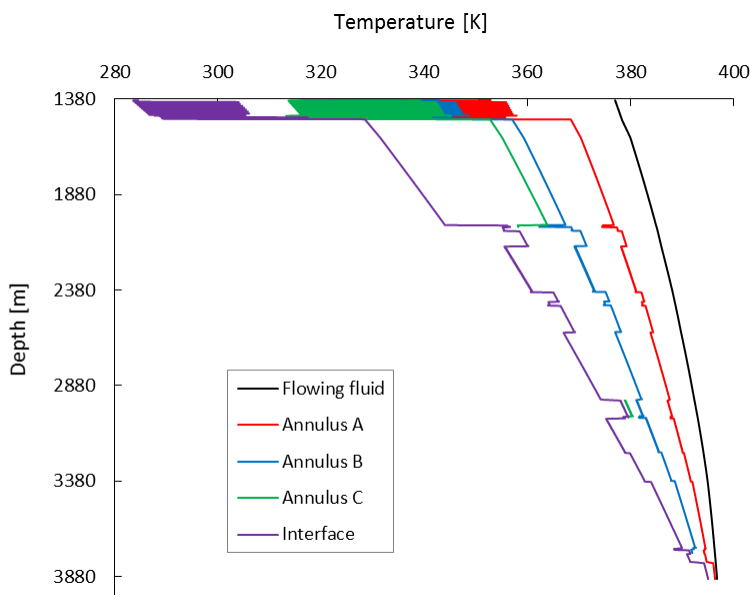


Figure 4.34 – Well A temperature profiles while using 10 VIT joints.

It can be seen in Figure 4.34 that the wellbore temperature profiles are highly affected by the use of the VIT joints, as expected. Since the VIT system shows different thermal resistances depending on the position considered in the analysis, a significant variation in the temperature profiles was observed in the annuli as well as in the wellbore/formation interface. Thus, the amplitudes of the temperature variations in the VIT region were of 47.2, 41.3, 39.3 and 33.5 K for annuli A, B and C and at the interface, respectively.

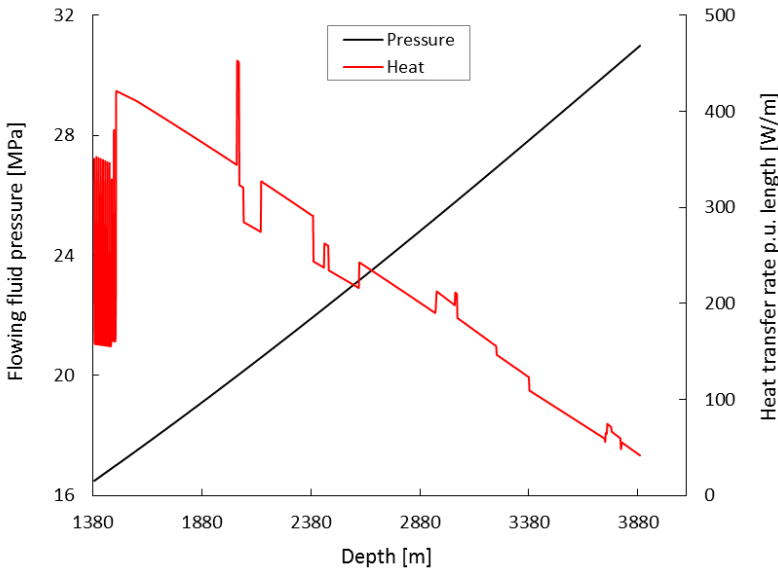


Figure 4.35 – Well A pressure and heat transfer profiles while using 10 VIT joints.

As observed in Figure 4.35, the pressure profile was not significantly influenced by the presence of the VIT joints - the flowing fluid wellhead pressure changed from 16.47 MPa for a bare pipe simulation against 16.49 MPa for the VIT assisted well. Also, as shown for the temperature profiles (Figure 4.34), the variations can also be seen in the plot of the heat transfer rate along the wellbore (see Figure 4.35). In the regions near the connection, the heat transfer rate, q' , reached values close to 379 W/m, while near the center of the VIT joints, this value was 156 W/m. Furthermore, it is clear the use VIT close to the wellhead significantly reduces the radial heat transfer.

A close-up view of the VIT performance shows the variation of q' and the radiation heat transfer coefficient of the evacuated cavity along the well (Figure 4.36). For the nodes close to the weld, where the temperature difference between the external surface of the inner tube and the internal surface of the outer tube is lower, the h_r was $7.2 \text{ W/m}^2\cdot\text{K}$, while near the center of the VIT, h_r was $6.0 \text{ W/m}^2\cdot\text{K}$.

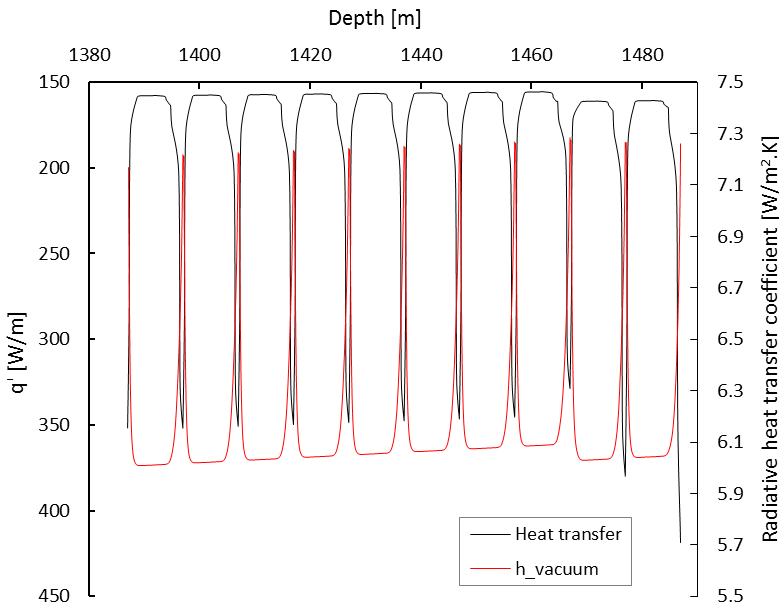


Figure 4.36 – Heat transfer behavior on the VIT joints.

It is important to realize that the heat transfer coefficients due to forced convection (in the tubing string) and natural convection (in the annular space) are affected by the presence of the VIT joints. The forced convection coefficient is more affected by the VIT geometry variation. On the other hand, the natural convection coefficients are affected by the change in insulation caused by VIT, which tends to reduce the temperatures of the surfaces in the annuli and, hence, their respective Rayleigh numbers. Figure 4.37 shows the variation in the heat transfer coefficients along the wellbore. It is possible to observe large variations in all heat transfer coefficients in the VIT assisted section of the well.

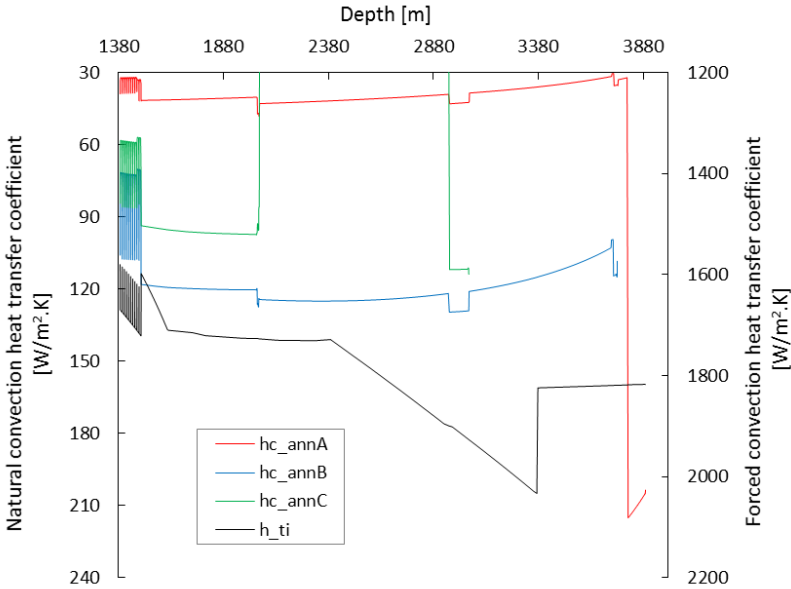


Figure 4.37 – Convection heat transfer coefficients behavior along the well A.

In order to observe the insulation capability of the VIT joints, both internal and external surfaces temperature profiles were plotted in Figure 4.38. Near the connections, the temperature difference is small (because of the small thermal resistance), and increases sharply away from the connection reaching a plateau 2.3 m and 1.6 m away from the center of the connection for the lower and upper VIT connection, respectively. Although, the VIT joint presents a symmetry plane in the z axis, the boundary conditions as well as the numerical error lead to a non-symmetrical thermal behavior offered by the insulated joints. Hence, for the center position, the average temperature difference reached the value of 50.9 K considering the 10 VIT joints.

It has been observed from previous results that the VIT is the element of the wellbore that affects the heat transport towards the rock formation the most. Its thermal performance is highly dependent on the emissivity of the tubes surfaces, which can be affected in a number of ways (Siegel and Howell, 1992). Thus, a sensitivity analysis of the emissivity was performed in order to evaluate its effect on the wellbore thermal behavior. Figure 4.39, Figure 4.40 and Figure 4.41 show the annulus A temperature profiles along the VIT joints considering 0.65, 0.75 and 0.85 emissivity for three production times of 0^+ , 1 and 10 days.

As expected, the three graphs (in Figure 4.39, Figure 4.40 and Figure 4.41) showed a similar behavior for the external VIT surface temperature profile (see Figure 4.38).

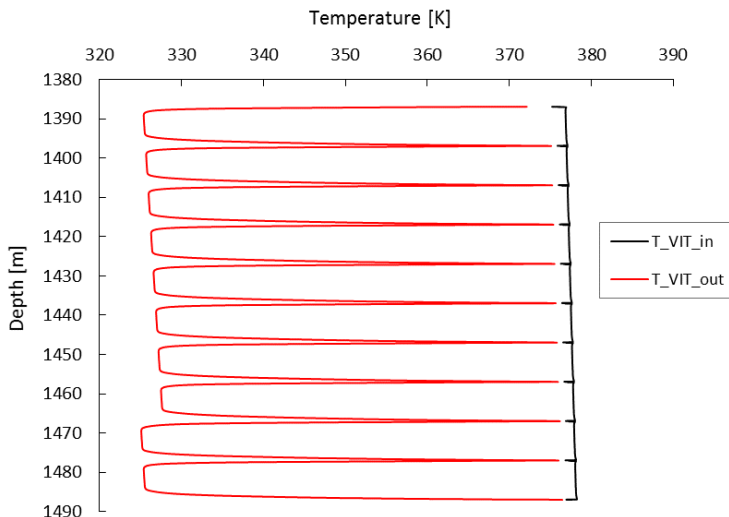


Figure 4.38 – VIT temperature profiles at the internal and external surfaces.

Close to the connections, the temperature profiles of the annular fluid are the same regardless of the surface emissivity. In addition, it can be seen that a large temperature difference between the 8th and the 9th joints occurred, which can be associated with the additional thermal resistance caused by the presence of the cement sheath of the 30" casing resulting in a temperature drop.

As the time increases, the wellbore thermal resistances diminish their importance in the heat transfer process. This is noticed by observing the smallest annular temperature drop between the 8th and the 9th VIT joint temperature profile in Figure 4.40 and Figure 4.41.

Table 4.10 shows the average temperature of the external surface of the VIT joints for the 9 cases evaluated. The results show that the difference between employing a low or a more conservative value of emissivity for the VIT were 1.9, 2.3 and 2.6 K for production time steps of 0+, 1 and 10 days, respectively. While these temperature changes are somewhat small, one should consider that an inaccuracy of this magnitude can represent a considerable uncertainty in the decision-making process regarding the use of VIT tubes.

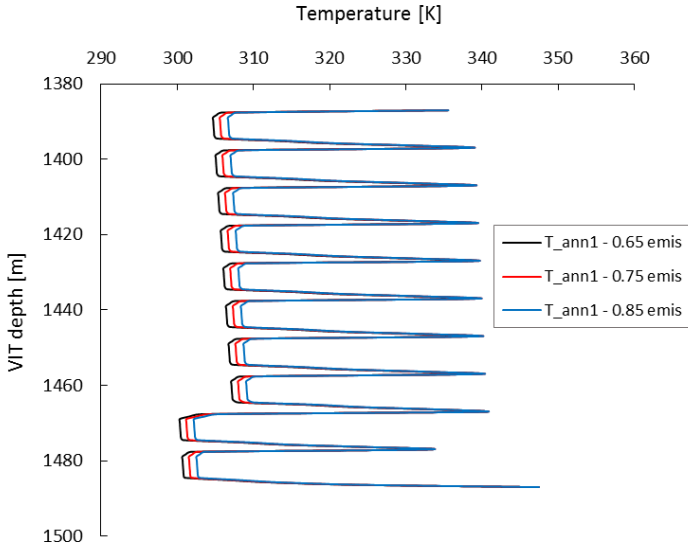


Figure 4.39 – Annulus A temperature calculated assuming three different values of VIT cavity surface emissivity for a 0⁺-day production time.

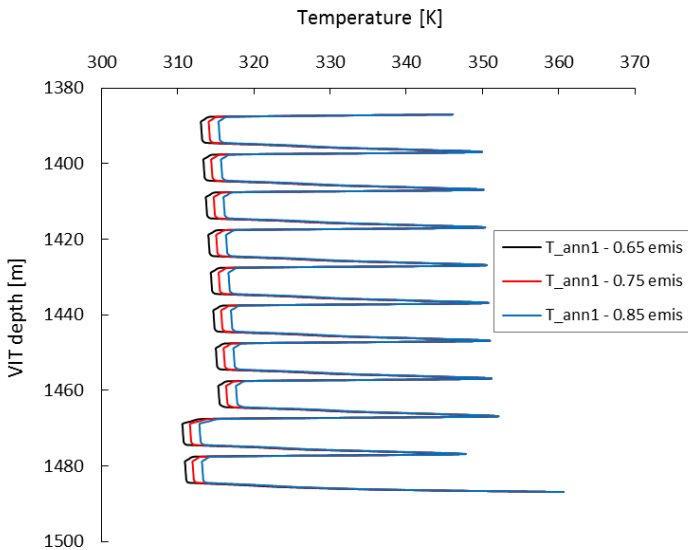


Figure 4.40 – Annulus A temperature calculated assuming three different values of VIT cavity surface emissivity for a 1-day production time.

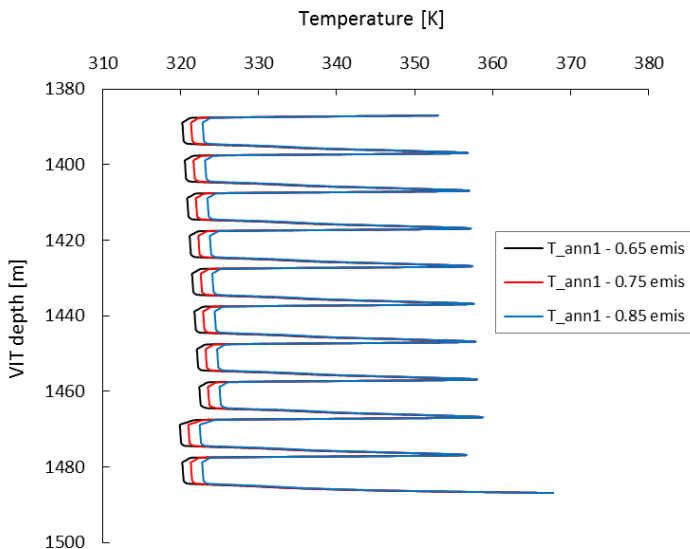


Figure 4.41 – Annulus A temperature calculated assuming three different values of VIT cavity surface emissivity for a 10-day production time.

Table 4.10 – Average simulated annulus A temperature at the center position of the VIT joint for different production time steps.

Emissivity	Annulus A average temperature [K] at various production times		
	0 ⁺ d	1 d	10 d
0.65	305.7	313.9	321.1
0.75	306.5	314.9	322.2
0.85	307.6	316.2	323.7

4.3.2 Comparison of the integrated model with the commercial software

The first attempt to validate the coupled model has been carried out by comparing the results from simulations performed with the proposed model and the commercial software WellCat™. To this end, well A was modeled with 60 VIT joints considering the same

simulation/operational parameters previously described in section 4.1.2. The choice for this number of VIT joints is justified by the extension of annulus B, where high heat transfer rates can be found.

Figure 4.42 to Figure 4.47 show the fluid temperatures for well A using the present model (Figure 4.42 and Figure 4.43) and the commercial software (Figure 4.44, Figure 4.45, Figure 4.46 and Figure 4.47) for two different production times. Figure 4.44 and Figure 4.45 show the temperature profiles for a single k-value to characterize the VIT joints, i.e. 0.074 W/m.K. Figure 4.46 and Figure 4.47 show the results for simulations assuming 2 k-values: one for the connection section, which comprises 6% of the VIT length (i.e. the same as the carbon steel material, 16 W/m.K), and another for the remaining length of the VIT (0.074 W/m.K), a methodology also considered in Barcelos *et al.* (2017).

It is important to mention that the value of 0.074 W/m.K is the same used by Ferreira *et al.* (2012) in well B, as recommended by the VIT supplier as the design k-value for VIT joints to be installed in well B. Therefore, for the simulations employing the commercial software for well A, the use of this k-value is only an approximation since there are no guidelines for the k-value for well A.

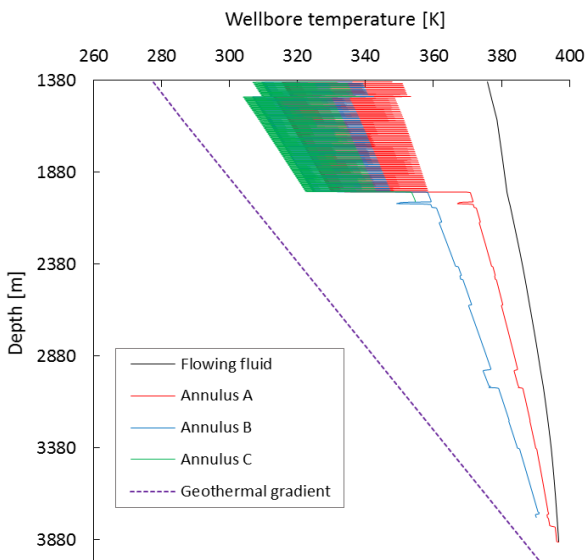


Figure 4.42 – Wellbore fluid temperature profiles for a simulation at 1-day production time using the present model.

The large temperature variations predicted by the present model (which considers the two-dimensional nature of the heat transfer process in the VIT joints) caused the curves to overlap, as can be seen in Figure 4.42 and Figure 4.43. The same overlapping is observed in Figure 4.46 and Figure 4.47, however, here, they are caused by the two different k -values used to represent the VIT's thermal performance.

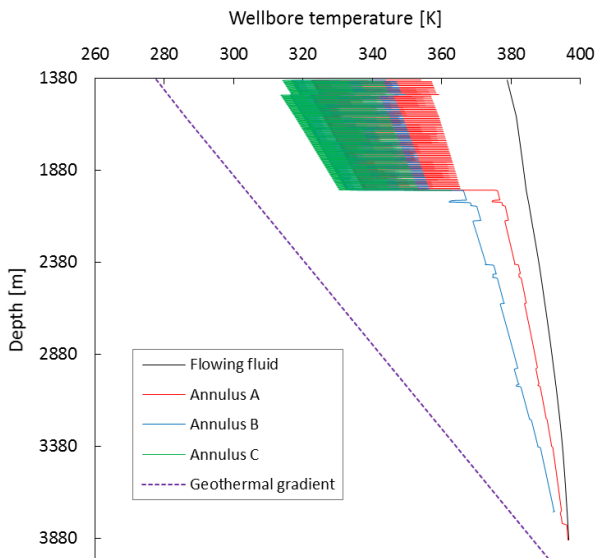


Figure 4.43 – Wellbore fluid temperature profiles for a simulation at 10-day production time using the present model.

The use of a single k -value (Figure 4.44 and Figure 4.45) yielded a dramatic temperature drop in all annuli, suggesting that this approach is questionable, which somehow explains the use of artificially high k -values to compensate for the high annular temperature drop. Differently, the use of two k -values reduced the average temperatures in annuli, however, a large temperature difference of up to 68 K close to the wellhead still remained at specific locations (with respect to annulus A for simulation at 1-day production time). The model proposed in this work showed that, in addition to the temperature differences being much smaller than those given by the two k -values approach, the temperature range is also lower. For example, the temperature difference close to the wellhead is about 31 K with respect to annulus A for the simulation at 1-day production time.

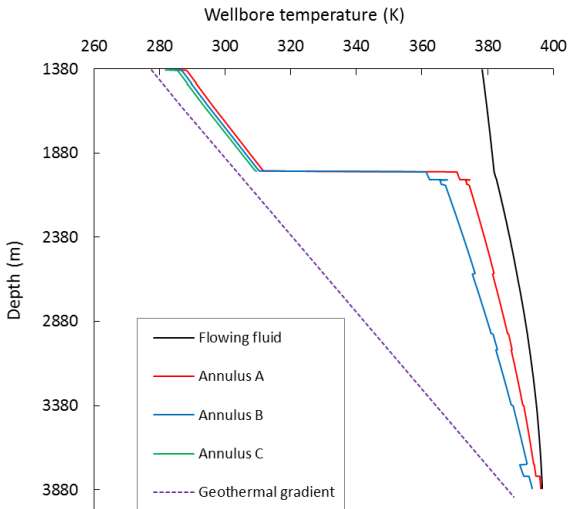


Figure 4.44 – Wellbore fluid temperature profiles for a simulation at 1-day production time with the commercial software using a single k-value for the VIT joints.

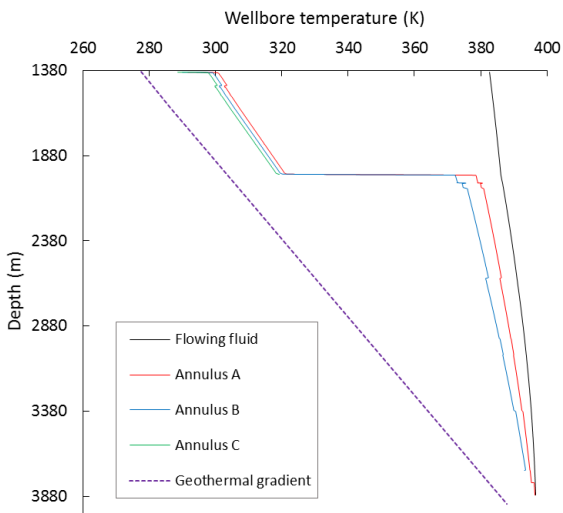


Figure 4.45 – Wellbore fluid temperature profiles for a simulation at 10-day production time with the commercial software using a single k-value for the VIT joints.

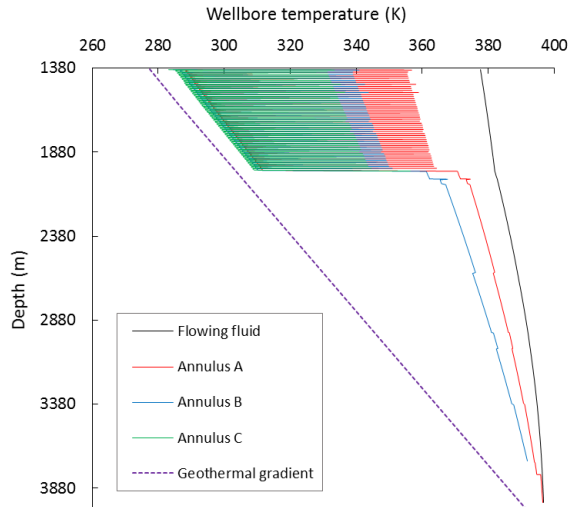


Figure 4.46 – Wellbore fluid temperature profiles for a simulation at 1-day production time with the commercial software using two k-values (one for the connection and another for the VIT body) for the VIT joints.

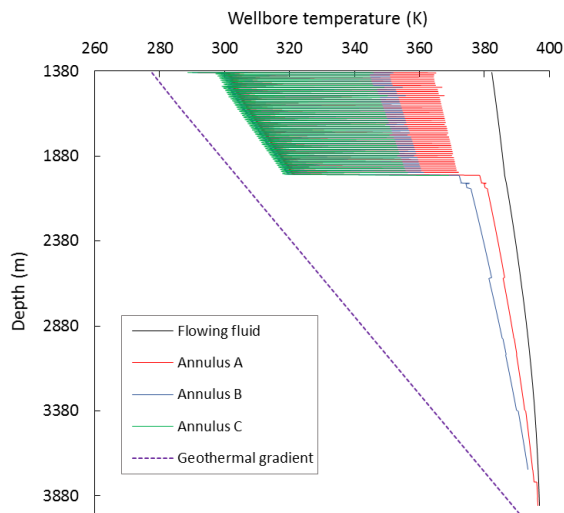


Figure 4.47 – Wellbore fluid temperature profiles for a simulation at 10-day production time with the commercial software using two k-values (one for the connection and another for the VIT body) for the VIT joints.

Table 4.11 shows the average temperature computed for all annuli in each simulation performed at the production time steps of 1 and 10 days.

Table 4.11 – Summary of annuli average temperatures for simulations using the present model and the commercial software (WellCat) for annuli A, B and C.

Production time	Annulus average temperature [K]					
	1-day			10-day		
Model	A	B	C	A	B	C
Present model	371.0	361.7	321.6	375.1	367.9	330.8
Wellcat (2 k-values)	367.6	359.8	306.0	373.0	366.9	318.6
Wellcat (1 k-value)	366.3	358.6	303.6	371.3	365.7	314.5

As expected, the average temperature in each annulus increased as the production time increased. The present model showed the largest average temperatures for all simulations, which may be indicating that the k-value used here (which was designed to be used in well B) was overestimated. Furthermore, although not ideal, the use of 2 k-values as input parameters in the commercial software may be a good strategy to a better representation of the VIT system thermal resistance.

It is also important to realize that the different annuli have distinct temperature variations depending on the wellbore depth. For instance, while annulus A comprises whole simulation domain, annulus C comprises the range from 1,387 m (seabed) to the 13 3/8" casing TOC, which is located at 2,040 m of depth. Therefore, the average temperature of annulus C is much lower than that of annulus A, which is in direct contact with the higher temperatures in the wellbore.

The effect of the thermal insulation provided by the VIT system on the pressure increase was also investigated. Figure 4.49 and Figure 4.49 show the annuli pressure profiles for simulations performed at 1 and 10-day production times, respectively, using the three thermal approaches.

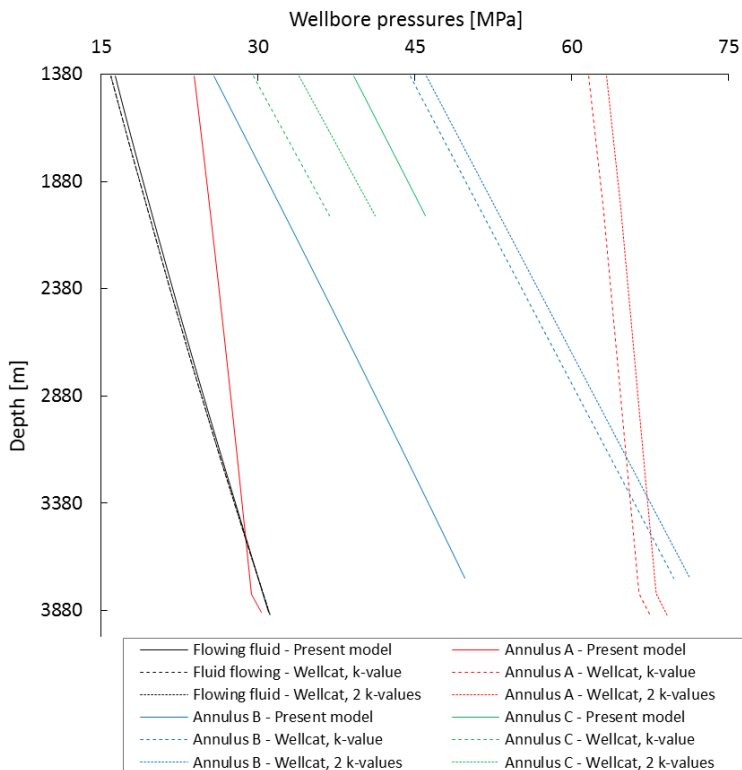


Figure 4.48 – Pressure profiles in each annuli for a 1-day production time using the three approaches.

The flowing fluid pressure profiles predicted by the three calculation methods agreed well. However, the pressure profiles for annuli A and B showed higher values for the commercial software simulations. Here two points deserve attention with regard to the large difference in the value of APB calculated from the different approaches: (i) as abovementioned, the commercial code does not handle compressible fluids, as the N_2 present in annulus A, properly, generating high pressures; (ii) the commercial software tends to generate conservative loads while VIT joints are employed, due to the uncertainties on the simplification of using the k-value concept. Regarding annulus C, the present model predicted a higher value for 1-day of production, while the pressure profiles for a 10-day production time were similar for all approaches. The reason for this may lie in the difference in how the approaches face the deformation of cemented

casings and deal with the fluid expansion behavior. It should be remembered that the average temperature in annulus C was much lower than in other annuli, which strongly influences the fluid expansion and, consequently, the increase in pressure.

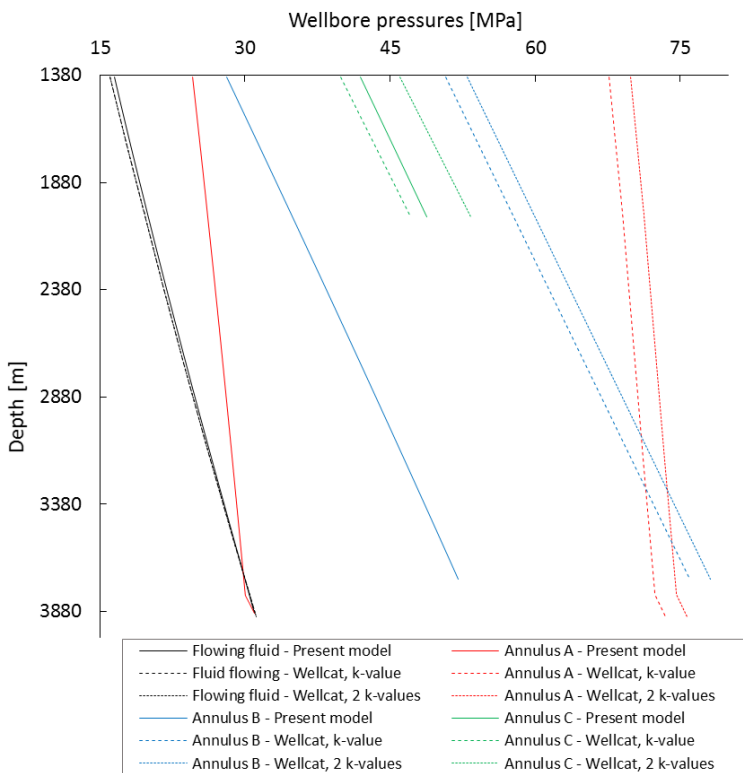


Figure 4.49 – Pressure profiles in each annuli for a 10-day production time using the three approaches.

The stress analysis also shows that when the commercial software is used (assuming a single or a combination of two k-values), a tube collapse is predicted due to an excessive pressure difference on the 6 5/8” tubing string. In the present model, however, all loads presented much lower values than the tubular mechanical resistances.

Figure 4.50 shows the annuli pressure profiles variation results from simulations performed for various production times.

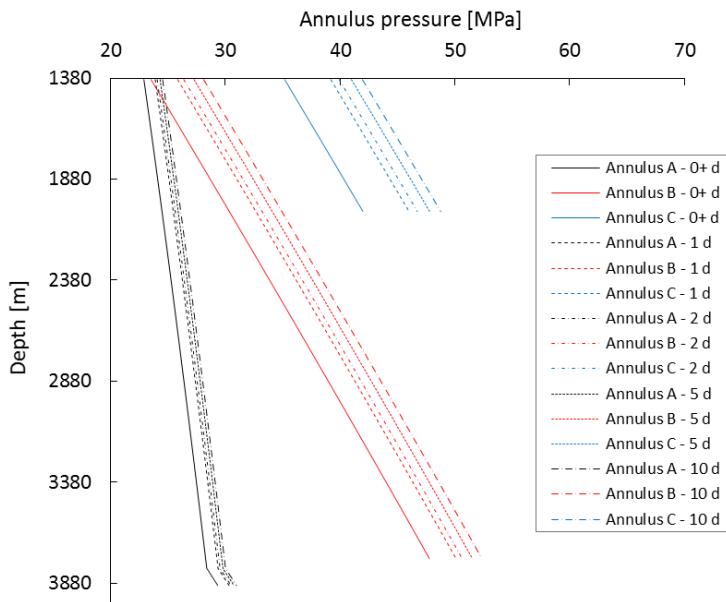


Figure 4.50 – Annuli pressure profiles as a function of the production time for simulations performed using the present model.

The pressure profile in Annulus C is more affected by the production time, which indicates that the deformation of tubulars has a significant effect on the pressure increase. This is because the VIT joints covered almost the entire depth range of annulus C, thus reducing the heat transfer toward the annuli.

Table 4.12 summarizes the APB loads for each simulation performed with the present model.

Table 4.12 – Summary of the APB variation as a function of the production time for all annuli

Annulus	APB [MPa] and APB_T [MPa] at various production times				
	0^+ d	1 d	2 d	5 d	10 d
A	0.84	1.82	1.99	2.25	2.47
	(0.83)	(1.74)	(1.90)	(2.13)	(2.34)
B	9.58	11.90	12.43	13.32	14.16
	(3.14)	(15.82)	(17.81)	(20.83)	(23.36)

C	21.22	25.24	25.97	27.04	28.00
	(43.77)	(43.08)	(43.08)	(43.10)	(43.16)

The results shown in Table 4.12 reinforce the hypothesis that annulus C is less affected by the annular space heating process along the time. Even though the APB load due to fluid expansion caused by the heating was the highest among all annuli, the increase in pressure was basically time independent, while the total APB varied significantly due to tubular deformation.

Figure 4.51, Figure 4.52 and Figure 4.53 show the local deformation for the 6 $\frac{5}{8}$ " tubing, 10 $\frac{3}{4}$ " and 13 $\frac{3}{8}$ " casings relative to the external diameter considering 0⁺, 1 and 10 days of production time.

In essence, the local values of tube deformation in the presence of VIT joints were negative, indicating that all tubes experienced a reduction in the external diameter throughout the wellbore. As mentioned above, annulus C experienced the largest diameter variation, but still lies within a comfortable zone with respect to the elastic limit of the material.

Furthermore, since the tube strain is computed locally, as is the heat transfer rate, for the VIT range depth, the strain varies significantly following the heat transfer behavior.

It is important to notice that all tubes experienced a reduction in the external diameter for very short production times. For a 1-day production, the values of strain experienced by the 6 $\frac{5}{8}$ " tubing and 10 $\frac{3}{4}$ " casing along the VIT range depth were quite the same as presented in Figure 4.52. Furthermore, since the current mechanical model neglected the fact that an evacuated gap separates the inner and the outer tubes forming the VIT, the strain behavior of the 6 $\frac{5}{8}$ " tubing requires attention. This is because, for a bare tube, there is always a backpressure that contributes to the pressure in each annulus at each iteration loop. For the case of using VIT joints, the backpressure does not exist.

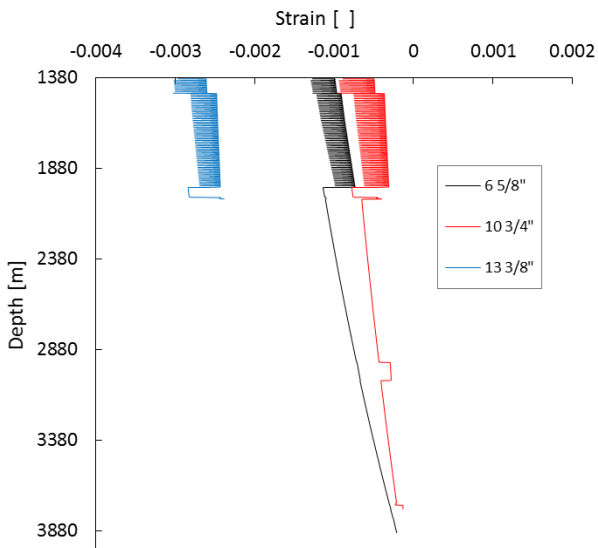


Figure 4.51 – Deformation of the tubes for 0^+ -day production time. Simulation using VIT joints.

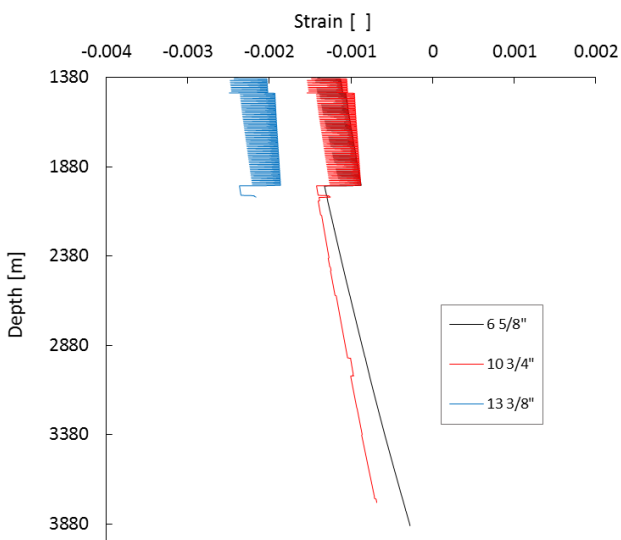


Figure 4.52 – Deformation of the tubes for a 1-day production time. Simulation using VIT joints.

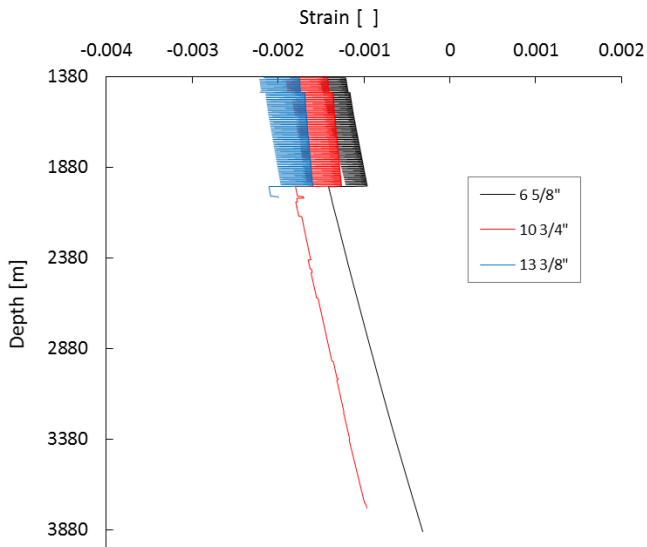


Figure 4.53 – Deformation of the tubes for a 10-day production time. Simulation using VIT joints.

Table 4.13 shows the volume variation for the simulations performed using the present model for various production times.

Table 4.13 – Summary of the annulus volume variation as a function of the production time

Annulus	Annulus volume [m ³] and volume variation [%] for various production times				
	0 ⁺ d	1 d	2 d	5 d	10 d
A	63.61	63.47	63.45	63.42	63.39
	-0.01	-0.15	-0.18	-0.21	-0.23
B	44.07	44.36	44.41	44.48	44.53
	-0.17	0.12	0.16	0.23	0.29
C	53.59	53.30	53.29	53.27	53.26
	0.59	0.50	0.49	0.47	0.45

According to Table 4.13, annulus C showed a large volume change for a very short transient production time, while annulus B presented a negative volume variation. Then, as the time increases, the

volume variation in annulus B significantly increased while a reverse effect occurred in annulus C. The volume in annulus A always experienced a contraction as time increased. Considering the volume variation in the annuli, the deformation of the tubes and the APB results, the following remarks can be made:

- the annulus C fluid expansion was significant for a very short production time, i.e., when the wellbore is still thermally unaffected and subjected to high heat transfer rates. Thus, the insulation provided by the VIT system dramatically reduced the heat transfer. As a result, the APB contribution due to fluid expansion remained almost unchanged. However, the overall APB increased due to a reduction in the annulus volume resulting from a significant deformation of the 13 $\frac{3}{8}$ " casing, while the 20" casing internal diameter remained constant because of the mechanical support provided by the cement.
- with respect to annulus B, initially, the volume reduction was caused by the 13 $\frac{3}{8}$ " casing, which, due to the inexpressive annulus B fluid expansion and the substantial load produced by the annulus C fluid expansion against annulus B, suffered a diameter reduction. Then, the annulus B experienced a significant increase in pressure due to fluid expansion, while in annuli A and C the fluids did not experience a large variation as a function of time.

Finally, the effect of using VIT systems on the APB was assessed by performing simulations for well A with and without the insulated tubes at production times of 0⁺, 1 and 10 days, as can be seen in Figure 4.54, Figure 4.55 and Figure 4.56.

The use of VIT joints has a direct effect on the heat transfer and the reduction of the pressure increase in the annuli. In terms of the reduction in the global APB value, Table 4.14 summarizes the APB expected for the three annuli at three different production time steps (0⁺, 1 and 10-day production times) for the cases of a wellbore with and without VIT.

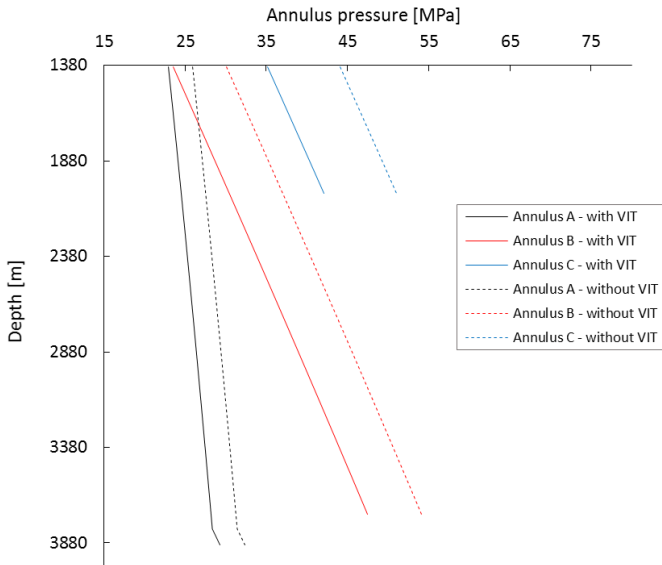


Figure 4.54 – Influence of VIT joints on the pressure profiles of each annulus for a 0⁺-day production time.

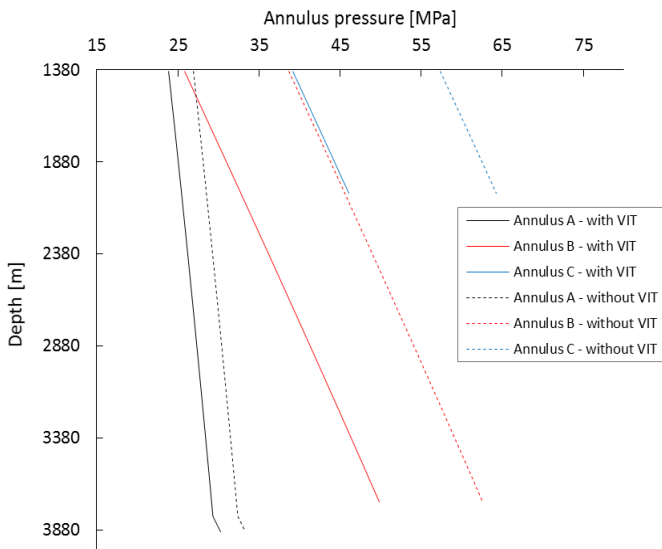


Figure 4.55 – Influence of VIT joints on the pressure profiles of each annulus for a 1-day production time.

As expected, using VIT joints led to a drop in the pressure increase throughout the wellbore. Annulus C was the most affected by the VITs, since it was almost fully assisted by them, while annulus B and C had only the upper part covered by the VIT joints. Annulus A was the least affected since it was filled with N_2 , which provides a relief on the increase in pressure due to its high compressibility.

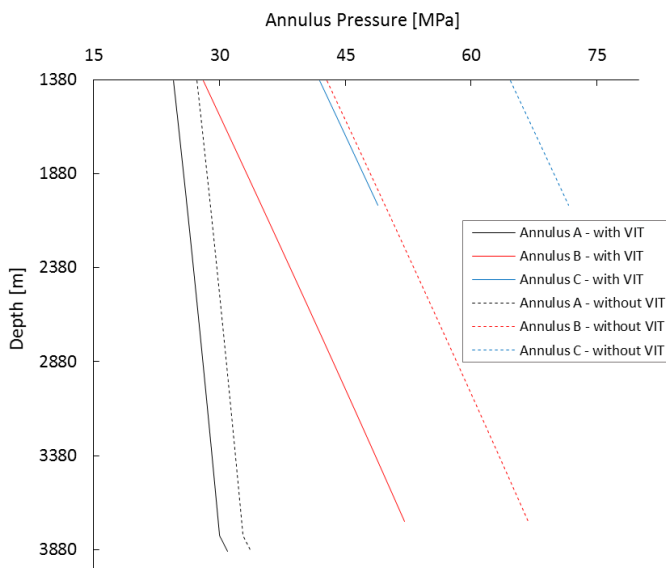


Figure 4.56 – Influence of VIT joints on the pressure profiles of each annulus for a 10-day production time.

Table 4.14 – Summary of the APB in all annuli for simulations performed for 0^+ , 1 and 10-day production times

Time [d]	String type	APB in annulus [MPa]		
		A	B	C
0^+	Without VIT	3.86	16.18	30.17
	With VIT	0.84	9.58	21.22
	% reduction	-78.2	-40.8	-29.7
1	Without VIT	4.86	24.70	43.40
	With VIT	1.82	11.90	25.24
	% reduction	-62.6	-51.8	-41.8

10	Without VIT	5.30	28.85	50.76
	With VIT	2.47	14.16	28.09
	% reduction	-53.4	-50.9	-44.7

Even though annulus A experienced the larger APB percentage reduction considering the simulations performed with and without VIT joints, in absolute pressure terms, annuli B and C showed higher APB drops – 22.67 MPa for annulus C after 10 days of production. This is because annulus A is filled with N₂ that works well in sustaining pressure due to its high compressibility.

4.4 Evaluation of the Integrated Model using a Real VIT Assisted Well

In this section, the integrated model results are compared with field data and with the Wellcat™ software for simulations of well B, which is assisted by 108 VIT joints. As mentioned before, according to the commercial supplier of the VIT joints used in this well, the single k-value used in Wellcat™ was 0.074 W/m.K.

4.4.1 Validation of the Integrated Model

Figure 4.57 shows a complete set of flowing fluid pressure and temperature data available for well B while oil and gas are produced in steady-state (kick off data are not available for this well). The sampling frequency of the PDG and wellhead pressure and temperature data was approximately 1 data point per hour. Using the PDG pressure and temperature as an input, the calculated wellhead pressure and temperature at 0⁺ and 10-day production times agreed well with the field data. At this point, it is important to realize that despite the fact that short production time simulations were performed (i.e. 0⁺-day production time), the results were used just as an illustration for comparison purposes.

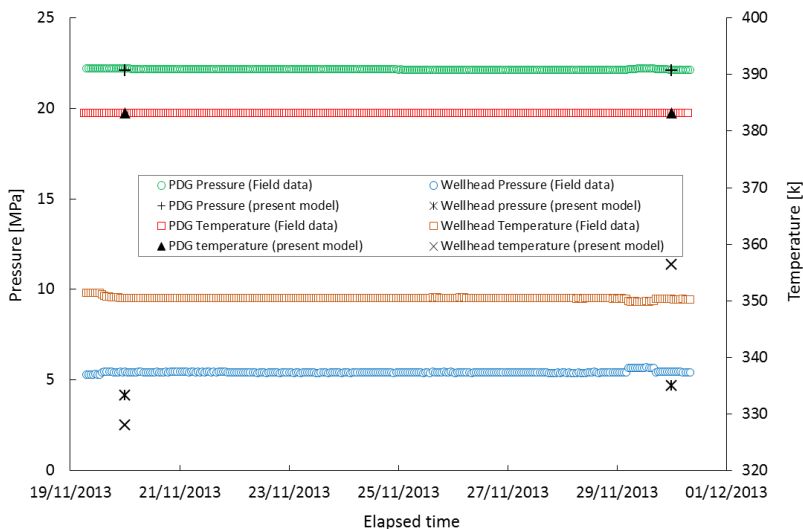


Figure 4.57 – Field data and simulation results for the well B.

The simulated thermal and pressure profiles along the wellbore and the field data obtained for the two end points of the tubing string (*i.e.* at the wellhead and PDG depths) for the flowing fluid showed a good agreement. For a production time of 0^+ day (very short transient), the hydrocarbon pressure and temperature at the wellhead were 4.13 MPa and 328.0 K, respectively. At steady state, the simulated hydrocarbon stream pressure and temperature at the wellhead were 4.67 MPa and 356.4 K, respectively. The present model showed deviations of 0.74 MPa (13.7 %) and 6.1 K at the wellhead depth. It is noteworthy that for well B the uncertainties regarding the input parameters and the boundary conditions were larger than those for well A. Figure 4.58 shows a set of the flowing fluid and production annulus pressure data available for the well B during the steady state production.

As observed, the calculated annulus wellhead pressure for a 10-day production time (steady state) showed a considerable deviation with respect to the field data. According to the present model, the pressure in annulus A was 26.58 MPa after 10 days of production, while the measured pressure was 16.52 MPa. The deviation of about 37.9 % can be explained by the following: (i) the mechanical model considers the VIT joint as a single tube, that is, it totally neglects the deformation of the outer tube over the vacuum gap, instead, considers that the outer tube deforms against the flowing production fluid, resulting in lower

pressures and (ii) the uncertainties associated with the many input parameters and also boundary conditions, such as the geothermal gradient.

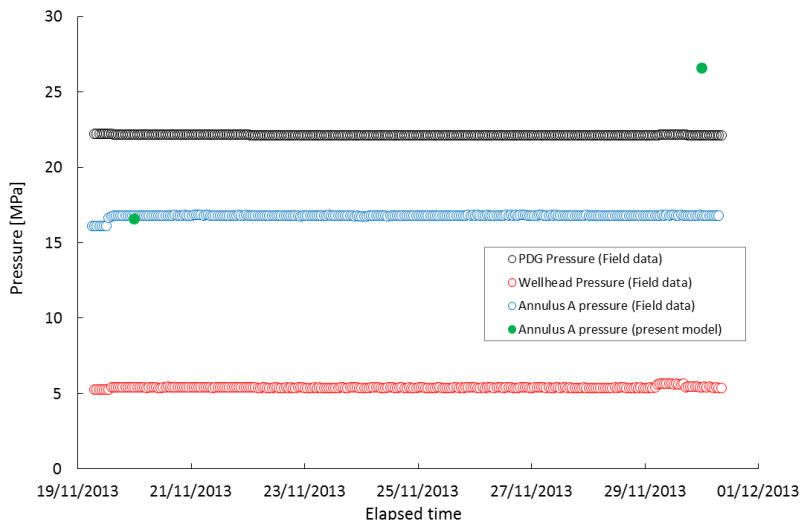


Figure 4.58 – Pressure data set for well B along the production time.

In order to compare the results generated by the present model and by the commercial software, Figure 4.59 shows the hydrocarbon stream pressure and temperature profiles for production times of 0^+ and 10 days (present model) and 12 h, 1 day and 10 days (commercial software). Due to the high computational cost associated with the present model, only simulations for 0^+ and 10-day production times were considered in this study.

As expected, the temperature profile for the 0^+ -day production time is quite different from the other simulated times. Thus, for very short times the temperature profile is affected only by the wellbore thermal resistances and the absolute temperatures along the wellbore are supposed to be much lower than the temperatures computed for longer times. The agreement between the present model and WellCat is very good given the different time steps regarding the transient simulations. For steady-state production (10-day production time), the thermal results agree reasonably well, showing deviations of the order of 6.5 K at the wellhead position. It is important to realize that this temperature difference is around 4.5 K at the bottom of the VIT column, which

means that in nearly 1,100 m of VIT joints the deviation between the models was around 2 K.

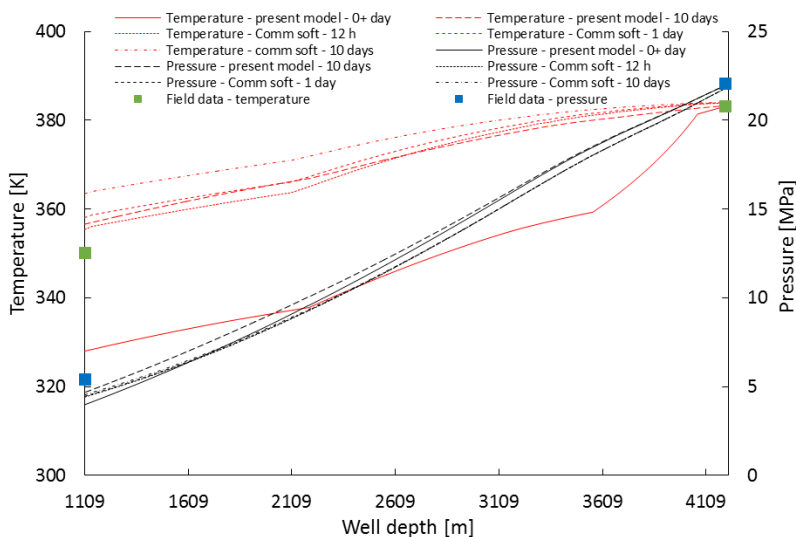


Figure 4.59 – Temperature and pressure profiles for the hydrocarbon stream for simulations performed with the present model and using the commercial software for well B.

The calculated pressure profiles are also consistent for this deviated well, although different multiphase flow models have been used, i.e., Beggs and Brill (1973) in the present model and Hagedorn and Brown (1965) in the commercial software. Deviations of the order of 0.13 MPa (2.7%) were obtained at steady state, revealing a very good agreement between the thermal-hydraulic models.

Table 4.15 summarizes the average temperatures in annuli A, B and C for a 10-day production time using the present model and the commercial software with one and two k-values.

Table 4.15 – Summary of the average temperatures in the annuli for simulations at 10-day production time using the present model and the commercial software (WellCat)

Model	Annulus average temperature [K]		
	A	B	C
Present model	359.6	355.2	320.3
Wellcat	365.8	356.2	312.3

(2 k-values) Wellcat (single k-value)	363.2	355.4	307.9
---	-------	-------	-------

Different from the results for well A, the average temperature in annuli A and B calculated by the present model showed the lowest values among the three simulations performed. Moreover, as expected, the 2 k-values simulation showed results closer to the present model. One should remember that, in this particular well, a single k-value of 0.074 W/m.K was calibrated by the supplier of the VIT joints. This appears to be a conservative k-value, as it leads to higher average temperature in annuli A and B. Also, the large difference between the average temperatures in annuli A and B calculated by the commercial software may be questionable since these annuli have almost the same length. Conversely, the average temperature in annulus C predicted by the present model was the largest among the three approaches. This is due to the short length of annulus C, which is more influenced by the heat transfer in the region close to the seabed.

In terms of the annuli pressure response, Figure 4.64 shows the pressure profiles for simulations performed for a 10-day production time using the present model and the commercial software, respectively. For the latter, a single k-value of 0.074 W/m.K and two k-values of 16 W/m.K for the connection section (6% of the VIT length) and 0.074 W/m.K for the VIT evacuated body section have been used.

A comparison between the models shows that the pressure loads calculated by the commercial code for annuli A and B are much larger than those quantified by the present model. Even though the only field data available are for annulus A, they reveal that, although the agreement of the present model is far from outstanding, it is much better than the commercial software. As expected, the approach using two k-values resulted in pressure loads higher than those with the single k-value. In annulus C, the pressure profiles followed the average annulus C temperature results shown in Table 4.15.

The stress analysis applied to well B during hydrocarbon production indicated that all predicted loads were within the mechanical limits of the tubes. However, caution must be exercised when examining the high load difference between the present model and the commercial code.

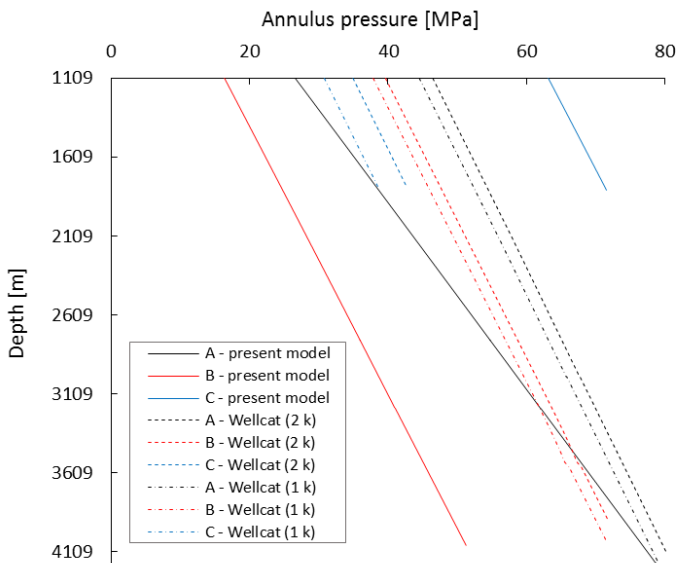


Figure 4.60 – Pressure profiles in the three annuli of well B for simulations for 10-day production time.

4.4.2 Thermal-structural study of well B

Initially, the well thermal-hydraulic behavior is illustrated in Figure 4.61, which shows the heat transfer rate per unit length and the superficial velocities of the liquid and gas hydrocarbons.

As can be seen in Figure 4.61, the marked changes in liquid superficial velocity are caused by changes in tubing string diameter at the depths of 2,171, 3,500 and 4,000 m. With respect to the gas superficial velocity, the blue curve shows that up to a depth of 3,196 m, the flow was single-phase liquid. From there, a two-phase hydrocarbon mixture was formed and, at the bottom of the VIT string, the gas velocity increased considerably due to: (i) the reduction of the tubing string diameter that increased the pressure gradient, and (ii) the fact that the tubing string became hotter with the use of the VIT system. The pressure gradient is a function of the three contributions: frictional, gravitational and accelerational. In the present system, the accelerational contribution is mainly a localized effect related to the tubing diameter change. The frictional is strongly influenced by the hydrocarbon mixture

vapor content, so it becomes less important as the depth increases. The gravitational contribution also depends on the vapor content, but is also influenced by the well inclination. It can be observed that the pressure gradient decreased up to depth of around 3,100 m. Close to this depth two events take place: the beginning of the hydrocarbon mixture vaporization and the wellbore verticalization, i.e., the KOP is at 3,013 m. Hence, more gas into the tubing and higher gravitational pressure gradient contributes to the faster decrease of the absolute pressure of the flowing fluid.

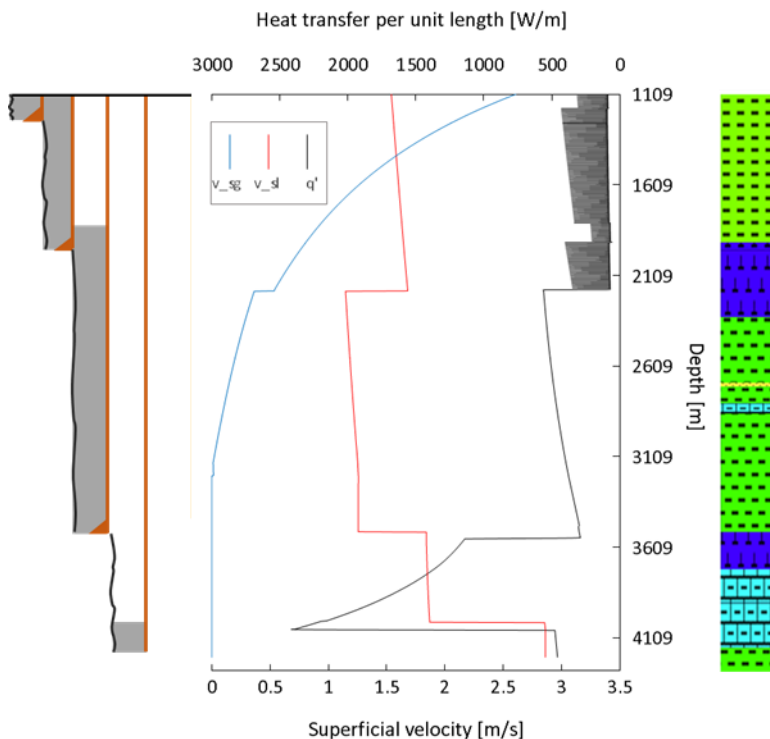


Figure 4.61 – Heat exchange and hydrocarbon liquid and gas superficial velocities for a simulation at 0⁺-day production.

On the other hand, larger variations in the heat transfer rate are due to the presence of the TOC and casing seat, that is, the interface between the annulus fluid and the cement in an annulus. Likewise, as previously observed, the use of VIT joints yields a large variation (range

from 2,171 m depth to the wellhead) in the heat transfer rate due to the large difference between the thermal resistances of the VIT evacuated body and the connection region. Figure 4.62 shows the order of magnitude of the various components arranged in the wellbore.

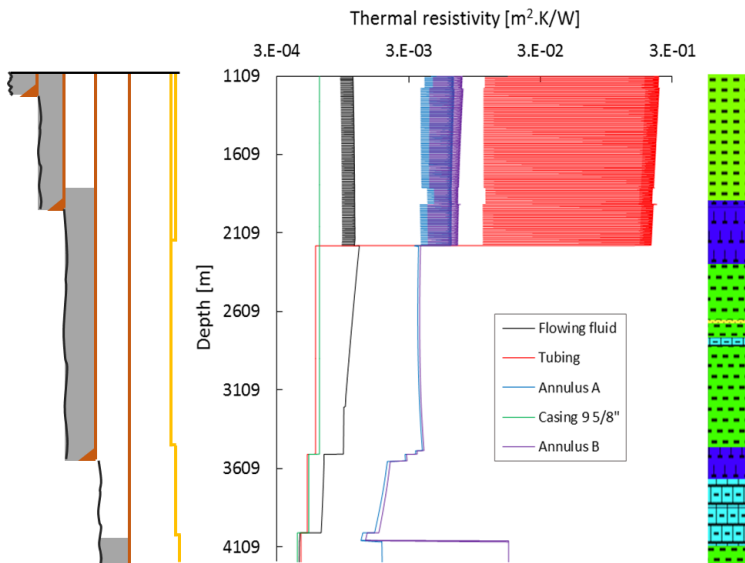


Figure 4.62 – Thermal resistivity profiles of the wellbore components for a simulation at 0^+ -production time.

Firstly, the difference between the values of fluid and solid thermal resistivity deserve some attention. As described in Chapter 3, while for a single tube the thermal resistivity is a function only of the geometry and thermal conductivity, for the annulus and flowing fluids it depends on the heat transfer coefficient, which can depend on the local temperature (i.e. tubing outer surface and casing inner surface temperatures in the case of the annulus fluid).

A qualitative assessment of the components of the overall thermal conductance reveals that the natural convection thermal resistivity and the thermal resistivity associated with the forced convection of the flowing fluid differ by one order of magnitude, since the heat transfer coefficient of the flowing fluid is much higher than that of fluids in the annuli. The scales of the thermal resistivity in annuli A and B are equivalent, even though annulus A contains a water based fluid and annulus B a synthetic fluid. It should be noted that annuli B and C are

filled with the same base fluid. The thermal resistivity of the tubes is virtually constant up to the VIT bottom. From there, the thermal resistivity dramatically increases by about two orders of magnitude, changing from 0.0115 to $0.2400 \text{ m}^2 \cdot \text{K}/\text{W}$.

Figure 4.63 and Figure 4.64 show the wellbore temperature profiles for 0^+ and 10-day production times, respectively.

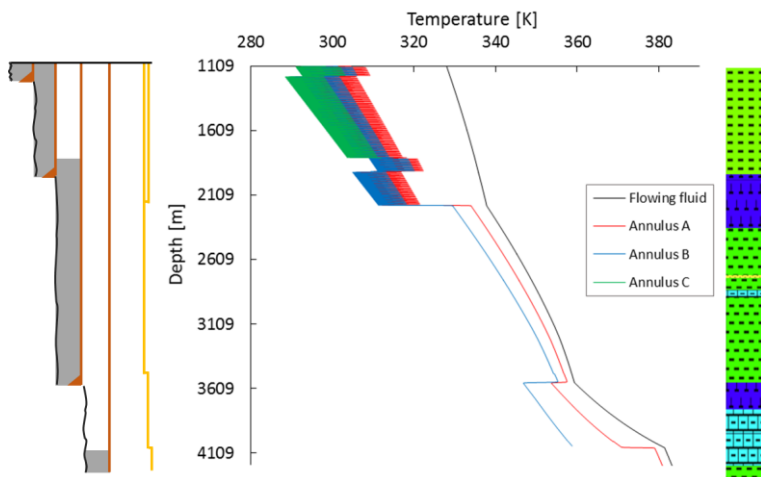


Figure 4.63 – Wellbore fluid temperature profiles for a 0^+ -day production time.

For very short production times, as previously reported, the effect of the wellbore components on the temperature profiles become more evident, i.e., the annulus fluid/cement transitions at 1,802 and 4,050 m deep, the casing seats at 1,909 and 3,543 m deep and the VIT joints bottom at 2,171 m. Figure 4.63 clearly shows that the effect of the VIT joints is much stronger than that offered by the cement sheaths in terms of temperature drop along the wellbore.

As previously discussed, the heat transfer in the wellbore is not affected by thermal resistances other than those in the wellbore until the 0^+ time is reached. Henceforth, in the case of using VIT joints, both the wellbore and the formation play an important role in the heat transfer process, since the VIT thermal resistance is larger than that offered by formation.

After 10 days of production the wellbore thermal behavior changes greatly showing the relevance of the VIT presence. Basically, other wellbore components and the different formation layers have less influence on the wellbore temperature profiles.

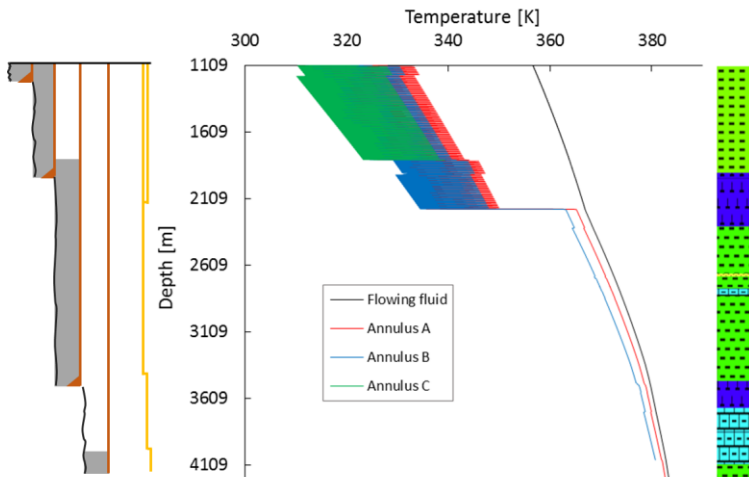


Figure 4.64 – Wellbore fluid temperature profiles for a 10-day production time.

Table 4.16 summarizes the APB for simulations performed for 0^+ and 10-day production times with the present model.

Even though the complete history of the pressure behavior over the production time is not shown, it can be seen from Table 4.16 that annulus C was more affected by both the fluid expansion and tube deformation. Also, while the fluid expansion contribution decreased over time, the overall APB increased revealing the strong contribution of tube deformation to APB for this case.

Table 4.16 – Summary of the APB for simulations for 0^+ and 10-day production times according to the present model

Annulus	APB [MPa] and APB _T [MPa] (in brackets)	
	0^+ d	10 d
A	5.67	15.67
	(5.85)	(16.15)
B	3.55	5.56
	(9.35)	(16.43)
C	17.49	22.62
	(41.16)	(39.02)

Figure 4.65 and Figure 4.66 show the local deformation profile for the 6 $\frac{3}{8}$ " tubing, 10 $\frac{3}{4}$ " and 13 $\frac{3}{8}$ " casings relative to the external diameter considering 0^+ and 10 days of production time.

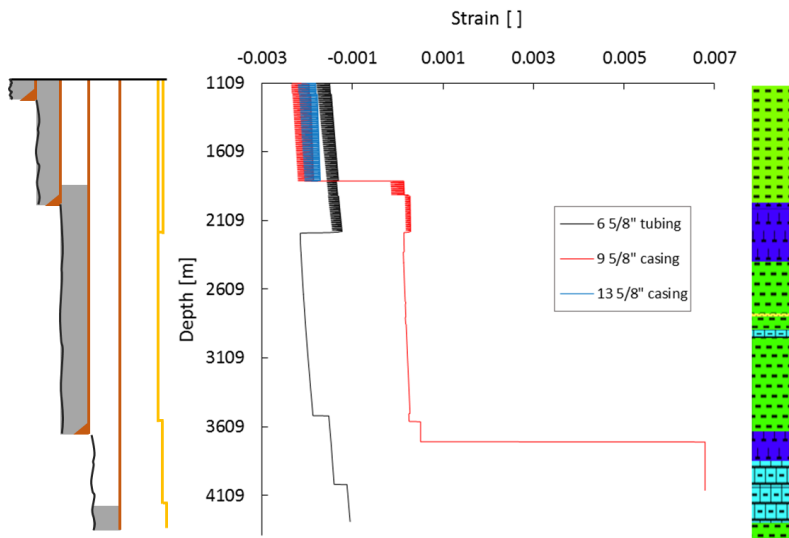


Figure 4.65 – Tube deformations for a 0^+ -day production time for well B.

Firstly, it is important to realize that the $6 \frac{5}{8}$ " tubing (i.e. the tubing is formed by a combined pipe diameters, that is, $6 \frac{5}{8}$ ", $5 \frac{1}{2}$ " and $4 \frac{1}{2}$ "") yielded the discontinuities observed in the strain profile. Basically, the local deformation of the $6 \frac{5}{8}$ " tubing and the $13 \frac{3}{8}$ " casing were negative, indicating that these tubes experienced a reduction in the external diameter along the wellbore. Conversely, the $9 \frac{5}{8}$ " production casing experienced a small variation in the external diameter up to the $13 \frac{3}{8}$ " casing seat. From there, a large positive variation in the external diameter was observed, at a section facing the open hole. One should consider that unknown mechanical properties of the formation rock along uncemented sections may lead to an excessive deformation that, in turn, may cause an inaccurate pressure load prediction, as observed below the $13 \frac{3}{8}$ " casing seat. Furthermore, at open hole sections the heat transfer rate is large, once only low thermal resistances (i.e. annuli and tubes thermal resistances) are taken into account in the heat transfer calculation.

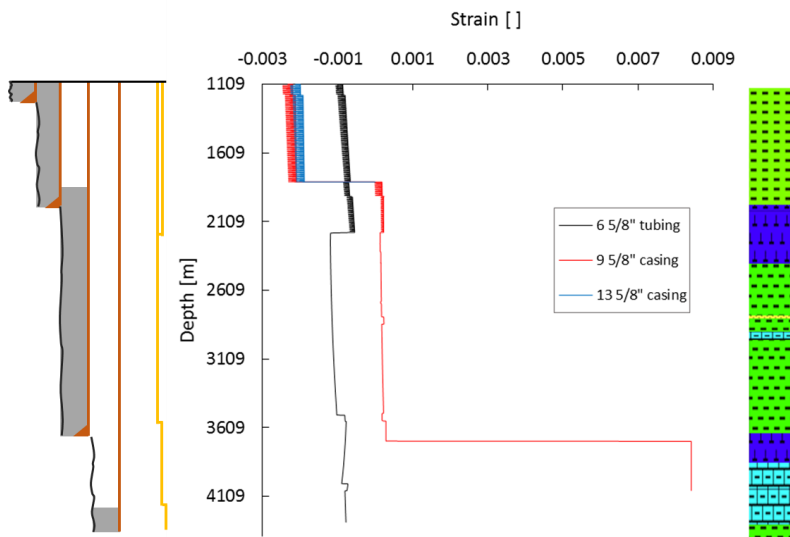


Figure 4.66 – Tube deformations for a 10-day production time for well B.

The main point of attention is the deformation experienced by the 9 5/8", as mentioned above. As time increased, the deformation also increased, leading to a pressurization of annulus A and C, as observed in Table 4.16.

Table 4.17 shows the volume variation for the simulations performed using the present model for 0⁺ and 10-day production times. Note that the initial volume of annulus A, B and C were 61.35, 89.06 and 61.94 m³, respectively.

Table 4.17 – Summary of the annulus volume variation as a function of the production time for well B

Annulus	Annulus volume [m ³] and volume variation [%] at 0 ⁺ and 10-day production times	
	0 ⁺ d	10 d
A	61.36	61.39
	0.01	0.04
B	89.44	89.91
	0.38	0.85
C	62.74	62.60
	0.80	0.67

Finally, it is possible to observe from Table 4.17 that annulus C behaved different from the other annuli, showing a volume reduction over time. This is because annulus C is supported by the cement behind the 20" casing. Thus, for well B, the wellbore mechanical configuration allowed the fluid in annulus B to expand, and the tubes forming annulus B forced annuli A and C, thereby increasing their absolute pressures.

5 CONCLUSIONS AND FUTURE RESEARCH NEEDS

The main challenges that motivated this thesis were the heat transfer behavior through VIT joints and the effect of the heat exchange between the wellbore and the formation on the wellbore integrity. The study was, hence, divided in two parts: the theoretical investigation of the heat transfer through stand-alone VIT joints, and the incorporation of the resulting thermal model (the 2-D ETN model) in a multi-physics wellbore simulator. Then, the effect of VIT joints in the wellbore completion was parametrically assessed and further validated using field data from two offshore wells. The numerical model was used to integrate the different physical models for several interconnected phenomena in the wellbore showing a good agreement with both field data and computational results from a third-party commercial software package (WellCatTM). Under those circumstances, the following two sections will report the main conclusions and recommendations of the present study.

5.1 Conclusions

Among the potential solutions to preserve wellbore integrity from pressure buildup in the concentric annuli, VIT systems appear as an alternative to reduce radial heat transfer from the well to the formation. Based on a detailed heat transfer analysis in VIT joints, this thesis developed a thermal model to calculate the temperature distribution along the tubing string. This thermal model was subsequently incorporated into a wellbore simulator.

Regarding the stand-alone VIT joint, the following conclusions can be drawn:

- The 3-D FVM results suggested a significant influence of axial heat conduction through the tubing walls at regions distant up to 1 m from the connection. Since these effects cannot be captured by 1-D radial heat transfer models, a 2-D ETN model was proposed as a low-computational cost alternative to a full 3-D analysis.
- The ETN model was validated with the FVM results and then parametrically assessed. The results showed that the length and the emissivity of the materials forming the annulus gap had major effect on the VIT insulation capability.

- A methodology was developed to allow the quantification of the VIT effective thermal conductivity, k_{ef} , and the VIT effective overall heat transfer coefficient, U_{ef} .
- Larger VIT tubing diameters (for instance the 6 5/8" x 5 1/2" system) do not mean better insulation since larger systems have narrower evacuated annulus gap, which directly influenced the heat transfer rate through the VIT.

With respect to the thermal-hydraulic model initially developed by Hafemann *et al.* (2015) and Barcelos *et al.* (2017), and further validated in this thesis, the main conclusions were:

- Two real offshore wells were used to validate the model. For well A, the model agreed well with both field data (i.e. deviations of 2.5% and 3.3 K for the pressure and temperature of the flowing fluid at the wellhead depth, respectively) and with the commercial code WellCat (i.e. deviations of 3.4% and 3.7 K, for the same condition) for 1-day production time. Regarding well B, the pressure and temperature deviations at the wellhead were 13.7 % and 6.1 K for the field data and 2.7 % and 6.5 K for the commercial software, for a 10-day production time. The results can be considered a very good agreement, given the uncertainties of the input data.
- A comprehensive investigation of well A was carried out to evaluate the influence of operating parameters, annulus fluid, formation types, as well as the available approaches to handle the annulus convection and the transient heat conduction in the formation on the wellbore heat transfer. It has been shown that:
 - The production time is of key importance to any wellbore thermal analysis, as the wellbore thermal resistances play an important role in the heat transmission during the early production stage. Therefore, the use of a modeling framework capable of handling all time scales experienced by the well during production seems like a more reliable approach to simulate the thermal diffusion from the wellbore to the formation;
 - The larger thermal resistances in the wellbore (cement sheaths and annulus fluid) are still smaller than the formation thermal resistance, for the case of a well without VIT joints. Therefore, from the wellbore modeling standpoint, during the early stages of production, any

change in the wellbore thermal model (e.g., the use of different correlations) may cause larger changes in the wellbore thermal behavior. As the production time increases, the formation drives the wellbore heat transmission. Furthermore, the thermal model is more affected by the variation of the formation layer properties due to the implementation of the Cheng *et al.* (2011) approach, which considers both the wellbore and formation heat capacities on the calculation of the transient dimensionless temperature.

- The actual well simulated in this work used nitrogen in annulus “A” in connection with a gas-lift operation which was to be pursued during later stages of the well operation. The thermal aspects of this configuration were explored in the thesis, revealing a significant reduction of the heat transfer to the outward annuli and of the wellhead temperature. Although appropriate in a particular scenario involving gas-lift production during later stages, the use of N₂ in the production annulus to reduce the heat transport to the outward annuli is not common and should be looked more carefully, as the gas may contain traces of hydrogen sulfide or even carbon dioxide which cause corrosion of the production casing when in contact with water, and/or leakage through the casing threads if an inappropriate connection is employed.

The mechanical model was applied to well A and the results were validated with field data and compared with those from a commercial software. Then the above mentioned model was applied to well B. The conclusions about this study are cited as follows:

- The model allowed the quantification of both contributions to the APB, namely the annulus fluid expansion and the local tube deformation. This is particularly important to the identification of factors leading to unsafe operating conditions, to the support of well design and eventually changes in wellbore mechanical schematics.
- Deviations as low as 3.71 % were observed for the entire data set with respect of the wellhead annulus A pressure. For short production times, the deviations relative to field data due to the APB are larger. As the production time increases, the

deviation decreases, reaching a value around 2% at steady state.

- Analogous to the heat transfer behavior, as the production time increases, the deformation of the tubes becomes less affected by the wellbore components.
- The magnitude of the pressures in the wellbore increased dramatically when brine was employed as a packer fluid. This behavior reinforces the idea of using compressible fluids, like N_2 , to mitigate APB.
- A comparison between the present model and the commercial software WellCat revealed that the latter overestimated the pressure in the annuli. Also, the high-pressure difference in annulus A could be associated to how the commercial software handles compressible fluids (such as N_2).
- Unknown mechanical and/or thermal properties of the formation rock along uncemented sections may lead to an excessive deformation that, in turn, may cause an inaccurate pressure load prediction.

In order to demonstrate the effect of VIT joints on the wellbore thermal-structural behavior, two synthetic case studies were carried out using 10 and 60 insulated joints, respectively. The main findings are as follows:

- Significant temperature variations were observed in the annuli and wellbore/formation interface. These temperature oscillations were driven by the changes in the local VIT thermal resistance, which is the dominating thermal resistance in the physical domain.
- A sensitivity study on the value of the surface emissivity in the evacuated gap showed that, even for the case with only 10 VIT joints, the average annuli temperature difference were as large as 2.6 K.
- A comparison of the present model with the commercial software using a single k-value or a combination of two k-values showed that the present model showed the largest average temperatures for all simulations, which indicates that such k-values were poorly designed for well A. Also, another key point is that when 2 k-values are used as input parameters in the commercial software, although not ideal, it may be a

good strategy for a better representation of the VIT system thermal resistance.

- A stress analysis of the well assisted by 60 VIT joints (i.e. the artificial case study) showed that using the commercial software for both approaches (assuming a single k-value or two k-values), the load due to the pressure difference over the 6 5/8" tubing string would lead to collapse, while for the present model all loads presented much lower values than the tubular mechanical resistances. The large load difference is due, in part, to the different manners in which the models handle the gas filled annulus A.
- As the strain is computed locally, and since the heat transfer varies significantly along the VIT length, the strain also varies significantly, since it is thermally dependent.

Regarding the performance of the integrated model in predicting the behavior of well B, the following conclusions can be drawn:

- Even though a considerable deviation with respect to field data for the pressure increase in annulus A at steady state was observed (37.9%), the present model showed a much better agreement than the best version (single k-value) of the commercial software (deviation of nearly 165%). This large deviation can be explained by the two following points: (i) the deformation of the outer tubing of the VIT is neglected in the mechanical model, and (ii) the many uncertainties related to the input parameters and boundary conditions, such as the geothermal gradient.
- The average temperature in annuli A and B calculated by the present model showed the lowest values among the three assessed approaches. Moreover, as expected, the two k-value simulation showed results closer to those of the present model. A single k-value of 0.074 W/m.K was set by the VIT commercial supplier specifically for well B. This conservative k-value was employed leading to a higher annuli A and B average temperatures.
- The stress analysis pointed out that all predicted loads were within the tubes mechanical limits. However, caution must be exercised when examining the high load difference between the present model and the commercial code.

5.2 Future Research Needs

Although two actual wells were used to evaluate the models developed in this thesis, more work is needed to confirm the robustness of the integrated model and to gain more confidence in the results. Considering the progress made in this work, the following recommendations for future research can be listed:

- Development of a two-dimensional formation heat diffusion model to estimate the heat transport between the rock formation and the seabed to show the heat loss to the sea;
- Development of a structural model to take into account the deformation of the VIT outer tubing over the inner tubing due to the pressure increase in the production annulus. This may cause the deformation of the inner tubing that was neglected in this work.
- Using parallel computation to reduce the computational cost for performing the VIT simulations.
- A comprehensive study about the effect of fluid and formation properties uncertainties on the APB is needed to improve the reliability of the mathematical models.
- Carry out experiments in standalone VIT joints (under laboratory conditions) to validate the thermal models presented in this thesis.

REFERENCES

- [1] ALCOFRA, E. L. M., **Aumento de pressão de fluido confinado no anular de poços de petróleo**, Pontifícia Universidade Católica do Rio de Janeiro, 104 pp, Dissertação de Mestrado, 2014.
- [2] AL SHAIBI, R. A. (2015, January 26). **Mukhaizna Steam Injectors Thermal Efficiency & Insulated Tubing Pilot Evaluation**. Society of Petroleum Engineers. doi:10.2118/172930-MS
- [3] ALVES, I.N., ALHANATI, F.J.S. & SHOHAM, O., **A unified model for predicting flowing temperature distribution in wellbores and pipelines**, SPEPE 7 (6), 363-367, 1992.
- [4] AMARA, D. CAPATINA, and L. LIZAIK, **Numerical coupling of petroleum wellbore and reservoir models with heat transfer**. In Proceedings of the European Conference on Computational Fluid Dynamics ECCOMAS CFD 2006.
- [5] ANSARI, A. M., SYLVESTER, N. D., SARICA, C., SHOHAM, O., & BRILL, J. P. (1994, May 1). **A Comprehensive Mechanistic Model for Upward Two-Phase Flow in Wellbores**. Society of Petroleum Engineers. doi:10.2118/20630-PA
- [6] API, **Bulletin on Formulas and Calculations For Casing, Tubing, Drill Pipe and Line Pipe Properties**, API 5C3 Ed.6, 2008.
- [7] AZIZ, K., & GOVIER, G. W. (1972, July 1). **Pressure Drop In Wells Producing Oil And Gas**. Petroleum Society of Canada. doi:10.2118/72-03-04
- [8] AZZOLA, J.H., PATTILLO, P.D., RICHEY, J.F. & SEGRETTO, S.J., **“The Heat Transfer Characteristics of Vacuum Insulated Tubing”**. SPE Annual Technical Conference and Exhibition. Houston. TX. USA. 26-29 September 2004.
- [9] AZZOLA, J.H., TSELEPIKADIS, D.P., PATTILLO, P.D., RICHEY, J.F., TINKER, S.J., MILLER, R.A. & SEGRETTO, S.J., 2007, **“Application of Vacuum Insulated Tubing to Mitigate Annular Pressure Buildup”**. SPE Drilling and Completion Journal, Vol. 22, pp 46-51.

- [10] BAHONAR, M, AZAIEZ, J and CHEN, Z. (2009). **A Semi-Unsteady-State Wellbore Steam/Water Flow Model for Prediction of Sandface Conditions in Steam Injection Wells.** Journal of Canadian Petroleum Technology, 49 (9) 13-21 SPE 1499063.
- [11] BAHONAR, M., AZAIEZ, J. and CHEN, Z. (2011, January 1). **Two Issues in Wellbore Heat Flow Modelling Along With the Prediction of Casing Temperature in the Steam Injection Wells.** Society of Petroleum Engineers. doi:10.2118/137134-PA
- [12] BARBOSA, Jr., J.R., HEWITT, G.F., **Gas-liquid two-phase flow in vertical pipes (A description of models used in the GRAMP2 programme)**, 2006, Annual Report.
- [13] BARBOSA, Jr., J.R., HEWITT, G.F., KÖNIG, G., RICHARDSON, S.M., 2002, **Liquid entrainment, droplet concentration and pressure gradient at the onset of annular flow in a vertical pipe.** Int. J. Multiphase Flow, 943–961.
- [14] BARCELOS, J. G. A., HAFEMANN, T.E., FERREIRA, M.V.D., BARBOSA, Jr., J.R., SILVA, A.K. “A new approach for calculating Annular Pressure Buildup in na offshore well”, IV Journeys in Multiphase Flows (JEM 2017) March 27-31, 2017, São Paulo, SP, Brazil .
- [15] BARNEA, D., BRAUNER, N., 1985, **Hold-up of the liquid slug in two-phase intermittent flow**, Int. J. Multiphase Flow 11, 43-49.
- [16] BAXENDELL, P.B. and THOMAS, R., 1961, **The Calculation of Pressure Gradients in High Rate Flowing Wells.** Journal of Petroleum Technology 13 (10), 1023.
- [17] BELKIN, H.H., MACLEOD, A.A., MONRAD, C.C., ROTHFUS, R.R., 1959, **Turbulent liquid flow down vertical walls.** AIChE J. 5, 245-248.
- [18] BEGGS, H. D. and BRILL, J. P., 1973. **A Study of Two-Phase Flow in Inclined Pipes.** SPE 4007.
- [19] BELLARBY, J. “**Well Completion Design**”, 1st Edition, Developments in Petroleum Science, Vol 56, 1st Ed Elsevier, 2009.
- [20] BHARATHAN, D., WALLIS, G.B., 1983, **Air-water counter-current annular flow.** Int. J. Multiphase Flow, 9(4), 349-366.

- [21] BLOYS, J. B. et al. (2008, January 1). **Trapped Annular Pressure Mitigation: Trapped Annular Pressure - A Spacer Fluid That Shrinks**. Society of Petroleum Engineers. doi:10.2118/112872-MS
- [22] BRADFORD, D. W., FRITCHIE, D. G., GIBSON, D. H., GOSCH, S. W., PATTILLO, P. D., SHARP, J. W. and TAYLOR, C. E. (2004, June 1). **Marlin Failure Analysis and Redesign: Part 1 - Description of Failure**. Society of Petroleum Engineers. doi:10.2118/88814-PA
- [23] BRENNEN, C.E., **Fundamentals of Multiphase Flows**, California Institute of Technology, Pasadena, California, Cambridge University Press 2005, ISBN 0521 848040.
- [24] BRILL, J. P., **Multiphase flow in wells**, SPE 16242, Journal of Petroleum Technology, January, 15-21 (1987).
- [25] BRILL, J. P., and ARIRACHAKARAN, S. J., **State of the Art in Multiphase Flow**, SPE 23835, Journal of Petroleum Technology, 44 (5), 538-541 (1992).
- [26] BRILL, J. P., and MUKHERJEE, H., **Multiphase Flow in Wells**, 1999, 164 pp, SPE Monograph Series Vol. 17 ISBN:978-1-61399-295-1 Society of Petroleum Engineers
- [27] CAMACHO, C. A., **Comparison of Correlations for Predicting Pressure Losses in High Gas-Liquid Ratio Vertical Wells**, M.S. thesis, University of Tulsa, (1970).
- [28] CAMARGO, R. M. T., “**Hidrodinâmica e Transferência de calor no Escoamento Intermitente Horizontal**”, Universidade Estadual de Campinas, 142 pp. Dissertação de mestrado, 1991.
- [29] CANDIA, O. C. and CRUZ, M. A. V., **Prediction of Pressure, Temperature, and Velocity Distribution of Two-Phase Flow in Oil Wells**, Journal of Petroleum Science and Engineering 46 (2005) 195– 208. doi:10.1016/j.petrol.2004.11.003
- [30] CAREY, V.P., 1992, **Liquid-Vapor Phase-Change Phenomena: An Introduction to the Thermophysics of Vaporization and Condensation Processes in Heat Transfer Equipment**, Hemisphere Publishing Co., Washington.
- [31] CARSLAW, H. S. and JAEGER, J. C., **Conduction of Heat in Solids** (1959), Oxford Science Publications 2nd Edition, ISBN 0198533683.

- [32] CHEN, J.C., **Correlation for boiling heat transfer to saturated fluids in convective flow**, Industrial & Engineering Chemistry Process Design and Development, (5) 322-&, 1966.
- [33] CHENG, H.; HILLS, J. H.; AZZORPARDI, B. J. **A Study of the Bubble to Slug Transition in Vertical Gas-Liquid Flow in Columns of Different Diameter**. International Journal of Multiphase Flow, v. 24, n. 3, p. 431–452, 1998.
- [34] CHENG, W. L., HUANG, Y. H., LU, D. T. and YIN, H. R., **A novel analytical transient heat-conduction time function for heat transfer in steam injection wells considering the wellbore heat capacity**, Energy 36 (2011) 4080-4088. doi:10.1016/j.energy.2011.04.039
- [35] CHIU, K., and THAKUR, S. C. (1991, January 1). **Modeling of Wellbore Heat Losses in Directional Wells Under Changing Injection Conditions**. Society of Petroleum Engineers. doi:10.2118/22870-MS
- [36] CHURCHILL, S.W. and CHU, H.H.S., 1975. **Correlating Equations for Laminar and Turbulent Free Convection from a Horizontal Cylinder**. International Journal of Heat and Mass Transfer. vol 18. 1049.
- [37] COLLIER, J.G. and THOME, J. R. (1994) **Convective Boiling and Condensation**. 3rd Ed. Oxford University Press.
- [38] CORRADINI, M.L., “**Fundamentals of Multiphase Flow**”, Department of Engineering Physics, University of Wisconsin, Madison, 1997.
- [39] COULTER, D. and BARDON, M. 1979. **Revised Equation Improves Flowing Gas Temperature Prediction**. Oil & Gas J 77 (9): 107-115.
- [40] DE CACHARD, F., DELHAYE, J.M., 1996, **A slug-churn flow model for small-diameter airlift pumps**. Int. J. Multiphase Flow 22(4), 627-649.
- [41] DESHPANDE, S., BISHOP, A. and KARANDIKAR, B., “**Heat transfer to air-water plug slug flow in horizontal pipes**”, Ind. Eng. Chem Res, Vol 30, No. 9, 1991.
- [42] DROPKIN, D; SOMMERSCALES, E. **Heat Transfer by Natural Convection in Liquids Confined by Two Parallel Plates Inclined**

- at Various Angles with Respect to the Horizontal**, Journal of Heat Transfer; Trans., ASME, Series C (February, 1965) 87, 77-84.
- [43] DUKLER, A. E. and TAITEL, Y., “**Flow Pattern Transitions in Gas-Liquid Systems: Measurement and Modeling**,” Multiphase Science and Technology, 2, 1-94 (1986).
- [44] DUNS, H. and ROS, N. C. J., 1963. **Vertical Flow of Gas and Liquid Mixtures in Wells**, Proceedings of the 6th World Petroleum Congress, Tokyo.
- [45] EICKMEIER, J., ERSOY, D., and RAMEY, H. 1970. **Wellbore Temperatures and Heat Losses During Production or Injection Operations**. Journal of Canadian Petroleum Technology 9 (02): 115-121. PETSOC-70-02-08. <http://dx.doi.org/10.2118/70-02-08>
- [46] ELLIS, R. C., FRITCHIE, D. G., GIBSON, D. H., GOSCH, S. W. and PATTILLO, P. D. (2004, June 1). **Marlin Failure Analysis and Redesign: Part 2 - Redesign**. Society of Petroleum Engineers. doi:10.2118/88838-PA
- [47] ERIKSEN, K., PANAMARATHUPALAYAM, B., FOXENBERG, W. E. and CHUMAKOV, E. (2014, October 14). **A Novel High Temperature Insulating Packer Fluid**. Society of Petroleum Engineers. doi:10.2118/171284-MS
- [48] EZELL, L.G., FONTENOT, S., ROBINSON, E., CUNNINGHAM, L. and PATRICKIS. A., 2010. **High Performance Aquous Insulating Packer Fluid Improved Flow Assurance and Reduced Annular Pressure Buildup in Ultra Deepwater Wells**. SPE Deepwater Drilling and Completions Conference. Galveston. TX. USA. October.
- [49] FANCHER, G. H. Jr. and BROWN, K. E., 1963. **Predictions of Pressure Gradients for Multiphase Flow in Tubing**. SPE 440.
- [50] FEENEY, S. (1997, August 1). **Vacuum-Insulated Tubing for Subsea Completions**. Society of Petroleum Engineers. doi:10.2118/0897-0802-JPT
- [51] FERREIRA, M. V. D., DOS SANTOS, A. R. and VANZAN, V. (2012, January 1). **Thermally Insulated Tubing Application to Prevent Annular Pressure Buildup in Brazil Offshore Fields**. Society of Petroleum Engineers. doi:10.2118/151044-MS

- [52] FERREIRA, M.V.D., BARCELOS, J., COSTA, C.A.S., BARBOSA Jr., J.R. and DA SILVA, A.K., **Thermal analysis of vacuum insulated tubing (VIT) for offshore oilwells**, 15th Brazilian Congress of Thermal Sciences and Engineering, November 10-13, 2014, Belém, PA, Brazil
- [53] FOROUZANFAR, F., PIRES, A. P., & REYNOLDS, A. C. (2015, September 28). **Formulation of a Transient Multi-Phase Thermal Compositional Wellbore Model and its Coupling with a Thermal Compositional Reservoir Simulator**. Society of Petroleum Engineers. doi:10.2118/174749-MS
- [54] FRIEDEL, L., 1979, **Improved friction pressure drop correlations for horizontal and vertical two-phase pipe flow**. European Two-Phase Flow Group Meeting, Ispra, Italy, paper E2.
- [55] FRICKE, J. **Physical aspects of heat transfer and the development of thermal insulations**, in Proc. of the International Conference And Workshop EMPA Duebendorf, 2001. 13–22.
- [56] GOMEZ, L. E. et al., **A Unified Mechanistic Model for Steady-State Two-Phase Flow in Wellbores and Pipelines**, SPE Annual Technological Conference Exhibition, Houston, Texas, USA, SPE 56520, (1999).
- [57] GOSCH, S. W., HORNE, D. J., PATTILLO, P. D., SHARP, J. W. and SHAH, P. C. (2004, June 1). **Marlin Failure Analysis and Redesign: Part 3 - VIT Completion With Real-Time Monitoring**. Society of Petroleum Engineers. doi:10.2118/88839-PA
- [58] GOSLINE, J.E., **Experiments on the vertical flow of gas-liquid mixtures in glass pipes**, Trans. AIME (1936), Vol. 118, 56.
- [59] GOVAN, A.H., HEWITT, G.F., OWEN, D.G., BOTT, T.R., 1988, **An improved CHF modelling code**. Proc. 2nd UK National Heat Transfer Conference, IMechE, Glasgow, paper C175.
- [60] GREALISH, F. and RODDY, I., **State of the Art on Deep Water Thermal Insulation Systems**, OMAE2002-28464, 21th International Conference on Offshore Mechanics and Arctic Engineering, Oslo, Norway, 2002. June 23–28.

- [61] GRIFFITH, P. and WALLIS, G.B., “**Two-Phase Slug Flow**”, Journal of Heat Transfer; Trans., ASME, pp. 307-320, August, 1961.
- [62] GUO, B., DUAN, S. and GHALAMBOR, A., **Simple Model for Predicting Heat Loss and Temperature Profiles in Thermal Injection Lines and Wellbores with Insulations**, SPE 86983, SPE International Thermal Operations and Heavy Oil Symposium and Western Regional Meeting, Bakersfield, California, 2004, March.
- [63] HAFEMANN, T. E., FERREIRA, M.V.D., BARBOSA, Jr., J.R. and SILVA, A.K., Modelling of multiphase fluid flow and heat transfer in a pre-salt well to predict APB”, IV Journeys in Multiphase Flows (JEM 2015), March 23-27, 2015, Campinas, SP, Brazil.
- [64] HAGEDORN, A. R. and BROWN, K. E., 1965. **Experimental Study of Pressure Gradients Occurring During Continuous Two-Phase Flow in Small-Diameter Vertical Conduits**. SPE 39th Annual Fall Meeting Paper, pp. 475–484.
- [65] HAGOORT, J., 2004. **Ramey’s wellbore heat transmission revisited**. Soc.Pet.Eng. (Document ID 87305).
- [66] HALAL, A. S., & MITCHELL, R. F. (1994, June 1). **Casing Design for Trapped Annular Pressure Buildup**. Society of Petroleum Engineers. doi:10.2118/25694-PA
- [67] HASAN, A. R., and KABIR, C. S. (1991, January 1). **Heat Transfer During Two-Phase Flow in Wellbores; Part I- Formation Temperature**. Society of Petroleum Engineers. doi:10.2118/22866-MS
- [68] HASAN, A.R. and KABIR, C.S., 1994. **Aspects of heat transfer during two-phase flow in wellbores**. SPEPF 9 (3), 211–216.
- [69] HASAN, A.R. and KABIR, C.S., **A mechanistic model for computing fluid temperature profiles in gas-lift wells**, SPEPF 11 (3), 179–185, 1996.
- [70] HASAN, A.R., KABIR, C.S. and AMEEN, M., 1996. **A fluid circulating temperature model for workover operations**. SPEJ 1 (2), 133–144.

- [71] HASAN, A.R., KABIR, C.S. and WANG, X., 1998. **Wellbore two-phase flow and heat transfer during transient testing**. SPEJ 3 (2), 174–180.
- [72] HASAN, A. R. and KABIR, C. S., 1999. **A Simplified Model for Oil/Water Flow in Vertical and Deviated Wellbores**. SPE 54131.
- [73] HASAN, A.R. and KABIR, C.S., **Fluid flow and heat transfer in wellbores**, Society of Petroleum Engineers, Richardson, Texas, 2002.
- [74] HASAN, A.R., KABIR, C.S. and LIN, D., 2005. **Analytic wellbore temperature model for transient gas-well testing**. SPEREE 8 (3), 240–247.
- [75] HASAN, A.R., KABIR, C.S. and WANG, X., 2009. **A robust steady-state model for flowing-fluid temperature in complex wells**. SPEPO 24 (2), 269–276.
- [76] HASAN, A.R., IZGEC, B., KABIR, C.S., 2010. **Sustaining production by managing annular pressure buildup**. SPEPO 25 (2), 195–203.
- [77] HEWITT, G.F., WALLIS, G.B., 1963, **Flooding and associated phenomena in falling film in a vertical tube**, Proc. Multiphase Flow Symposium, Philadelphia, PA, 62-74.
- [78] HORN, C. and LIVELY, G., A. **New Insulation Technology: Prediction versus Results from the First Field Installation**, OTC13136, 2001 Offshore Technology Conference, Houston, Texas, 2001.
- [79] HU, J. SAGEN, G. CHUPIN, T. HAUGSET, A. EK, T. SOMMERSEL, Z. G. XU, and MANTECON, C., **Integrated wellbore/reservoir dynamic simulation**. SPE Asia Pacific Oil & Gas Conference and Exhibition, 2007.
- [80] HUDSON, J. D., DYKHNO, L. A., LORIMER, S. E., SCHOPPA, W., & WILKENS, R. J. (2000, January 1). **Flow Assurance for Subsea Wells**. Offshore Technology Conference. doi:10.4043/11968-MS
- [81] INCROPERA, F.P., DEWITT, D. P., BERGMAN, T. L. and LAVINE, A. S., **“Fundamentals of Heat and Mass Transfer”**. John Wiley & Sons. Inc. New York. 2007.

- [82] ISHII, M. and HIBIKI, T., (2006) **Thermo-fluid Dynamics of Two-Phase Flow**, 2nd Ed. Springer.
- [83] IZGEC, B., KABIR, C.S., ZHOU, D., HASAN, A.R., 2007. **Transient fluid and heat flow modeling in coupled wellbore/reservoir systems**, SPE Paper 102070. SPE Res Eval Eng 10 (3), 294–301 June.
- [84] JAVORA, P. H., GOSCH, S., & PEARCY, R. (2002, January 1). **Development and Application of Insulating Packer Fluids in the Gulf of Mexico**. Society of Petroleum Engineers. doi:10.2118/73729-MS
- [85] JAYANTI, S., BRAUNER, N., 1994, **Churn Flow**, *Chapter 8*, In: *Multiphase Science and Technology*, Volume 8: *Two-Phase Flow Fundamentals*. Eds: G.F. Hewitt et al. Begell House, Inc., New York.
- [86] JAYANTI, S., HEWITT, G.F., 1992, **Prediction of the slug to churn transition in vertical two-phase flow**. *Int. J. Multiphase Flow*, 18, 847-860.
- [87] JENSEN, M.K., 1987, **The liquid film and the core region velocity profiles in annular two-phase flows**. *Int. J. Multiphase Flow*, 13, 615-628.
- [88] KABIR, C.S., HASAN, A.R., KOUBA, G.E. and AMEEN, M., **Determining circulating fluid temperature in drilling, workover, and well control operations**, SPEDC 11 (2), 74–79, 1996.
- [89] KANG, Y., SAMUEL, R., GONZALES, A., LIU, Z. (2015, November 23). **Heat Transfer Modeling of Wellbore with Vacuum-Insulated-Tubing (VIT)**. Society of Petroleum Engineers. doi:10.2118/178449-MS
- [90] KARRA, S., CHUDIACK, M., SINHA, A., & BOSER, G. (2014, June 10). **SAGD Vacuum Insulated Tubing vs. Bare Tubing - Concentric and Eccentric Configurations: A Comparative Thermal Computational Fluid Dynamics Study**. Society of Petroleum Engineers. doi:10.2118/170177-MS
- [91] KIM, D. and GHAJAR, A., “**Heat transfer measurements and correlations for air-water flow of different flow patterns in a horizontal pipe**”, *Experimental Thermal and Fluid Science* 25 pp 659-676, 2002.

- [92] KIM, D.S., BAKER, B., MANNAN, S.K., HIBNER, E.L., PUCKETT, B.C., BRUNSON, T., SCOGSBERG, L. (2005, January 1). **Mechanical and corrosion performance of welded alloy 925 VIT in sour environment**. NACE International.
- [93] KIM, D.S. and CERNOCKY, P., **Fracture, Fatigue and Stress Corrosion Performance of Vacuum Insulated Tubing Weldment**, 15th International Offshore and polar Engineering Conference, Seoul, Korea, June 19-24, 2005. ISSN 1098-6189.
- [94] KIRKPATRICK, C. 1959. **Advances in Gas-Lift Technology**. Paper API-59-024 presented at the Drilling and Production Practice, New York.
- [95] KLEIN, S.A. and ALVARADO, F.L., 2014, **Engineering Equation Solver (EES)**, F-Chart Software, Professional Version 9.192.
- [96] KLEMENTICH, E. F. and JELLISON, M. J. (1986, April 1). **A Service-Life Model for Casing Strings**. Society of Petroleum Engineers. doi:10.2118/12361-PA
- [97] LESEM, L. B., GREYTOK, F., MAROTTA, F. and MCKETTA, J. J., (1957): “**A Method of Calculating the Distribution of Temperature in Flowing Gas Wells**”. SPE. Published in Petroleum Transactions, AIME, Volume 210, pages 169-176.
- [98] LEVY, S., 1999, **Two-Phase Flow in Complex Systems**, John Wiley and Sons Inc., New York.
- [99] LI, X. X., WU, Y., ZHAO, X., GAO, P., QIN, Q. and YU, M. (2012, January 1). **A Cyclic-Steam Injection in Fuyv Reservoir**, Daqing. Society of Petroleum Engineers. doi:10.2118/151976-MS
- [100] LIMA, I. N. R. C., “**Estudo Experimental da Transferência de Calor no Escoamento Bifásico Intermitente Horizontal**” São Paulo: Universidade Estadual de Campinas, 135p. Dissertação de mestrado, 2009.
- [101] LIVESCU, S., DURLOFSKY, L.J., AZIZ, K., GINESTRA, J. C., 2008. **Application of a new fully-coupled thermal multiphase wellbore flow model**. SPE Paper 113215, presented at the SPE Improved Oil Recovery Symposium, Tulsa, OK, April 19-23, 2008.
- [102] LIVESCU, S., DURLOFSKY, L.J., AZIZ, K., 2009. **Development and application of a fully-coupled thermal compositional**

- wellbore flow model**. SPE Paper 121306, presented at the SPE Western Regional Meeting, San Jose, CA, March 24-26, 2009.
- [103] LYONS, W., **Working guide to drilling equipment and operations**, 1st edition 2010, Gulf Professional Publishing, Elsevier, ISBN: 978-85617-843-3.
- [104] MARSHALL, D. W. & BENTSEN, R. G. (1982, January 1). **A Computer Model to Determine the Temperature Distributions In a Wellbore**. Petroleum Society of Canada. doi:10.2118/82-01-05
- [105] MAY, C.J., **Efficiency of flowing wells**, Trans. AIME (1935), Vol. 114, 99.
- [106] MCKECHNIE, J.G. and HAYES, D.T., **Pipeline Insulation Performance for Long Distance Subsea Tie-Backs**, Long Distance Subsea Tiebacks Conference, Amsterdam, 2001, November 26–28.
- [107] MEDINA, M. G., BEDINO, H., SIERRA, S., SCAGLIARINI, S., ROMERO, D., ROCHA, R. and ROSAS, R. R. (2014, March 4). **Case History: Casing Collapse During Concentric Drilling Operation Leads To New Casing Design Approach for HP/HT Wells With Low Reservoir Pressure and/or N₂ Injection**. Society of Petroleum Engineers. doi:10.2118/167929-MS
- [108] MELVE, B., **Design Requirements for High Temperature Flowline Coatings**, OMAE2002-28569, 21th International Conference on Offshore Mechanics and Arctic Engineering, Oslo, Norway, 2002. June 23–28.
- [109] MIRHOSSEINI, M. and SABOONCHI, A., **View factor calculation using the Monte Carlo method for a 3D strip element to circular cylinder**, International Communications in Heat and Mass Transfer, 38 (2011) 821-826. Doi: 10.1016/j.icheatmasstransfer.2011.03.022
- [110] MISHIMA, K., ISHII, M., 1984, **Flow regime transition criteria for two-phase flow in vertical tubes**. Int. J. Heat Mass Transfer 27, 723-734.
- [111] MOE, B. and ERPELDING, P., **Annular pressure buildup: What it is and what to do about it**. SPE Journal of Deepwater Technology, 603-272-9427. August 2000.

- [112] MOORE, T.V. and WILDE, H.D., **Experimental measurements of slippage in flow through vertical pipes**, Trans. AIME (1931), Vol. 92, 296.
- [113] MOORE, T.V. and SCHILTHUIS, R.J., **Calculations of pressure drops in flowing wells**, Trans. AIME (1933), Vol. 103, 170.
- [114] MORÉ, J.J., **The Levenberg-Marquardt Algorithm: Implementation and Theory**, Numerical Analysis, ed. G. A. Watson, Lecture Notes in Mathematics 630, Springer Verlag, pp 105–116, 1977.
- [115] MOSS, J.T; WHITE, P.D. **How to Calculate Temperature Profiles in a Water Injection Well**, Oil and Gas Journal (March 9, 1959) 57, No 11, 174.
- [116] MUKHERJEE, H., & BRILL, J. P. (1983, May 1). **Liquid Holdup Correlations for Inclined Two-Phase Flow**. Society of Petroleum Engineers. doi:10.2118/10923-PA
- [117] NELSON, K. 2002. **AOGCC will rule on annular pressure management at PrudhoeBay. Pressure exceeded design burst rating**. *Petroleum News* 8(4).
- [118] NIAN, Y. L., CHENG, W. L., LI, T. T. and Wang, C. L., (2014). **Study on the effect of wellbore heat capacity on steam injection well heat loss**. *Applied Thermal Engineering*. 70. 763-769. 10.1016/j.applthermaleng.2014.05.056.
- [119] NICKLIN, D.J., WILKES, J.O., DAVIDSON, J.F., 1962, **Two-phase flow in vertical tubes**. Trans. Inst. Chem. Engrs. 40, 61-68.
- [120] NOWINKA, J., XIE, J., KIS, P., HENSLEY, R., GONZALEZ, M., & WILLIAMS, D. (2005, January 1). **Vacuum Insulated Tubing Design and Performance Evaluation for Deepwater Completions**. Society of Petroleum Engineers. doi:10.2118/92448-MS
- [121] OMLAND, T.H., HODNE, H., SAASEN, A., MJOLHUS, S., AMUNDSEN, P.A. **Drilling Fluid Weight Material Sedimentation- Part II Sedimentation of suspensions**, accepted for publication in *Petroleum Science and Technology*, Taylor & Francis Inc, December 2009.
- [122] OUDEMAN, P., & BACARREZA, L. J. (1995, June 1). **Field Trial Results of Annular Pressure Behavior in a High-Pressure/High-**

- Temperature Well.** Society of Petroleum Engineers. doi:10.2118/26738-PA
- [123] OUDEMAN, P., & KEREM, M. (2006, December 1). **Transient Behavior of Annular Pressure Build-up in HP/HT Wells.** Society of Petroleum Engineers. doi:10.2118/88735-PA
- [124] ORKISZEWSKI, J., 1967. **Predicting two-phase pressure drops in vertical pipe.** Journal of Petroleum Technology, 1546: 829–838.
- [125] PAN, B. L. and OLDENBURG, C. M., **T2 well - An Integrated Wellbore-Reservoir Simulator.** Computers & Geosciences, 65:46–55, 2014.
- [126] PATTILLO, P. D., PAYNE, M. L., WEBB, T. R., & SHARADIN, J. H. (2003, January 1). **Application of Decision Analysis to a Deepwater Well Integrity Assessment.** Offshore Technology Conference. doi:10.4043/15133-MS
- [127] PATTILLO, P. D., BELLARBY, J. E., ROSS, G. R., GOSCH, S. W., & MCLAREN, G. D. (2004, September 1). **Thermal and Mechanical Considerations for Design of Insulated Tubing.** Society of Petroleum Engineers. doi:10.2118/79870-PA
- [128] PATTILLO, P. D., COCALES, B. W., & MOREY, S. C. (2006, December 1). **Analysis of an Annular Pressure Buildup Failure During Drill Ahead.** Society of Petroleum Engineers. doi:10.2118/89775-PA
- [129] PATTILLO, P., **Recent Advances in Complex Well Design,** SPE Distinguished Lecturer Series, Houston, 2011.
- [130] PAUCHON, C., BANERJEE, S., 1986, **Interphase momentum effects in averaged multifield model. Part I: Void propagation in bubble flows,** Int. J. Multiphase Flow, 12, 559-573.
- [131] PETALAS, N., & AZIZ, K. (2000, June 1). **A Mechanistic Model for Multiphase Flow in Pipes.** Petroleum Society of Canada. doi:10.2118/00-06-04
- [132] PHILIP, F., **Managed pressure drilling — what’s in a name?,** Drilling Contractor journal, March/April 2006, pp. 36-39.
- [133] POETTMAN, F. H., & CARPENTER, P. G. (1952, January 1). **The Multiphase Flow of Gas, Oil, and Water Through Vertical Flow**

Strings with Application to the Design of Gas-lift Installations.
American Petroleum Institute.

- [134] POURAFSHARY, P. “**A coupled wellbore/reservoir simulator to model multiphase flow and temperature distribution**”, PhD Thesis, University of Texas at Austin, December 2007.
- [135] POURAFSHARY, P., VARAVEI, A., SEPEHRNOORI, K. and PODIO, A.L., **A compositional wellbore/reservoir simulator to model multiphase flow and temperature distribution.** Journal of Petroleum Science and Engineering 69 (1–2), 40–52 Nov, 2009.
- [136] PUCKNELL, J. K., MASON, J. N. E., & VERVEST, E. G. (1993, January 1). **An Evaluation of Recent “Mechanistic” Models of Multiphase Flow for Predicting Pressure Drops in Oil and Gas Wells.** Society of Petroleum Engineers. doi:10.2118/26682-MS
- [137] PURDY, I. L., & CHEYNE, A. J. (1991, January 1). **Evaluation of Vacuum-Insulated Tubing for Paraffin Control at Norman Wells.** Society of Petroleum Engineers. doi:10.2118/22102-MS
- [138] PUSHKINA, O.L., SOROKIN, Y.L., 1969, **Breakdown of liquid film motion in vertical tubes.** Heat Transfer – Soviet Research 1(5) 56-69.
- [139] RAITHBY, G.D. and HOLLANDS, K.G.T., 1975, **A General Method of Obtaining Approximate Solutions to Laminar and Turbulent Free Convection Problems,** Advances in Heat Transfer, Vol. 11, pp. 265-315, Academic Press, New York, NY.
- [140] RAMEY Jr., H.J., **Wellbore heat transmission,** Journal of Petroleum Technology, 14 (4), 427-435, Trans., AIME, 225, 1962.
- [141] RAYMOND, L.R., **Temperature distribution in a circulating drilling fluid,** Journal of Petroleum Technology, 21 (3), 333-341, 1969.
- [142] ROSLAND, H. A., EFFENDHY, E. and PARK, S. J. (2013, March 26). **HPHT Well Basis of Design Case Study: Offshore Thailand Advanced Tubular Analyses Experience.** International Petroleum Technology Conference. doi:10.2523/IPTC-17104-MS
- [143] RUSCHAU, G., ROGERS, R. H., WOODLEY, S., & WRIGHT, E. J. (2010, January 1). **Evaluation and Qualification of Materials for Subsea Insulation Systems.** Society of Petroleum Engineers. doi:10.2118/131618-MS

- [144] SAGAR, R.K., DOTY, D.R. and SCHMIDT, Z., **Predicting temperature profiles in a flowing well**, SPEPE 6 (6), 441–448, 1991.
- [145] SANTOS, H. L., ROCHA, J. S., FERREIRA, M. V., LIMA, V., SOUZA, C. O., BORGES, A. and SILVA, E. C. (2015, October 27). **APB Mitigation Techniques and Design Procedure**. Offshore Technology Conference. doi:10.4043/26294-MS
- [146] SATHUVALLI, U. B., PAYNE, M. L., PATTILLO, P. D., RAHMAN, S., & SURYNARAYANA, P. V. (2005, January 1). **Development of a Screening System to Identify Deepwater Wells at Risk for Annular Pressure Build-up**. Society of Petroleum Engineers. doi:10.2118/92594-MS
- [147] SATHUVALLI, U. B., PILKO, R. M., GONZALEZ, R. A., PAI, R. M., SACHDEVA, P., and SURYNARAYANA, P. V. (2016, March 1). **Design and Performance of Annular Pressure Build-Up APB Mitigation Techniques**. Society of Petroleum Engineers. doi:10.2118/178886-MS
- [148] SATTER, A. (1967, January 1). **A Prediction Method for Conduction Heating of Reservoirs by Steam Injection**. Society of Petroleum Engineers. doi:10.2118/1950-MS
- [149] SHAHREYARAND, N. and FINLEY, D. (2014, March 25). **Importance of Thermal/Stress Loading Analysis for Tubulars in HPHT Wells**. Offshore Technology Conference. doi:10.4043/24852-MS
- [150] SHIRDEL, M. & SEPERHRNOORI, K. (2009, January 1). **Development of a Coupled Compositional Wellbore/Reservoir Simulator for Modeling Pressure and Temperature Distribution in Horizontal Wells**. Society of Petroleum Engineers. doi:10.2118/124806-MS
- [151] SHIU, K.S. and BEGGS, H.D., **Predicting temperatures in flowing oil wells**, Journal of Energy Resources Technology, 102 (2), 1980.
- [152] SHOUSHARI, M. A., AL-KAYIEM H. H., IRAWAN, S., & SAAID, I. (2012, January 1). **Developing Novel Wellbore Heat Transfer Strategies for HPHT Wells**. Society of Petroleum Engineers. doi:10.2118/154768-MS

- [153] SHOHAM, O., **Mechanistic Modeling of Gas-Liquid Two-phase Flow In Pipes**, Textbook Society of Petroleum Engineers, Richardson, Texas, 408 pp, ISBN:978-1-55563-107-9, 2006.
- [154] SINGH, P., WALKER, J., LEE, H. S., GHARFEH, S., THOMASON, B., & BLUMER, D. (2006, January 1). **An Application of Vacuum Insulation Tubing (VIT) for Wax Control in an Arctic Environment**. Offshore Technology Conference. doi:10.4043/18316-MS
- [155] SONG, X. and GUAN, Z., **Coupled modeling circulating temperature and pressure of gas-liquid two phase flow in deep water wells**, Journal of Petroleum Science and Engineering, 92–93(2012)124–131. doi:10.1016/j.petrol.2012.06.017
- [156] SQUIER, D., SMITH, D., and DOUGHERTY, E. 1962. **Calculated Temperature Behavior of Hot-Water Injection Wells**. Journal of Petroleum Technology 14 (04): 436-440. SPE-95-PA. <http://dx.doi.org/10.2118/95-PA>
- [157] STONE, T.W., BENNETT, J., LAW, D.H.S. and HOLMES, J.A., **Thermal simulation with multisegment wells**, SPE Paper 78131. SPE Res Eval Eng 5 (3), 206–218 June, 2002.
- [158] STONE, T.W., EDMUNDS, N.R. and KRISTOFF, B.J., **A comprehensive wellbore/reservoir simulator**, SPE Paper 18419, presented at the SPE Symposium on Reservoir Simulation, Houston, TX, Feb. 6-8, 1989.
- [159] SULTAN, N. W., FAGET, J. B. P., FJELDHEIM, M., & SINET, J.C. (2008, January 1). **Real-Time Casing Annulus Pressure Monitoring in a Subsea HP/HT Exploration Well**. Offshore Technology Conference. doi:10.4043/19286-MS
- [160] TAITEL, Y and DUKLER, A.E., **A model for predicting flow regime transition in horizontal and near horizontal gas-liquid flow**, AIChE Journal, Volume 22, Issue 1, pages 47–55, January 1976.
- [161] TAITEL, Y., BARNEA, D., DUKLER, A.E., 1980, **Modelling of flow pattern transitions for steady upward gas-liquid flow in vertical tubes**, AIChE J. 26, 345-354.
- [162] VARGO, R. F., PAYNE, M., FAUL, R., LEBLANC, J. and GRIFFITH, J. E. (2003, September 1). **Practical and Successful**

- Prevention of Annular Pressure Buildup on the Marlin Project.** Society of Petroleum Engineers. doi:10.2118/85113-PA
- [163] VERSLUYS, J., **Mathematical development of the theory of flowing oil wells**, Trans. AIME (1930), Vol. 86, 192.
- [164] WALLIS, G.B., 1969, **One Dimensional Two-Phase Flow**, McGraw-Hill, New York.
- [165] WATKINS, L., **New Pipeline Insulation Technology Introduced**, Pipeline & Gas Journal (2000). April.
- [166] WellCat™, Landmark Graphics Corporation, WellCat Training Manual (2006) 270p., Houston, USA.
- [167] WHITE, E.T. and BEARDMORE, R.H., 1962, **The velocity of rise of single cylindrical air bubbles through liquids contained in vertical tubes**. Chem. Eng. Sci. 17, 351-361.
- [168] WILLHITE, G. P. (1967, May 1). **Overall Heat Transfer Coefficients in Steam and Hot Water Injection Wells**. Society of Petroleum Engineers. doi:10.2118/1449-PA
- [169] WILLIAMSON, R., SANDERS, W., JAKABOSKY, T., SERIO, M., & GRIFFITH, J. E. (2003, January 1). **Control of Contained-Annulus Fluid Pressure Buildup**. Society of Petroleum Engineers. doi:10.2118/79875-MS
- [170] WU, Y.S. and PRUESS, K., **An Analytical Solution for Wellbore Heat Transmission in Layered Formations**, SPE Reservoir Engineering, 531-538, November 1990.
- [171] XIAO, Z-Q, 1987. **The calculation of oil temperature in a well**. SEP 17125, 1 – 14.
- [172] XIONG, W., BAHONAR, M. and CHEN, Z. (2015, June 9). **Development of a Thermal Wellbore Simulator With Focus on Improving Heat Loss Calculations for SAGD Steam Injection**. Society of Petroleum Engineers. doi:10.2118/174408-MS
- [173] YANG, J., TANG, H., LIU, Z., YANG, L., HUANG, X., YAN, D. and TIAN, R., “**Prediction model of casing annulus pressure for deepwater well drilling and completion operation**”, Petroleum Exploration and Development, 2013, 40(5): 661–664

- [174] YIN, F. and GAO, D. (2014, August 25). **Improved Calculation of Multiple Annuli Pressure Buildup in Subsea HPHT Wells**. Society of Petroleum Engineers. doi:10.2118/170553-MS
- [175] YUE, H., PANG, W., DUAN, Y., ZHANG, T., HE, Z., DENG, D., HOU, Q., DU, J., ZHAO, X. and FENG, X. (2013, June 11). **Integral Completion Technique for Heavy Oil Thermal Recovery**. Society of Petroleum Engineers. doi:10.2118/165518-MS
- [176] ZAMORA, M. and BELL, R., (2004), **Improved Wellsite Test for Monitoring Barite Sag**, AADE 2004 Drilling Fluids Conference, (AADE-04-DF-HO-19).
- [177] ZHANG, H., WANG, Q., SARICA, C. and BRILL, J. P., **Unified Model of Heat Transfer in Gas-Liquid Pipe Flow**, Society of Petroleum Engineers - Production & Operation, 2006.
- [178] ZHAO, X., **Mechanistic-Based models for slug flow in vertical pipes**, PhD Thesis, Texas Tech University, 2005.
- [179] ZUBER, N. and FINDLAY, J.A., **Average Volumetric Concentration in Two-Phase Flow Systems**, J. Heat Transfer 87 (1965), 453-468.

APPENDIX A

This appendix shows the schematic representations of the VIT equivalent thermal circuits considering two different geometries based on the connection types employed: API (VIT 3 ½" x 2 ¾", see Figure A.2) or premium (VIT 6 ⅝" x 5 ½", see

Figure A.3). Such thermal circuits represent half VIT joint since symmetry planes are applied, so boundary conditions at each end are insulated. Each heat transfer mode embedded into the network is represented by thermal resistances in the radial and/or axial directions, and so connecting the nodal points. Hence, the thermal networks have been built to represent the VIT components: inner and outer tubes, weld, connection and the evacuated cavity.

Figure A.1 depicts the legend used in both VIT thermal networks. Such legend takes into account the nomenclatures which have been used to define temperatures represented by the nodes, the heat transfer mode and the heat flow direction, as well as some VIT geometric characteristics.

Thermal resistance [place, region (1~5) or interface (12, 23, 34, 45, 5F), heat transfer mode, specification]	Heat transfer mode: CR – radial conduction CA – axial conduction Conv – convection Rad - radiation
Temperature [place, region/interface, specification]	Place: int – internal tube ext – external tube vac - vacuum con – connection sol - weld F – VIT extremity i - internal e - external
Specification: m – mean vertical yl – lower ys – upper d – right side e – left side Fluido – fluid ∞ - Surrounding environment	

Figure A.1 – Nomenclature for the VIT thermal network.

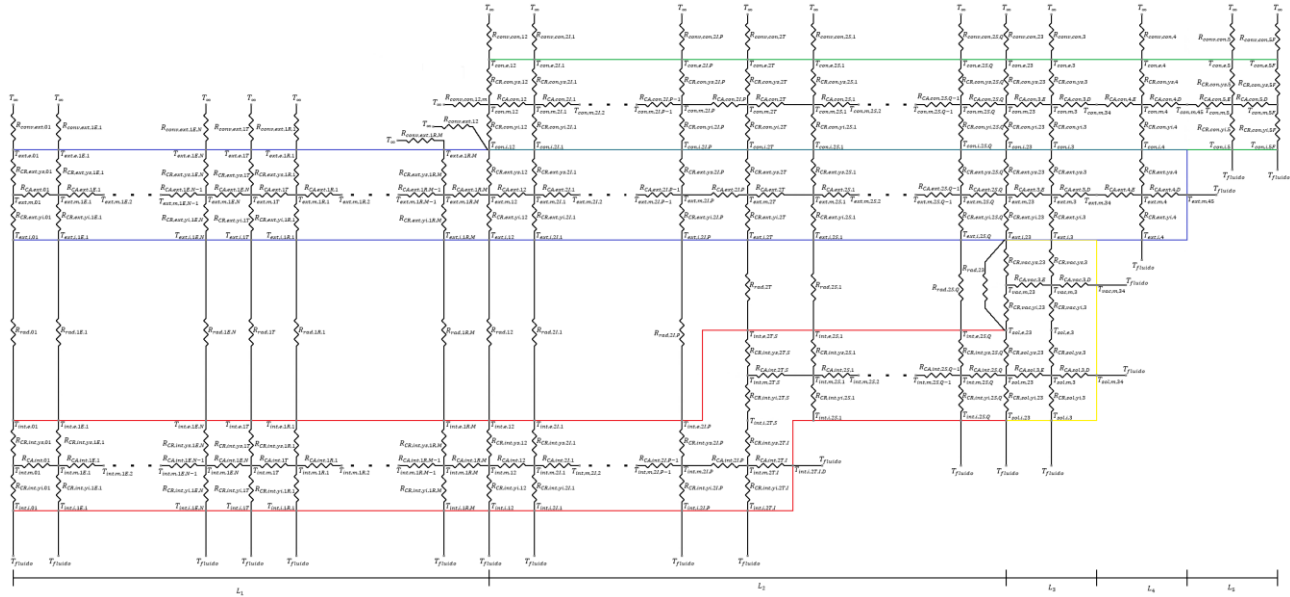


Figure A.2 – VIT 3 1/2" x 2 3/8" equivalent thermal circuit.

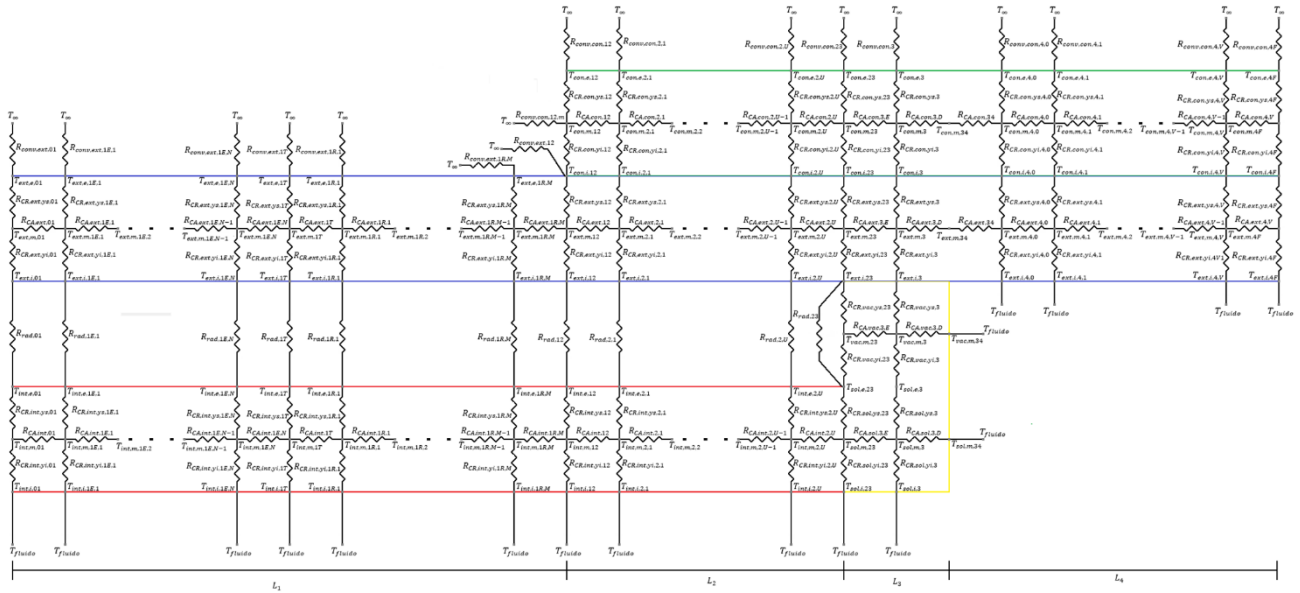


Figure A.3 – VIT 6 5/8" x 5 1/2" equivalent thermal circuit.

APPENDIX B

This appendix describes in detail the equations obtained from the VIT nodal network illustrated in Appendix A forming the system of equations. At steady state, the basic equation to represent the energy balance for the VIT cylindrical coordinates axisymmetric system on a unit area basis for a generic node into the VIT thermal network, in terms of temperature and thermal resistances is of the form

$$\frac{T_{i,j-1} - T_{i,j}}{R_{i,j-1}} + \frac{T_{i,j+1} - T_{i,j}}{R_{i,j+1}} + \frac{T_{i-1,j} - T_{i,j}}{R_{i-1,j}} + \frac{T_{i+1,j} - T_{i,j}}{R_{i+1,j}} = 0 \quad \text{B.1}$$

where a node is defined by the (i, j) combination into the VIT mesh, $T_{i,j}$ is the central node, and $T_{i,j+1}$, $T_{i+1,j}$, $T_{i,j-1}$ and $T_{i-1,j}$ are the temperatures at the adjacent nodes. The thermal resistances between adjacent nodes and the central node are given by $R_{i,j-1}$, $R_{i,j+1}$, $R_{i-1,j}$ and $R_{i+1,j}$.

The present appendix was organized in order to first present the basic thermal resistances equations as a function of the reference heat exchange area, which in turn, is calculated as a function of the external diameter of the VIT outer tube. It is worthwhile mentioning that the thermal resistance (resistivity) is calculated here in $(m^2 \cdot K)/W$. Then, all representative energy balance equations are quantified for each location into the VIT network.

The thermal resistances for all heat transfer modes involved in the thermal circuit are shown in the following sub-sections.

B.1 CONDUCTION

Radial conduction resistance between two adjacent nodes displayed at the same axial position i is calculated as a function of the geometry at that position and of the thermal conductivity as follows

$$R_{CR} = \frac{r_{he}}{k_s} \cdot \ln \left(\frac{r_{ext,j}}{r_{int,j}} \right) \quad \text{B.2}$$

where r_{he} is the heat exchange reference radius, k_s is the thermal conductivity of the carbon-steel tubing and $r_{ext,j}$ and $r_{int,j}$ are, respectively, the outer and inner radii.

With respect to the axial conduction between two adjacent nodes displayed at the same position j , the thermal resistance is calculated according to the following equation

$$R_{CA} = \frac{l_{axial}}{k_s} \quad \text{B.3}$$

where l_{axial} is the axial length between the two adjacent nodes. It should be noted that this resistance is influenced by the VIT mesh size.

B.2 CONVECTION

Convection heat transfer is applied at the VIT boundaries, while the VIT inner and outer surface walls are in contact with fluid. In the case of the internal VIT surface wall, which is in contact with the flowing fluid, a forced convection is taking place. For this situation, the forced convection thermal resistance is given by

$$R_{conv} = \frac{r_{he}}{r_{int,j}} \cdot \frac{1}{h_{ti}} \quad \text{B.4}$$

where $r_{int,j}$ is the radius related to the VIT inner wall. Thus, j can be the position 1 or 5 depending on the axial position. The forced convection heat transfer coefficient, h_{ti} , may be calculated using Chen's correlation (1963) as follows

$$h_{ti} = 0.023 \left[\frac{G(1-x)d}{\mu_l} \right]^{0.8} \left[\frac{\mu_l c_{pl}}{k_l} \right]^{0.4} \left(\frac{k_l}{d} \right) F \quad \text{B.5}$$

where F is a flow parameter defined by the ratio of the two-phase Reynolds number to the liquid Reynolds number, based on the liquid hold-up. Although this approach was developed based on convective boiling data, the heat transfer is computed as a function of two different contributions: a convective and a nucleate boiling. Here, just the first

contribution has been considered. F is calculate as a function of the Martinelli's parameter as follows

$$F = \begin{cases} 1 & \text{if } X_{tt}^{-1} \leq 0.1 \\ 2.35 \cdot (0.213 + X_{tt}^{-1})^{0.736} & \text{if } X_{tt}^{-1} > 0.1 \end{cases}, \quad \text{B.6}$$

where the Martinelli's parameter is defined as

$$X_{tt} = \left(\frac{1-x}{x} \right)^{0.9} \left(\frac{\rho_g}{\rho_l} \right)^{0.5} \left(\frac{\mu_l}{\mu_g} \right)^{0.1}. \quad \text{B.7}$$

Regarding to the VIT outer wall, the system is in contact with the annular cavity stagnant fluid. Under these circumstances, natural convection heat transfer takes place and for this reason, the convection thermal resistance may be calculated in this manner

$$R_{freeconv} = \frac{r_{he}}{r_{ext,j}} \cdot \frac{1}{h_c} \quad \text{B.8}$$

where $r_{ext,j}$ is the radius related to the VIT outer wall. Thus, j can be the position 7 or 9 depending on the axial position. The natural convection heat transfer coefficient, h_c , may be calculated considering the correlation for annulus gap provided by Hasan and Kabir (1994) based on the hydraulic diameter, d_h , as follows

$$h_c = \frac{0.1 \cdot \left(r_{int,cas} / r_{ext,j} \right)^{0.15} \cdot Ra^{0.3}}{d_h^{0.1} \cdot k_{ann} \cdot (r_{int,cas} - r_{ext,j})^{0.9}}. \quad \text{B.9}$$

where $r_{int,cas}$ is the casing internal radius, k_a is the annulus fluid thermal conductivity, Ra is the Rayleigh number for the annulus gap, calculated using the annulus fluid properties as follows

$$Ra = \frac{\beta g \rho_a^2 c_{p_a} \cdot (r_{int,cas} - r_{ext,j})^3 \cdot (T_{ext,j} - T_{int,cas})}{\mu_a \cdot k_a} \quad \text{B.10}$$

and the hydraulic diameter is defined as

$$d_h = 2 \cdot (r_{int,cas} - r_{ext,j}) \cdot \quad \text{B.11}$$

B.3 RADIATION

Radiative heat transfer takes place at the VIT's evacuated cavity, as well as between the inner casing wall and the VIT outer surface forming the production annular space. In both cases the radiative thermal resistance is defined as

$$R_{rad} = \frac{r_{he}}{r_{ext,j}} \cdot \frac{1}{h_r} \quad \text{B.12}$$

where $r_{ext,j}$ may be the external radius of the inner tubing forming the VIT cavity or the external radius of the VIT outer tubing forming the production annulus, depending on the situation, and h_r is the radiation heat transfer coefficient which is calculated considering that in both cases the cavity is formed by long concentric cylinders

$$h_r = \frac{\sigma \cdot (T_{surf1} + T_{surf2}) \cdot (T_{surf1}^2 + T_{surf2}^2)}{\frac{1}{\varepsilon} + \frac{(1-\varepsilon)}{\varepsilon} \left(\frac{r_{surf1}}{r_{surf2}} \right)} \cdot \quad \text{B.13}$$

where σ is the Stefan-Boltzmann constant, ε is the emissivity of the surfaces forming the cavity, i.e., is the same for all surfaces, and T_{surf1} and T_{surf2} are the temperature at the internal cavity surface and external cavity surface, respectively. r_{surf1} and r_{surf2} are the radii of the internal and external surface of the cavity. It should be noted that $r_{ext,j}$ is similar to r_{surf1} , that is in turn similar to r_{heat} in the case of the radiation exchange between the annulus production surfaces. With respect to the VIT cavity, r_{surf2} is the internal radius of the outer VIT tube.

B.4 ENERGY BALANCE - SYSTEM OF EQUATIONS

As abovementioned, the energy balance equations were developed in terms of the temperature difference between the temperature at the node and the adjacent nodes and the thermal

resistances as shown in Eq. B.1. According to Figures A.2 and A.3, there are a maximum of 9 nodes displayed along the VIT radial direction. Hence, in this case 9 energy balance equations are required, with the first and the ninth equations depending, respectively, on the fluid temperature due to the forced convection in the tubing and the casing inner surface temperature due to the natural convection and radiation in the annulus gap. Some examples on how the energy balance equations have been developed are shown in the following documentation.

By convention, the adopted direction of the heat flow is upward and from the center to out of the VIT, flowing radially, in the latter case. As the equations are quite similar along the VIT axial direction, respecting the geometry aspects, only three examples are presented, in other words, the energy balance equations applied at nodes located in three different positions along the r direction.

B.4.1 Lower extremity of the VIT joint

At this location the boundary condition of adiabatic wall is applied thus, no heat exchange takes place between the lower extremity of the VIT and the last tubing arranged before the VIT joints.

Figure B.4 shows the equivalent thermal circuit used to develop the system of equations for the present location. The following equations describe the energy balance applied at each node along the r axis, i.e., in this location $i = 1$ and j varies from 5 to 9.

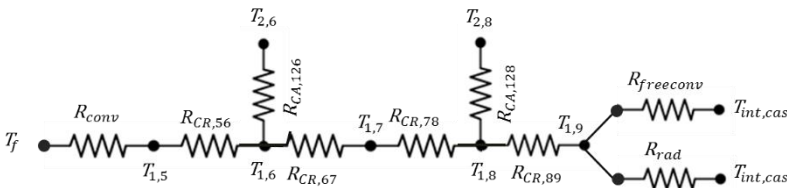


Figure B.4 - Thermal network for the lower extremity of the VIT.

The energy balance equation at node (1,5) is given by

$$\frac{T_f - T_{1,5}}{R_{conv}} - \frac{T_{1,5} - T_{1,6}}{R_{CR,56}} = 0 \tag{B.14}$$

The previous equation is rewritten to be in function of temperature as

$$\left(\frac{1}{R_{conv}}\right)T_f - \left(\frac{R_{conv} + R_{CR,56}}{R_{conv} \cdot R_{CR,56}}\right)T_{1,5} + \left(\frac{1}{R_{CR,56}}\right)T_{1,6} = 0 \quad \text{B.15}$$

Replacing R_{conv} and $R_{CR,56}$ by the thermal resistances equations obtained in the previous sections gives

$$h_{ti} \left(\frac{r_{1,5}}{r_{he}}\right)T_f - \left(\frac{h_{ti} \frac{r_{he}}{r_{1,5}} + \frac{r_{he}}{k_s} \ln\left(\frac{r_{1,6}}{r_{1,5}}\right)}{h_{ti} \frac{r_{he}^2}{r_{1,5} \cdot k_s} \cdot \ln\left(\frac{r_{1,6}}{r_{1,5}}\right)}\right)T_{1,5} + \left(\frac{k_s}{r_{he}} \cdot \frac{1}{\ln\left(\frac{r_{1,6}}{r_{1,5}}\right)}\right)T_{1,6} = 0. \quad \text{B.16}$$

Equation at node (1,6) is of the form

$$\frac{T_{1,5} - T_{1,6}}{R_{CR,56}} - \frac{T_{1,6} - T_{2,6}}{R_{CA,126}} - \frac{T_{1,6} - T_{1,7}}{R_{CR,67}} = 0. \quad \text{B.17}$$

The previous equation can be rewritten as follows

$$\left(\frac{1}{R_{CR,56}}\right)T_{1,5} - \left(\frac{R_{CR,56} \cdot R_{CA,126} + R_{CR,56} \cdot R_{CR,67} + R_{CA,126} \cdot R_{CR,67}}{R_{CR,56} \cdot R_{CA,126} \cdot R_{CR,67}}\right)T_{1,6} + \left(\frac{1}{R_{CA,126}}\right)T_{2,6} + \left(\frac{1}{R_{CR,67}}\right)T_{1,7} = 0 \quad \text{B.18}$$

substituting the thermal resistances yields

$$\begin{aligned}
& \left(\frac{k_s}{r_{he}} \cdot \frac{1}{\ln\left(\frac{r_{1,6}}{r_{1,5}}\right)} \right) T_{1,5} \\
& - \frac{k_s \left(l_{1,2} \cdot \ln\left(\frac{r_{1,6}}{r_{1,5}}\right) + r_{he} \cdot \ln\left(\frac{r_{1,6}}{r_{1,5}}\right) \ln\left(\frac{r_{1,7}}{r_{1,6}}\right) + \right. \\
& \left. \frac{l_{1,2} \cdot \ln\left(\frac{r_{1,7}}{r_{1,6}}\right)}{l_{1,2} \cdot \ln\left(\frac{r_{1,6}}{r_{1,5}}\right) \ln\left(\frac{r_{1,7}}{r_{1,6}}\right)} \right) T_{1,6} + \left(\frac{k_s}{l_{1,2}} \right) T_{2,6} \\
& + \left(\frac{k_s}{r_{he}} \cdot \frac{1}{\ln\left(\frac{r_{1,7}}{r_{1,6}}\right)} \right) T_{1,7} = 0.
\end{aligned} \tag{B.19}$$

The energy balance applied at node (1,7) gives

$$\frac{T_{1,6} - T_{1,7}}{R_{CR,67}} - \frac{T_{1,7} - T_{1,8}}{R_{CR,78}} = 0 \tag{B.20}$$

Equation (B.20) can be rewritten as follows

$$\left(\frac{1}{R_{CR,67}} \right) T_{1,6} - \left(\frac{R_{CR,67} + R_{CR,78}}{R_{CR,67} \cdot R_{CR,78}} \right) T_{1,7} + \left(\frac{1}{R_{CR,78}} \right) T_{1,8} = 0 \tag{B.21}$$

and substituting the thermal resistances in the previous equation produces

$$\begin{aligned}
& \left(\frac{k_s}{r_{he}} \cdot \frac{1}{\ln\left(\frac{r_{1,7}}{r_{1,6}}\right)} \right) T_{1,6} - \frac{k_s}{r_{he}} \left(\frac{\ln\left(\frac{r_{1,7}}{r_{1,6}}\right) + \ln\left(\frac{r_{1,8}}{r_{1,7}}\right)}{\ln\left(\frac{r_{1,7}}{r_{1,6}}\right) \cdot \ln\left(\frac{r_{1,8}}{r_{1,7}}\right)} \right) T_{1,7} \\
& + \left(\frac{k_s}{r_{he}} \cdot \frac{1}{\ln\left(\frac{r_{1,8}}{r_{1,7}}\right)} \right) T_{1,8} = 0.
\end{aligned} \tag{B.22}$$

The energy balance applied at node (1,8) yields

$$\frac{T_{1,7} - T_{1,8}}{R_{CR,78}} - \frac{T_{1,8} - T_{2,8}}{R_{CA,128}} - \frac{T_{1,8} - T_{1,9}}{R_{CR,89}} = 0. \quad \text{B.23}$$

Rewriting Eq. B.23, such equation takes the form of

$$\begin{aligned} & \left(\frac{1}{R_{CR,78}} \right) T_{1,7} \\ & - \left(\frac{R_{CR,78} \cdot R_{CA,128} + R_{CR,78} \cdot R_{CR,89} + R_{CA,128} \cdot R_{CR,89}}{R_{CR,78} \cdot R_{CA,128} \cdot R_{CR,89}} \right) T_{1,8} \\ & + \left(\frac{1}{R_{CA,128}} \right) T_{2,8} + \left(\frac{1}{R_{CR,89}} \right) T_{1,9} = 0 \end{aligned} \quad \text{B.24}$$

Replacing $R_{CR,78}$, $R_{CA,128}$ and $R_{CR,89}$ by the thermal resistances shown in the previous section produces

$$\begin{aligned} & \left(\frac{k_s}{r_{he}} \cdot \frac{1}{\ln\left(\frac{r_{1,8}}{r_{1,7}}\right)} \right) T_{1,7} \\ & - \frac{k_s}{r_{he}} \left(\frac{l_{1,2} \cdot \ln\left(\frac{r_{1,8}}{r_{1,7}}\right) + r_{he} \cdot \ln\left(\frac{r_{1,8}}{r_{1,7}}\right) \ln\left(\frac{r_{1,9}}{r_{1,8}}\right)}{l_{1,2} \cdot \ln\left(\frac{r_{1,8}}{r_{1,7}}\right) \cdot \ln\left(\frac{r_{1,9}}{r_{1,8}}\right)} \right. \\ & \left. + \frac{l_{1,2} \cdot \ln\left(\frac{r_{1,9}}{r_{1,8}}\right)}{l_{1,2} \cdot \ln\left(\frac{r_{1,8}}{r_{1,7}}\right) \ln\left(\frac{r_{1,9}}{r_{1,8}}\right)} \right) T_{1,8} + \left(\frac{k_s}{l_{1,2}} \right) T_{2,8} \\ & + \left(\frac{k_s}{r_{he}} \cdot \frac{1}{\ln\left(\frac{r_{1,9}}{r_{1,8}}\right)} \right) T_{1,9} = 0. \end{aligned} \quad \text{B.25}$$

Finally, the energy balance equation at node (1,9) is defined as

$$\frac{T_{1,8} - T_{1,9}}{R_{CR,89}} - \frac{T_{1,9} - T_{int,cas}}{R_c} - \frac{T_{1,9} - T_{int,cas}}{R_{rad}} = 0, \quad \text{B.26}$$

that can be rewritten producing

$$\left(\frac{1}{R_{CR,89}}\right) \cdot T_{1,8} - \left(\frac{R_{CR,89} \cdot R_c + R_{CR,89} \cdot R_{rad} + R_c \cdot R_{rad}}{R_{CR,89} \cdot R_c \cdot R_{rad}}\right) \cdot T_{1,9} + \left(\frac{R_c + R_{rad}}{R_c \cdot R_{rad}}\right) \cdot T_{int,cas} = 0 \tag{B.27}$$

Substituting the thermal resistances at the present equation yields

$$\left(\frac{k_s}{r_{he}} \cdot \frac{1}{\ln\left(\frac{r_{1,9}}{r_{1,8}}\right)}\right) \cdot T_{1,8} - \left(\frac{\frac{1}{h_c \cdot k_s} \cdot \ln\left(\frac{r_{1,8}}{r_{1,7}}\right) + \frac{1}{h_r \cdot k_s} \cdot \ln\left(\frac{r_{1,8}}{r_{1,7}}\right) + \frac{1}{h_c \cdot h_r} \cdot \frac{1}{r_{1,9}}}{\frac{1}{h_c \cdot h_r} \cdot \frac{r_{he}}{r_{1,9} \cdot k_s} \ln\left(\frac{r_{1,8}}{r_{1,7}}\right)}\right) T_{1,9} + \left(\frac{r_{1,9}}{r_{he}} \cdot (h_c + h_r)\right) T_{int,cas} = 0 \tag{B.28}$$

B.4.2 Interface between sections 2 and 3

At this location there is an interface between the weld and the evacuated enclosure. Thus, a parallel circuit takes place in this interface as detailed in Figure B.5. The following equations show the energy balance applied at each node along the r axis at the interface between sections 2 and 3, i.e., $i = 9$ and j varies from 1 to 9.

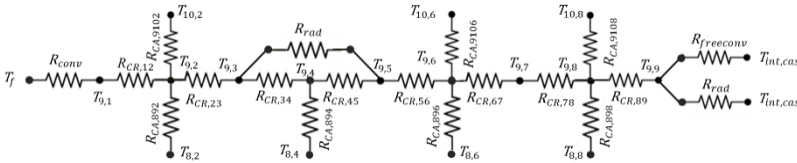


Figure B.5 - Thermal network for the interface between sections 2 and 3.

Hence, the energy balance equation at node (9,1) is given by

$$\frac{T_f - T_{9,1}}{R_{conv,91}} - \frac{T_{9,1} - T_{9,2}}{R_{CR,12}} = 0 \tag{B.29}$$

Equation (B.29) is then rewritten to be in function of temperature as

$$\left(\frac{1}{R_{conv,91}}\right)T_f - \left(\frac{R_{conv,91} + R_{CR,12}}{R_{conv,91} \cdot R_{CR,12}}\right)T_{9,1} + \left(\frac{1}{R_{CR,12}}\right)T_{9,2} = 0 \quad \text{B.30}$$

Replacing $R_{conv,91}$ and $R_{CR,12}$ by the thermal resistances equations obtained in the previous sections gives

$$h_{ti} \left(\frac{r_{9,1}}{r_{he}}\right) T_f - \left(\frac{\frac{h_{ti}}{r_{9,1}} + \frac{1}{k_s} \ln\left(\frac{r_{9,2}}{r_{9,1}}\right)}{h_{ti} \frac{r_{he}}{r_{9,1} \cdot k_s} \cdot \ln\left(\frac{r_{9,2}}{r_{9,1}}\right)}\right) T_{9,1} + \left(\frac{k_s}{r_{he}} \cdot \frac{1}{\ln\left(\frac{r_{9,2}}{r_{9,1}}\right)}\right) T_{9,2} = 0. \quad \text{B.31}$$

The energy balance applied at node (9,2) yields

$$\frac{T_{9,1} - T_{9,2}}{R_{CR,12}} + \frac{T_{8,2} - T_{9,2}}{R_{CA,892}} - \frac{T_{9,2} - T_{10,2}}{R_{CA,9102}} - \frac{T_{9,2} - T_{9,3}}{R_{CR,23}} = 0. \quad \text{B.32}$$

Rewriting Eq. (B.32) gives

$$\begin{aligned} & \left(\frac{1}{R_{CR,12}}\right)T_{9,1} \\ & - \left(\frac{R_{CR,12} \cdot R_{CA,892} \cdot R_{CA,9102} + R_{CR,12} \cdot R_{CA,892} \cdot R_{CR,23}}{R_{CR,12} \cdot R_{CA,892} \cdot R_{CA,9102} \cdot R_{CR,23}}\right. \\ & \left. + \frac{R_{CR,12} \cdot R_{CA,9102} \cdot R_{CR,23} + R_{CA,892} \cdot R_{CA,9102} \cdot R_{CR,23}}{R_{CR,12} \cdot R_{CA,892} \cdot R_{CA,9102} \cdot R_{CR,23}}\right) T_{9,2} \\ & + \left(\frac{1}{R_{CA,892}}\right)T_{8,2} + \left(\frac{1}{R_{CA,9102}}\right)T_{10,2} + \left(\frac{1}{R_{CR,23}}\right)T_{9,3} = 0 \end{aligned} \quad \text{B.33}$$

substituting the thermal resistances yields

$$\begin{aligned}
& \left(\frac{k_s}{r_{he}} \cdot \frac{1}{\ln\left(\frac{r_{9,2}}{r_{9,1}}\right)} \right) T_{9,1} \\
& - \frac{k_s}{r_{he}} \left(\frac{l_{8,9} l_{9,10} \cdot \ln\left(\frac{r_{9,2}}{r_{9,1}}\right) + r_{heat} l_{8,9} \ln\left(\frac{r_{9,2}}{r_{9,1}}\right) \ln\left(\frac{r_{9,3}}{r_{9,2}}\right) +}{l_{8,9} l_{9,10} \cdot \ln\left(\frac{r_{9,2}}{r_{9,1}}\right) \ln\left(\frac{r_{9,3}}{r_{9,2}}\right)} \right. \\
& \left. + \frac{r_{he} l_{9,10} \ln\left(\frac{r_{9,2}}{r_{9,1}}\right) \ln\left(\frac{r_{9,3}}{r_{9,2}}\right) + l_{8,9} l_{9,10} \cdot \ln\left(\frac{r_{9,3}}{r_{9,2}}\right)}{l_{8,9} l_{9,10} \cdot \ln\left(\frac{r_{9,2}}{r_{9,1}}\right) \ln\left(\frac{r_{9,3}}{r_{9,2}}\right)} \right) T_{9,2} \\
& + \left(\frac{k_s}{l_{89}} \right) T_{8,2} + \left(\frac{k_s}{l_{9,10}} \right) T_{10,2} + \left(\frac{k_s}{r_{he}} \cdot \frac{1}{\ln\left(\frac{r_{9,3}}{r_{9,2}}\right)} \right) T_{9,3} = 0.
\end{aligned} \tag{B.34}$$

The energy balance applied at node (9,3) gives

$$\frac{T_{9,2} - T_{9,3}}{R_{CR,23}} - \frac{T_{9,3} - T_{9,4}}{R_{CR,34}} - \frac{T_{9,3} - T_{9,5}}{R_{rad}} = 0 \tag{B.35}$$

Equation (B.35) can be rewritten as follows

$$\begin{aligned}
& \left(\frac{1}{R_{CR,23}} \right) T_{9,2} \\
& - \left(\frac{R_{CR,23} \cdot R_{CR,34} + R_{CR,23} \cdot R_{rad} + R_{CR,34} \cdot R_{rad}}{R_{CR,23} \cdot R_{CR,34} \cdot R_{rad}} \right) T_{9,3} \\
& + \left(\frac{1}{R_{CR,34}} \right) T_{9,4} + \left(\frac{1}{R_{rad}} \right) T_{9,5} = 0
\end{aligned} \tag{B.36}$$

and substituting the thermal resistances in the previous equation produces

$$\begin{aligned}
& \left(\frac{k_s}{r_{he}} \cdot \frac{1}{\ln\left(\frac{r_{9,3}}{r_{9,2}}\right)} \right) T_{9,2} \\
& - \frac{k_s \left(\frac{1}{r_{9,3} h_r} \ln\left(\frac{r_{9,3}}{r_{9,2}}\right) + \frac{1}{k_s} \ln\left(\frac{r_{9,3}}{r_{9,2}}\right) \ln\left(\frac{r_{9,4}}{r_{9,3}}\right) + \right. \\
& \left. \frac{1}{r_{9,3} h_r} \cdot \ln\left(\frac{r_{9,3}}{r_{9,2}}\right) \ln\left(\frac{r_{9,4}}{r_{9,3}}\right) \right)}{r_{he}} T_{9,3} + \left(\frac{k_s}{r_{he}} \cdot \frac{1}{\ln\left(\frac{r_{9,4}}{r_{9,3}}\right)} \right) T_{9,4} \\
& + \frac{1}{r_{9,3} h_r} \cdot \ln\left(\frac{r_{9,3}}{r_{9,2}}\right) \ln\left(\frac{r_{9,4}}{r_{9,3}}\right) T_{9,3} + \left(\frac{k_s}{r_{he}} \cdot \frac{1}{\ln\left(\frac{r_{9,4}}{r_{9,3}}\right)} \right) T_{9,4} \\
& + \left(\frac{r_{9,3} h_r}{r_{he}} \right) T_{9,5} = 0.
\end{aligned} \tag{B.37}$$

The energy balance applied at node (9,4) yields

$$\frac{T_{9,3} - T_{9,4}}{R_{CR,34}} + \frac{T_{8,4} - T_{9,4}}{R_{CA,894}} - \frac{T_{9,4} - T_{9,5}}{R_{CR,45}} = 0. \tag{B.38}$$

Rewriting Eq. (B.38), such equation takes the form of

$$\begin{aligned}
& \left(\frac{1}{R_{CR,34}} \right) T_{9,3} \\
& - \left(\frac{R_{CR,34} \cdot R_{CA,894} + R_{CR,34} \cdot R_{CR,45} + R_{CA,894} \cdot R_{CR,45}}{R_{CR,34} \cdot R_{CA,894} \cdot R_{CR,45}} \right) T_{9,4} \\
& + \left(\frac{1}{R_{CA,894}} \right) T_{8,4} + \left(\frac{1}{R_{CR,45}} \right) T_{9,5} = 0
\end{aligned} \tag{B.39}$$

Replacing $R_{CR,34}$, $R_{CA,894}$ and $R_{CR,45}$ by the thermal resistances shown in the previous section produces

$$\begin{aligned}
& \left(\frac{k_s}{r_{he}} \cdot \frac{1}{\ln\left(\frac{r_{9,4}}{r_{9,3}}\right)} \right) T_{9,3} \\
& - \frac{k_s \left(l_{8,9} \cdot \ln\left(\frac{r_{9,4}}{r_{9,3}}\right) + r_{he} \cdot \ln\left(\frac{r_{9,4}}{r_{9,3}}\right) \ln\left(\frac{r_{9,5}}{r_{9,4}}\right) \right)}{r_{he} \left(l_{8,9} \cdot \ln\left(\frac{r_{9,4}}{r_{9,3}}\right) \ln\left(\frac{r_{9,5}}{r_{9,4}}\right) \right)} \\
& + \frac{l_{8,9} \cdot \ln\left(\frac{r_{9,5}}{r_{9,4}}\right)}{l_{8,9} \cdot \ln\left(\frac{r_{9,4}}{r_{9,3}}\right) \ln\left(\frac{r_{9,5}}{r_{9,4}}\right)} T_{9,4} + \left(\frac{k_s}{l_{8,9}} \right) T_{8,4} \\
& + \left(\frac{k_s}{r_{he}} \cdot \frac{1}{\ln\left(\frac{r_{9,5}}{r_{9,4}}\right)} \right) T_{9,5} = 0.
\end{aligned} \tag{B.39}$$

The energy balance applied at node (9,5) produces

$$\frac{T_{9,3} - T_{9,5}}{R_{rad}} + \frac{T_{9,4} - T_{9,5}}{R_{CR,45}} - \frac{T_{9,5} - T_{9,6}}{R_{CR,56}} = 0 \tag{B.40}$$

Equation (B.40) is rewritten as follows

$$\begin{aligned}
& \left(\frac{1}{R_{rad}} \right) T_{9,3} \\
& - \left(\frac{R_{CR,45} \cdot R_{CR,56} + R_{CR,45} \cdot R_{rad} + R_{CR,56} \cdot R_{rad}}{R_{CR,45} \cdot R_{CR,56} \cdot R_{rad}} \right) T_{9,5} \\
& + \left(\frac{1}{R_{CR,45}} \right) T_{9,4} + \left(\frac{1}{R_{CR,56}} \right) T_{9,6} = 0
\end{aligned} \tag{B.41}$$

and substituting the thermal resistances in the previous equation produces

$$\begin{aligned}
h_r \left(\frac{r_{9,3}}{r_{he}} \right) T_{9,3} - \frac{k_s}{r_{he}} & \left(\frac{1}{r_{9,3} h_r} \ln \left(\frac{r_{9,5}}{r_{9,4}} \right) + \frac{1}{k_s} \ln \left(\frac{r_{9,5}}{r_{9,4}} \right) \ln \left(\frac{r_{9,6}}{r_{9,5}} \right) + \right. \\
& \left. \frac{1}{r_{9,3} h_r} \cdot \ln \left(\frac{r_{9,5}}{r_{9,4}} \right) \ln \left(\frac{r_{9,6}}{r_{9,5}} \right) \right. \\
& \left. + \frac{1}{r_{9,3} h_r} \ln \left(\frac{r_{9,6}}{r_{9,5}} \right) \right) T_{9,5} \\
& + \frac{1}{r_{9,3} h_r} \cdot \ln \left(\frac{r_{9,5}}{r_{9,4}} \right) \ln \left(\frac{r_{9,6}}{r_{9,5}} \right) \Big) T_{9,5} \\
& + \left(\frac{k_s}{r_{he}} \cdot \frac{1}{\ln \left(\frac{r_{9,5}}{r_{9,4}} \right)} \right) T_{9,4} + h_r \left(\frac{r_{9,3}}{r_{he}} \right) T_{9,6} \\
& = 0.
\end{aligned} \tag{B.42}$$

The energy balance equation at node (9,6) yields

$$\frac{T_{9,5} - T_{9,6}}{R_{CR,56}} + \frac{T_{8,6} - T_{9,6}}{R_{CA,896}} - \frac{T_{9,6} - T_{10,6}}{R_{CA,9106}} - \frac{T_{9,6} - T_{9,7}}{R_{CR,67}} = 0. \tag{B.43}$$

Rewriting Eq. (B.43) gives

$$\begin{aligned}
& \left(\frac{1}{R_{CR,56}} \right) T_{9,5} \\
& - \left(\frac{R_{CR,56} \cdot R_{CA,896} \cdot R_{CA,9106} + R_{CR,56} \cdot R_{CA,896} \cdot R_{CR,67}}{R_{CR,56} \cdot R_{CA,896} \cdot R_{CA,9106} \cdot R_{CR,67}} \right. \\
& \left. + \frac{R_{CR,56} \cdot R_{CA,9106} \cdot R_{CR,67} + R_{CA,896} \cdot R_{CA,9106} \cdot R_{CR,67}}{R_{CR,56} \cdot R_{CA,896} \cdot R_{CA,9106} \cdot R_{CR,67}} \right) T_{9,6} \\
& + \left(\frac{1}{R_{CA,896}} \right) T_{8,6} + \left(\frac{1}{R_{CA,9106}} \right) T_{10,6} + \left(\frac{1}{R_{CR,67}} \right) T_{9,7} = 0
\end{aligned} \tag{B.44}$$

substituting the thermal resistances yields

$$\begin{aligned}
& \left(\frac{k_s}{r_{he}} \cdot \frac{1}{\ln\left(\frac{r_{9,6}}{r_{9,5}}\right)} \right) T_{9,5} \\
& - \frac{k_s}{r_{he}} \left(\frac{l_{8,9} l_{9,10} \cdot \ln\left(\frac{r_{9,6}}{r_{9,5}}\right) + r_{he} l_{8,9} \ln\left(\frac{r_{9,6}}{r_{9,5}}\right) \ln\left(\frac{r_{9,7}}{r_{9,6}}\right) +}{l_{8,9} l_{9,10} \cdot \ln\left(\frac{r_{9,6}}{r_{9,5}}\right) \ln\left(\frac{r_{9,7}}{r_{9,6}}\right)} \right. \\
& \left. + \frac{r_{he} l_{9,10} \ln\left(\frac{r_{9,6}}{r_{9,5}}\right) \ln\left(\frac{r_{9,7}}{r_{9,6}}\right) + l_{8,9} l_{9,10} \cdot \ln\left(\frac{r_{9,7}}{r_{9,6}}\right)}{l_{8,9} l_{9,10} \cdot \ln\left(\frac{r_{9,6}}{r_{9,5}}\right) \ln\left(\frac{r_{9,7}}{r_{9,6}}\right)} \right) T_{9,6} \\
& + \left(\frac{k_s}{l_{89}} \right) T_{8,6} + \left(\frac{k_s}{l_{9,10}} \right) T_{10,6} + \left(\frac{k_s}{r_{he}} \cdot \frac{1}{\ln\left(\frac{r_{9,7}}{r_{9,6}}\right)} \right) T_{9,7} = 0.
\end{aligned} \tag{B.45}$$

The energy balance applied at node (9,7) gives

$$\frac{T_{9,6} - T_{9,7}}{R_{CR,67}} - \frac{T_{9,7} - T_{9,8}}{R_{CR,78}} = 0 \tag{B.46}$$

Equation (B.46) can be rewritten as follows

$$\left(\frac{1}{R_{CR,67}} \right) T_{9,6} - \left(\frac{R_{CR,67} + R_{CR,78}}{R_{CR,67} \cdot R_{CR,78}} \right) T_{9,7} + \left(\frac{1}{R_{CR,78}} \right) T_{9,8} = 0 \tag{B.47}$$

and substituting the thermal resistances in the previous equation produces

$$\begin{aligned}
& \left(\frac{k_s}{r_{he}} \cdot \frac{1}{\ln\left(\frac{r_{9,7}}{r_{9,6}}\right)} \right) T_{9,6} - \frac{k_s}{r_{he}} \left(\frac{\ln\left(\frac{r_{9,7}}{r_{9,6}}\right) + \ln\left(\frac{r_{9,8}}{r_{9,7}}\right)}{\ln\left(\frac{r_{9,7}}{r_{9,6}}\right) \cdot \ln\left(\frac{r_{9,8}}{r_{9,7}}\right)} \right) T_{9,7} \\
& + \left(\frac{k_s}{r_{he}} \cdot \frac{1}{\ln\left(\frac{r_{9,8}}{r_{9,7}}\right)} \right) T_{9,8} = 0.
\end{aligned} \tag{B.48}$$

The energy balance equation at node (9,8) is given by

$$\frac{T_{9,7} - T_{9,8}}{R_{CR,78}} + \frac{T_{8,8} - T_{9,8}}{R_{CA,898}} - \frac{T_{9,8} - T_{10,8}}{R_{CA,9108}} - \frac{T_{9,8} - T_{9,9}}{R_{CR,89}} = 0. \quad \text{B.49}$$

Rewriting Eq. (B.49) gives

$$\begin{aligned} & \left(\frac{1}{R_{CR,78}} \right) T_{9,7} \\ & - \left(\frac{R_{CR,78} \cdot R_{CA,898} \cdot R_{CA,9108} + R_{CR,78} \cdot R_{CA,898} \cdot R_{CR,89}}{R_{CR,78} \cdot R_{CA,898} \cdot R_{CA,9108} \cdot R_{CR,89}} \right. \\ & \left. + \frac{R_{CR,78} \cdot R_{CA,9108} \cdot R_{CR,89} + R_{CA,898} \cdot R_{CA,9106} \cdot R_{CR,89}}{R_{CR,56} \cdot R_{CA,896} \cdot R_{CA,9106} \cdot R_{CR,67}} \right) T_{9,8} \\ & + \left(\frac{1}{R_{CA,898}} \right) T_{8,8} + \left(\frac{1}{R_{CA,9108}} \right) T_{10,8} + \left(\frac{1}{R_{CR,89}} \right) T_{9,9} = 0 \end{aligned} \quad \text{B.50}$$

substituting the thermal resistances yields

$$\begin{aligned} & \left(\frac{k_s}{r_{he}} \cdot \frac{1}{\ln\left(\frac{r_{9,8}}{r_{9,7}}\right)} \right) T_{9,7} \\ & - \frac{k_s}{r_{he}} \left(\frac{l_{8,9} l_{9,10} \cdot \ln\left(\frac{r_{9,8}}{r_{9,7}}\right) + r_{he} l_{8,9} \ln\left(\frac{r_{9,8}}{r_{9,7}}\right) \ln\left(\frac{r_{9,9}}{r_{9,8}}\right) +}{l_{8,9} l_{9,10} \cdot \ln\left(\frac{r_{9,8}}{r_{9,7}}\right) \ln\left(\frac{r_{9,9}}{r_{9,8}}\right)} \right. \\ & \left. + \frac{r_{he} l_{9,10} \ln\left(\frac{r_{9,8}}{r_{9,7}}\right) \ln\left(\frac{r_{9,9}}{r_{9,8}}\right) + l_{8,9} l_{9,10} \cdot \ln\left(\frac{r_{9,9}}{r_{9,8}}\right)}{l_{8,9} l_{9,10} \cdot \ln\left(\frac{r_{9,8}}{r_{9,7}}\right) \ln\left(\frac{r_{9,9}}{r_{9,8}}\right)} \right) T_{9,8} \\ & + \left(\frac{k_s}{l_{89}} \right) T_{8,8} + \left(\frac{k_s}{l_{9,10}} \right) T_{10,8} + \left(\frac{k_s}{r_{he}} \cdot \frac{1}{\ln\left(\frac{r_{9,9}}{r_{9,8}}\right)} \right) T_{9,9} = 0. \end{aligned} \quad \text{B.51}$$

Finally, the energy balance applied at node (9,9) produces

$$\frac{T_{9,8} - T_{9,9}}{R_{CR,89}} - \frac{T_{9,9} - T_{int,cas}}{R_c} - \frac{T_{9,9} - T_{int,cas}}{R_{rad}} = 0, \quad \text{B.52}$$

that can be rewritten producing

$$\begin{aligned} & \left(\frac{1}{R_{CR,89}} \right) \cdot T_{9,8} \\ & - \left(\frac{R_{CR,89} \cdot R_c + R_{CR,89} \cdot R_{rad} + R_c \cdot R_{rad}}{R_{CR,89} \cdot R_c \cdot R_{rad}} \right) T_{9,9} \\ & + \left(\frac{R_c + R_{rad}}{R_c \cdot R_{rad}} \right) \cdot T_{int,cas} = 0 \end{aligned} \tag{B.53}$$

Substituting the thermal resistances at the present equation yields

$$\begin{aligned} & \left(\frac{k_s}{r_{he}} \cdot \frac{1}{\ln \left(\frac{r_{9,9}}{r_{9,8}} \right)} \right) \cdot T_{9,8} \\ & - \left(\frac{\frac{1}{h_c \cdot k_s} \cdot \ln \left(\frac{r_{9,8}}{r_{9,7}} \right) + \frac{1}{r_{9,9}} \cdot \frac{1}{h_r \cdot k_s} \cdot \ln \left(\frac{r_{9,8}}{r_{9,7}} \right) + \frac{1}{h_c \cdot h_r} \cdot \frac{1}{r_{9,9}}}{\frac{1}{h_c \cdot h_r} \cdot \frac{r_{he}}{r_{9,9} \cdot k_s} \ln \left(\frac{r_{9,8}}{r_{9,7}} \right)} \right) T_{9,9} \\ & + \left(\frac{r_{9,9}}{r_{he}} \cdot (h_c + h_r) \right) T_{int,cas} = 0 \end{aligned} \tag{B.54}$$

B.4.3 Interface between sections 1 and 2

At this location, the coupling region is exposed to the annulus fluid radially. Figure B.6 illustrates the equivalent thermal circuit for such location. The following equations describe the energy balance applied at each node along the r axis, i.e., $i = 13$.

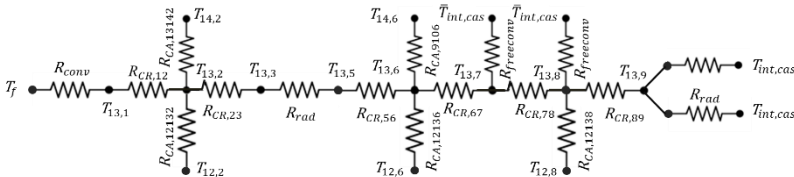


Figure B.6 - Thermal network for the interface between section 1 and 2.

The energy balance equation at node (13,1) is defined similarly to Eq. (B.29), given by

$$\frac{T_f - T_{13,1}}{R_{conv}} - \frac{T_{13,1} - T_{13,2}}{R_{CR,12}} = 0. \quad \text{B.55}$$

Rewriting Eq. (B.55) and substituting the thermal resistances yields

$$\begin{aligned} h_{ti} \left(\frac{r_{13,1}}{r_{he}} \right) T_f - \left(\frac{\frac{h_{ti}}{r_{13,1}} + \frac{1}{k_s} \ln \left(\frac{r_{13,2}}{r_{13,1}} \right)}{h_{ti} \frac{r_{he}}{r_{13,1} \cdot k_s} \cdot \ln \left(\frac{r_{13,2}}{r_{13,1}} \right)} \right) T_{13,1} \\ + \left(\frac{k_s}{r_{he}} \cdot \frac{1}{\ln \left(\frac{r_{13,2}}{r_{13,1}} \right)} \right) T_{13,2} = 0. \end{aligned} \quad \text{B.56}$$

Also, the energy balance applied at node (13,2) is similar to that for the node (9,2) previously presented

$$\frac{T_{9,1} - T_{9,2}}{R_{CR,12}} + \frac{T_{8,2} - T_{9,2}}{R_{CA,892}} - \frac{T_{9,2} - T_{10,2}}{R_{CA,9102}} - \frac{T_{9,2} - T_{9,3}}{R_{CR,23}} = 0. \quad \text{B.57}$$

Rewriting Eq. (B.57) gives

$$\begin{aligned} \left(\frac{1}{R_{CR,12}} \right) T_{9,1} \\ - \left(\frac{R_{CR,12} \cdot R_{CA,892} \cdot R_{CA,9102} + R_{CR,12} \cdot R_{CA,892} \cdot R_{CR,23}}{R_{CR,12} \cdot R_{CA,892} \cdot R_{CA,9102} \cdot R_{CR,23}} \right. \\ \left. + \frac{R_{CR,12} \cdot R_{CA,9102} \cdot R_{CR,23} + R_{CA,892} \cdot R_{CA,9102} \cdot R_{CR,23}}{R_{CR,12} \cdot R_{CA,892} \cdot R_{CA,9102} \cdot R_{CR,23}} \right) T_{9,2} \\ + \left(\frac{1}{R_{CA,892}} \right) T_{8,2} + \left(\frac{1}{R_{CA,9102}} \right) T_{10,2} + \left(\frac{1}{R_{CR,23}} \right) T_{9,3} = 0 \end{aligned} \quad \text{B.58}$$

substituting the thermal resistances yields

$$\begin{aligned}
& \left(\frac{k_s}{r_{he}} \cdot \frac{1}{\ln\left(\frac{r_{13,2}}{r_{13,1}}\right)} \right) T_{13,1} \\
& - \frac{k_s}{r_{he}} \left(\frac{l_{12,13} l_{13,14} \ln\left(\frac{r_{13,2}}{r_{13,1}}\right) + r_{he} l_{12,13} \ln\left(\frac{r_{13,2}}{r_{13,1}}\right) \ln\left(\frac{r_{13,3}}{r_{13,2}}\right) +}{l_{12,13} l_{13,14} \ln\left(\frac{r_{13,2}}{r_{13,1}}\right) \ln\left(\frac{r_{13,3}}{r_{13,2}}\right)} \right. \\
& \left. + \frac{r_{he} l_{13,14} \ln\left(\frac{r_{13,2}}{r_{13,1}}\right) \ln\left(\frac{r_{13,3}}{r_{13,2}}\right) + l_{12,13} l_{13,14} \ln\left(\frac{r_{13,3}}{r_{13,2}}\right)}{l_{12,13} l_{13,14} \ln\left(\frac{r_{13,2}}{r_{13,1}}\right) \ln\left(\frac{r_{13,3}}{r_{13,2}}\right)} \right) T_{13,2} \\
& + \left(\frac{k_s}{l_{12,13}} \right) T_{12,2} + \left(\frac{k_s}{l_{13,14}} \right) T_{14,2} + \left(\frac{k_s}{r_{he}} \cdot \frac{1}{\ln\left(\frac{r_{13,3}}{r_{13,2}}\right)} \right) T_{13,3} \\
& = 0.
\end{aligned} \tag{B.59}$$

The energy balance equation at node (13,3) is defined as

$$\frac{T_{13,2} - T_{13,3}}{R_{CR,23}} - \frac{T_{13,3} - T_{13,5}}{R_{rad}} = 0. \tag{B.60}$$

Eq. (B.60) is rewritten to produce

$$\left(\frac{1}{R_{CR,23}} \right) T_{13,2} - \left(\frac{R_{CR,23} + R_{rad}}{R_{CR,23} \cdot R_{rad}} \right) T_{13,3} + \left(\frac{1}{R_{rad}} \right) T_{13,5} = 0 \tag{B.61}$$

Substituting the thermal resistances in the previous equation, the energy balance assumes the form

$$\begin{aligned}
& \left(\frac{k_s}{r_{he}} \cdot \frac{1}{\ln\left(\frac{r_{13,3}}{r_{13,2}}\right)} \right) T_{13,2} - \frac{k_s}{r_{he}} \left(\frac{\frac{1}{k_s} \ln\left(\frac{r_{13,3}}{r_{13,2}}\right) + \frac{1}{r_{13,3} h_r}}{\frac{1}{r_{13,3} h_r} \cdot \ln\left(\frac{r_{13,3}}{r_{13,2}}\right)} \right) T_{13,3} \\
& + \left(\frac{r_{13,3} h_r}{r_{he}} \right) T_{13,5} = 0.
\end{aligned} \tag{B.62}$$

The energy balance applied at node (13,5) gives

$$\frac{T_{13,3} - T_{13,5}}{R_{rad}} - \frac{T_{13,5} - T_{13,6}}{R_{CR,56}} = 0. \quad \text{B.63}$$

Thus, Eq. (A.63) is rewritten to yield

$$\left(\frac{1}{R_{rad}}\right) T_{13,3} - \left(\frac{R_{CR,56} + R_{rad}}{R_{CR,56} \cdot R_{rad}}\right) T_{13,5} + \left(\frac{1}{R_{CR,56}}\right) T_{13,6} = 0 \quad \text{B.64}$$

Substituting the thermal resistances in Eq. (B.64) produces

$$\begin{aligned} \left(\frac{r_{13,3} h_r}{r_{he}}\right) T_{13,3} - \frac{k_s}{r_{he}} \left(\frac{\frac{1}{k_s} \ln\left(\frac{r_{13,6}}{r_{13,5}}\right) + \frac{1}{r_{13,3} h_r}}{\frac{1}{r_{13,3} h_r} \cdot \ln\left(\frac{r_{13,6}}{r_{13,5}}\right)} \right) T_{13,5} \\ + \left(\frac{k_s}{r_{he}} \cdot \frac{1}{\ln\left(\frac{r_{13,6}}{r_{13,5}}\right)} \right) T_{13,6} = 0. \end{aligned} \quad \text{B.65}$$

In order to simplify the convective-radiate heat transfer modeling at the axial boundary of the coupling, average casing temperature and average natural convective heat transfer coefficients were used to determine the wall temperatures at nodes located in these regions, as shown in Figure B.4. It was applied the same correlation for calculating h_c in the annulus gap, i.e., Hasan and Kabir (2002).

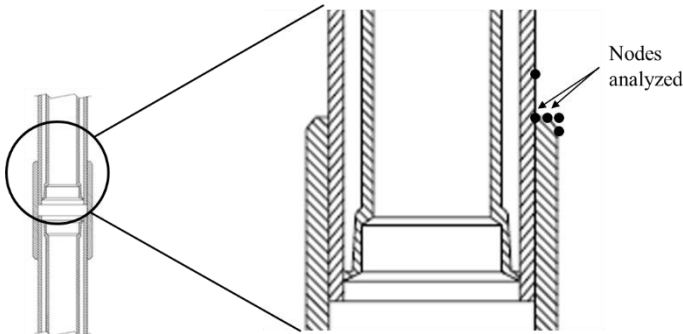


Figure B.7 - Boundary conditions at the coupling tip.

Using average values was possible since the variation of h_c between the upward and the downward nodes relative to the actual node is less than 3 %. Also, the radiation heat transfer coefficient, h_r , was neglected, once the scale of h_c is about 10 times higher than h_r .

Hence, the energy balance applied at node (13,7) yields

$$\frac{T_{13,6} - T_{13,7}}{R_{CR,67}} - \frac{T_{13,7} - \bar{T}_{int,cas}}{R_c} - \frac{T_{13,7} - T_{13,8}}{R_{CR,78}} = 0, \quad \text{B.66}$$

that is rewritten to produce

$$\begin{aligned} & \left(\frac{1}{R_{CR,67}} \right) T_{13,6} \\ & - \left(\frac{R_{CR,67} \cdot R_c + R_{CR,67} \cdot R_{CR,78} + R_c \cdot R_{CR,78}}{R_{CR,23} \cdot R_c \cdot R_{CR,78}} \right) T_{13,7} \\ & + \left(\frac{1}{R_{CR,78}} \right) T_{13,8} + \left(\frac{1}{R_c} \right) \bar{T}_{int,cas} = 0. \end{aligned} \quad \text{B.67}$$

Substituting the thermal resistances in Eq. (B.67) results

$$\begin{aligned} & \left(\frac{k_s}{r_{he}} \cdot \frac{1}{\ln\left(\frac{r_{13,7}}{r_{13,6}}\right)} \right) T_{13,6} \\ & - \frac{k_s}{r_{he}} \left(\frac{\left(\frac{r_{13,8}^2 - r_{he}^2}{r_{13,8}^2 - r_{13,7}^2}\right) \frac{1}{\bar{h}_c} \ln\left(\frac{r_{13,7}}{r_{13,6}}\right) + \frac{r_{he}}{k_s} \ln\left(\frac{r_{13,7}}{r_{13,6}}\right) \ln\left(\frac{r_{13,8}}{r_{13,7}}\right)}{\left(\frac{r_{13,8}^2 - r_{he}^2}{r_{13,8}^2 - r_{13,7}^2}\right) \frac{1}{\bar{h}_c} \ln\left(\frac{r_{13,7}}{r_{13,6}}\right) \ln\left(\frac{r_{13,8}}{r_{13,7}}\right)} \right. \\ & \left. + \frac{\left(\frac{r_{13,8}^2 - r_{he}^2}{r_{13,8}^2 - r_{13,7}^2}\right) \frac{1}{\bar{h}_c} \ln\left(\frac{r_{13,8}}{r_{13,7}}\right)}{\left(\frac{r_{13,8}^2 - r_{he}^2}{r_{13,8}^2 - r_{13,7}^2}\right) \frac{1}{\bar{h}_c} \ln\left(\frac{r_{13,7}}{r_{13,6}}\right) \ln\left(\frac{r_{13,8}}{r_{13,7}}\right)} \right) T_{13,7} \\ & + \left(\frac{k_s}{r_{he}} \cdot \frac{1}{\ln\left(\frac{r_{13,8}}{r_{13,7}}\right)} \right) T_{13,8} + \bar{h}_c \left(\frac{r_{13,8}^2 - r_{13,7}^2}{r_{13,8}^2 - r_{he}^2} \right) \bar{T}_{int,cas} = 0. \end{aligned} \quad \text{B.68}$$

With respect to the node (13,8) the energy balance applied on it yields

$$\frac{T_{13,7} - T_{13,8}}{R_{CR,78}} + \frac{T_{12,8} - T_{13,8}}{R_{CA,12138}} - \frac{T_{13,8} - \bar{T}_{int,cas}}{R_C} - \frac{T_{13,8} - T_{13,9}}{R_{CR,89}} = 0. \quad \text{B.69}$$

Rewriting Eq. (B.69) gives

$$\begin{aligned} & \left(\frac{1}{R_{CR,78}} \right) T_{13,7} \\ & - \left(\frac{R_{CR,78} \cdot R_{CA,12138} \cdot R_C + R_{CR,78} \cdot R_{CA,12138} \cdot R_{CR,89}}{R_{CR,12} \cdot R_{CA,12138} \cdot R_{CA,9102} \cdot R_{CR,23}} \right. \\ & \left. + \frac{R_{CR,78} \cdot R_C \cdot R_{CR,89} + R_{CA,12138} \cdot R_C \cdot R_{CR,89}}{R_{CR,78} \cdot R_{CA,12138} \cdot R_C \cdot R_{CR,89}} \right) T_{13,8} \\ & + \left(\frac{1}{R_{CA,12138}} \right) T_{12,8} + \left(\frac{1}{R_C} \right) \bar{T}_{int,cas} + \left(\frac{1}{R_{CR,89}} \right) T_{13,9} = 0 \end{aligned} \quad \text{B.70}$$

substituting the thermal resistances yields

$$\begin{aligned}
& \left(\frac{k_s}{r_{he}} \cdot \frac{1}{\ln\left(\frac{r_{13,8}}{r_{13,7}}\right)} \right) T_{13,7} \\
& - \frac{k_s}{r_{he}} \left(\frac{\left(\frac{r_{13,8}^2 - r_{he}^2}{r_{13,8}^2 - r_{13,7}^2}\right) \frac{l_{12,13}}{\bar{h}_c} \ln\left(\frac{r_{13,8}}{r_{13,7}}\right) + r_{he} l_{12,13} \ln\left(\frac{r_{13,8}}{r_{13,7}}\right) \ln\left(\frac{r_{13,9}}{r_{13,8}}\right)}{\frac{l_{12,13}}{\bar{h}_c} \left(\frac{r_{13,8}^2 - r_{he}^2}{r_{13,8}^2 - r_{13,7}^2}\right) \ln\left(\frac{r_{13,8}}{r_{13,7}}\right) \ln\left(\frac{r_{13,9}}{r_{13,8}}\right)} \right. \\
& + \frac{r_{he}}{\bar{h}_c} \left(\frac{r_{13,8}^2 - r_{he}^2}{r_{13,8}^2 - r_{13,7}^2}\right) \ln\left(\frac{r_{13,8}}{r_{13,7}}\right) \ln\left(\frac{r_{13,9}}{r_{13,8}}\right) \\
& + \frac{l_{12,13}}{\bar{h}_c} \left(\frac{r_{13,8}^2 - r_{he}^2}{r_{13,8}^2 - r_{13,7}^2}\right) \ln\left(\frac{r_{13,8}}{r_{13,7}}\right) \ln\left(\frac{r_{13,9}}{r_{13,8}}\right) \\
& \left. + \frac{\frac{l_{12,13}}{\bar{h}_c} \left(\frac{r_{13,8}^2 - r_{he}^2}{r_{13,8}^2 - r_{13,7}^2}\right) \ln\left(\frac{r_{13,9}}{r_{13,8}}\right)}{\frac{l_{12,13}}{\bar{h}_c} \left(\frac{r_{13,8}^2 - r_{he}^2}{r_{13,8}^2 - r_{13,7}^2}\right) \ln\left(\frac{r_{13,8}}{r_{13,7}}\right) \ln\left(\frac{r_{13,9}}{r_{13,8}}\right)} \right) T_{13,8} + \left(\frac{k_s}{l_{12,13}}\right) T_{12,8} \\
& + \bar{h}_c \left(\frac{r_{13,8}^2 - r_{13,7}^2}{r_{13,8}^2 - r_{he}^2}\right) \bar{T}_{int,cas} + \left(\frac{k_s}{r_{he}} \cdot \frac{1}{\ln\left(\frac{r_{13,9}}{r_{13,8}}\right)}\right) T_{13,9} = 0.
\end{aligned} \tag{B.71}$$

Finally, the energy balance applied at node (13,9) may be obtained similarly to the node (9,9), thus

$$\frac{T_{13,8} - T_{13,9}}{R_{CR,89}} - \frac{T_{13,9} - T_{int,cas}}{R_c} - \frac{T_{13,9} - T_{int,cas}}{R_{rad}} = 0, \tag{B.72}$$

rewriting the present equation and substituting the thermal resistances the final equation is of the form

$$\begin{aligned}
& \left(\frac{k_s}{r_{he}} \cdot \frac{1}{\ln\left(\frac{r_{13,9}}{r_{13,8}}\right)} \right) \cdot T_{13,8} \\
& - \left(\frac{\frac{1}{h_c k_s} \cdot \ln\left(\frac{r_{13,9}}{r_{13,8}}\right) + \frac{1}{r_{13,9} h_r k_s} \cdot \ln\left(\frac{r_{13,9}}{r_{13,8}}\right) + \frac{1}{h_c h_r} \cdot \frac{1}{r_{13,9}}}{\frac{1}{h_c h_r} \cdot \frac{r_{he}}{r_{13,9} k_s} \ln\left(\frac{r_{13,9}}{r_{13,8}}\right)} \right) T_{13,9} \\
& + \left(\frac{r_{13,9}}{r_{he}} \cdot (h_c + h_r) \right) T_{int,cas} = 0.
\end{aligned} \tag{B.73}$$

APPENDIX C

This appendix describes the GRAMP2 (General Runge-Kutta Annular Modeling Program), a flow pattern based prediction code which has been applied to deal with the multiphase flow in the well A. The original version of GRAMP2 can be found in the report provided by Barbosa and Hewitt (2006).

C.1 THE SEPARATED FLOW MODEL

The one-dimensional, steady-state momentum conservation equation for two-phase gas-liquid flow in a constant cross-section area channel can be written in terms of the total pressure gradient, dp/dz . This is as follows (Carey, 1992; Collier and Thome, 1994; Levy, 1999):

$$\frac{dp}{dz} = \left(\frac{dp}{dz}\right)_{acc} + \left(\frac{dp}{dz}\right)_{fric} + \left(\frac{dp}{dz}\right)_{grav} , \quad \text{C.1}$$

where the subscripts *acc*, *fric* and *grav* denote the individual contributions due to flow acceleration, friction and gravity, respectively.

C.2 THE BUBBLE FLOW REGIME

In the bubble flow region, the Friedel (1979) correlation for frictional pressure drop in conjunction with the Zuber et al. (1967) correlation for void fraction are probably sufficiently accurate to calculate the total pressure gradient. In this region the frictional component is usually much smaller than the gravitational one.

Thus, the friction factor is obtained as a function of the Reynolds number considering the flow mixture as a liquid, Re_{lo} , through the equation suggested by Friedel (1979):

$$f = \begin{cases} 16/Re_{lo} & Re_{lo} < 2300 \\ \frac{143.38}{(\ln Re_l)^{4.5}} + 1.069 \times 10^{-3} & 2300 \leq Re_{lo} \leq 8000 \\ 7.9 \times 10^{-2} Re_{lo}^{-\frac{1}{4}} & 8000 < Re_{lo} \leq 24000 \\ 4.6 \times 10^{-2} Re_{lo}^{-\frac{1}{5}} & Re_{lo} > 24000 \end{cases} \quad C.2$$

With respect to the gravitational pressure drop calculated as a function of the void fraction from Zuber (1967) is given by

$$\varepsilon = \frac{U_{gs}}{U_m C_0 + V_{gj}}, \quad C.3$$

where, V_{gj} corresponds to the drift flux velocity and is obtained from (Zuber, 1967); Collier e Thome, 1994) as

$$V_{gj} = 1.53(1 - \varepsilon)^2 \left(\sigma_l g \frac{\rho_l - \rho_g}{\rho_l^2} \right)^{\frac{1}{4}}. \quad C.4$$

C.3 THE BUBBLE TO SLUG REGIME TRANSITION

The transition from bubble flow to slug flow has been successfully predicted by a simple criterion which dictates that the transition to slug flow takes place when the average void fraction reaches a critical value of around 0.25 (Taitel *et al.*, 1980; Mishima and Ishii, 1984; Pauchon and Banerjee, 1986).

C.4 THE SLUG FLOW REGIME

For the slug flow region, it was selected the model of de Cachard and Delhaye (1996). This is a simple and yet comprehensive model, which captures some of the important aspects of the slug flow regime such as the opposite directions of wall shear in both slug and Taylor bubble regions.

In this model, steady and fully developed slug flow is described as a succession of identical unit cells. A unit cell consists of a cylindrical

Taylor bubble surrounded by a falling liquid film and of a liquid slug, as illustrated in Figure C.1.

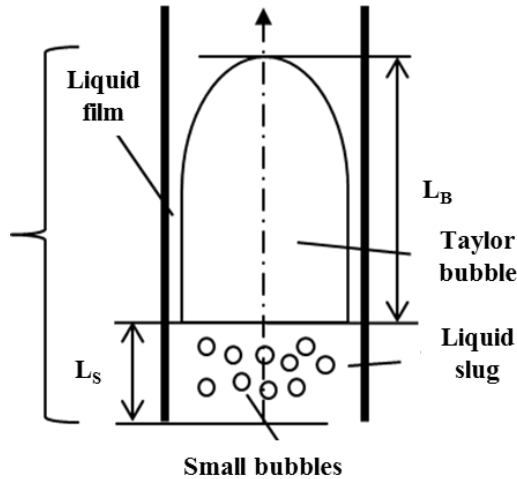


Figure C.1 – Unit cell of slug regime (Hafemann, 2015).

A very complex feature of slug flow is the understanding and prediction of the mechanisms by which gas becomes entrained in the form of small bubbles in the liquid slug. A criterion for the existence of non-aerated slugs is written in terms of the Bond number as follows:

$$Bo = \frac{(\rho_l - \rho_g)gd^2}{\sigma_l} \geq 140 \quad . \quad C.5$$

In most simulations reported here, values of Bond number are of the order of 1,300 and, therefore, gas entrainment within the slug cannot be disregarded. In the original paper of de Cachard and Delhaye (1996) gas entrainment in the slug was neglected since $Bo \approx 140$ in their studies. In what follows, an extension of the de Cachard and Delhaye model taking into account slug entrainment is presented.

The fraction of the unit cell transit time corresponding to the Taylor bubble is:

$$\beta = \frac{L_B}{L_B + L_S} \quad , \quad C.6$$

The integration of the instantaneous continuity equations for the gas, liquid and the mixture produces the following equations for the region of Taylor bubble and the liquid slug when relating to the mixture superficial velocity, U_m , as follows

$$U_m = \varepsilon_B V_{B,g} + (1 - \varepsilon_B) V_{B,l} , \quad \text{C.7}$$

$$U_m = \varepsilon_S V_{S,g} + (1 - \varepsilon_S) V_{S,l} . \quad \text{C.8}$$

The unit slug flow model is complemented with closure expressions for the Taylor bubble velocity, $V_{B,g}$, the falling film velocity, $V_{B,l}$, and the slug void fraction, ε_S . The following approximations were made: (i) the flow in the liquid film is fully developed, (ii) the flow in the slug is fully developed and (iii) there is no slip between the gas and the liquid in the liquid slug, i.e., $V_{S,g} = V_{S,l}$.

For the Taylor bubble velocity, the Nicklin *et al.* (1962) expression is used:

$$V_{B,g} = 1.2U_m + V_0 , \quad \text{C.9}$$

The coefficient 1.2 in the above equation is the turbulent flow velocity profile coefficient in the liquid slug. V_0 is the rise velocity of a Taylor bubble in quiescent liquid. De Cachard and Delhaye (1996), among others (Wallis, 1969), adopted the general correlation by White and Beardmore (1962):

$$V_0 = \gamma \sqrt{gd} , \quad \text{C.10}$$

where:

$$\gamma = 0.345 \left[1 - \exp\left(-\frac{0.01N_f}{0.345}\right) \right] \left[1 - \exp\left(\frac{3.37 - Bo}{m}\right) \right] , \quad \text{C.11}$$

and the dimensionless viscosity and the empirical parameter m are defined as

$$N_f = \frac{\sqrt{d^3 g (\rho_l - \rho_g) \rho_l}}{\mu_l} , \quad \text{C.12}$$

and

$$m = \begin{cases} 10 & N_f > 250 \\ 69/N_f^{-0.35} & 18 < N_f < 250 \\ 25 & N_f < 18 \end{cases} . \quad \text{C.13}$$

The liquid film around the Taylor bubble is modelled as a thin film falling, without interfacial shear stress, inside a vertical cylinder. For laminar film flow, the film thickness, δ , is related to the mean film velocity by the Nusselt relationship:

$$\delta \left(\frac{g\rho_l^2}{\mu_l^2} \right)^{1/3} = (3Re_\delta)^{1/3} , \quad \text{C.14}$$

where Re_F is the falling film Reynolds number, given by

$$Re_F = -V_{B,l} \frac{\rho_l \delta}{\eta_L} \quad (V_{B,l} < 0) . \quad \text{C.15}$$

For turbulent flow, according to Belkin *et al.* (1959) and Wallis (1969), a new relationship is proposed as follows

$$\delta \left(\frac{g\rho_l^2}{\mu_l^2} \right)^{1/3} = 0.159Re_\delta^{2/3} . \quad \text{C.16}$$

The two relations fit together for $Re_F \cong 750$. Making use of the definition of the film Reynolds number and of the geometrical relationship between the film thickness and the Taylor bubble void fraction, the equation of the film thickness is rewritten as a function of the bubble void fraction

$$\delta = \frac{d}{2} \left(1 - \varepsilon_B^{1/2} \right) , \quad \text{C.17}$$

Hence, the falling film velocity can be calculated as

$$V_{B,l} = \begin{cases} -0.333 \left(\frac{gd^2 \rho_l}{\mu_l} \right) (1 - \varepsilon_B^{1/2})^2 & \text{if } Re_\delta < 750 \\ -11.2 \left[gd (1 - \varepsilon_B^{1/2}) \right]^{1/2} & \text{if } Re_\delta > 750 \end{cases} . \quad \text{C.18}$$

The void fraction in the liquid slug is calculated using the model of Barnea and Brauner (1985):

$$\varepsilon_s = 0,058 \left[d_c \left(\frac{2f_m U_m^3}{d} \right)^{0,4} \left(\frac{\rho_l}{\sigma_l} \right)^{0,6} - 0,725 \right]^2 , \quad \text{C.19}$$

where, for vertical flows:

$$d_c = 2 \left[\frac{0,4\sigma_l}{g(\rho_l - \rho_g)} \right]^{0,5} . \quad \text{C.20}$$

The friction factor, f_m , is evaluated based on the mixture velocity

$$f_m = 0,046 \left(\frac{U_m d \rho_l}{\mu_l} \right)^{-0,2} . \quad \text{C.21}$$

In the liquid slug region, the frictional pressure gradient is given by

$$-\left. \frac{dP}{dz} \right|_{fric,S} = \frac{2f_S \rho_S U_m^2}{d} , \quad \text{C.22}$$

where f_S is the liquid slug friction factor calculated using the Blasius relationship. ρ_S is the equivalent density of the slug and η_L is the equivalent viscosity of the slug. These are calculated as follows:

$$\frac{1}{\rho_S} = \frac{x_S}{\rho_g} + \frac{(1 - x_S)}{\rho_l} , \quad \text{C.23}$$

$$\frac{1}{\mu_S} = \frac{x_S}{\mu_g} + \frac{(1 - x_S)}{\mu_l} . \quad \text{C.24}$$

where x_S is the slug gas mass fraction assuming homogeneous flow within the slug. By equating the liquid and gas velocities in the slug, one obtains

$$x_S = \frac{\rho_g \varepsilon_S}{[\rho_l(1 - \varepsilon_S) + \rho_g \varepsilon_S]} . \quad \text{C.25}$$

In the Taylor bubble, once the liquid film is fully developed, its weight is fully balanced by the wall friction force. Thus, the friction term is the opposite of the gravity term, that is

$$-\left. \frac{dP}{dz} \right|_{fric,B} = -g\rho_l(1 - \varepsilon_B) . \quad \text{C.26}$$

The average frictional component is thus

$$-\left. \frac{dP}{dz} \right|_{fric} = -(1 - \beta) \left. \frac{dP}{dz} \right|_{fric,S} - \beta \left. \frac{dP}{dz} \right|_{fric,B} . \quad \text{C.27}$$

The average gravitational component is given by:

$$\begin{aligned} -\left. \frac{dP}{dz} \right|_{grav} &= (1 - \beta)g[\rho_l(1 - \varepsilon_S) + \rho_g \varepsilon_S] \\ &\quad + \beta g[\rho_l(1 - \varepsilon_B) + \rho_g \varepsilon_B] . \end{aligned} \quad \text{C.28}$$

According to De Cachard and Delhaye (1996), the cell-averaged void fraction is calculated as

$$\varepsilon = (1 - \beta)\varepsilon_S + \beta\varepsilon_B . \quad \text{C.29}$$

C.5 THE SLUG TO CHURN REGIME TRANSITION

The slug to churn transition is calculated using the model of Jayanti and Hewitt (1992). This model postulates that the mechanism behind this transition is flooding in the Taylor bubble. They proposed the following modified form of the flooding correlation as the criterion for the occurrence of churn flow:

$$\sqrt{U_{B,g}^*} + m_{LTB} \sqrt{U_{B,l}^*} > 1, \quad \text{C.30}$$

where $U_{B,g}^*$ and $U_{B,l}^*$ are the dimensionless superficial Taylor bubble and superficial falling liquid film velocities. These are given by

$$U_{B,g}^* = U_{B,g} \frac{\sqrt{\rho_g}}{\sqrt{gd(\rho_l - \rho_g)}}, \quad \text{C.31}$$

and

$$U_{B,l}^* = U_{B,l} \frac{\sqrt{\rho_l}}{\sqrt{gd(\rho_l - \rho_g)}}. \quad \text{C.32}$$

where $U_{B,g}$ and $U_{B,l}$ are determined by solving the following equations simultaneously

$$U_{B,g} = \left(1 - 4 \frac{\delta}{d}\right) \left[1.2(U_{ls} + U_{gs}) + 0.35 \sqrt{\frac{gd(\rho_l - \rho_g)}{\rho_l}}\right], \quad \text{C.33}$$

$$U_{B,l} = U_{B,g} - (U_{gs} - U_{ls}). \quad \text{C.34}$$

It is worthwhile mentioning that the superficial velocities, $U_{B,l}$ and $U_{B,g}$ are related to the actual velocities $V_{B,l}$ and $V_{B,g}$ by the following expressions

$$U_{B,g} = V_{B,g} \varepsilon_B \quad \text{C.35}$$

$$U_{B,l} = V_{B,l} (1 - \varepsilon_B) \quad \text{C.36}$$

Jayanti and Hewitt (1992) suggested that the thickness of the liquid film surrounding the Taylor bubble should be calculated using the Brotz empirical relationship:

$$\delta \left[\frac{g(\rho_l - \rho_g)\rho_l}{\mu_l^2} \right]^{1/3} = 0.1719 Re_\delta^{2/3}, \quad \text{C.37}$$

where m_{LTB} is an empirically fitted coefficient proposed by Jayanti and Hewitt (1992) to take into account the influence of the length of the falling film on the flooding velocity:

$$m_{LTB} = \begin{cases} 0.96 & \text{if } \frac{L_B}{d} > 120 \\ 0.1928 + 0.01089 \frac{L_B}{d} - 3.754 \times 10^{-5} \left(\frac{L_B}{d} \right)^2 & \\ \text{if } \frac{L_B}{d} \leq 120 & \end{cases}, \quad \text{C.38}$$

The length of the Taylor bubble, L_B , can be determined from a mass balance on the liquid phase:

$$U_{ls} = V_{S,l}(1 - \varepsilon_S) \frac{L_S}{L_B + L_S} - V_{B,l} \frac{L_B}{L_B + L_S}. \quad \text{C.39}$$

Jayanti and Hewitt (1992) suggest that close the slug/churn transition $V_{S,l} = U_m$, $L_S = 12d$ and $\varepsilon_S = 0.5$.

C.6 THE CHURN FLOW REGIME

The churn flow model utilized in the present study is that proposed by Jayanti and Brauner (1994). They put forward a model particularly devoted to the prediction of pressure gradient and void fraction in churn flow. In their model, force balances on the gas core and on the two-phase mixture are as follows

$$-\frac{dP}{dz} = \frac{4\tau_i}{d\sqrt{\varepsilon}} + \rho_g, \quad \text{C.40}$$

$$-\frac{dP}{dz} = \frac{4\tau_w}{d\sqrt{\varepsilon}} + g[\rho_l(1 - \varepsilon) + \rho_g\varepsilon]. \quad \text{C.41}$$

In Eq. (C.41), τ_w is the average wall shear stress (accounting for the fact that only the liquid is in contact with the wall). Jayanti and Brauner (1994) suggested that τ_w may be calculated based on the net flow rate alone and that its time-varying nature can be neglected. Thus,

$$\tau_w = \frac{1}{2} \rho_l f_l \left(\frac{U_{ls}}{1 - \varepsilon} \right)^2, \quad \text{C.42}$$

where the liquid friction factor f_l is estimated using single phase flow relationships as follows

$$f_l = \begin{cases} 16/Re_l & \text{if } Re_l \leq 2100 \\ 0.079Re_l^{-1/4} & \text{if } Re_l > 2100 \end{cases}. \quad \text{C.43}$$

In a similar manner, the average interfacial shear stress can be written as,

$$\tau_i = \frac{1}{2} \rho_g f_i \left(\frac{U_{gs}}{\varepsilon} \right)^2, \quad \text{C.44}$$

where f_i is the interfacial friction factor, which is estimated by an average of the correlations by Bharathan and Wallis (1983) (for the post-flooding regime in counter-current flow) and by Wallis (1969) (for annular flow). Thus,

$$f_i = \frac{1}{2} (f_{i,Wallis} + f_{i,Bharathan}), \quad \text{C.45}$$

where,

$$f_{i,Wallis} = 0.005 + 0.375(1 - \varepsilon), \quad \text{C.46}$$

and

$$f_{i,Bharathan} = 0.005 + 10^{(-0.56 + \frac{9.07}{d^*})} \left[\frac{d^*(1 - \varepsilon)}{4} \right]^{(1.63 + \frac{4.74}{d^*})}, \quad \text{C.47}$$

where

$$d^* = d \sqrt{\frac{(\rho_l - \rho_g)g}{\sigma_l}} . \quad \text{C.48}$$

For situations in that $d^* > 160$, then the interfacial friction coefficient is rewritten according to the following equation

$$f_{i,Bharathan} = 0.005 \left[1 + 55 \left(\frac{d^*(1 - \varepsilon)}{4} \right)^{1.63} \right] . \quad \text{C.49}$$

Jayanti and Brauner (1994) compared the pressure gradient predictions using the above model with the experimental results by Owen (1986). They claimed that almost all data points (covering a liquid mass flux range of 5 to 400 kg m⁻²s⁻¹ in a 0.0318 m ID pipe) are predicted well and lie within $\pm 20\%$ of the measured pressure gradient.

C.7 THE CHURN TO ANNULAR REGIME TRANSITION

The large number of mechanisms behind the transition to annular flow leads to many formulations of criteria to describe this transition. The most commonly used is the *flow reversal* condition due to its easy experimental observation and because there are simple relationships to determine it (HEWITT and WALLIS, 1963; PUSHKINA and SOROKIN, 1969; TAITEL *et al.*, 1980).

The most commonly used is the Hewitt and Wallis (1963) correlation which uses the flooding correlation:

$$\sqrt{U_{gs}^*} + \sqrt{U_{ls}^*} \approx 1 , \quad \text{C.50}$$

with zero liquid down flow, i.e., $U_{ls}^* = 0$.

C.8 THE ANNULAR FLOW REGIME

In the annular flow regime, the liquid phase is present as a film coating the inner wall of the pipe and also as droplets entrained in the gas core. Droplets are created at the crests of disturbance waves

travelling on the film and are subsequently deposited onto the liquid film by the action of the turbulence in the gas stream.

The description of the annular flow model starts with mass and momentum balances over the gas core and liquid film regions respectively. A schematic of an incremental length of pipe in which annular flow takes place is shown in Figure A.1 – Nomenclature for the VIT thermal network.

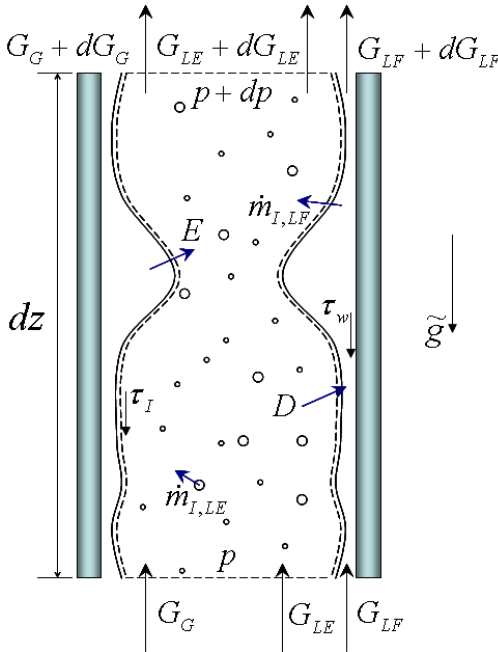


Figure C.2 – Mass and momentum conservation balances applied to an incremental annular flow length (Barbosa and Hewitt, 2006).

The following assumptions are made:

- The flow is steady;
- The flow is one-dimensional;
- The film thickness is uniform around the perimeter of the pipe;
- Mechanical equilibrium, i.e., the pressure is constant over an entire pipe cross-section;
- The core flow is homogeneous, i.e., there is no slip between gas and entrained droplets

Mass conservation balances provide the following set of equations:

$$\frac{d}{dz}G_{LF} = \frac{4}{d}(D - E - \dot{m}_{i,LF}), \quad \text{C.51}$$

$$\frac{d}{dz}G_{LE} = \frac{4}{d}(D - E - \dot{m}_{i,LE}), \quad \text{C.52}$$

$$\frac{d}{dz}G_g = \frac{4}{d}(\dot{m}_{i,LF} + \dot{m}_{i,LE}). \quad \text{C.53}$$

where D and E are the deposition and the entrainment mass flow rates of droplets per unit perimeter area. $\dot{m}_{i,LF}$ and $\dot{m}_{i,LE}$ are the interfacial mass flow rates from or to the liquid film and droplets per unit perimeter area due to evaporation and condensation. In the present formulation, it is assumed that vaporization and condensation takes place only through the film interface (the droplet stream phase change is negligible).

In order to reduce the number of mass balance equations to be integrated in the annular regime from 3 to 2, the droplet entrained fraction is defined as follows

$$ef = \frac{G_{LE}}{G_{LE} + G_{LF}} = \frac{x_{LE}}{x_{LE} + x_{LF}}, \quad \text{C.54}$$

Thus, the equation for the entrained mass fraction gives

$$\frac{d}{dz}x_{LE} = \frac{4(E - D)}{dG}, \quad \text{C.55}$$

and then, using the overall balance

$$\frac{d}{dz}x_{LE} + \frac{d}{dz}x_{LF} + \frac{d}{dz}x = 0, \quad \text{C.56}$$

it is possible to derive an equation for the entrained fraction as a function of distance:

$$\frac{d}{dz}ef = \frac{1}{(1-x)} \left[\frac{4}{dG} (E - D) + ef \frac{d}{dz}x \right]. \quad C.57$$

Through the differential equation one can integrate the entrained fraction along the annular flow and then, calculate the void fraction and the pressure drop. In order to define the entrainment and deposition rates it has been used the method proposed by Govan e Hewitt (1988). The entrainment rate is given by

$$E = \begin{cases} 0 & \text{if } G_{LF} \leq G_{LFC} \\ 5.75x10^{-5}G_g \left[\frac{\rho_l \cdot (G_{LF} - G_{LFC})^2}{d\sigma_l\rho_g^2} \right]^{0.316} & \text{if } G_{LF} > G_{LFC} \end{cases} \quad C.58$$

From the mass balance is defined the liquid film mass flux as

$$G_{LF} = G_l(1 - ef) \quad , \quad C.59$$

and the critical liquid film mass flux, G_{LFC} , is defined as

$$G_{LFC} = \frac{\mu_l}{d} \exp \left[5.8504 + 0.4249 \left(\frac{\mu_g}{\mu_l} \right) \left(\frac{\rho_l}{\rho_g} \right)^{0.5} \right]. \quad C.60$$

The droplets deposition rate is expressed as

$$D = Ck_d \quad , \quad C.61$$

where C is the concentration of droplets into the core

$$C = \frac{G_{LE}}{\frac{G_g}{\rho_g} + \frac{G_{LE}}{\rho_l}} \quad , \quad C.62$$

and k_d the droplet deposition transfer coefficient given by

$$k_d = \begin{cases} 0.185 \sqrt{\frac{\sigma_l}{\rho_g d}} & \text{if } \frac{C}{\rho_g} < 0,3 \\ 0.083 \sqrt{\frac{\sigma_l}{\rho_g d}} \left(\frac{\rho_g}{C}\right)^{0.65} & \text{if } \frac{C}{\rho_g} \geq 0,3 \end{cases} \quad \text{C.63}$$

At a given distance along the pipe, the entrained fraction is calculated from Eq. (C.57). The determination of boundary conditions for this equation depends on the situation in what the annular flow is created: if the annular flow regime is created artificially (e.g., in an adiabatic experimental apparatus) the entrained fraction at the onset of annular flow, or simply initial entrained fraction, ef_0 , is generally known and obviously dependent on the method by which the liquid flow is injected into the test section; if the annular regime is created naturally, i.e., those resulting from a flow transition from the churn flow regime due to an increase in quality, a calculation method is required to determine the initial entrained fraction. Barbosa *et al.* (2002) proposed an empirical correlation to calculate ef_0 taking into account the effect of the proximity to the churn flow boundary and the presence of droplets generated through the process of droplet formation associated with that flow regime (Azzopardi, 1983). This is given by

$$ef_0(\%) = 0.95 + 342.55 \sqrt{\frac{\rho_l G_l}{\rho_g G_g}} d^2. \quad \text{C.64}$$

Thus, the momentum equation may be rewritten assuming the two-phase mixture with homogeneous droplet core. The resulting equation takes the form

$$-\frac{dP}{dz} = \frac{4}{d} \tau_w + [\rho_l(1 - \varepsilon_c) + \rho_c \varepsilon_c] g + G^2 \frac{d}{dz} \left[\frac{x_c^2}{\rho_c \varepsilon_c} + \frac{(1 - x_c)^2}{\rho_l(1 - \varepsilon_c)} \right], \quad \text{C.65}$$

where ε_c is the fraction of the pipe cross-sectional area occupied by the gas core and δ is the average film thickness. These variables are related by

$$\varepsilon_c = 1 - \frac{4\delta}{d}, \quad \text{C.66}$$

where τ_w is the wall shear stress and x_c is the core equivalent mass fraction defined as

$$x_c = \frac{G_{LE} + G_g}{G} = ef(1 - x_g) + x_g, \quad \text{C.67}$$

where ef is the fraction of the liquid flow entrained as droplets. The homogeneous core quality is expressed as follows

$$\hat{x}_c = \frac{G_g}{G_{LE} + G_g} = \frac{x_g}{x_g(1 - ef) + ef}, \quad \text{C.68}$$

ρ_c is the homogeneous core density, which can be defined as:

$$\rho_c = \left[\frac{\hat{x}_c}{\rho_g} + \frac{(1 - \hat{x}_c)}{\rho_l} \right]^{-1}. \quad \text{C.69}$$

The homogeneous core and liquid film velocities are defined similarly, given by:

$$u_c = \frac{Gx_c}{\rho_c \varepsilon_c}, \quad \text{C.70}$$

$$u_{LF} = \frac{G(1 - x_c)}{\rho_l(1 - \varepsilon_c)}. \quad \text{C.71}$$

The interfacial shear stress, τ_i , was assumed to be given by a correlation due to Wallis (1969):

$$\tau_i = \frac{1}{2}(\rho_g + C)V_{GC}^2 f_i. \quad \text{C.72}$$

Based on the concentration of droplets into the core gas, i.e., the entrained fraction, and the homogeneous core velocity, defined as

$$V_{GC} = \frac{G_g}{\rho_g} + \frac{G_{LE}}{\rho_l}, \quad \text{C.73}$$

Thus, Eq. C.72 is rewritten as

$$\tau_i = \frac{1}{2} \rho_c u_c^2 f_i \quad \text{C.74}$$

where f_i is the modified Fanning friction factor given by

$$f_i = f_{GC} \left[1 + 360 \frac{\delta}{d} \right], \quad \text{C.75}$$

where

$$f_{GC} = 0.079 Re_{GC}^{-0.25}, \quad \text{C.76}$$

and

$$Re_{GC} = \frac{(G_g + G_{LE})d}{\mu_g}. \quad \text{C.77}$$

A triangular relationship takes place among the liquid film flow rate, the film thickness and the wall shear stress. The liquid film thickness can be determined by matching the known value of the film flow rate at a certain distance with the integral of a hypothetical velocity profile across the film.

Several hypothetical profiles have been suggested in the literature. It has been used the profile suggested by Jensen (1987) as the most accurate one, i.e., the Double Velocity Profile will be used.

In dimensionless coordinates, the liquid film flow rate is defined as (note that the integral takes into account curvature effects):

$$\dot{M}_{LF}^+ = \frac{\dot{M}_{LF}}{\pi d \mu_l} = \int_0^{\delta^+} u_{LF}^+ \left(1 - \frac{y^+}{Re^+} \right) dy^+, \quad \text{C.78}$$

where y^+ and δ^+ are the co-ordinate with origin at the wall and the film thickness in dimensionless form. These are given by:

$$y^+ = \frac{\rho_l u^* y}{\mu_l}, \quad \text{C.79}$$

and

$$\delta^+ = \frac{\rho_l u^* \delta}{\mu_l}. \quad \text{C.80}$$

Re^+ is the dimensionless pipe radius is given by

$$Re^+ = \frac{\rho_l u^* d}{2\mu_l}. \quad \text{C.81}$$

where u_{LF}^+ is the dimensionless liquid film velocity defined as

$$u_{LF}^+ = \frac{u_{LF}}{u^*}, \quad \text{C.82}$$

where u^* is the friction velocity is defined as follows

$$u^* = \sqrt{\frac{\tau_w}{\rho_l}}. \quad \text{C.83}$$

The Universal Velocity Profile (UVP) used on the integration of the liquid film is defined according to Von Kármán as

$$u_{LF}^+ = \begin{cases} y^+ & \text{if } y^+ \leq 5 \\ -3.05 + 5\ln(y^+) & \text{if } 5 < y^+ \leq 30. \\ 5.46 + 2.5\ln(y^+) & \text{if } y^+ > 30 \end{cases}. \quad \text{C.84}$$

The Double Velocity Profile (DVP) uses the UVP in the integration of the film flow rate expressed in Eq. (C.78) up to $y^+ = \delta^+/2$ and an inverted reflection of the UVP for $\delta^+/2 \leq y^+ \leq \delta^+$. In terms of the liquid film flow rate the DVP is given by

$$\dot{M}_{LF}^+ = \begin{cases} \frac{1}{2}\delta^{+2} - \frac{1}{3}\delta^{+3} & \text{if } \delta^+ \leq 10 \\ -3.05\delta^+ + 5\delta^+\ln\left(\frac{\delta^+}{2}\right) + \frac{1}{Re^+} [17.22 - 22.26\delta^+ \\ + 0.594\delta^{+2} - 2.5\delta^{+2}\ln\left(\frac{\delta^+}{2}\right)] & \text{if } 10 < \delta^+ \leq 60 \\ 5.5\delta^+ + 2.5\delta^+\ln\left(\frac{\delta^+}{2}\right) + \frac{1}{Re^+} [1146 - 63.9\delta^+ \\ + 3.688\delta^{+2} - 1.25\delta^{+2}\ln\left(\frac{\delta^+}{2}\right)] & \text{if } \delta^+ > 60 \end{cases} \quad \text{C.85}$$

An expression for the wall shear stress is obtained from the elimination of the pressure gradient from separate force balances on the liquid film and on the homogeneous core (neglecting the accelerational pressure gradient)

$$\tau_w = \frac{R^2 - R_i^2}{2R} \left[(\rho_l - \rho_c)g + \frac{2R\tau_i}{R_i(R^2 - R_i^2)} \right]. \quad \text{C.86}$$

where R and R_i are the pipe radius and the distance from the pipe center line to the film surface, respectively.

Equations (C.74) to (C.85) provide a unique triangular relationship (Hewitt, 1961) between the liquid film flow rate, the liquid film thickness and the wall shear stress. This means that at any point within the channel, if two of the parameters are known, the third one can be calculated.

APPENDIX D

Table D.1 – Reservoir fluid composition from well A based on PVT analysis – flash at 40°C

Component	Dead oil [% mol]	Flash gas [% mol]	Reservoir fluid [% mol]
CO ₂	-	4.45	3.36
N ₂	-	0.60	0.45
C ₁	-	72.35	54.54
C ₂	-	7.69	5.79
C ₃	0.47	6.41	4.95
IC ₄	0.25	1.26	1.01
NC ₄	0.90	3.00	2.48
IC ₅	0.72	0.92	0.87
NC ₅	1.41	1.37	1.38
C ₆	3.22	1.16	1.66
C ₇	5.59	0.48	1.73
C ₈	7.23	0.30	2.01
C ₉	6.05	0.02	1.5
C ₁₀	4.96	-	1.22
C ₁₁	4.28	-	1.05
C ₁₂	3.86	-	0.95
C ₁₃	4.09	-	1.01
C ₁₄	3.34	-	0.82
C ₁₅	3.22	-	0.79
C ₁₆	2.54	-	0.62
C ₁₇	2.09	-	0.51
C ₁₈	2.17	-	0.53
C ₁₉	2.04	-	0.50
C ₂₀₊	41.58	-	10.24
Total molar mass	0.5754 lbm/mol	0.0547 lbm/mol	0.1828 lbm/mol
Molar mass C ₂₀₊	0.9259/mol		
Flash GOR	1,368 std ft ³ / std barrel		
API	29.76 °API		

APPENDIX E

Table E.1 – Reservoir fluid composition from well B based on PVT analysis – flash at 40°C

Component	Dead oil [% mol]	Flash gas [% mol]	Reservoir fluid [% mol]
CO ₂	-	3.62	2.15
N ₂	-	0.99	0.59
C ₁	-	61.40	36.46
C ₂	-	11.02	6.54
C ₃	0.37	10.73	6.52
IC ₄	0.14	1.87	1.17
NC ₄	0.60	4.47	2.90
IC ₅	0.52	1.34	1.01
NC ₅	0.93	1.90	1.51
C ₆	2.28	1.84	2.02
C ₇	4.88	0.22	2.11
C ₈	6.59	0.46	2.95
C ₉	6.32	0.13	2.64
C ₁₀	5.69	0.02	2.32
C ₁₁	4.85	-	1.97
C ₁₂	4.55	-	1.85
C ₁₃	4.52	-	1.84
C ₁₄	3.92	-	1.59
C ₁₅	3.72	-	1.51
C ₁₆	3.02	-	1.23
C ₁₇	2.58	-	1.05
C ₁₈	2.64	-	1.07
C ₁₉	2.35	-	0.96
C ₂₀₊	39.53	-	16.06
Total molar mass	269 kg/mol	28.21 kg/mol	126 kg/mol
Molar mass C ₂₀₊	444 kg/mol		
Flash GOR	114.78 std m ³ /std m ³		
API	26.93 °API		

APPENDIX F

The Beggs and Brill (1973) correlation, is one of the few published correlations capable of handling all flow directions. It was developed using 1" and 1 1/2" sections of pipe that could be inclined at any angle from the horizontal.

The Beggs and Brill multiphase correlation deals with both the friction pressure loss and the hydrostatic pressure difference. First the appropriate flow regime for the particular combination of gas and liquid rates (Segregated, Intermittent or Distributed) is determined. The liquid holdup, and hence, the in-situ density of the gas-liquid mixture is then calculated according to the appropriate flow regime, to obtain the hydrostatic pressure difference. A two-phase friction factor is calculated based on the "input" gas-liquid ratio and the Fanning friction factor. From this the friction pressure loss is calculated using "input" gas-liquid mixture properties. A more detailed discussion of each step is given in the following documentation.

In order to characterize the hydrodynamics, the Froude dimensionless number, N_{FR} , is used to indicate how well a particular model works in relation to a real system. The Froude number is defined as

$$N_{FR} = \frac{v_m^2}{g \cdot d} \quad \text{F. 1}$$

The flow pattern is a function of the following two parameters:

$$L_1 = \exp(-4.64 - 3.757X - 0.481X^2 - 0.0207X^3) \quad \text{F. 2}$$

$$L_2 = \exp(1.061 - 4.602X - 1.609X^2 - 0.179X^3 + 0.000635X^5) \quad \text{F. 3}$$

where

$$X = \ln(\lambda_l) \quad \text{F. 4}$$

and the no-slip hold-up is calculated as

$$\lambda_l = \frac{v_{sl}}{v_{sl} + v_{sg}}. \quad \text{F. 5}$$

Determining flow regimes

- If $N_{FR} < L_1$, the flow regime is segregated;
- If $N_{FR} \geq L_1$ and $N_{FR} \geq L_2$, the flow regime is distributed;
- If $L_2 > N_{FR} > L_1$, the flow regime is defined as intermittent.

For ascendant flow the constants used to calculate the liquid hold-up for each flow regime is shown in Table F.1.

Table F.1 – Beggs and Brill hold-up constants

Flow regime	Constant			
	a	b	c	
Segregated	0.9800	0.4846	0.0868	
Intermittent	0.8450	0.5351	0.0173	
Distributed	1.0650	0.5824	0.0609	
	d	e	f	g
Segregated uphill	0.0110	-3.7680	3.5390	-1.6140
Intermittent uphill	2.9600	0.3050	-0.4473	0.0978
Distributed uphill	No correction, $C = 0$ and $\psi = 1$			

Beggs and Brill (1973) derived an equation of the form

$$H_l(0) = \frac{a \cdot \lambda_l^b}{N_{FR}^c} \quad \text{F. 6}$$

to calculate the liquid hold-up. However, it must be corrected for the wellbore inclination. The following equations were used to deal with the inclination angle

$$\psi = 1 + C \cdot (\sin(1.8 \cdot \theta) - 1/3) \cdot (\sin(1.8 \cdot \theta))^3 \quad \text{F. 7}$$

where

$$C = (1 - \lambda_l) \cdot \ln(d \cdot \lambda_l^e) \cdot (N_{LV}^f \cdot N_{FR}^g). \quad \text{F. 8}$$

The new hydrodynamic parameter, the liquid velocity number is defined as

$$N_{LV} = v_{sl} \left(\frac{\rho_l}{g \cdot \lambda_l} \right)^{0.25}. \quad \text{F. 9}$$

The actual value of liquid hold-up can be calculated as follows

$$H_l(\theta) = H_l(0) \cdot \psi \quad \text{F. 10}$$

With respect to the two-phase frictional pressure gradient is calculated using:

$$\left(\frac{dp}{dz} \right)_f = \frac{-f_{tp} \cdot \rho_n \cdot v_m^2}{2d} \quad \text{F. 11}$$

where

$$f_{tp} = f \cdot \exp(s). \quad \text{F. 12}$$

In the previous equation f is the Fanning friction factor (no slip friction factor) considering the mixture as a one-phase flow. s is calculated as follows:

$$s = \frac{\ln(r)}{-0.0523 + 3.182 \ln(r) - 0.8725 (\ln(r))^2 + 0.01853 (\ln(r))^4}, \quad \text{F. 13}$$

since s is unbounded in the interval $1 \leq r \leq 1.2$, for this interval

$$s = \ln(2.2r - 1.2), \quad \text{F. 14}$$

where r is defined as

$$r = \frac{\lambda_l}{H_l^2(\theta)}. \quad \text{F. 15}$$

APPENDIX G

In this appendix several annular gap natural convection heat transfer correlations and formation thermal models which are employed in this thesis are described in detail.

G.1 EVALUATION OF THE ANNULUS NATURAL CONVECTION MODEL

Even though the thermal transport through the annulus has been modeled by taking into account the natural convection and the radiative heat transfer as presented by Hasan and Kabir (2002), there is a lack of information regarding the effect of different correlations on the overall heat exchange throughout the wellbore/formation radius. Therefore, assessing the annulus natural convection in an isolated manner may lead to a misreading of the role of the convection resistance in the wellbore, especially when a much larger thermal resistance exists in the wellbore configuration, as seen in VIT assisted wellbores. Hence, four different natural convection correlations for annular enclosures have been selected and assessed in this thesis.

G.1.1 Hasan and Kabir (1991)

A correlation was proposed based on an adaptation of the Dropkin and Sommerscales (1965) relationship for natural convection between two vertical parallel plates ($5 \times 10^4 < Ra < 7.17 \times 10^8$).

$$h_c = \frac{0.049 \cdot (Gr \cdot Pr)^{1/3} \cdot Pr^{0.074} \cdot k}{r_{out} \cdot \ln(r_{out}/r_{int})} \quad G. 1$$

where the Rayleigh number is given by

$$Ra = Gr \cdot Pr = \frac{g \cdot \beta \cdot (T_{int} - T_{out})(r_{out} - r_{int})^3}{\nu \cdot \alpha} \quad G. 2$$

and $Pr = \nu/\alpha$ is the Prandtl number.

G.1.2 Hasan and Kabir (2002)

According to Hasan and Kabir (2002), using the full value of h_c given by Eq. (3.39) may lead to an underestimation of annuli fluid temperatures. Hence, these authors developed a new correlation to estimate h_c , based on the Fishenden and Saunders (1950) work, as follows

$$h_c = \frac{0.1 \cdot (r_{out}/r_{int})^{0.15} \cdot Ra^{0.3}}{d_h^{0.1} \cdot k \cdot (r_{out} - r_{int})^{0.9}}. \quad G. 3$$

G.1.3 Zhou (2013)

In his thesis, Zhou (2013) proposed a new approach based on previous correlations (Dropkin and Sommerscales (1965); Holman (1981); Fishenden and Saunders (1950)), to deal with the annulus gap heat transfer as follows

$$h_c = \begin{cases} \frac{k_a}{r_{out} \cdot \ln(r_{out}/r_{int})} & \text{if } Ra \leq 6000 \\ \frac{0,13Ra^{0,25}k}{r_{out} \cdot \ln(r_{out}/r_{int})} & \text{if } 6000 < Ra \leq 5 \times 10^4 \\ \frac{0.049(Gr \cdot Pr)^{1/3} Pr^{0.074} k}{r_{out} \ln(r_{out}/r_{int})} & \text{if } 5 \times 10^4 < Ra \leq 7,17 \times 10^8 \end{cases} \quad G. 4$$

G.1.4 Xiong *et al.* (2015)

Xiong *et al.* (2015) developed a new correlation for the Nusselt number based on Computational Fluid Dynamics (CFD) simulation results. The approach took into account the convective transport in real-size annuli between different sets of tubings and casings. The proposed correlation is given by

$$h_c = \frac{0.9512 \left(\frac{r_{int}}{r_{out}}\right)^{1.0987} \cdot k \cdot Ra^{0.2469}}{d_h}. \quad G. 5$$

G.2 EVALUATION OF THE FORMATION MODEL

Applying a radial energy balance on the formation leads to the following one-dimensional transient governing equation of energy conservation in cylindrical coordinates

$$\frac{1}{r} \frac{\partial T_{ft}}{\partial r} + \frac{\partial^2 T_{ft}}{\partial^2 r} = \frac{1}{\alpha_{ft}} \frac{\partial T_{ft}}{\partial t}, \quad \text{G. 6}$$

where T_{ft} and α_{ft} are the formation temperature and thermal diffusivity, respectively. Given the appropriate boundary conditions, Eq. (G. 6) can be solved using Laplace Transforms or other analytical methods. When coupled with the heat transmission inside the wellbore, and considering a constant heat transfer rate from the wellbore to the formation, the temperature of the interface between the wellbore and the formation can be written as (Hasan and Kabir, 1991)

$$T_{wf} = \frac{k_{ft} T_{ft,i} + r_{to} U_t f(t) T_f}{k_{ft} + r_{to} U_t f(t)}, \quad \text{G. 7}$$

where $f(t)$ is the transient dimensionless temperature. In this thesis several formation models are compared in order to estimate the $f(t)$ transient function.

G.2.1 Ramey (1962)

The first key work to provide a solution for T_{wf} used the Carslaw and Jaeger solution (1959) for an infinitely long cylinder with a constant wall heat flux (Ramey, 1962). In this work, a transient dimensionless temperature for long times (more than 7 days) is defined as

$$f(t) = \ln(2\sqrt{t_D}) - 0.2886, \quad \text{G. 8}$$

where t_D is the dimensionless time function, which represents the transient diffusion time as follows

$$t_D = \frac{\alpha_{ft} \cdot t}{r_{wb}^2}. \quad \text{G. 9}$$

G.2.2 Hasan & Kabir (1991)

Using the principle of superposition, Hasan and Kabir (1991) provided an analytical solution for $f(t)$. The results were plotted and fitted to yield two new $f(t)$ functions depending on the production time

$$f(t) = \begin{cases} 1.1281\sqrt{t_D} \cdot (1 - 0.3\sqrt{t_D}), & \text{if } t_D \leq 1.5 \\ [0.4063 + 0.5 \ln(t_D)] \cdot \left[1 + 0.6/t_D\right], & \text{if } t_D > 1.5 \end{cases} \quad \text{G.10}$$

G.2.3 Chiu and Thakur (1991)

Based on the exact solution of Carslaw and Jaeger (1959) for $f(t)$, Chiu and Thakur (1991) derived a new correlation expression valid for all times,

$$f(t) = 0.982 \ln(1 + 1.81t_D). \quad \text{G.11}$$

G.2.4 Cheng *et al.* (2011)

Cheng *et al.* (2011) developed a new correlation for $f(t)$ that takes into account the wellbore heat capacity,

$$f(t) = \ln(2\sqrt{t_D}) - 0.2886 + \frac{1}{4t_D} \left[1 + \left(1 - \frac{1}{\omega} \right) \cdot \ln(4t_D) + 0.5772 \right], \quad \text{G.12}$$

where ω is the ratio of the formation heat capacity and the wellbore heat capacity:

$$\omega = \frac{(\rho c_p)_{ft}}{(\rho c_p)_{wb}}, \quad \text{G.13}$$

where ρ is the density and c_p is the specific heat capacity.

In this thesis, a hybrid approach has been proposed to estimate $f(t)$ while considering the existing models of Ramey, 1962; Hasan and Kabir, 1991 and Cheng *et al.* (2011), based on the t_D , as follows

$$f(t) = \begin{cases} 1.1281\sqrt{t_D} \cdot (1 - 0.3\sqrt{t_D}), & \text{if } t_D \leq 0.5 \\ \ln(2\sqrt{t_D}) - 0.2886 \\ + \frac{1}{4t_D} \left[1 + \left(1 - \frac{1}{\omega}\right) \cdot \ln(4t_D) + 0.5772 \right], & \text{if } 0.5 < t_D \leq 20 \\ \ln(2\sqrt{t_D}) - 0.2886, & \text{if } t_D > 20 \end{cases}, \quad \text{G.14}$$

The reason for adopting this approach meets the observations made by Cheng *et al.* (2011) and Hasan and Kabir (1991). The former pointed out that, for very short transient ($t_D < 0.5$), the correlation based on the ratio between the formation and wellbore heat capacities should not be employed since there is no significant contribution of the formation to the wellbore thermal behavior. The latter stated that, for very short and for long transients, their approach presented an excellent agreement with the exact solution for the transient diffusion in the formation.